Universitat de València
DEPARTAMENT DE FÍSICA ATÒMICA
MOLECULAR I NUCLEAR

High-Gradient Accelerating Structure Studies and their Application in Hadrontherapy

TESI DOCTORAL EN FÍSICA

Silvia Verdú Andrés

Desembre de 2012

Supervisors:
Ugo Amaldi
Ángeles Faus-Golfe

Prof. UGO AMALDI, President of TERA Foundation,
Dra. ÁNGELES FAUS GOLFE, Científic Titular del Consejo Superior de Investigaciones Científicas (CSIC),

CERTIFIQUEM:

Que la present memòria *High-gradient accelerating structure studies and their application in hadrontherapy* ha estat realitzada baix la nostra direcció en el Departament de Física Atòmica Molecular i Nuclear de la Universitat de València per Silvia Verdú Andrés i constitueix la seua Tesi Doctoral.

I per a que així conste, firmem el present Certificat.

Firmat: Ugo Amaldi

Firmat: Ángeles Faus Golfe

Resumen

Este proyecto de tesis doctoral tiene como objetivo el estudio de las cavidades de aceleración de alto gradiente y su aplicación al campo de la hadronterapia, en particular, al desarrollo de un acelerador lineal (*linac*) para hadronterapia.

Las reducidas dimensiones de los *linacs* que usan estructuras de Radio-Frecuencia (RF) de alto gradiente contribuyen a su menor coste y los hacen muy atractivos para su aplicación en una amplia variedad de campos, desde los láseres a electrones libres (*Free-Electron Lasers* - FELs) hasta los aceleradores para hadronterapia. Sin embargo, el funcionamiento de las estructuras de RF de alto gradiente está limitado por la aparición de arcos eléctricos (*RF breakdowns*), que pueden provocar pérdidas de partículas del haz. Estas pérdidas pueden a su vez ocasionar graves daños en la superficie de la estructura de aceleración, emisión de radiación, activación de la estructura y pérdida del vacío, que finalmente repercutirán en el funcionamiento de la estructura. Los estudios realizados con motivo del desarrollo de los colisionadores lineares CLIC (*Compact Linear International Collider*) y NLC (*Next Linear Collider*) investigaron el funcionamiento de estructuras de RF de alto gradiente operando entre 12 y 30 GHz. Recientemente una estructura de aceleración de CLIC a 12 GHz alcanzó un gradiente de aceleración de 100 MV/m [1]. Este hecho, junto con una mayor comprensión del fenómeno de RF breakdown, ha estimulado el uso de estructuras de RF de alto gradiente en otros campos.

La existencia de aceleradores compactos y de bajo consumo energético que proporcionasen haces con las características apropiadas para su uso en hadronterapia contribuiría enormemente a la difusión y el desarrollo de esta técnica de tratamiento de tumores. La tecnología de alto gradiente puede ayudar en la realización de una máquina compacta y de bajo consumo energético. El *cyclinac*, la combinación de un ciclotrón y un linac de alto gradiente, es un concepto propuesto por la fundación *Fondazione per la Adroterapia Oncologica* (TERA) y ha sido especialmente diseñado para la hadronterapia. Su alta frecuencia de repetición y la posibilidad de variar la energía del haz en pocos milisegundos, pulso a pulso, actuando en la potencia de RF que alimenta la estructura, lo hacen apropiado para tratar órganos en movimiento.

El primer prototipo de un módulo de un linac para tratamiento de tumores con protones, o protonterapia, conocido como *LInac BOoster* (LIBO), ha sido construido y testeado por TERA [2]. Este prototipo opera a la frecuencia de 3 GHz. Esta frecuencia no se había utilizado nunca en la aceleración de protones, aunque es común en los

linacs de electrones de hasta 20 MeV utilizados ampliamente en el medio hospitalario.

Una evolución interesante del concepto de LIBO es la estructura llamada CABOTO: *Carbon Booster for Therapy in Oncology*, que es una adaptación de LIBO para hadronterapia. CABOTO permite acelerar moléculas de hidrógeno e iones de carbono hasta unos 400 MeV/u provenientes de un acelerador de rango de energía limitado como podría ser un ciclotrón. Las dimensiones de CABOTO podrían reducirse si se pudiesen conseguir altos gradientes de aceleración en sus celdas sin comprometer el buen funcionamiento del acelerador. Por otra parte, aumentar la frecuencia de resonancia de las celdas podría permitir conseguir aceleradores más cortos que consumiesen menos energía. Las frecuencias estudiadas por los colisionadores lineales tales como CLIC, entre 12 y 30 GHz, conducen a celdas de dimensiones muy reducidas, que complican su producción y manipulación, y consecuentemente encarecen la fabricación del acelerador. A este respecto, la frecuencia de 5.7 GHz podría ser una solución de compromiso.

En este contexto, varios tests de alta potencia de cavidades de aceleración operando entre 3 y 5.7 GHz han sido proyectados y realizados en el marco del programa de alto gradiente de TERA para entender el comportamiento, y especialmente, evaluar los límites de funcionamiento de dichas cavidades a altos gradientes de campo. Además estos tests han permitido la comprobación de la validez de los modelos de operación a altos gradientes de estructuras de RF recientemente propuestos: el modelo de flujo de potencia (*power flow model*) [3], que asocia la limitación de alto gradiente a una cantidad electromagnética acuñada con el nombre de vector de Poynting modificado, porque tiene en cuenta no sólo el flujo de potencia real sino también el imaginario, y el modelo de estrés (*stress model*) [4], que cuantifica la dependencia de la tasa de *RF breakdowns* en función del campo eléctrico aplicado a la superficie de una estructura cristalina. A tal efecto, una colaboración entre la fundación TERA y el grupo de diseño de estructuras de RF de CLIC en el CERN (*Centre Européen pour la Recherche Nucleaire*) ha sido establecida. Dicho programa comprende el diseño, realización y test de RF de:

- Una cavidad de 3 GHz con una única celda de aceleración.
- Tres cavidades de 5.7 GHz con una única celda de aceleración cada una de ellas.
- Una sección de una estructura de aceleración de CABOTO, con múltiples celdas, cuya frecuencia vendrá determinada de acuerdo a la experiencia adquirida en la realización y test de alta potencia de RF de las cavidades anteriores.

La primera parte de este trabajo de investigación se centra en el programa de alto gradiente de TERA. En particular, describe el diseño y realización de las cavidades con una única celda de 3 y 5.7 GHz. La geometría de las celdas fue determinada en un estudio previo a este trabajo con el programa de simulación de campos electromagnéticos *Superfish* [5–7]. La geometría final de la cavidad, incluyendo el diseño de la apertura de acoplamiento, fue estudiada en este trabajo con el programa de simulación de campos electromagnéticos *HFSS* [8].

Este trabajo de investigación se ocupa asimismo de los tests de RF de la cavidad de 3 GHz realizados en las instalaciones de la *CLIC Test Facility* (CTF3) en el CERN y también del test de RF del prototipo de una estructura de aceleración de 5.7 GHz diseñada para aumentar la energía final del haz de electrones del FEL SPARC (*Sorgente Pulsata e Amplificata di Radiazione Coerente*) del *Istituto Nazionale di Fisica Nucleare - Laboratori Nazionali di Frascati* (INFN - LNF) [9, 10], realizado en KEK (*High Energy Accelerator Research Organization*).

Los resultados obtenidos para las estructuras operando entre 3 y 5.7 GHz fueron confrontados con los datos recogidos por los estudios de alto gradiente realizados en el marco del desarrollo de los colisionadores lineales CLIC y NLC, correspondientes a un rango de frecuencias entre 12 y 30 GHz. Este trabajo permitió extender el rango de frecuencias de datos experimentales de 3 a 30 GHz. Los datos recabados sirvieron para verificar la validez del modelo de flujo de potencia (*power flow model*) y del modelo de estrés (*stress model*). Ambos modelos se ajustaban bien a los datos experimentales recogidos en este trabajo, por lo que los modelos parecen válidos para describir el funcionamiento de estructuras de RF de alto gradiente operando en el rango de frecuencias estudiado.

El programa de alto gradiente de TERA aún no ha finalizado: el test de alta potencia de RF de las cavidades de una única celda operando a 5.7 GHz será realizado próximamente en las dependencias de ADAM S.A. [11], de forma similar a los tests de alta potencia de RF descritos en este trabajo.

La segunda parte de este trabajo presenta el diseño y funcionamiento de un linac compacto y de bajo consumo expresamente diseñado para hadronterapia, CABOTO. La alta frecuencia de resonancia del linac, 5.7 GHz, permite el uso de altos gradientes de aceleración (entre 32 y 34 MV/m, correspondientes a un campo eléctrico máximo de pico de unos 170 MV/m) y un consumo reducido. La geometría de las celdas de CABOTO fue optimizada con el objeto de maximizar la *effective shunt impedance* (entre 100 y 130 MΩ/m) y así reducir el consumo del linac a partir de simulaciones realizadas con *Superfish* y gestionadas por el código *Superfisherman*. en cuyo desarrollo la autora de este trabajo fue partícipe. Iones de carbono completamente ionizados, $^{12}C^{+6}$, son acelerados hasta una energía de 150 MeV/u en un ciclotrón isócrono y luego vienen inyectados en CABOTO, donde a lo largo de sus 24 metros de longitud pueden alcanzar una energía de 410 MeV/u. El linac está dividido en 16 unidades, cada una de las cuales viene alimentada por su propio klystron de 12 MW, por lo que en total CABOTO necesita 192 MW de potencia instalada. La división del linac en unidades independientemente alimentadas permite variar la energía final del haz cambiando la potencia que alimenta a las diferentes unidades. De esta forma, el alcance del haz de iones de carbono proporcionado por CABOTO puede variarse con un paso de 2 milímetros. El estudio de las características del haz de CABOTO se realizó con los programas de simulación de dinámica del haz *DESIGN* [12], *LINAC* [13] y *TRAVEL* [14]. La alta frecuencia de repetición de CABOTO, 300 Hz, combinada con un sistema de retroalimentación en 3D, permite el tratamiento de órganos en movimiento.

Los resultados de los test de RF se pueden usar también para estimar el fun-

cionamiento de otras estructuras de RF a alto gradiente, como las estructuras de aceleración de CABOTO, asumiendo que los resultados obtenidos para una estructura operando a cierta frecuencia pueden ser reescalados a otra estructura operando en la misma frecuencia pero con diferente geometría a la de la primera estructura simplemente en función de cantidades electromagnéticas como el campo eléctrico o el vector de Poynting modificado. De acuerdo con este razonamiento, y en base a los datos experimentales recabados en este trabajo, la tasa de RF breakdowns que se podría esperar durante la operación a alto gradiente de CABOTO satisfacería los requisitos clínicos.

CABOTO se perfila así como un plausible candidato para liderar la nueva generación de aceleradores para hadronterapia, que debería ofrecer la posibilidad de utilizar las mejores técnicas de irradiación y facilitar el acceso de este tratamiento de tumores a una mayor parte de la población.

Abstract

Recent progress on high-gradient performace of normal-conducting accelerating structures, in particular the achievement of 100 MV/m of accelerating gradient in the accelerating structures for the Compact Linear International Collider (CLIC), and a deeper understanding of breakdown phenomenology encourage the use of normal-conducting accelerating structures for other applications.

The field of hadrontherapy would benefit greatly from compact, efficient accelerators and gantries that make the setup and operation of a hadrontherapy facility more affordable. High-gradient technology could help in the realization of a compact, efficient machine. The cyclinac is an accelerator concept specially designed for its application in hadrontherapy which takes advantage of high-gradient technology. The concept was proposed by TERA foundation and it consists of a cyclotron which serves as the injector of a high-gradient linac. Its high-repetition rate and the possibility to vary the beam energy from pulse to pulse by acting only on the RF system (without the need of absorbers) in few miliseconds, makes it suitable for the treatment of moving organs.

However, high-gradient operation of RF cavities is limited by the undesired RF breakdown phenomena (vacuum RF arcs). RF breakdowns cause beam losses, and through losses, material activation, cavity surface damages, radiation and vacuum deterioration, and therefore, compromise the reliability of the accelerator. TERA foundation initiated a high-gradient test program to understand the maximum operation limit of a cyclinac without compromising its reliability. The TERA high-gradient test program consists of a series of high-power tests of standing-wave single-cell cavities working between 3 and 5.7 GHz. The high-power tests should give insight which frequency shows the best performances for being used in the cyclinac, as well as the highest operation field at which the linac could operate reliably.

The first section of this doctoral thesis tackles the preparation and high-power testing of different RF structures within the framework of the TERA high-gradient test program and performed in close collaboration with the

CLIC-RF structure development group at CERN.

The section is divided into four chapters. The first chapter is a brief introduction to the field of high-gradient linear accelerators. The second chapter introduces the TERA high-gradient test program, presents its main motivations and objectives and describes the main features of the test devices. The third chapter is devoted to the design, production and performance measurements at low and high power of a 3 GHz single-cell cavity. The fourth chapter reports on the design studies, production and low power measurements of a series of 5.7 GHz single-cell cavities. The fifth chapter explains the high-power measurements of a 5.7 GHz travelling-wave structure.

The second section of the thesis deals with the design of a high-gradient linac for hadrontherapy and discusses its performance. The breakdown probability of the machine is evaluated according to the results obtained from the high-power tests.

The section is divided into two chapters. The first chapter gives an introduction to the field of accelerators for hadrontherapy, with special focus on the different linac-based solutions proposed for hadrontherapy applications. The second chapter presents the design and feasibility study of a high-gradient linac for hadrontherapy.

This work has been developed under the umbrella of ENLIGHT, the European Network for LIGht ion Hadron Therapy, within the framework of PARTNER, the PARticle Therapy Network for European Radiotherapy, a training platform funded by the European FP7 Programme [15].

Contents

Chapter 1

High-Gradient Normal-Conducting RF Linear Accelerators

RF breakdown is a serious constraint for the operation of RF structures at high gradients, as this phenomenon limits the maximum gradient that can be excited while maintaining reliable operation. The achievement of higher gradients would be useful to either reduce the machine dimensions or increase the energy range of accelerators. Many studies have permitted a deeper understanding on RF breakdown phenomena, which translated into enhanced high-gradient performances of RF structures. Most of the progress was based on a better RF design of the devices and more sophisticated manufacturing techniques. This chapter introduces the basics of RF linear accelerators and discusses the performance limitations, state-of-the-art and applications of the high-gradient RF structures, with special emphasis on the models which try to explain the nature of RF breakdowns.

1.1 Basics of RF Linear Accelerators

In 1928 Rolf Widerøe proposed and tested the first linear accelerator. In a linac, charged particles are accelerated in a straight line either by a steady electric field or by a time-varying field. The most successful way to accelerate charged particles is to use radio-frequency RF fields, as higher accelerating voltages can be achieved in resonant RF cavities compared to those obtainable in electrostatic accelerators of similar dimensions. Therefore most of the linear accelerators proposed for hadrontherapy are based on acceleration by means of RF fields.

In the following, the basis of particle acceleration by means of RF fields is presented. The concepts introduced in this chapter are explained in detail in [16–19].

1.1.1 Particle Acceleration with RF Fields

Different types of RF accelerators have been developed. Their specific design depends on the input and output beam energy, the beam intensity and the kind of particle that has to be accelerated.

RF fields are alternating-current electromagnetic fields and for accelerator applications typically lie in the in the frequency range between 10 MHz to 30 GHz. A linear accelerator consists of an array of cavities or cells where RF electromagnetic fields are generated and timed such that a particle absorbs and accumulates energy from each section as it travels through them.

The RF field sign is reversed every half period $T/2$, where T is the period of the RF cycle. The motion of the particles which travel through the accelerator must be synchronized with the RF field frequency f ($f = 1/T$) to ensure that the particles are exclusively exposed to accelerating RF phases and not to decelerating ones. Hence, a particle must run from an accelerating cavity to the next one during the time $T/2$ it takes the field to reverse sign. During this half period $T/2$, the particle has to travel through the beam pipe that connects two successive cavities to be shielded from the field. The distance d between the centers of two accelerating cavities has thus to be

$$d = vT\,\frac{\Delta\phi}{2\pi}, \tag{1.1}$$

where v is the velocity of the particle and $\Delta\phi$ is the phase shift from one cavity to the contiguous one. Eq. (1.1) is known as the *synchronicity condition*. When v increases during acceleration, either $\Delta\phi$ must decrease or d must increase, so that the synchronicity condition is preserved. Fig. 1.1 illustrates a coupled-cell cavity for non-relativistic particle acceleration in which ϕ is fixed by the coupling between cells and d increases from cell to cell to keep synchronism.

The electric field configurations for different phase shifts, also called structure modes, are represented in Fig. 1.2. Each mode presents advantages and disadvantages that will not be discussed in this document.

The simplest cavity of a linear accelerator is designed in such a way that electromagnetic modes which predominantly have electric field components in the direction of propagation of the particles (longitudinal components). The wave equation in cylindrical coordinates (r, θ, z) for the E_z component in a cylindrical waveguide is

$$\frac{\partial^2 E_z}{\partial r^2} + \frac{1}{r}\frac{\partial E_z}{\partial r} + \left(k_c^2 - \frac{n^2}{c^2}\right)E_z = 0 \tag{1.2}$$

where r is the position vector, k_c is the cut-off wave vector separating propagating from evanescent solutions and c is the speed of light in vacuum. The solution of Eq. (1.2) are the Bessel functions J_n, which represent many modes n for the field component E_z consistent with the boundary conditions:

$$E_z = A\,J_n(k_c r) \tag{1.3}$$

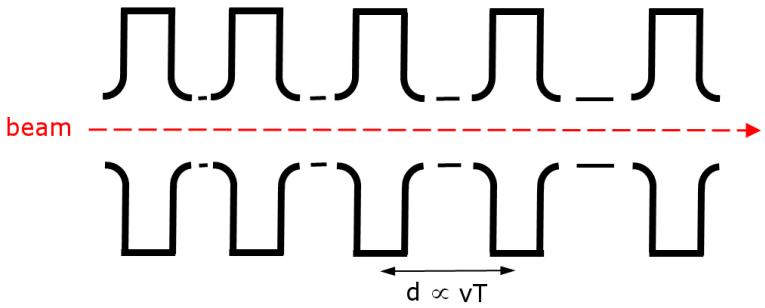

Figure 1.1: *Acceleration of non-relativistic particles in a coupled-cell cavity. The synchronicity condition imposes that the distance d between the center of two accelerating cavities has to be proportional to the velocity of the particle v times the period of the RF cycle T.*

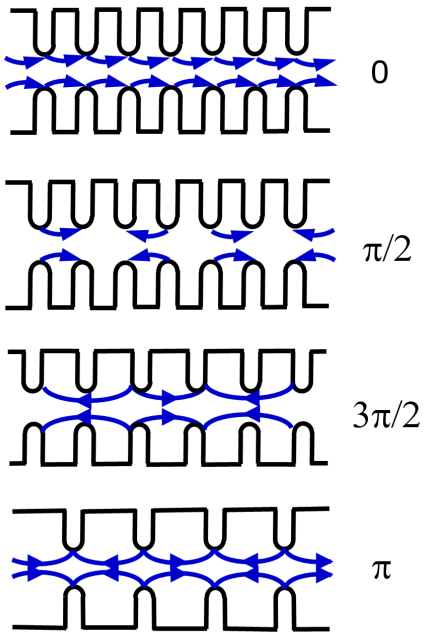

Figure 1.2: *Instantaneous electric field configurations for different structure modes.*

There are two kinds of modes: the TE modes (just the transversal components of the electric field are different from zero) and the TM modes (just the transversal components of the magnetic field are different from zero). Hence, only TM modes can be useful for acceleration. The solutions $TM_{\theta rz}$ are characterized by three indexes: θ and r indicate the number of halfwaves for the electric field in the azimuthal and the radial coordinates and z indicates the number of halfwaves for the electric field in the longitudinal direction. The selection of the appropriate mode gives a more efficient use of the field for acceleration. In Fig. 1.3 the simplest TM mode, the TM_{010}, is shown. TM_{010} means that the magnetic field has only transversal components and that the electric field has only radial component with a node in the cavity wall. This is the mode most commonly used for particle acceleration.

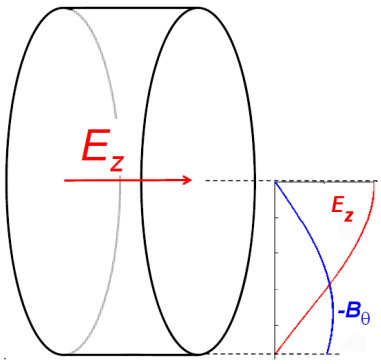

Figure 1.3: *Electric and magnetic fields of the TM_{010} mode in a cylindrical cavity.*

Cavity geometry plays an important role on the field distribution and it also influences important quantities such as the efficiency with which the energy stored in the cavity is used in order to accelerate the particles. Fig. 1.4 shows the typical geometry of a cell for low-velocity particles and the name of its parameters. The next section introduces the basic electromagnetic quantities which characterize an accelerating cavity and the figures of merit which describe its performances.

1.1.2 Basic Electromagnetic Quantities of a Single RF Cavity

Energy can be transferred from an electromagnetic wave to an electrically-charged particle in an RF cavity. Consider the accelerating gap shown in Fig. 1.5(a) and suppose that the electric field seen by a particle with velocity v is harmonically varying in time with *frequency* ω as follows:

$$E_z(r = 0, z, t) = E(0, z)e^{j(\omega t(z)+\phi)}, \tag{1.4}$$

where $t(z) = \int_0^z dz/v(z)$ is the time when the particle is at position z and ϕ is the RF phase when the particles crosses the middle of the gap, z=0, at t=0.

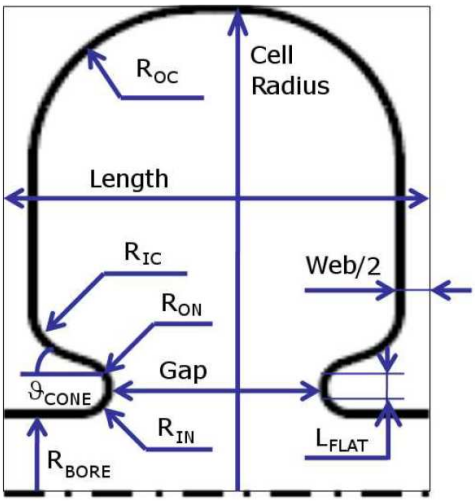

Figure 1.4: *Cell geometry and name of its parameters.* R_{OC} *and* R_{IC} *stand for outer and inner corner radii, respectively.* R_{ON} *and* R_{IN} *refer to the outer and inner nose radii.*

The energy gain ΔW of a particle with charge q passing through the gap is

$$\Delta W = q \int_{-L/2}^{L/2} E(0,z) \cos\left(\omega t(z) + \phi\right) dz \tag{1.5}$$

which can be written as follows

$$\Delta W = q V_0 T \cos\phi \tag{1.6}$$

if we define the axial RF voltage V_0 as the voltage gain experienced by a particle that travels through a constant DC field equal to the field in the gap at time $t = 0$,

$$V_0 = \int_{-L/2}^{L/2} E(0,z) dz \tag{1.7}$$

The *transit time factor* T is defined as

$$T = \frac{\int_{-L/2}^{L/2} E(0,z) \cos\omega t(z) dz}{\int_{-L/2}^{L/2} E(0,z) dz} - \tan\phi_S \frac{\int_{-L/2}^{L/2} E(0,z) \sin\omega t(z) dz}{\int_{-L/2}^{L/2} E(0,z) dz} \tag{1.8}$$

If the cells are all symmetric, $E(-z) = E(z)$ and $t(-z) = -t(z)$, then the numerator of the second term becomes zero, giving

$$T = \frac{\int_{-L/2}^{L/2} E(0,z) \cos\omega t(z) dz}{\int_{-L/2}^{L/2} E(0,z) dz} \tag{1.9}$$

From this expression we clearly understand that $|T| \leq 1$ and measures the reduction in energy gain caused by the sinusoidal time variation of the electric field.

In first approximation, supposing the change of particle velocity in the gap is small compared with the initial velocity and assuming that the E-field has a square profile like the one shown in Fig. 1.5(b), T is simply

$$T = \frac{\sin \pi L/\beta\lambda}{\pi L/\beta\lambda} \tag{1.10}$$

where λ is the free space wavelength and β is the normalized speed of the particle.

The spot size of real beams is not infinitesimal but occupies some space around the beam axis. Beam particles experience an electric field $E(r,z)$ as the one shown in Fig. 1.5(c), different from the on-axis field $E(0,z)$. Analytical expressions of $E(r,z)$ are derived and shown in [16].

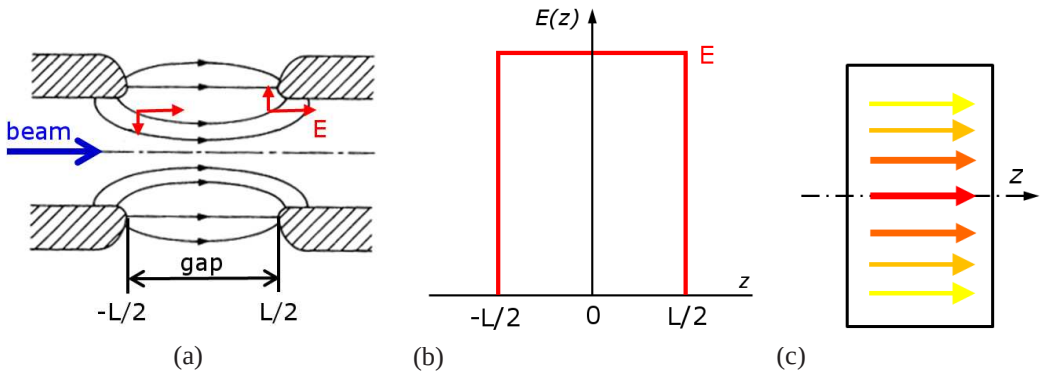

Figure 1.5: a) *Accelerating gap*; b) *E-field square profile*; c) *E-field distribution. The color scale expresses the intensity of the E-field: dark red represents the highest E-field intensity and yellow represents the lowest E-field intensity.*

In multi-cell structure, the synchronous particle refers to a virtual particle which always travels synchronized with the accelerating field. Beam particles with different velocity than the synchronous particle will arrive at different relative times with respect to the synchronous particle during their motion along the structure. In consequence they will see different accelerating voltages and increase their velocities according to the accelerating gradient they are subject to. Take as example the synchronous particle M_1 and two particles of the beam, a fast particle P and a slow particle P', with velocity different from the velocity of M_1 (see Fig. 1.6). The particle P (P'), early (late) in time with respect to the synchronous particle M_1, will see a smaller (larger) accelerating voltage and consequently will get less (more) acceleration. This particle will arrive late (early) in time with respect to M_1 in the next gap, becoming particle P' (P). These particles are considered stable points because their phases oscillate around

the synchronous particle phase during acceleration. Particles M_1, N_1, M_2 and N_2 are all particles seeing the same accelerating voltage and will see the same phase of the accelerating field as they go through the linac. Particles Q and Q' also have velocities close to the synchronous particle one, but do not behave like P and P'. Particles Q and Q' are sitting on the falling slope of the sinusoidal variation of accelerating voltage with time, so the particle Q (Q'), early (late) in time with respect to N_1, will see a larger (smaller) accelerating voltage and will hence get more (less) acceleration. In the next gap, this particle will thus arrive even earlier (later) with respect to N_1. Particles Q and Q' are unstable points because they move away from the synchronous particle N_1 as they travel from gap to gap. Fig. 1.7 shows the energy gain variation with time and the corresponding effective potential energy function U which leads to the restoring force responsible of pulling back (out) the stable (unstable) particles. This is the principle of *phase stability*.

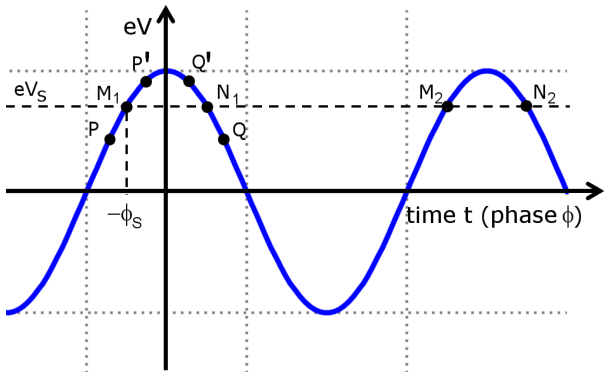

Figure 1.6: *Phase stability principle.*

The difference in energy gain of any beam particle W with respect to the synchronous particle energy gain W_S obeys the following equation:

$$\frac{d\,(W - W_S)}{ds} = qE_0T\,(\cos\phi - \cos\phi_S) \tag{1.11}$$

where q is the charge of the particle, E_0 is the average electric field, T is the transit-time factor, and ϕ is the phase of the particle.

The frequency Ω of small energy and phase oscillations of beam particles around a reference particle is:

$$\Omega^2 = -\frac{qE_0\omega\sin\phi_S}{mv_S^3} \tag{1.12}$$

where ω is the RF frequency, m is the particle mass and v_S is the velocity of the synchronous particle. In energy W – phase ϕ phase space, the curve corresponding to the maximum energy W_{max} for which a stable trajectory is possible is called separatrix. The oscillation around the synchronous particle ϕ_S is bounded to this curve. Particles

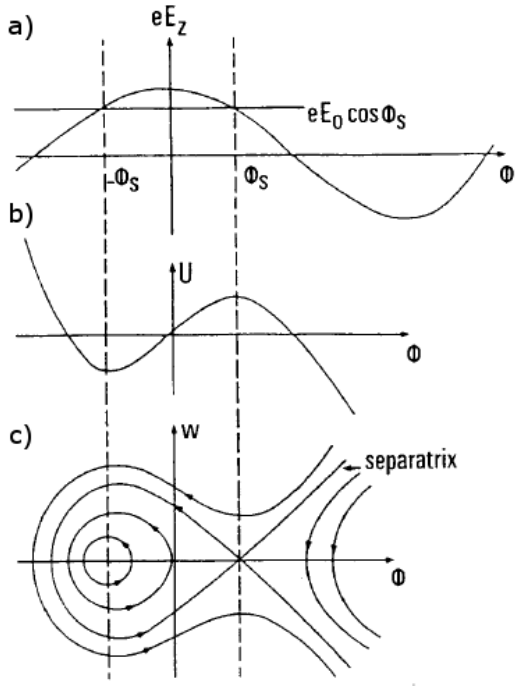

Figure 1.7: *a) Energy gain evolution in time. b) Effective potential energy function with time. c) Phase stability diagram.*

inside the separatrix are all describing stable trajectories thanks to the focusing properties of the effective potential energy function U in this region. The area enclosed by the separatrix is called *RF bucket*. The maximum energy W_{max} achieved by a particle is when $\phi = 0$ and the maximum phase ϕ_{max} is achieved when $W = 0$. Fig. 1.7(c) shows the phase stability diagram.

The phase space trajectories of beam particles trace out an ellipse. The area of this ellipse is proportional to the so-called *longitudinal emittance* of the beam. Liouville's theorem states that the longitudinal emittance of a beam of non-interacting particles remains constant for adiabatic processes. The theorem thus does not apply in case of particle losses, dissipative processes or damping processes [20].

The synchronous phase ϕ_S determines the longitudinal beam emittance. The maximum phase amplitude of the RF bucket is proportional to the synchronous phase. For small synchronous phases, the phase acceptance width Φ is approximately $3|\phi_S|$. The longitudinal beam acceptance hence increases with the synchronous phase. On the other hand, the synchronous phase also influences the maximum achievable accelerating gradient. The smaller the synchronous phase is, the larger the energy gain will be. The choice of the phase is simpler for relativisitic particles. Phase oscillations become very slow at relativistic velocities, so in practice particles get trapped in phase around the initial phase. In this case, the crest of the wave can be used for acceleration.

Figures of merit

The figures of merit which describe the accelerating performance of a single RF cavity are:

Accelerating gradient The average electric field, E_0, is the average over the length L of the electric field along the direction of propagation of the beam for a given moment in time when $E(t)$ is maximum. Physically it gives a measure of how much field is available for acceleration for a particle at $\phi_S = 0$. It depends on the cavity shape, on the resonating mode and on the frequency but not on the choice of L. In the case of a multi-cell cavity, the natural choice for L is the geometric cell length.

In normal-conducting structures for slow particle acceleration, the cells typically incorporate nose cones that enhance particle acceleration, as nose cones concentrate E_z near the beam for a certain fixed stored energy. See Fig. 1.4 with the main cell geometry parameters.

The accelerating gradient is given by the product E_0T. It takes into account the time variation of the electric field while the particles traverse the cavity. In terms of this parameter, the energy gain (Eq. (1.6)) becomes

$$\Delta W = qE_0TL\cos\phi_S \tag{1.13}$$

This expression is known as *Panofsky equation* [16].

Shunt impedance The shunt impedance R_s is a measure of how well we can concentrate the electric RF field in the region where the particles pass and are accelerated. In other words, it is the effectiveness of producing a certain axial voltage V_0 with the available energy in the cavity. This energy is dissipated in the cavity walls due to the finite electric conductivity. Consequently, one has to maximize the shunt impedance in order to minimize the power consumption for a fixed acceleration voltage. It is given by

$$R_s = \frac{V_0^2}{P_0} \tag{1.14}$$

For a given electric field, the shunt impedance increases linearly with the cavity length, as the RF voltage and the dissipated power also do. In order to avoid the dependence of these parameters with the field level and the cavity length one introduces the *shunt impedance per unit of length*

$$Z = \frac{R_s}{L} \tag{1.15}$$

where L is the tank length over which the acceleration takes place.

Usually one is interested in maximizing the particle energy gain per unit of dissipated power P_0. The peak energy gain of a particle occurs when $\phi = 0$, and is $\Delta W_{\phi=0} = qV_0T$. We can define a new parameter of the cavity

$$ZTT = \left[\frac{\Delta W_{\phi=0}}{q}\right]^2 \frac{1}{P_0 L} = \frac{[V_0 T]^2}{P_0 L} = \frac{[E_0 T]^2}{P_0/L} = ZT^2 \tag{1.16}$$

known as *effective shunt impedance per unit of length*. ZTT (usually given in $M\Omega/m$) measures the effectiveness per unit of dissipated power for delivering energy to a particle in a given length. In cavity design one of the main objectives is to find the geometry that maximizes the effective shunt impedance per unit of length.

Quality factor The internal quality factor Q_0 takes into account the lossy behavior of the resonator due to the finite conductivity σ_d of the cavity walls. It is proportional to the ratio of stored energy U over dissipated energy U_d per cycle,

$$Q_0 = 2\pi \frac{U}{U_d} = \frac{\omega U}{P_0} \tag{1.17}$$

where ω is the resonant frequency of the cavity and P_0 is the power dissipated in the cavity by electrical resistance.

Extra power is extracted out of the cavity when it is connected to a waveguide through a coupling slot. The loaded quality factor Q_{load} is defined as

$$Q_{load} = \frac{\omega U}{P_{load}} = \frac{\omega U}{P_0 + P_{ext}} \tag{1.18}$$

where P_{ext} is the external power flowing out of the slot and P_{load} is the total power lost. Q_{load} is also related to the width of the resonance peak of a cavity

$$Q_{load} = \frac{\omega}{\Delta_H} \tag{1.19}$$

where Δ_H is the full width half maximum of the resonance peak (also denoted as resonance bandwidth). The coupling factor β_C of waveguide to cavity system is a measure of how much power coming from the power transfer line (external load) is being used to feed the cavity. The coupling factor is given by the ratio of the intrinsic quality factor Q_0 over the external quality factor Q_{ext}:

$$\beta_C = \frac{Q_0}{Q_{ext}} = \frac{P_{ext}}{P_0} \tag{1.20}$$

and fixes the quantity of power reflected by the coupling slot, given by the square of the reflection coefficient Γ,

$$\Gamma = \frac{1 - \beta_C}{1 + \beta_C}, \tag{1.21}$$

as well as the resonance bandwidth of the system. The coupling factor depends critically on the geometry and location of the coupling slot.

Defining the external quality factor Q_{ext} with an equation similar to Eq. (1.17), the loaded quality factor can be written as follows

$$\frac{1}{Q_{load}} = \frac{1}{Q_0} + \frac{1}{Q_{ext}} \tag{1.22}$$

In a free running cavity (when the excitation signal is switched off) the stored energy U varies with time according to

$$\frac{dU(t)}{dt} = -P_{load} = -\frac{\omega}{Q_{load}}U \tag{1.23}$$

and integrating

$$U(t) = U_0 e^{-t/\tau_\omega}, \tau_\omega = \frac{Q_{load}}{\omega} \tag{1.24}$$

where τ_ω is named *filling time*.

The filling time gives an idea of how long it takes to fill the cavity. For the same quality factor, the filling time is smaller for structures operating at high frequencies due to their smaller dimensions. One is interested in minimizing the filling time as much as possible because it is directly related to the overall power consumption.

Some of the power which is injected into the cavity is transferred to the beam as a result of the interaction between the beam and the cavity fields. The power P_{beam} delivered to the beam is

$$P_{beam} = I\frac{\Delta W}{q} \tag{1.25}$$

where I is the beam current and ΔW is the energy gain. Hence, the total power P_{total} required for operation is equal to

$$P_{total} = P_{beam} + P_{load} \tag{1.26}$$

Frequency Scaling of Cavity Parameters

In the selection of the operating frequency f it is important to understand how the basic geometric parameters and electromagnetic quantities of a normal-conducting single cavity scale with frequency. Assume an RF cavity with fixed accelerating gradient E_0, fixed energy gain ΔW and fixed length L. The cell radius changes proportionally to f^{-1}. The transit-time factor T and fields do not vary with the frequency. As the cell length L is fixed, the surface area of the cavity is proportional to f^{-1}, and the total

volume of the cavity is proportional to f^{-2}. Therefore, the stored energy U (volumetric quantity) is proportional to f^{-2}. The shunt impedance R_S of normal-conducting metals scales with $f^{1/2}$, so the shunt impedance per unit of length Z and the effective shunt impedance per unit of length ZTT are both scaling with $f^{1/2}$. The power dissipated P_0 in the cavity walls, which linearly depends on R_S, is proportional to $f^{-1/2}$. The quality factor Q_0, defined by Eq. (1.17), is thus scaling with $f^{-1/2}$ [16, 19]. In consequence, normal-conducting cavities operating at high frequencies require less power than those operating at low frequencies, at expenses of degrading the quality factor. Table 1.1 summarizes the dependence of each quantity on the frequency.

Table 1.1: *Scaling of basic electromagnetic quantities with frequency for normal-conducting single-cavities assuming a fixed accelerating gradient E_0, fixed energy gain ΔW and fixed length L.*

Quantity		**f scaling**
Cell radius	R	f^{-1}
Surface area	$\mathcal{S}$	f^{-1}
Volume	$\mathcal{V}$	f^{-2}
Transit-time factor	T	1
Fields	E, B	1
Stored energy	U	f^{-2}
Shunt impedance	R_S	$f^{1/2}$
Shunt impedance per unit of length	Z	$f^{1/2}$
Effective shunt impedance per unit of length	ZTT	$f^{1/2}$
Dissipated power	P_0	$f^{-1/2}$
Quality factor	Q_0	$f^{-1/2}$

1.1.3 Particle Acceleration in Multi-Gap Structures

Higher accelerating voltages can be achieved in a multi-gap structure than in a single-gap structure for the same input power. According to Eq. (1.14), the voltage excited in a single-gap structure of shunt impedance R_S which is fed by a power P is $V = \sqrt{R_S P}$. If the same amount of power P is used to feed an array of n cavities of shunt impedance R_S each, being the power uniformly distributed among all the cavities, then the voltage excited in each gap is $V_{gap} = \sqrt{R_S P/n}$ and the total voltage excited in the structure is $V_{ngaps} = \sqrt{nRP}$.

Cavities belonging to an array are not usually fed by independent power sources, which would require many power sources and large amount of waveguides, but they are interconnected by coupling holes opened on the cavity endcaps. These structures are called coupled-cavity structures and we distinguish two types: traveling-wave structures and standing-wave structures. The main characteristics of both kinds of structures are presented in the following section.

Traveling-wave structures

The *synchronicity condition* requires that an electromagnetic wave and a particle stay in phase so that the particle is continually accelerated. While the phase velocity of a wave propagating through an homogeneous waveguide is always above the speed of light, particles cannot exceed the speed of light. The traveling-wave structure is a waveguide "loaded" with some irises or disks in order to reduce the phase velocity of the propagating wave. The distance between two consecutive disks is adjusted in such a way that wave and particle are synchronized. Seen from another perspective, a traveling-wave structure is an array of cavities with openings in the cavity endcaps to allow the power flow through the structure. The cavity endcaps are the so-called disks or irises.

In a traveling-wave structure power is fed via an input coupler located at one end of the structure, then travels through the structure exciting an accelerating voltage in the different cells of the structure, goes out the structure via an output coupler and finally is absorbed in some power load (see Fig. 1.8).

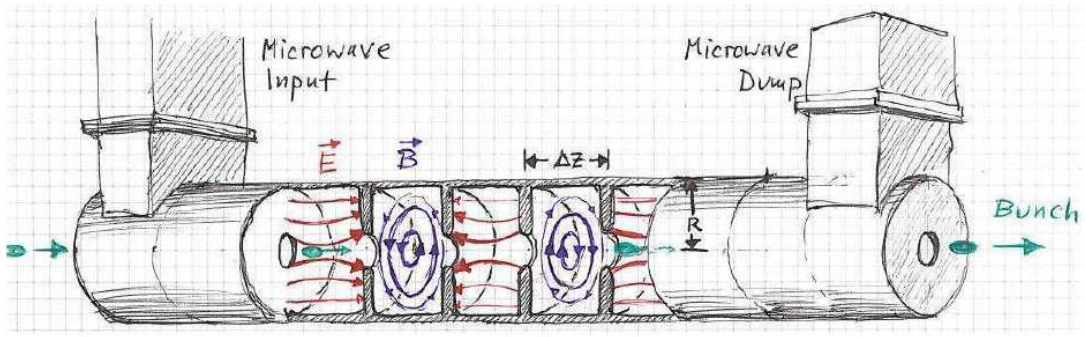

Figure 1.8: *Artist's view of traveling-wave structure (courtesy of A. Streun, PSI) [21].*

Traveling-wave structures are designed such that the phase velocity of the propagating wave is equal to the velocity of the particles to be accelerated. That is the wave and particle are synchronous. In this case, they will be accelerated or decelerated at a constant rate along the structure. Maximum acceleration will be achieved when particles travel on the crest of the wave.

If all the cells which compose the structure are equal, then the group velocity v_{group}, loaded quality factor Q_{load} and shunt impedance per unit of length Z remain constant along the structure. Such a structure is known as *constant-impedance structure*, and transmitted power and accelerating gradient decrease exponentially along the structure as follows:

$$P(z) = P_0 e^{-2\alpha z} \tag{1.27}$$

$$E(z) = E_0 e^{-\alpha z} \tag{1.28}$$

where α is the attenuation coefficient, given by:

$$\alpha = \frac{\omega}{2v_{group}Q_{load}} \tag{1.29}$$

The filling time, or time required for the RF power to travel from the input coupler to the output coupler, is:

$$t_{fill} = \frac{L}{v_{group}} = \alpha L \frac{2Q_{load}}{\omega} \tag{1.30}$$

where L is the length of the structure.

For constant-impedance structures, the power is maximum at the first cell of the structure and it drops throughtout the length of the structure, as determined by Eq. (1.27). This may pose a limitation to the highest average accelerating gradient achievable for high-gradient performance structures, in case that the accelerating gradient excited in the first cell reaches the maximum at which operation is still reliable. A solution is to make the accelerating gradient constant throughout all the structure by progressively reducing the irises size along the structure length, so that the structure is "tapered". Higher average accelerating gradients can hence be achieved in this kind of structures, within the breakdown limits, at the expenses of complicating their design. This kind of structures are known as *constant-gradient structures* and they are primarily done to maximize the overall shunt impedance of the structure.

Standing-wave structures

In a standing-wave structure, RF power propagates in both upstream and downstream directions. The standing-wave field pattern can be thought of as the sum of two waves with the same frequency traveling with the same velocity in opposite directions along the same medium. It characterizes by the existence of nodes, locations with zero displacement, and antinodes, locations with maximum displacement. The pattern does not travel in any direction, but simply oscillates.

There is a subtle difference between the filling time of a standing-wave structure and the filling time of a traveling wave structure. Whereas the filling time of a traveling-wave structure is the time required for the RF power to travel from the input coupler to the output coupler, the filling time of a standing-wave structure corresponds to the time it takes to build-up the fields in the structure. In other words, in a traveling-wave structure fields build-up in space from cavity to cavity along the structure, while they build-up in time in a standing-wave structure. Fig. 1.9 shows a simplified scheme of how RF power fills both a traveling-wave and a standing-wave structures. Indeed, standing-wave structures fill in a more uniform way than traveling-wave structures, however, for standing-wave structures the field near the coupler do tend to get closer to its steady state value faster than the field does near the ends of the structure.

The filling time of a standing-wave structure is given by the following expression:

$$t_{fill} = \frac{2Q_{load}}{\omega} \tag{1.31}$$

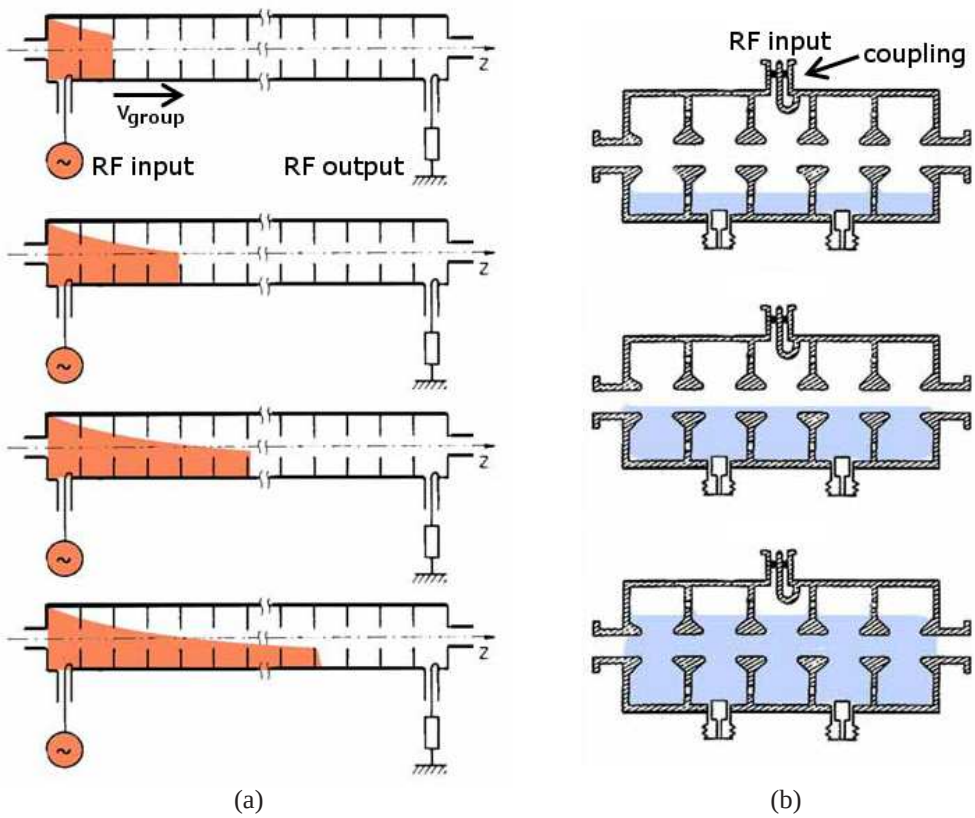

(a) (b)

Figure 1.9: *RF power filling: a) a traveling-wave structure with group velocity v_{group}; b) a standing-wave structure (courtesy of W. A. Barletta) [24, 25].*

There will be as many possible modes of operation as number of cavities that compose a standing-wave structure. The 0 and π modes are specially interesting for optimal acceleration. However, their group velocity v_{group} is zero, which makes the structures operating at these modes very sensitive to mechanical tolerances, changes in RF frequency or beam current. Any slight perturbation could change the operating mode of the structure. The operation in the $\pi/2$ mode is more stable, as it lays on the middle of the pass-band where the group velocity is the greatest, at half way between the 0-mode and the π-mode [22, 23]. Half the cells of a structure operating in the $\pi/2$-mode have zero fields, being useless for acceleration. To reduce the dimensions of $\pi/2$-mode structures, the cells with zero fields, the so-called *coupling cells*, are placed off-axis. From the beam's point of view, such structures operate in the π-mode, even if electrically operate in the $\pi/2$-mode.

A particle traveling with velocity close to the speed of light and passing through each cavity of the structure at the moment when the field reaches its crest, will receive the maximum acceleration qV. This particle should necessarily enter the cavity before the field reaches its crest and leave the cavity after the field starts diminishing. In case

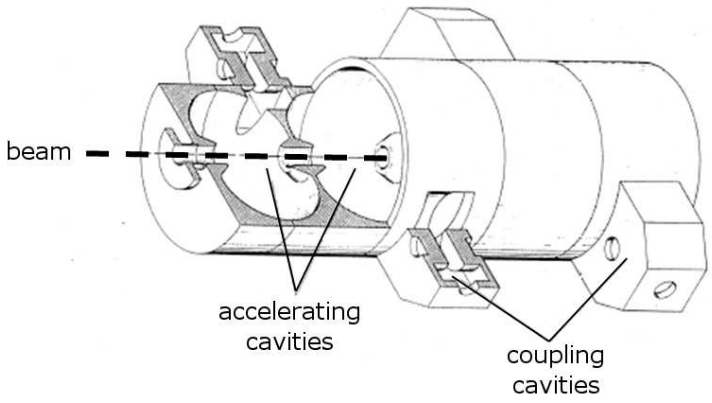

Figure 1.10: *Artist's view of a $\pi/2$-mode standing-wave structure (courtesy of W. A. Barletta) [24].*

of slow particles, the transit time is longer and the particles will consequently be less accelerated.

In standing-wave structures, the energy gain depends on the length of the RF pulse used to feed the structure. There will always be a transient during the filling of the structure for which power will be reflected. Hence, the minimum power to reach a certain stored energy and in consequence, a certain accelerating gradient, will not only depend on the shunt impedance but also on the coupling coefficient.

1.2 Particle Beam Focusing in Linear Accelerators

The electric field pattern in a cavity presents a radial component (see Fig. 1.5(a)) which will focus the particles at the cavity entrance and defocuse them at the cavity exit. In case of acceleration of non-relativistic particles in RF structures, the field increases with time as the particle passes through the gap, according to the phase stability principle. Therefore, the focusing force acting on the particle at the gap entrance will be smaller than the defocusing force exerted on the particle at the gap exit, resulting in a net defocusing effect. Seen from another perspective, the required longitudinal phase stability ($\phi_S = 0$) implies transverse defocusing due to the Maxwell's equation $\nabla E = 0$.

This net transverse defocusing has to be compensated by external magnetic fields in order to ensure stable transverse motion. Solenoids or quadrupoles can be used for this purpose. The magnetic field B of an ideal quadrupole presents zero field on-axis, is linear with the distance from the axis and its vertical and horizontal components are decoupled:

$$B_x = -gx, \; B_y = gy \tag{1.32}$$

where g is the focusing strength of the quadrupole. Quadrupoles focus in one plane while defocusing in the another due to Maxwell's equation $\nabla \times B = 0$, so in order to have overall focusing, the simplest solution is to alternate quadrupoles with opposite gradients in what is called FODO lattice. An illustration of the beam envelope in a FODO lattice is shown in Fig. 1.11.

Particle trajectories will oscillate around an equilibrium orbit in both horizontal and vertical planes in the so-called *betatron oscillations*, given by the Hill's equation [17].

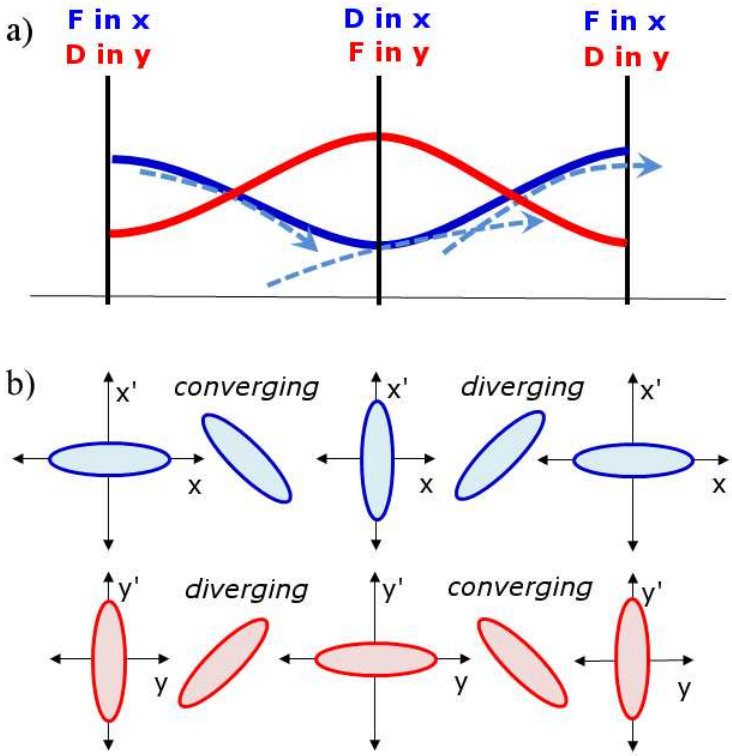

Figure 1.11: *The beam envelope is the envelope that contains the trajectories of all the beam particles: a) beam envelope for both transverse planes, x (blue) and y (red), and some particle trajectories in the x-plane (dashed blue lines) in a FODO lattice (F – focusing, D – defocusing); b) transverse phase space ellipse evolution in a FODO lattice.*

1.3 RF breakdowns, a Limitation to High-Gradient Performance

An electric discharge or arc is the current flow through a spontaneously occuring conductive path between two points at different electric potential. The phenomenon is of special interest in a number of areas of physics, astrophysics, atmospheric science and engineering. Electrical discharges generated in a controlled manner are used in many technological applications like arc welding or fluorescent lamps. For other devices such RF structures, the appearance of electrical discharges - associated to the excitation of high fields in the structures - is an undesired effect that in most of the cases compromises the operation of the device. One of the aspects of RF breakdown which is detrimental is surface damage from ion bombardment of the structure surface. Another is the energy released during RF breakdowns, which induces random beam kicks that in worst case scenario can lead to beam losses if the kick is strong enough. Repeated or strong beam losses can severely damage the RF structure with final consequences on the structure performances. For instance, structure detuning, bad coupling and/or more sparking. Electrical discharges appear in RF structures even though they are under ultra high vacuum (UHV) - where no media is hardly available for electricity conduction - if high enough electric potential difference is sustained between two points of the structure. In that particular case, the electrical discharge receives the name of vacuum arc. The accelerator community refers to the phenomenon as electric or RF breakdown.

1.3.1 Experimental Evidence

The breakdown rate *BDR* is the magnitude that quantifies the number of breakdowns N_{bd} observed during the operation of an RF structure:

$$BDR\,[bpp/m] = \frac{N_{bd}\,[breakdowns]}{N_{pulses}\,[pulses]\,L\,[m]} \tag{1.33}$$

where N_{pulses} is the number of RF pulses sent to the structure during the measurement and L is the length of the structure. The breakdown rate is typically given in breakdowns per pulse per meter (bpp/m).

RF breakdowns are typically identified by the sudden, abrupt increase of emitted current and/or reflected RF power 1.12. The RF breakdown is accompanied by high currents, which produce X-rays when they hit the structure walls, and a sound burst in the copper due to rapid heating. In addition there is the emission of light from the plasma which forms during breakdown. The pressure inside the structure rises during RF breakdown.

The high-gradient performance of an RF structure is greatly influenced by the interior surface state. Sharp edges like the ones present in pits, tips, grain boundaries or chips and scratches generated during manufacturing and manipulation of the structure

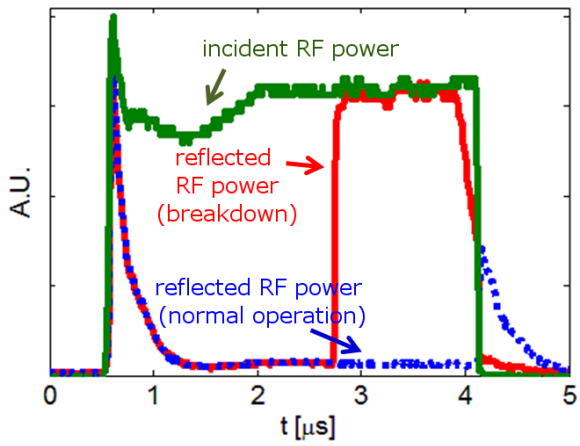

Figure 1.12: *Reflected RF power for normal operation and during RF breakdown.*

can become a source of RF breakdowns. Impurities like dust or cleaning fluid remains must be avoided for the same reason. A smooth surface is necessary to achieve outstanding performances in high-gradient RF structures. Some theories indicate that whiskers and voids observed in the surfaces after the application of high fields could be the origin of RF breakdowns. At the same time, the RF breakdown itself is the mechanism that smooths the surface imperfections down during the so-called RF conditioning process, in which the power sent into the structure is slowly increased as the incidence of breakdowns stabilizes for a given power level. This process is essential for achieving the best performances of an RF structure operating at high fields.

1.3.2 In Search for a Comprehensive Model of RF Breakdown

The overall features of RF breakdown have been understood for some time but only now a quantitative picture is emerging for the complex succession of events which occur during breakdown. A collaboration between the Institute of Physics of the Helsinki University and CERN aims to provide a set of codes to model the different processes involved in the RF breakdown, from the mollecular dynamics involved in metallic surfaces influenced by the application of an external electric field to the formation and evolution of a plasma in the nearbies of a surface emitter [26]. Modelling is necessary to understand the conditions that trigger RF breakdown, which could help to exploit at maximum the possiblities of currently working RF structures and to design and produce new RF structures with outstanding performances. A historical overview on the models of RF breakdown is given in the following.

The first attempt to describe quantitatively the limitation to high-gradient operation came from W. D. Kilpatrick, who in 1957 provided a threshold to the maximum field beyond which the safe operation was not guaranteed [27]. The *Kilpatrick criterion*

was based on experimental data. It assumed that the avalanche process previous to RF breakdown and fed by currents from field emission and from secondary-electron emission by ion collision onto the electrodes was the responsible of RF breakdown. The status of the electrodes was thought to play a role in the limitation to high-gradient operation.

The criterion was applicable to both DC and RF structures. The following expression of the Kilpatrick criterion for RF structures corresponds to T. J. Boyd [16]:

$$f\,[MHz] = 1.64\,(E_K\,[MV/m])^2\,e^{-8.5/(E_K[MV/m])} \tag{1.34}$$

where f is the RF frequency and E_K is the Kilpatrick limit for the electric field. The criterion predicts that higher fields can be reached with higher frequencies.

The Kilpatrick criterion was obsolet in the 80s, when many experiments had already gone beyond the threshold set by Kilpatrick, as results of improved surface treatments and clean vacuum systems.

Another theory suggested that the field emission currents emitted by microscopic emitters in the structure surface were triggering the RF breakdown. Electrons can tunnel a potential barrier by application of high electric fields in the so-called field emission effect described by the Fowler-Nordheim expression. The field emission current is dubbed as dark current because no light accompanies the emission of electrons.

The field emission probability depends on the geometry of the surface imperfections, which can greatly change the local field value. The field enhancement factor β_{FE} is the ratio of the ideal macroscopic field over the local microscopic field. The Fowler-Nordheim expression including the field enhancement factor is:

$$\frac{\mathrm{d}(log_{10}I[A]/(E_S[V/m])^2)}{\mathrm{d}(1/E_S[V/m])} = -\frac{2.84\times10^9(\phi[eV])^{1.5}}{\beta_{FE}} \tag{1.35}$$

where I is the field-emission (intensity peak) current, E_S is the peak surface electric field, ϕ is the work function of the material, the minimum energy required to remove an electron from a solid. In the case of copper, $\phi_{Cu} = 4.5$ eV. The presence of impurities or crystallografic defects can affect the value of the work function [28]. The field enhancement factor β_{FE} can be simply calculated by plotting I/E_S^2 versus $1/E_S$ on semilog paper, which is called the Fowler-Nordheim plot [29]. Typical intensities are in the order of the μm for $\beta_{FE}E_S \sim$ GV/m. As the field enhancement factor β_{FE} is related to the surface quality, it is a good estimator of the level of RF conditioning of the structures. Expected values of β_{FE} for isolated molten craters resulting from RF breakdown activity are between 5 and 10. However, typical measured values of β_{FE} in high-gradient performance RF structures are between 40 and 100. Such high values might be explained assuming that the contribution of nearby tips sums up in the so-called “tip-on-tip” effect.

Indeed any kind of emitter with high enough β_{FE} contributes to recreate the necessary scenario for the RF breakdown. The emitter starts supplying electrons by the

field-emission mechanism. In case of high field emission currents, the emitter can become considerably hot, activating the mechanism of thermoionic emission: the emitter will partially evaporate, releasing electrons, ions and neutral species that will contribute to the formation of a cloud of species in the vicinities of the emitter. This cloud will screen the electric potential seen by the surface, limiting the intensity of the current originated by field emission. Collisions between electrons and neutral species will raise the number of ions, with the subsequent formation of plasma (neutral or quasineutral gas composed by charged and neutral species that exhibits a collective behaviour). Electrons move faster than ions in a plasma and will drain to the electrode first, contributing to the formation of a region with positive space charge known as plasma sheath. The presence of this sheath can increase the local field in the emitter up to 10 GV/m, with dramatic consequences for the emitter. The emitter will melt due to the emission of very high current densities and the metal liquid will evaporate. In consequence, the plasma will be fed with more neutrals and ions. The positive ions will be accelerated from the plasma sheath (positively charged) to the electrode surface (negatively charged). The impact of the ions onto the surface will lead to the formation of craters and the redistribution of emitters in its surroundings. Some neutrals and ions will also be extracted from the surface during the ion bombardment and incorporated into the plasma. The new emitters will initiate another breakdown unless their β_{FE} is too small or the electric field applied is reduced [30, 31].

The *power flow model* proposed in 2009 [3] claims that the available power to feed the field-emission mechanism, and not the peak surface electric field, is the quatity that limits high-gradient operation of RF structures. The model assumes that the field emission currents work at expenses of the RF field and trigger the RF breakdown. The current density will depend on the available power, the field enhancement factor and material of the emitter. The available power is given by the RF power passing through the emitter surface, described by the Poynting vector. In the model, a local field quantity that takes into account active and reactive power flow in the structures, the modified Poynting vector, is proposed as a candidate to explain the limit to high-gradient structure performances due to RF breakdown. Higher powers would increase the temperature of the emitter above the threshold beyond which the emitter could initiate the RF breakdown process. The inclusion of the reactive part of the Poynting vector allows to extend the validity of the model to the standing-wave structures, which present no real power flow.

The modified Poynting vector S_C is therefore divided into two parts, one which describes the active power flow, given by the real part of the conventional Poynting vector $\mathfrak{R}\left\{\overline{S}\right\}$, and another which describes the reactive power flow, given by the imaginary part of the conventional Poynting vector $\mathfrak{I}\left\{\overline{S}\right\}$ and conveniently weighted to fit the experimental data of several high-gradient structures operating between 12 and 30 GHz, both travelling and standing-wave structures. The modified Poynting vector is:

$$S_C = \left\| \Re\left\{\bar{S}\right\} \right\| + \frac{1}{6} \left\| \Im\left\{\bar{S}\right\} \right\| \tag{1.36}$$

Fig. 1.13 shows the square root of the scaled modified Poynting vector for different experimental data [3]. The scaled modified Poynting vector is the modified Poynting vector S_C scaled to a BDR of 10^{-6} bpp/m and a pulse length of 0.2 μs by applying the scaling law: $BDR \propto S_C^{15} t_{pulse}^5$.

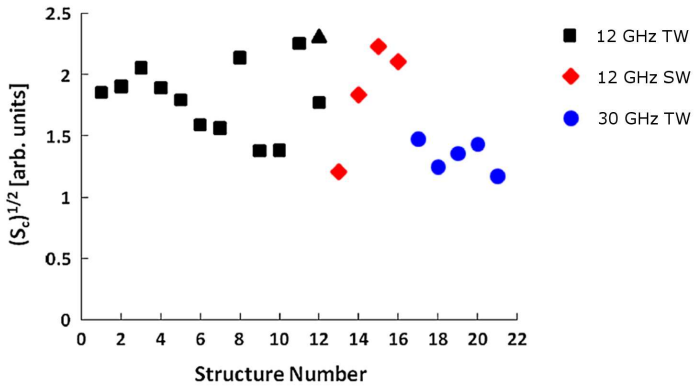

Figure 1.13: *Square root of the scaled modified Poynting vector calculated for the high-gradient performances of several accelerating structures [3].*

The *stress model* ascribes the existence of a limit for high-gradient RF structure performances to imperfections in the crystalline structure of the surface. It is based on two experimental observations. Firstly, the advances on the preparation of very good surfaces in the last years have not prevented the appearance of RF breakdowns during high-gradient operation, which suggests that something else than surface imperfections left over from machining and manipulation may trigger RF breakdown. Secondly, the appearance of superficial features like whiskers and voids after the application of high fields indicates the presence of defects in the crystalline structure of copper. Crystalline structures like copper are generally not so strong and can be easily deformed. The plasticity is possible thanks to the movement of line imperfections or dislocations through the crystalline structure. It must be noticed that the number of dislocations also multiplies by deformation. The stress model suggests that the RF breakdown is activated by any defect mechanism. Thereby, the breakdown rate will be associated to the number of defects in the crystalline structure of copper. The stress exerted on the surface by the application of an external electric field can be responsible of the generation of new defects. According to this reasoning, the breakdown rate follows an exponential growing fit to the electric field:

$$BDR\,[bpp/m] \propto e^{\frac{\epsilon_0 \Delta V}{kT}(E_{max}[MV/m])^2} \tag{1.37}$$

where ϵ_0 is the permittivity in free space, ΔV is the defect volume, and k is the Boltzmann constant. Resulting defect volumes for different experimental data are $\Delta V = [0.8, 13] \cdot 10^{-25}$ m^3 [4].

While the application of a high enough electric field to a metallic surface results in ion bombardment of the surface and the creation of craters, high enough magnetic fields can cause surface cracking. The cyclic surface heating from induced eddy currents experienced by RF structures causes thermal expansions in the structure surface. For very high magnetic fields, the thermal-induced stress can exceed the yield strenght of the material. The fatigue will provoke the formation of microcracks in the structure surface [32], which may behave as field emitters. Surface fatigue is then an undesired process that must be avoided by keeping the surface temperature rise below 50 degrees [34].

The surface temperature rise ΔT which causes the stress is calculated as follows [35]:

$$\Delta T = \frac{P_d \sqrt{t_{pulse}}}{2\sqrt{\pi \rho \kappa c_\epsilon}} \tag{1.38}$$

where t_{pulse} is the RF pulse length, ρ is the material density, κ is the heat conductivity, c_ϵ is the specific heat and P_d is the surface density power, given by:

$$P_d = \frac{R_S H_{max}^2}{2} \tag{1.39}$$

being R_S the surface resistance of the material and H_{max} the maximum magnetic field strenght. The surface resistance is defined as:

$$R_S = \sqrt{\frac{\mu_0 \pi f}{\sigma_C}} \tag{1.40}$$

with μ_0 as the free space permeability, f the resonant frequency of the structure and σ_C the electric conductivity of the material. The thermomechanical properties of OFE copper, commonly used in the construction of high-gradient RF structures, are summarized in Table 1.2.

Table 1.2: *Thermo-mechanical properties of OFE copper.*

Density, ρ	8.95×10^3	kg/m^3
Electric conductivity, σ_C	5.8×10^7	S
Heat conductivity, κ	391	W/m $\cdot$ K
Specific heat, c_ϵ	385	J/kg $\cdot$ K

1.3.3 State-of-the-art of High-Gradient RF Structures

The RF breakdown studies carried out in the last two decades were motivated by the research and development of the future linear colliders for High Energy Physics (HEP). The Compact Linear Collider (CLIC) [36] and the Next Linear Collider (NLC) [37] projects devoted significant effort to raise the achievable high gradients from 20–30 MV/m up to 100–120 MV/m. Experience gained during design, production and testing of many RF structures served to lay down the guidelines which would finally lead to the successful operation of an unloaded accelerating structure of CLIC at 100 MV/m accelerating gradient (corresponding to approximately 200 MV/m peak surface electric field) [38]. Such achievement was possible thanks to a better understanding of RF breakdown phenomena, an enhanced RF design, the improvement in structure fabrication techniques and a careful RF conditioning. The RF design took into account the limit to high-gradient operation established by the modified Poynting vector [1]. The CLIC accelerating structures follow a sophisticated fabrication process, that is: high precision diamond machiend pieces are cleaned with light etching, diffusion bonded under hydrogen molecules H_2 at 1000^0C and finally vacuum baked at 650^0C for several days [39].

1.3.4 Applications of High-Gradient Structures

The main interest of high-gradient RF structures relies on their reduced dimensions and low cost, and several groups all over the world consider to use this technology or are already using it in new facilities or to upgrade existing ones for applications different than the HEP. The satisfactory operation of CLIC structures may have contributed to explore the possibilities of higher gradients. The linear colliders inspected the operation of structures resonating between 12 and 30 GHz. Nowadays, many groups are considering the use of 5.7 GHz for their facilites, as it still offers reduced dimensions and costs but the production of structures operating at that frequency is technically more affordable. The main uses of high-gradient RF structures are:

Linear Colliders

The ATLAS and CMS experiments have recently had experimental evidence of a new particle, a boson, in the mass region around 126 GeV [40, 41]. More data have to be analysed to determine the properties of this new particle. A future linear collider would serve to explore the physics existent in the same energy range that is nowadays being studied in the Large Hadron Collider (LHC) at CERN (Geneva, Switzerland) but making use of leptonic collisions, much cleaner than hadronic collisions. Circular machines cannot be used for this purpose because the synchrotron radiation loss during lepton acceleration makes the machine really inefficient.

Different linear collider projects addressed to provide the future linear collider have coexisted in the last two decades. The goal output beam energy goes from 0.5 center-

of-mass TeV in the case of the suspended NLC project to 3 center-of-mass TeV for CLIC. The realization of a linear collider that reaches such high energies within reasonable dimensions and costs entails the use of high gradient RF structures. The CLIC accelerating structures require an accelerating gradient of 100 MV/m to keep the total collider length below 50 kms.

Free Electron Lasers (FEL)

The design and construction of the fourth-generation light sources driven by FEL linacs is experiencing a boom in the last years. These facilities excel at providing very high X-ray intensities (brightness over 10^{20}) in really short bunches (below 1 ps) [42], which allows the high-resolution study of mollecular processes (in the order of fs) and even imaging on the atomic scale (in the order on nm). The light sources are used in chemistry, physics, biology, materials, medicine, pharmatheuticals,...

Some FEL-based light sources are already in operation, like the Linac Coherent Light Source (LCLS) in SLAC (California, EEUU) [43], the Spring8 Angstrom Compact free electron LAser (SACLA) in RIKEN (Hyogo, Japan) [44] and the Free Electron Laser for Multidisciplinary Investigations (FERMI) in ELETTRA (Trieste, Italy) [45]. Others are under construction, like the European XFEL in DESY (Hamburg, Germany) and the SwissFEL in PSI (Villingen, Switzerland).

Motivated by the huge number of fields that could benefit from the access to an X-ray source of this type, the use of high-gradient structures is being explored due to the promising reduced dimensions and costs, very attractive characteristics to encourage the acquisition of FELs in small research centers or universities. High gradients would also allow the acceleration of more energetic beams, reason why one module operating at 3 GHz has been replaced by two modules at 5.7 GHz in the photoinjector of the light source SPARC (Sorgente Pulsata Auto-amplificata di Radiazione Coerente) in INFN-LNF (Frascati, Italy). Further information on the energy upgrade of SPARC and the high-power testing of a module prototype is found in chapter 5.

Compton back-scattering lasers

The Extreme Light Insfrastructure (ELI) in Bucharest (Romania) is a facility which aims to provide high intensity MeV-photon beams for nuclear and fundamental physics studies. A high-frequency (5.7 GHz) RF linac will supply the 600 MeV electron beam which interacts with a laser source for the production of a more energetic laser by the Compton back-scattering process [48].

The Lawrence Livermore National Laboratory is currently building a compact, high brilliance Mono-Energetic Gamma-ray (MEGa-ray) source for nuclear photoscience applications based on a 250 MeV electron linac operating in X-band [49].

Proton and carbon ion linacs for medical purposes

Fast-cycling high-gradient linacs could be used for tumour treatment with ions, a technique known as hadrontherapy. The linac would boost the energy of the particles previously accelerated by a cyclotron in the scheme proposed by the Italian foundation TERA and dubbed as cyclinac. TERA is studying the feasibility of two different cyclinac boosters: CABOTO, a CArbon BOoster for Therapy in Oncology, and TULIP, a TUrning LInac for Protontherapy, which are described in chapter 6. The maximum accelerating gradient required for these machines is about 40 MV/m, which leads to a peak surface electric field in the range of 150–200 MV/m. The operating field was pushed to such high values in order to reduce as much as possible the size and cost, which would undoubtely help to spread the use of hadrontherapy. The performances of a CABOTO design operating at high gradients are discussed in chapter 7.

Chapter 2

TERA High-Gradient Test Program

The number of applications which could benefit from high-gradient technology is increasing thanks to its reduced facility footprint and electricity consumption. The hadrontherapy community requires just these features for its accelerators in order to allow the access of a larger number of patients which could benefit from this kind of tumour therapy. Cyclinacs would considerably reduce size and cost by using high gradients. As consequence, TERA initiated a high gradient test program to explore the limitations of high gradient RF structures operating at different frequencies and to quantify potential benefits.

2.1 Motivation and Goals

The hadrontherapy community would benefit from the design of compact, efficient accelerators for hadrontherapy, to facilitate the purchase, installation and operation of such machines in medical centers all over the world. The more patients which could access to this kind of treatment, would foster the development of the field and further the understanding of radiobiological mechanisms and the improvement of treatment modalities, with obvious positive consequences for the patients.

Electron linacs for conventional radiotherapy typically work at 3 GHz along with many research linacs, so the first linacs for hadrontherapy were designed for this frequency too. Advances on the studies of high-gradient structures in the framework of the development of a future linear collider has encouraged the consideration of higher frequencies in medical machines. The CLIC project first studied the feasibility of 30 GHz RF structures, although the CLIC nominal frequency changed later on to 12 GHz as result of an enhanced linac parameter optimization [50]. Such high frequencies were not pursued already in the early stages of the medical machine design because they required very tight machining tolerances, which raises the cost of the machine and complicates its manufacture. TERA is however considering the use of 5.7 GHz for its medical accelerators, despite the much reduced availability of test benches, power sources and components at 5.7 GHz in comparison to the more standard 3 GHz.

Nevertheless the situation is rapidly evolving as the use of 5.7 GHz technology is becoming popular in the last years. The C-band linac of SACLA@Spring8 succesfully accelerated 8 GeV electrons in February 2011; the installation of the 5.7 GHz linac for the Swiss FEL is foreseen for the beginning of 2015.

In 2009 TERA initiated a high gradient test program to compare the high-gradient performances of RF structures operating at different frequencies. The high-gradient performance studies carried out for the future linear colliders CLIC and NLC focused on frequencies between 12 and 30 GHz. The TERA high gradient test program extends the frequencies under study by exploring the high-gradient performances of RF structures operating in the frequency range of 3 to 5.7 GHz.

The test program aims to firstly experimentally compare the performances of high-gradient RF structures operating between 3 and 30 GHz, then evaluate scaling laws that relate breakdown rate, pulse length, electric field and modified Poynting vector, and finally examine the consistency of predictions done by models proposed to explain high-gradient performances of RF structures. These studies are important not only to explore the limitations of high-gradient structures but also to assist the design of future high-gradient RF structures. In addition, the test program will study the characteristic features of RF breakdowns and related phenomena in cavities similar to those of medical structures.

The ultimate goal of the TERA high gradient test program is to find the operation limits for high-gradient RF structures working between 3 and 5.7 GHz. This information can then be used to design other RF structures, optimizating in terms of efficiency, length and cost for reliable operation. In particular, TERA is interested in demonstrating the reliable operation of TERA-like cavities at peak surface electric fields of about 200 MV/m. This corresponds to between 35 to 40 MV/m accelerating gradient in CABOTO with E_S/E_0=4–5. The value coincides, not by chance, with the operation field goal of the CLIC project (100 MV/m accelerating gradient in CLIC accelerating structure).

The reason why breakdowns are important is that they induce random kicks on the beam which lead to emittance growth or even loss of the beam if the kick is strong enough. The BDR goal, for both CLIC and TERA, is about 10^{-6} bpp/m. The BDR goal of CLIC, actually 3×10^{-7} bpp/m, is estimated under the conservative assumption that all luminosity is lost on a pulse with a breakdown. CLIC parameters budget no more than 1% luminosity loss to this effect. The active length of acceleration of the linear collider is about 3×10^{4} m. Therefore, the BDR is limited to 3×10^{-7} bpp/m. In hadrontherapy accelerators, in case of tumour treatment with the spot scanning technique, beam losses lead to unwanted “cold spots”. The acceptable breakdown probability for hadrontherapy applications is approximately one breakdown per treatment session per patient. Assuming a treatment duration of 2 minutes with a high repatition beam (about 300 Hz) using a 24 meter-long linac, the goal BDR for the accelerators studied by TERA becomes 10^{-6} bpp/m. This condition can however be relaxed if the tumour volume is repainted several times during the same treatment session (multi-painting technique).

CLIC and TERA structures have different cell types (see Table 2.1), which have an important influence on the ratio peak surface electric field over accelerating gradient E_S/E_0, but their performances can be compared making use of the maxima electromagnetic quantity values reached, for example the peak surface electric field E_S or the modified Poynting vector S_C. Given the common study goals, a collaboration between TERA and the CLIC RF structure development group at CERN has been established.

Table 2.1: *Comparison of CLIC and TERA cells and common goals.*

	Cell shape	E_S/E_0	E_0 [MV/m]	E_S^{max} [MV/m]	$BDR_{required}$ [bpp/m]
TERA linacs	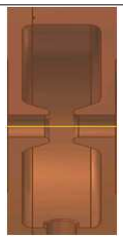	4–5	35–40	200	10^{-6}
CLIC structures	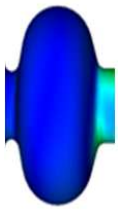	2	100	200	$< 10^{-6}$

2.2 Test Devices

The TERA high gradient test program has planned the design, prototyping and high-power testing of a set of cavities in order to determine the operation limits of high-gradient RF structures, evaluate the scaling laws that relate BDR, RF pulse length and electromagnetic quantities like E_S and S_C and use the results in the design of future RF structures. Like the accelerating cells of a cyclinac booster, the testing devices are standing-wave structures made of copper and have noses.

The first phase of the testing program consists of testing several single-cell cavities: one operating at 3 GHz and other three at 5.7 GHz. All the single-cell cavities are a cell magnetically coupled to a rectangular waveguide, a layout chosen for the sake of simplicity. Even though the cavities have a slightly different geometry, their high-gradient performances can be compared on the basis of the maxima values of electromagnetic quantities such as the peak surface electric field E_S and the modified Poynting vector S_C. The cavities of the cyclinac booster will be machined with conventional tooling, and so are the testing cavities, except from one of the 5.7 GHz single-cell cavities, for which diamond tooling was used (like it is done for state-of-the-art high-gradient per-

formance RF structures). The objective of using different tooling was to evaluate the influence of machining specifications, in particular, surface roughness, on the high-gradient performances of the RF structures. Two 5.7 GHz single-cell cavities were fabricated following the same design and procedures. One of the cavities will be used to evaluate the scaling laws, going up to high fields. The other cavity will be used to study the breakdown rate at low fields, with special interest in the damage caused to the cavity as result of long-term exposition to RF power. Table 2.2 summarizes the test devices and objectives of the TERA high gradient test program.

The second phase of the testing program foresees the design, prototyping and high-power testing of a multicell structure. The frequency will be determined according to the results of the high-power test of the single-cells.

At the moment of writing this work, the status of the test devices was the following. The 3 GHz single-cell cavity had been successfully high-power tested, so it was cut into two halves to inspect its interior surface. Chapter 3 describes the design, production and high-power testing of the 3 GHz cavity. The 5.7 GHz single-cell cavities were under preparation: the cavities were already tuned and the pieces brazed together and the short-circuit waveguide was being prepared. The high-power test of the 5.7 GHz single-cell cavities is foreseen for 2013. Chapter 4 covers the design, production and testing of the 5.7 GHz cavities.

A major issue for high-power testing cavities is that there are not many high-power test benches and little time is available for parasitical experiments. The 3 GHz single-cell cavity was tested in the CLIC Test Facility (CTF) at CERN (Geneva, Switzerland) in three different stages. The 5.7 GHz single-cell cavities may be tested with the 2.5 MW magnetron property of ADAM S.A. (Geneva, Switzerland). The design of the test devices adopted to the characteristics of the test facilities. Main issues were related to waveguide standards, flanges and maximum input power available to feed the test device.

During 2010 the author had the possibility to participate in the high-power testing of a 5.7 GHz traveling-wave structure in collaboration with the Istituto Nazionale di Fisica Nucleare - Laboratori Nazionali di Frascati (INFN-LNF, Frascati, Italy) and the High Energy Accelerator Research Organization KEK (Tsukuba, Japan). The structure was a prototype of the modules that are intended to substitute the 3 GHz module in the photoinjector of SPARC. The test was carried out at the end of 2010 at KEK, where at that time there was a test bench for 5.7 GHz structures. The high-power testing of this structure is of special importance for the subject of this work, as it represents the first experimental measurement of the high-gradient performances of a 5.7 GHz structure. The test allowed not only to evaluate the operation limit but also to characterize the RF breakdown and associated phenomena. The work is presented in chapter 5. The structure was made of copper and contained multiple cells. On the other hand, the results could be used as a startup to evaluate the feasibility of TERA designs at 5.7 GHz, discussed in chapter 7.

Table 2.2: *Main characteristics and status of the test devices of the TERA High Gradient Test Program and the INFN prototype.*

	TERA High Gradient Test Program				**INFN prototype**
	3 GHz Single-Cell Cavity	5.7 GHz Single-Cell Cavities		Multi-cell Structure	
No. devices	1	2	1	1	1
Frequency [GHz]	3	5.7	5.7	3 or 5.7	5.7
No. cells	1	1	1	> 1	> 1
Type	standing-wave	standing-wave	standing-wave	standing-wave	traveling-wave
Machining	conventional	conventional	diamond	conventional	conventional
Status	tested	in preparation	in preparation	to be designed	tested
Objectives		j) evaluate the influence of machining specifications on high-gradient performances jj) study the long-term RF power exposition effects on RF structures			
	i) determine operation limits ii) evaluate scaling laws				

Chapter 3

3 GHz Single-Cell Cavity Design and Test

The TERA high gradient test program started with the design, production and high-power testing of a 3 GHz single-cell cavity. A sketch of the cavity prototype, which has a geometry close to that needed for a full multi-cell accelerating structure for carbon ions, is shown in Fig. 3.1. The cavity was made of cooper and consisted of a cell operating in the TM_{010} mode magnetically coupled through a slot to a rectangular waveguide operating in the TE_{01} mode. The cavity included a cooling system. The cell had "noses" similar to all the TERA linac cells and its geometry was optimized to increase the effective shunt impedance ZTT. The waveguide was WR284, the standard used at the CLIC Test Facility (CTF3) at CERN, where the high-power tests were conducted. The tests were completed in March 2012. This chapter presents the cavity design, prototype preparation and cavity high-power testing, and finally discusses the testing results.

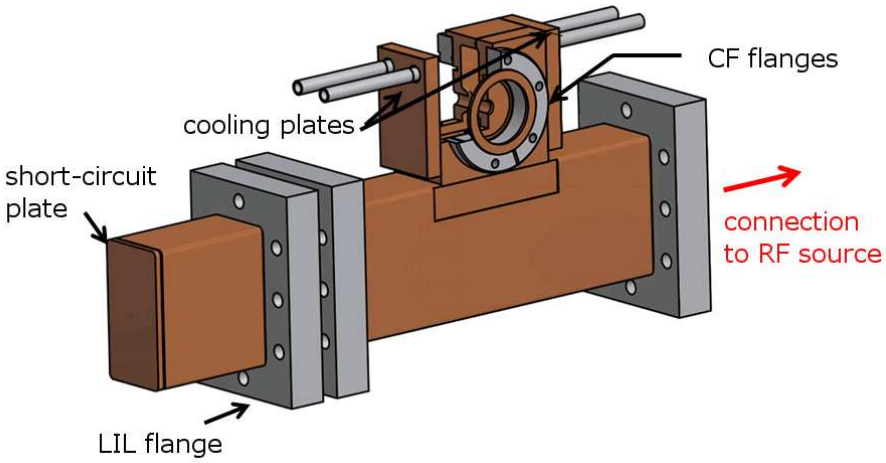

Figure 3.1: *Prototype sketch.*

3.1 Cavity Design

This section explains the reasoning behind the choices of the basic cavity layout, cell geometry, tuning methods and prototype characteristics. The first part of the section is dedicated to the simulation tools and procedure used to design the test cavity.

3.1.1 Simulation Tools for RF Design

Two programs were mainly used to study the linac cell geometry of the cyclinacs: *Poisson Superfish* and *Ansoft HFSS*. The design process can be shortened and simplified if the codes are embedded in optimization algorithms. In the following the main features of *Poisson Superfish* [7] and *Ansoft HFSS* [8] are presented together with the codes specifically designed to optimize their use.

Poisson Superfish is a collection of programs for calculating static electric and magnetic fields and also RF electromagnetic fields in 2D. All the programs generate a triangular mesh fitted to the boundaries of the geometry. Different materials can be chosen for the boundaries of the problem. The programs are 2D but can distinguish between radial (r,z) or cartesian (x,y) symmetry.

One of the *Poisson Superfish* programs, *CCLfish*, is specifically dedicated to Coupled-Cavity Linac (CCL) cell design. The program is a fast tool for optimizing the side-coupled linac cell geometry in 2D. The *CCLfish* program of *Poisson Superfish* serves to calculate the main electromagnetic quantities of CCL cells. *CCLfish* reads the cell geometry characteristics from a special formatted text file. It can then automatically tune the cell by adjusting the cell diameter, septum thickness, gap or cone angle accordingly to the users specifications. It computes the main electromagnetic quantities for the cell: frequency f, quality factor Q, effective shunt impedance ZTT, accelerating gradient E_0, maximum electric field E_{max} and maximum magnetic field H_{max} among others. Finally, it writes the final cell geometry parameters and electromagnetic quantities in another special formatted text file.

The author contributed to the development of a *Matlab* [53] macro able to administer inputs and outputs of *CCLfish* in order to reduce the time consumption in setting up, running and reading multiple simulations. *Superfisherman* is the name given to this macro. The macro makes *Superfish* run several simulations from just one *CCLfish*-like input file where different values are specified for a given cavity geometry. The macro stores the results from each simulation (main quantities of interest like quality factor Q, effective shunt impedance ZTT and maximum electromagnetic field magnitudes) in a common text file. After running the simulations *Superfisherman* gives the possibility to generate different plots from the summary file with the function *Make_Plot*. Fig. 3.2 shows an example of the variation of ZTT as a function of the gap length for different inner corner radii.

Another function, *Super_Gourmet*, allows the simulations of interest to be selected and generates a file where the results from these simulations are stored. *Make_Plot*

can be also used to generate different plots from this file. In Fig. 3.3 a sketch of the macro is shown. *Superfisherman* has been already employed to perform some linac feasibility studies [54–56].

HFSS (High Frequency Structure Solver) is a 3D electromagnetic field solver based on the Finite Element Method (FEM) algorithm which solves via adaptive meshing convergence. *HFSS* is useful for high-frequency component design and study, such as RF accelerating structures. When solving the eigenmodes for a given problem, *HFSS* provides the complex eigenvalues, from which the lossy nature of the model can be evaluated. It requires the user to specify geometry, material and boundaries of the model. *HFSS* was chosen among other 3D electromagnetic field solvers due to its high accuracy while meshing the model geometry and calculating important quantities for cavity design such as resonant frequency f and quality factor Q [18].

HFSS also includes a *Field Calculator Tool* for performing mathematical operations on all electromagnetic field values within the solved model to derive other quantities of interest for the user. It gives the possibility of importing the expression of electromagnetic quantities previously composed in the calculator and exporting them into a text file.

The most important design parameters - effective shunt impedance ZTT, accelerating gradient E_{acc} and modified Poynting vector S_C - were implemented in the *HFSS* calculator in this work. The expressions were composed following the theoretical description given in chapter 1.

The quantities introduced in the *HFSS* calculator were evaluated for the single cell of the present cavity design and were compared to the values computed with Superfish, with satisfactory agreement among both codes, as shown in section 3.1.4. The implemented expressions were used in the RF design of the TERA high-gradient performance 3 GHz and 5.7 GHz single-cell cavities. All *HFSS* simulations presented in this thesis were performed using version 12.

3.1.2 Design Goals of the 3 GHz Test Cavity

The main goal was to design a test cavity operating at 3 GHz which similar thermomechanical and electromagnetic characteristics allow to estimate the high-gradient performances of a regular accelerating cell of a TERA linac from the performances of the test cavity. For this reason, the test cavity was made of the same copper intended to be used for the TERA linac and following the same machining specifications which would be requested for the regular cells.

The geometry test cell was similar to the geometry of the regular accelerating cells of a TERA linac. Both cells have the characteristic “noses” used to enhance the acceleration and their geometry is optimized to maximize the effective shunt impedance. However, the test cell was designed to have a ratio maximum peak surface electric field over accelerating gradient E_{max}/E_0 of about 6.5, higher than the typical ratio of nominal TERA linac cells, between 4 and 5. The choice of a high E_{max}/E_0 is driven by energy consumption reasons in case of the test cell, while a smaller E_{max}/E_0 is chosen

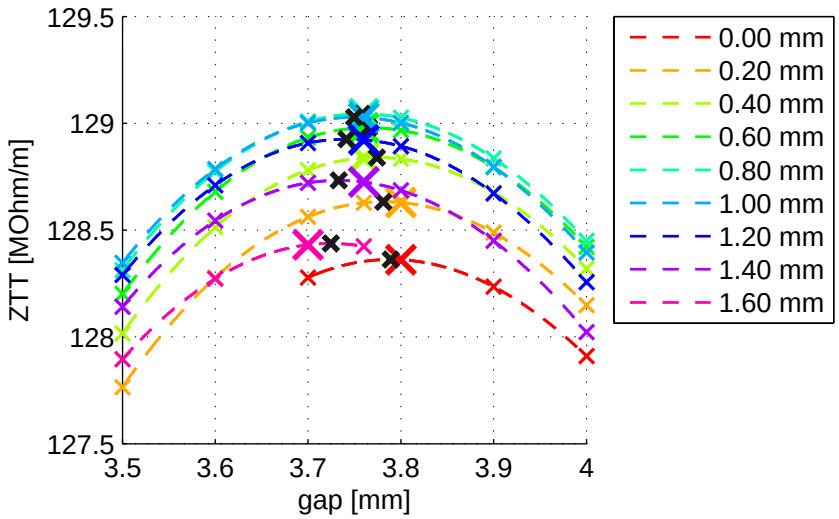

Figure 3.2: *Variation of ZTT as a function of the gap length for different inner corner radii [54]. Study performed using the Superfisherman macro.*

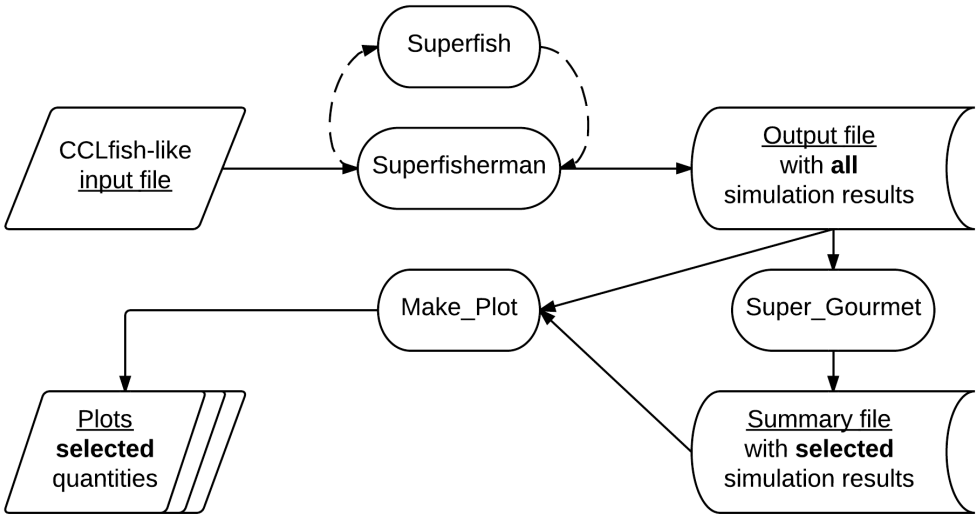

Figure 3.3: *Superfisherman architecture.*

for the regular accelerating cells of a TERA linac because the main interest is to reach very high accelerating gradients for low enough maximum peak surface electric fields.

Another difference between a regular accelerating cell of a typical TERA linac and the 3 GHz test cell is the way the power is coupled to the cell. The typical layout of the TERA linacs for a cyclinac consists of a series of tanks, each being a section of a side-coupled cell linac operating in the $\pi/2$ mode. In this mode, cells with zero field alternate with cells with maximum field. The first type of cells are called coupling cells, because their main role is to allow the power flow through the whole structure, and the other type of cells are known as accelerating cells. The net contribution of the coupling cells to acceleration is zero, so in a side-coupled cell linac, the coupling cells are moved off axis to increase the mean accelerating gradient. Two consecutive accelerating cells are then connected by a coupling cell and the beam pipe. The 3 GHz test cavity was envisaged as a single-cell cavity to simplify as much as possible the design and manufacture of the prototype. With no coupling cells available, another coupling scheme had to be chosen to couple the power to the single cell. The best option was to magnetically couple the single cell operating in TM_{010} mode with a rectangular waveguide operating in TE_{01} mode through an aperture or slot opened in the flat equator of the cell. This scheme had the advantage to allow the change of the coupling factor by simply adjusting the short-circuit position. The position of the coupling slot influenced the cell geometry, as its position limited the outer corner radius dimensions. This issue will be further explained in the following section.

The high power test was performed in CTF3, so the same waveguide standard (WR284) and the flange type (LIL - LEP Injector Linac) as the ones used in CTF3 were chosen for the test cavity.

One of the goals of the TERA high power test program is to use the test cavities for the study of the scaling laws which relate breakdown rate to electromagnetic quantities like the electric field and the modified Poynting vector. For nominal operation fields of the TERA linacs, the expected breakdown rates, in the order of 10^{-6} bpp/m, are too low for providing significative statistics within a reasonable duration of a breakdown rate measurement. Therefore, the scaling laws are evaluated for higher field values. For continued operation in high breakdown rate regime, the cavity surface will be spoiled much faster. Obviously, this differs from the nominal operation of a regular accelerating cell of a TERA linac, which in principle would not be operated at such high fields.

The final goal of the test program was to estimate the breakdown rate performance of a regular accelerating cell of CABOTO from the measurements performed for the 3 GHz test cavity. Even though the geometry of the test cell may be slightly different from the regular accelerating cell of a TERA linac, the comparison is still possible on the basis of the maxima fields reached in the structures. CABOTO operates 2.2 μs-long RF pulses for a maximum accelerating gradient E_0 between 32 and 34 MV/m in the design presented in chapter 7. A typical cell of CABOTO has E_{max}/E_0 between 4 and 5 and $\sqrt{S_{C,max}}/E_0$ around 0.024 $\frac{\sqrt{\mathrm{MW/mm^2}}}{\mathrm{MV/m}}$. For an accelerating gradient of 34

MV/m, the maximum electric field reached in CABOTO is around 170 MV/m and the modified Poynting vector is about 0.70 MW/mm^2. The test cavity should be operated at similar conditions to those for which CABOTO is designed in order to allow a more realistic estimation of the expected breakdown rate of CABOTO.

3.1.3 Design of Cell

The geometry of the 3 GHz test cell was similar to the low-energy cells of the high-gradient linacs designed by TERA. The operating mode was the TM_{010}, which presents a longitudinal electric field along the rotational axis of the cell and an azimutal magnetic field distribution. The cell had nose cones to enhance the electric field along the beam axis and improve particle acceleration.

The cell geometry was optimized to maximize the shunt impedance while reaching high surface electric fields with relatively low input power. The cell optimization was constrained by:

- A bore radius of R_{bore} = 3.5 mm. This corresponds to the value chosen for the proton linac LIGHT [57]. The beam pipe had the same aperture than the bore hole for simplicity. This choice did not lead to RF leakeage through the beam pipe, as its radius is about 10 times smaller than the radius required to propagate the TM_{01} mode.

- Machining and brazing constrained the geometry. The brazing plane direction was parallel to the rotation axis of the cell, as it can be seen in Fig. 3.4. The joint was in between the end of the outer corner radius for one half cell and the end of the equator flatness for the other one. The coupling slot had necessarily to fit in this flat region, and the border limits must be respected. Therefore, the outer corner radius was limited to 2 mm and so the optimization of the test cell. The nominal CABOTO accelerating cells do not present this contraint because the power feeding is done from the bore hole and coupling cells.

The cell geometry was optimized with *Superfisherman* in a previous study [5], which was the starting point of this work. The optimization procedure was the same as that described in [54]. After the optimization, all the cell geometry parameters, apart from the cell diameter, were fixed. Table 3.1 shows the cell geometry parameters following Fig. 1.4 notation. The cell diameter was adjusted later on in the design process to compensate the frequency shifts due to: a) coupling the cell to the waveguide through a slot and, b) thermally-induced deformations.

3.1.4 Design of Waveguide Coupler

The most important difference between the test cavities and the nominal accelerating cells in a side-coupled linac is the absence of coupling cells and therefore the need of a slot to couple the test cavity directly to the waveguide. The test cavity was

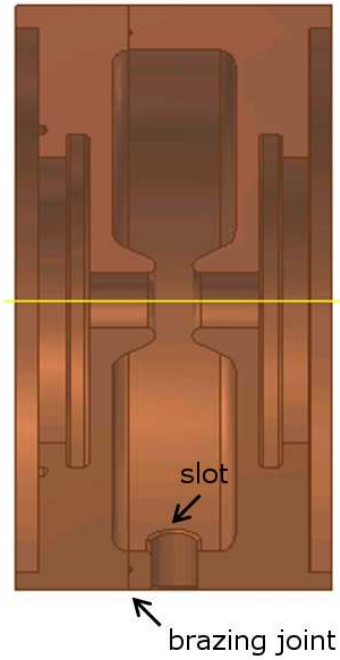

Figure 3.4: *Section of the technical drawing of the cell.*

Table 3.1: *Geometry parameters of the test cavity cell [5].*

Energy, E	70	MeV
Length, L	18.9	mm
Outer Corner Radius, R_{OC}	2	mm
Inner Corner Radius, R_{IC}	1.9	mm
Outer Nose Radius, R_{ON}	1	mm
Inner Nose Radius, R_{IN}	1	mm
Cone Angle, θ_{CONE}	25	deg
Flat Top Length, L_{FLAT}	0	mm
Wall Thickness, Web	3	mm
Bore Radius, R_{BORE}	3.5	mm
Gap Length, g	4.7	mm

magnetically coupled to a WR284 rectangular waveguide (dimensions: 7.214×3.404 cm^2) through a slot. The WR284 is the 3 GHz waveguide standard used in the CLIC Test Facility of CERN, where the high-power tests were carried out.

The coupling slot was a rectangular aperture with semicircular-shaped short sides (see Fig. 3.7). The slot design was driven by simplicity of manufacture and reduced probability to cause RF breakdowns. In this regard, wider slot apertures were preferred than narrower ones, because higher electric fields - associated to higher breakdown rates - are reached in narrow slots. Fig. 3.5 shows the waveguide-cavity coupling scheme chosen for the test cavity. This coupling scheme had the advantage of allowing the adjustment of the coupling strength by shifting the short-circuit position after machining and brazing together the different parts that constituted the cavity. The appropriate short-circuit position was found during the low power measurements and then, the waveguide was cut such that the short-circuit plate laid on the position determined by the low power measurements. The longest side of the slot is parallel to the magnetic field lines for a good magnetic coupling.

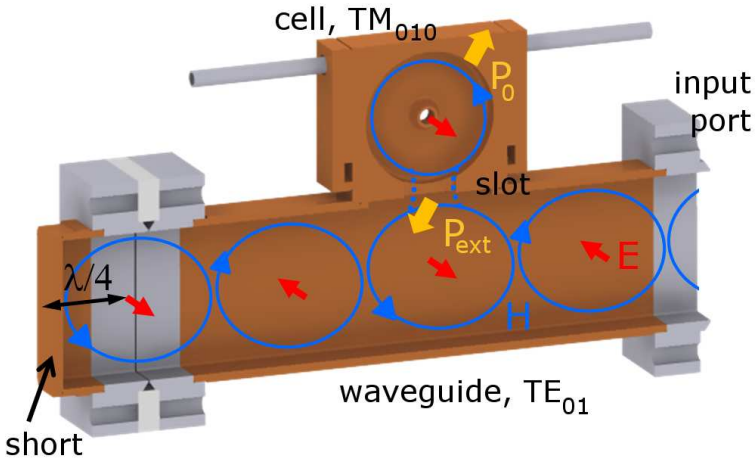

Figure 3.5: *Sketch of the waveguide-cell coupling scheme. The cell is connected to the waveguide by the coupling slot. The coupling factor can be adjusted by shifting the short-circuit position. In orange, the magnetic field lines; in red, the electric field lines. The short position was fixed after low power measurements. Distance between short plate and first electric field maximum is always $\lambda/4$ for boundary conditions.*

Mesh for *HFSS* simulations

Superfish cannot be used to solve 3D structures like the full cell-coupler-waveguide system; however *HFSS* can. Therefore, the design of the waveguide coupler was based on simulations performed with *HFSS*, assuming that the cavity walls were made in normal copper and that the cavity volume was under vacuum. The cavity volume was split into two halves through its symmetry plane (perfect electric wall), as shown

in Fig. 3.5. Only one half was simulated in order to minimize computing time and enhance simulation precision.

The selection of an appropriate mesh for the *HFSS* simulations was essential for an accurate calculation of the resonant frequency of the system, the coupling factor, and the main electromagnetic quantities in the cell (accelerating gradient E_0, maximum electric field E_{max}, maximum magnetic field H_{max} and maximum modified Poynting vector $S_{C,max}$, with respect to the incoming power P needed to excite such fields in the cell) using reasonable computing times and resources. Required frequency accuracy was in the order of the MHz, because mechanical tolerances cannot guarantee a better frequency precision. The results obtained with *HFSS* were compared to those of Superfish for the single cell. The single cell geometry was simulated in *Superfish* with a mesh size of 0.02 mm. The same 2D geometry was simulated in *HFSS* for a maximum element length $l_{element,max}$ of 3 mm inside the cell volume and a maximum surface deviation $\Delta_{surface,max}$ of 0.02 mm on the cell volume (the frequency accuracy strongly depends on $\Delta_{surface,max}$) using curvilinear elements. The *HFSS* model consisted in a 30-degree slice of the single cell. The frequency difference between *Superfish* and *HFSS* simulations was less than 1 MHz. A special mesh with maximum element length of 0.5 mm and a maximum surface deviation of 0.02 mm was implemented in a 2-millimeter radius cylindrical region around the bore hole axis in order to determine the accelerating gradient E_0. Table 3.2 contains the main electromagnetic quantities computed for the single cell with Superfish and *HFSS*. The selected mesh allowed the main electromagnetic quantities of interest to be calculated in *HFSS* with the appropriate accuracy. The power required to excite a maximum surface electric field of 150 MV/m in the cell was about 128 kW. The pulsed surface heating for this field level and RF pulses of 3 μs was around 2 degrees (transient increase of temperature within each pulse). The cell could reach a maximum electric field over 400 MV/m with only 1 MW of incoming power.

Table 3.2: *Main electromagnetic quantities computed for the single cell with Superfish and HFSS. The last column contains the relative difference between the computed quantities,* Δ.

Quantity		*Superfish*	*HFSS*12	$\Delta_{SF,HFSS}$[%]
Frequency, f_0	MHz	3018.8	3018.3	0.017
Quality factor, Q_0		8985	8985	0
E_0^2/P_{diss}	$\frac{(\mathrm{MV/m})^2}{\mathrm{kW}}$	4.44	4.43	0.2
Transit-time factor, T		0.893	0.892	0.11
Shunt impedance, Z	MΩ/m	83.9	83.9	0
Eff. shunt impedance, ZTT	MΩ/m	66.9	66.7	0.3
E_{max}/E_0		6.49	6.49	0
H_{max}/E_0	kA/MV	2.66	2.96	11
$\sqrt{S_{C,max}}/E_0$	$\frac{\sqrt{\mathrm{MW/mm^2}}}{\mathrm{MV/m}}$	0.029	0.032	10

The same $l_{element,max}$ and $\Delta_{surface,max}$ were chosen for the coupler. The waveguide did not require the definition of the $\Delta_{surface,max}$ because all its surfaces are flat. The $l_{element,max}$ was set to 5 mm. Table 3.3 summarizes the mesh used for the different parts of the cavity. Fig. 3.6 shows the mesh for the cell, coupler and waveguide.

Table 3.3: *Mesh used for the simulation of the cavity.*

	Cell core	**Cell outer cavity**	**Coupler**	**Waveguide**	
Max. El. Length, $l_{element,max}$	0.5	3	3	5	mm
Max. Surf. Dev., $\Delta_{surface,max}$	0.02	0.02	0.02	none	mm
Volume, V	120	24700	920	106400	mm^3
No. Tetraedra	35200	47000	1800	32800	

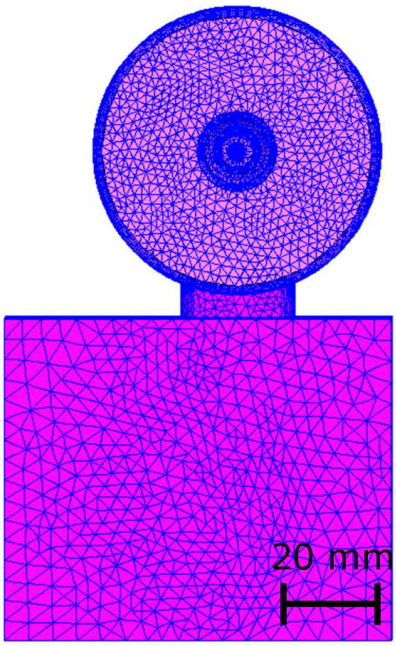

Figure 3.6: *Mesh used in HFSS for the simulation of the cavity.*

The coupling factor β_C is given by the ratio of the external quality factor Q_{ext} over the intrinsic quality factor Q_0, as shown in Eq. (1.20). The computational method used to calculate Q_{ext} and β_C was based on the evaluation of the quantities:

$$Q_E = \frac{\omega\sqrt{\mu_0\epsilon_0}\int\int\int_{Cavity}|E|^2\,dv}{\int\int_{Ref.Plane}|E|^2\,ds},\quad Q_H = \frac{\omega\sqrt{\mu_0\epsilon_0}\int\int\int_{Cavity}|H|^2\,dv}{\int\int_{Ref.Plane}|H|^2\,ds} \tag{3.1}$$

The integrals are evaluated over a reference plane in the waveguide which is a perfect-electric wall for the calculation of Q_E and a perfect-magnetic wall for the calculation of Q_H. The sum of both quantities, Q_E and Q_H, gives the external quality factor Q_{ext} of the system. Further explanations of the method are given in [58].

Two parameters were varied in the model to reach the desired coupling factor: the slot width w_{slot} and the slot length l_{slot}, shown in Fig. 3.7. The short position was fixed: the short-circuited side of the waveguide was placed one quarter of the longitudinal wavelength λ_Z from the slot center (for the TE_{01} mode propagating in the standard waveguide WR284, λ_Z is 138.7 mm), so that the maximum magnetic field was reached in the slot. Hence the coupling factor obtained for this configuration was the maximum coupling factor that could be obtained for certain slot dimensions. The goal value for the coupling factor β_C of the model (for a short position of $\lambda_Z/4$) was 1.5. The β_C of the real prototype would then be reduced from 1.5 (overcoupled cavity) to 1 (critically coupled cavity) by changing the short position. In practice the slot width was fixed by the position of the brazing line in the cell, so the coupling strength was finally tuned to 1.5 by changing the slot length.

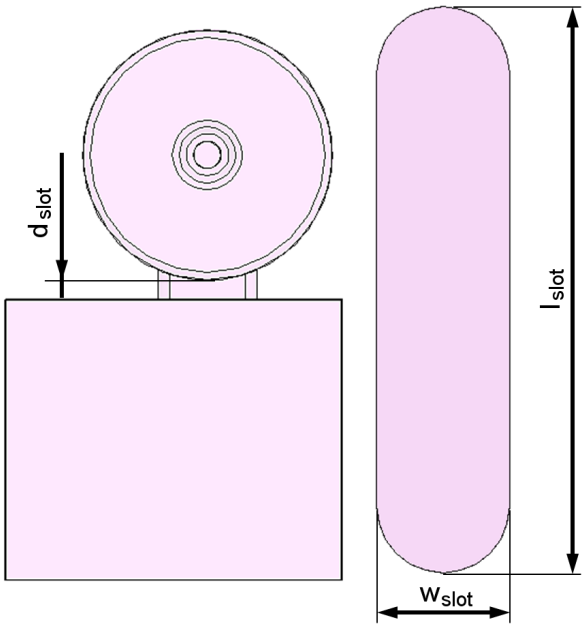

Figure 3.7: *Shape and dimensions of coupling slot.*

The coupling slot introduced a considerable frequency shift of about 20 MHz with respect to the frequency of the uncoupled cell. Table 3.4 shows the resonant frequency for the single cell and for the system cell-coupler-waveguide.

Table 3.4: *Frequency shift introduced by coupling slot.*

	Single cell	Cell, coupler and waveguide	
Frequency	3018.3	2998.6	MHz
Frequency shift		-19.7	MHz

The coupling slot is a critical point in high-gradient operation, as vacuum RF arcs (breakdowns) can occur there due to electric field enhancement. The maximum electric and magnetic field values and the maximum modified Poynting vector were evaluated to check if any of them was above acceptable values. Table 3.5 shows these quantities for two regions: the cell and the slot. The values of the electric and magnetic field in the coupler were less than half the values in the cell whereas the square root of the modified Poynting vector in the coupler was about one quarter of the value in the cell and thus were considered safe values. Fig. 3.8 shows the location of these quantities in the cavity.

Table 3.5: *Maximum electromagnetic quantities of interest for high-power performance cavities design evaluated in the cell and in the coupler of the cavity. The location where these quantities are found is shown in Fig. 3.8.*

Quantity	In cell	In coupler	
E_{max}/E_0	6.5	0.3	
H_{max}/E_0	3.0	1.6	kA/MV
$\sqrt{S_{C,max}}/E_0$	0.032	0.008	$\frac{\sqrt{\text{MW/mm}^2}}{\text{MV/m}}$

3.1.5 Frequency Tuning

Once the coupling slot dimensions were fixed, the model was tuned by changing the cell diameter. The operation frequency of the CLIC Test Facility (CTF) klystrons is 2998.5 MHz, with a frequency band of ±10 MHz. During cavity operation the resonant frequency decreases by 3 MHz with respect to the nominal resonant frequency as result of thermal expansions, as explained in [59]. Therefore, the frequency at which the designed cavity had to be tuned was about 3002 MHz.

A previous study showed that a machining precision of ±10 μm leads to a maximum frequency uncertainty of ±7 MHz [60]. In consequence, a tuning system was foreseen to ensure the operation of the cavity within the frequency band of the klystron. Different tuning methods were taken into consideration: tuning rods, dimple tuners and plastic deformation of the nose region. Fig. 3.9 shows a sketch of the different evaluated tuning methods. In the following, the main characteristics of each tuning method are discussed.

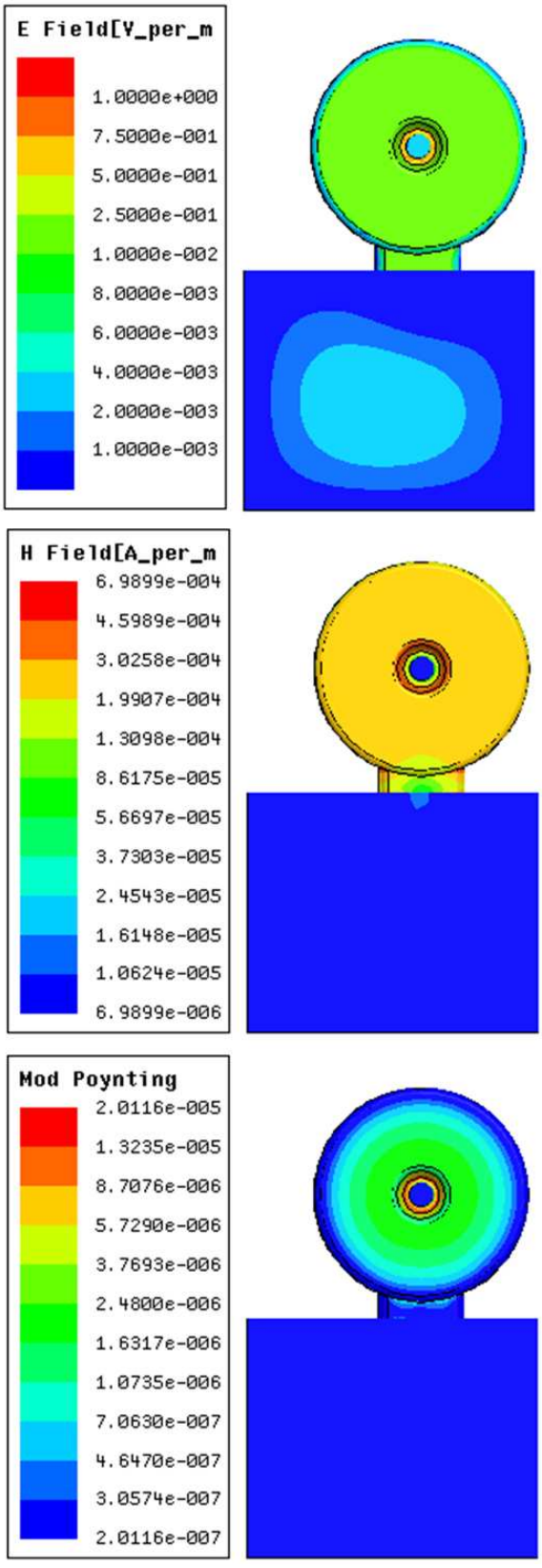

Figure 3.8: *Distribution of the electric and magnetic field and the modified Poynting vector in the cavity.*

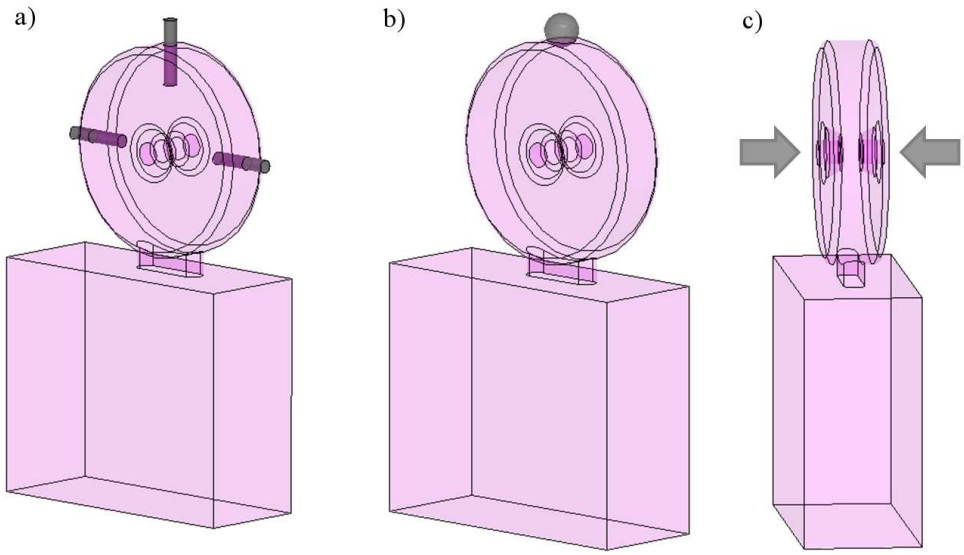

Figure 3.9: *Tuning methods: a) tuning rods; b) dimple tuner; c) plastic deformation of nose region. The last technique was the one chosen for the cavity under study.*

Tuning rods Not appropriate for high-gradient performance structures because they behave as coaxial conductors and multipacting can occur between the tuner and the cavity walls, spoiling the cavity performance.

Dimple tuner A maximum frequency increase of 1 MHz is provided with one unique dimple tuner of 6 mm-diameter and 75% penetration depth which is not enough for counteracting the maximum frequency uncertainty of about ±7 MHz expected from mechanical tolerances. It also brings some mechanical complications as it requires the cavity walls to be as maximum 1 mm thick in order to ease the dimpling and because the proximity of the dimpling tuner to the braze line could compromise the vacuum tightness of the prototype.

Plastic deformation of nose region This method consists in putting both cell noses closer by pressing the nose region from the exterior with a clamp. As both noses approach each other, the equivalent capacitance of the resonant circuit becomes higher, so the resonant frequency diminishes. A gap reduction of 0.1 mm leads to a reduction of about 12 MHz in resonant frequency, with an increase of about 1.5% in maximum electric field. The dependence of the frequency on the gap length is linear.

The nose deformation was selected as the best way to tune the cavity due to its simplicity and wide frequency shift. Therefore, the gap length of the cell, nominally 4.7 mm, was increased by 0.1 mm in order to shift the resonant frequency of the cavity

from 3002 MHz up to 3014 MHz. The cavity would be tuned in a subsequent step after having brazed together all the parts of the prototype.

3.1.6 Prototype Characteristics

The prototype, illustrated in Fig. 4.6, consisted of the following parts:

- Two copper halfcells (one of them including the slot aperture, as shown in Fig. 3.11).
- Two stainless steel CF flanges, each one to be placed at one side of the block formed by the two halfcells, to connect the diagnostic instrumentation (Faraday cup).
- Two copper cooling plates with stainless steel cooling pipes of 5.5 mm-diameter. The cooling system was sized to cool down 350 W (power corresponding to 260 MV/m peak surface electric field) with a 2.5 l/min water flow in turbulent regime. Further information on this topic can be found in [59].
- A copper open-ended WR284 waveguide. One end was terminated by a stainless steel LIL flange - to be connected to the CTF3 RF circuit - and the other was prepared to connect the short circuit plate. The waveguide had an aperture on one of its short sidewalls. Cell and waveguide were interconnected through this aperture by the slot aperture opened in one of the halfcells.
- A short circuit plate.

The cavity was made of UNS (Unified Numbering System) C10100 Oxygen-Free Electronic (OFE) copper alloy. This alloy has a very small concentration of oxygen (below 0.01%) which allows optimal performances under vacuum brazing. It has high electrical and thermal conductivities, 59.1×10^6 Ωm and 391.1 W/m·degree at 20°C respectively, which lead to relatively low energy losses by wall currents and good heat dissipation.

The prototype machining was done by VECA (Modena, Italy) [61]. The half-cell profiles were machined by milling. The machining tolerance band and surface arithmetical-mean roughness (Ra) requested for the half-cells were 20 μm and 0.4 μm, respectively. The surface roughness may play an important role in the achievement of the best high-gradient performances. The skin depth in copper for a 3 GHz electromagnetic field is about 0.5 μm, comparable with the requested surface roughness. Smaller roughness is much more expensive and requires more sophisticated tools as diamond tooling. As mentioned above, the scope of this study is to evaluate the high-gradient performances of cavities with the same electromagnetic and mechanical characteristics as the cells of a linac for hadrontherapy. These cells would be machined with normal tooling in order to keep a reasonable cost of the linac. Therefore, also the test cell were

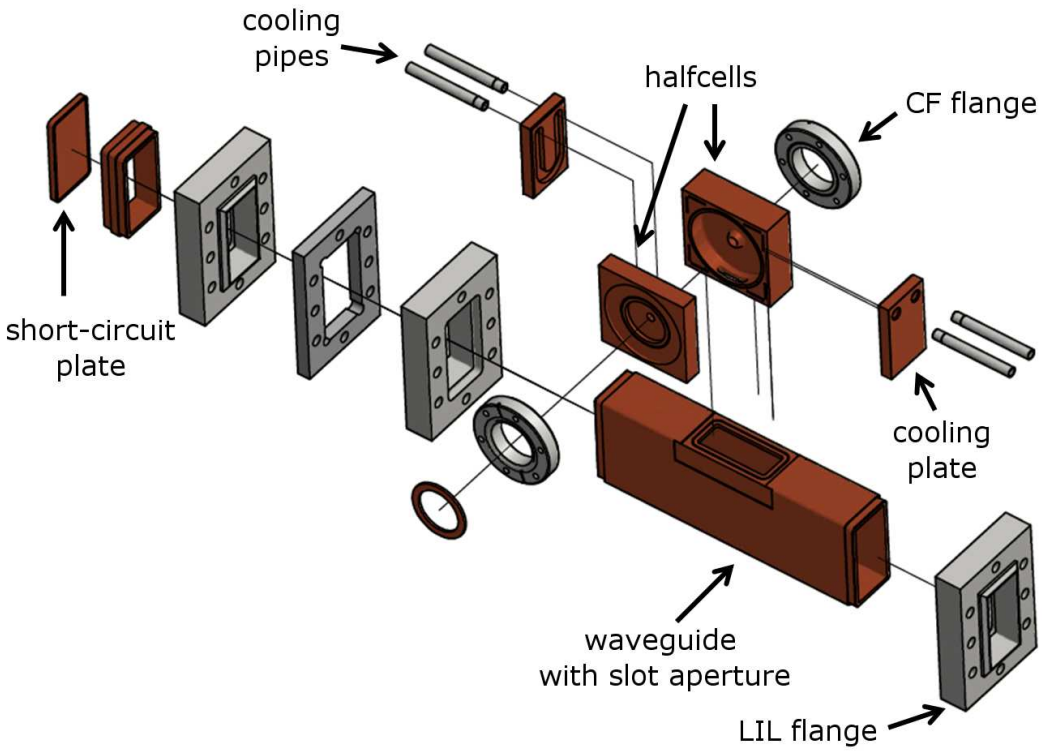

Figure 3.10: *Exploded view of the 3 GHz test prototype.*

machined with the same specifications. Sharp edges in coupler region were chamfered to avoid field enhancements which can lead to sparks.

The cleaning process is specially important in the preparation of high-gradient performance cavities, which operate under ultrahigh vacuum. Dirt and grease can compromise the result of brazing, and so the vacuum tightness, due to the presence of oxydes. Moreover, local field enhancement in the debris deposited on the surface may cause sparks. The cleaning process of the pieces of the 3 GHz test cavity, performed at the CERN workshops (Switzerland), consisted in three steps: degreasing with alkaline detergent under ultrasonic agitation, pickling in hydrochloric acid and passivation in acid solution. The cavity storage between high-power tests was done under nitrogen to avoid oxydation.

The vacuum furnace brazing procedure was performed by Bodycote (Annecy, France) [62]. The pieces of the prototype were brazed together with a silver-based alloy under vacuum at about 800°C in two steps. More information on the prototype production can be found in [63].

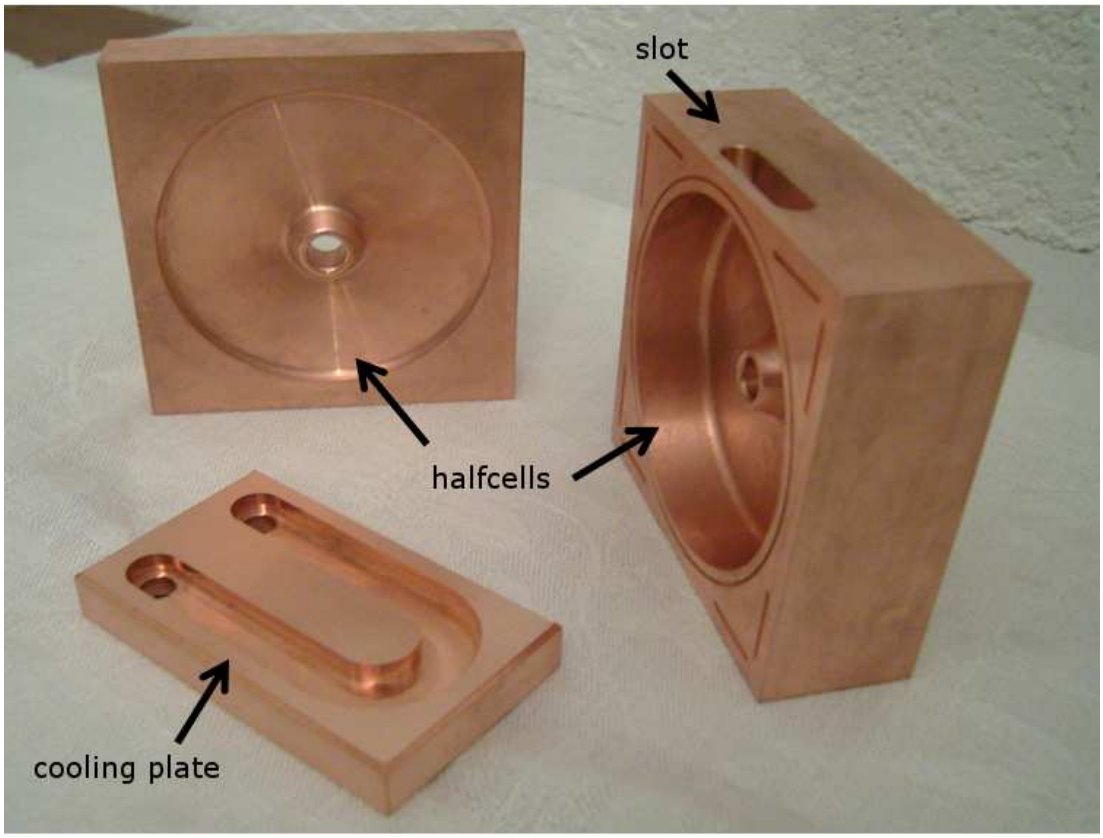

Figure 3.11: *Detail of the copper halfcells with slot aperture and one of the two cooling plates.*

After construction, the cavity was tuned by deformation of the nose region and matched by adjusting the length of the short-circuit waveguide end. These processes are explained in more detail in the following section.

3.2 Low Power Measurements, Tuning and Matching

The frequency and coupling factor of the cavity were tuned during the low power measurements performed in January 2010 at CERN (Geneva, Switzerland). The coupling factor dependence on the temperature was also evaluated. This section explains the selection of the resonant frequency and coupling factor, how the tuning was performed and how the coupling factor dependence on the temperature was evaluated.

3.2.1 Experimental Setup

One of the waveguide ends of the prototype was terminated with a movable short-circuit waveguide for the low power measurements performed in order to tune the

cavity and find the short position which matched the structure. The other end was connected to a waveguide-to-coaxial transition, as shown in Fig. 3.12. The measurements of the reflection coefficient Γ or ratio of reflected wave to one port for a wave incident to the same port were performed with a network analyzer connected to the transition. Pieces of aluminium foil were placed on the bore holes in order to avoid dust particles entering inside the cavity during the tuning and matching procedures. Two aluminium rods were placed on the outside part of the cavity, at the same level as the noses, and were pressed with a bar clamp. By screwing the clamp one could push the two cell noses together and hence reduce the resonant frequency of the cavity. The movable short circuit waveguide was adjusted by a micrometer screw which displaced the short circuit plate along the waveguide length in order to change the short circuit length.

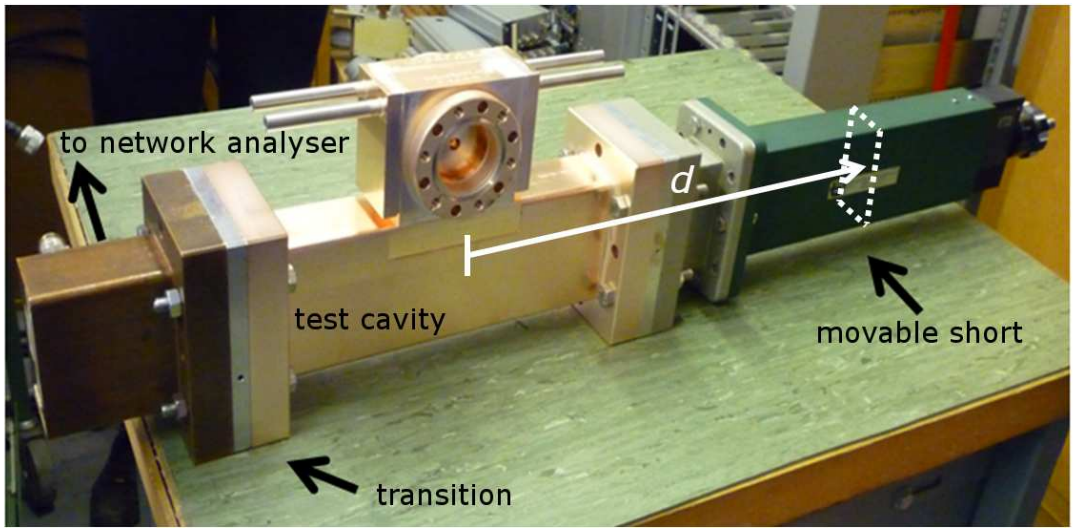

Figure 3.12: *Experimental setup for low power measurements of 3 GHz TERA single-cell cavity.*

3.2.2 Tuning and Impedance Matching

The measured resonant frequency f_0 of the brazed cavity in air before tuning was 3013.6 MHz. Because the cavity operates in vacuum the frequency must be compensated. The resonant frequency is proportional to the speed of light in the medium were the measurements are performed. The reflactive index for air is 1.0003. Consequently the resonant frequency of the cavity under vacuum will be about 1 MHz higher than the frequency measured in air. In addition, the resonant frequency decreases by 3 MHz during operation for thermo-mechanical reasons [59]. Therefore, if the cavity has to resonate at 2998.5 MHz under vacuum during the high-power test, the cavity has to be tuned during the low-power measurements, performed in air and using a negligible amount of power, down to 3000 MHz.

The gap length was reduced by screwing the clamp until the desired resonant frequency f_{goal}= 3000.2 MHz was achieved. The estimated corresponding shortening of the gap is about 0.14 mm, according to the estimations presented in section 3.1.5.

The short circuit length was changed until the structure was critically coupled. The cavity was critically matched (β_C =1) at the distance d = 320.63 mm, when d is the distance from the center of the slot to the short plate, as illustrated in Fig. 3.12. The maximum coupling factor β_C^{max} is found to be 1.55 at d=305.94 mm, which is in good agreement with calculations (β_C^{design} = 1.5 – 1.6).

For β_C equal to 1 (perfect matching), there are no reflections at all so all the incoming power is available for electromagnetic field excitation and corresponding power dissipation in the cavity walls. A lower β_C, for example equal to 0.8, means that the incoming power reflected by the cavity, given by $|\Gamma|^2$, is about 1.2%, as it can be calculated from Eq.(1.21). This quantity has to be taken into account if the accelerating gradient excited on the cell axis is evaluated from the power going into the cavity.

Lower power losses and lower temperature variation dependency are expected with a shorter length of the short circuit waveguide, so another matching position of the short closer to the cavity was searched and found at d=253.65 mm. Thus the distance from the center of the slot to the short d was reduced by half a wavelength (λ_Z=138.52 mm) for mechanical considerations. A reduction of the short circuit length by half a wavelength brings the system to the same electromagnetic conditions.

Swept-frequency network analyzers display the complex reflection coefficient Γ as function of frequency (reflected signal, see Fig. 3.13). The resonant frequency f_0, quality factor Q_0 and coupling factor β_C can be obtained from the reflected signal. The resonant frequency is the frequency for which the reflected signal is minimum. In Fig. 3.14 the reflected signal is represented in the Schmit chart. As the measurement corresponds to a resonant circuit, one obtains a circle. The coupling factor β_C is simply defined as:

$$\beta_C = \frac{1 - \Gamma(f_0)}{1 + \Gamma(f_0)} \tag{3.2}$$

If the expression of the reflection coefficient is developed in terms of f_0, β_C and Q_0, then:

$$\frac{1 + \Gamma(f)}{1 - \Gamma(f)} = \frac{1}{\beta_C}\left(1 + jQ_0\left(\frac{f}{f_0} - \frac{f_0}{f}\right)\right) \tag{3.3}$$

By plotting the imaginary part of $(1 - \Gamma(f)/1 + \Gamma(f))$ against $(f/f_0 - f_0/f)$ it is possible to find the quality factor of the resonant circuit Q_0 as the slope of the fitted line.

The values of f_0, Q_0 and β_C were calculated from the reflected signal measured after machining the short-end of the waveguide of the cavity in study. Table 3.8 contains the results of the calculations. The β_C was 0.92, equivalent to a reflection coefficient Γ of 0.042. Therefore, the power reflected $|\Gamma|^2$ was less than 0.2%.

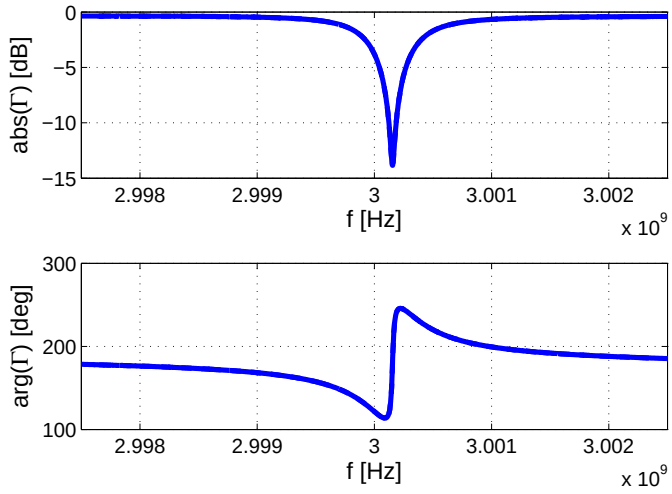

Figure 3.13: *Module (above) and argument (below) of the reflection coefficient measured for the cavity for different frequencies.*

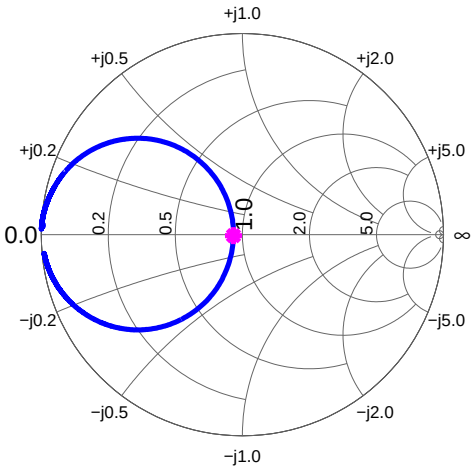

Figure 3.14: *Representation of the equivalent resonant circuit of the cavity in the Schmit chart. The point corresponding to the resonant frequency is shown in magenta.*

Table 3.6: *RF parameters of the cavity obtained from simulations and measurements: a) before tuning, b) after tuning, c) results from GdfidL simulations corresponding to another study of the same cavity [60] and d) results from HFSS simulations for the cavity with halfcell offset. The resonant frequency os the cavity in air is 1 MHz smaller than the frequency of the cavity under vacuum. Mechanical tolerances foresee a frequency uncertainty of ±7 MHz. Measured values are consistent with predictions performed using GdfidL and HFSS simulations.*

	Simulations in vacuum	Measurements in air	
Frequency	(3014)[a]	3014[a] / 3000[b]	MHz
Q value	~ 8900[c] / 8920[d]	9140	
Max. coupling factor β_C^{max}	1.6[c] / 1.5[d]	1.55	

3.2.3 Coupling Factor Dependence on Temperature

The cavity volume expands as the ambient temperature increases, leading to a decrease of the resonant frequency. The quality factor also goes down because resistivity increases with increasing frequency, as it can be seen in Fig. 3.15. The coupling factor β_C also varies with temperature as result of this volume variation.

The cavity was warmed up in order to estimate the variation of the coupling factor with temperature. Table 3.7 contains the frequency, quality factor and coupling factor measured at different temperatures. As the temperature could not be measured, it was estimated from the known dependence of frequency f_0 and quality factor Q_0 on the ambient temperature. Thermo-mechanical simulations performed for this cavity with *Ansys* [59] predicted that the frequency shift Δf with temperature T would be

$$\frac{\Delta f}{\Delta T} = -\frac{0.05 MHz}{degree} \tag{3.4}$$

The quality factor is inversely proportional to the square root of the electrical resistivity of the material ρ. In turn, the resistivity can be assumed as linearly proportional to the temperature for small temperature variations. So finally, the quality factor variation with temperature is given by

$$\frac{\Delta Q}{Q} = -\frac{\Delta T}{2T} \tag{3.5}$$

For a nominal temperature of $T = 298$ K, the quality factor diminishes about 4% if the temperature increases by 20 degrees. According to the measurements shown in Table 3.7, the coupling factor changes about 1% for a temperature increase of 20 degrees, which is consistent with theoretical predictions.

After the high-power measurements the cavity was cut into two halves in order to inspect the surface of the cell interior, as reported in section 3.3.4. Then we observed an offset between one halfcell and the other one. The offset led to a small variation on the fields excited inside the cell. The main electromagnetic quantities were evaluated

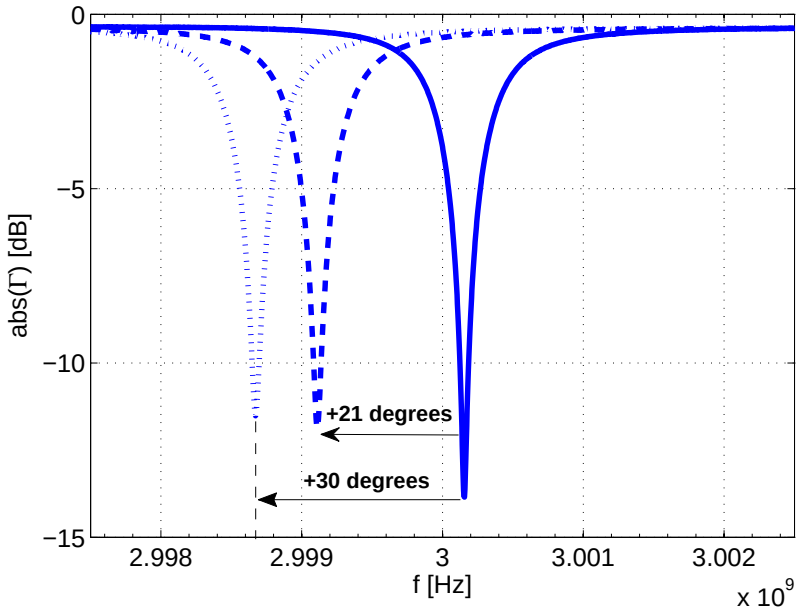

Figure 3.15: *Reflection signal of the cavity at different ambient temperatures.*

Table 3.7: *Data used to evaluate the coupling factor β_C dependence on temperature.*

Estimated				
Temperature, T	298	319	328	K
Measured				
Frequency in air, f_0	3000.2	2999.1	2998.7	MHz
Quality factor, Q_0	9140	8750	8600	
Coupling factor, β_C	0.92	0.87	0.86	

for the new geometry and were used for the elaboration of the data presented in the following.

Table 3.8 summarizes the main characteristics of the 3 GHz TERA single-cell ready for high-power testing. The resonant frequency, quality factor and coupling factor are the values measured during the low power tests. The ratios between electromagnetic quantities E_{max}/E_0, H_{max}/E_0 and $\sqrt{S_{C,max}}/E_0$) presented in Table 3.8 are the values obtained from HFSS simulations for the cell with offset.

Table 3.8: *Main characteristics of the 3 GHz test cavity.*

Cavity geometry		
Cell Radius, R_{cell}	64.5	mm
Gap Length, g	~4.7	mm
Slot Width, w_{slot}	6	mm
Slot Length, l_{slot}	25.5	mm
Measured electromagnetic quantities		
Frequency in air, f_0	3000.2	MHz
Quality factor, Q_0	9140	
Coupling factor, β_C	0.92	
Calculated electromagnetic quantities		
E_{max}/E_0	6.35	
H_{max}/E_0	2.92	kA/MV
$\sqrt{S_{C,max}}/E_0$	0.029	$\frac{\sqrt{\mathrm{MW/mm^2}}}{\mathrm{MV/m}}$
For operation at E_{max}=150 MV/m and t_{pulse}=3μs		
Required Power, P	~128	kW
Pulsed Surface Heating, ΔT	2	degrees
Mechanical		
Material	OFE10100 copper	
Tolerance band	20	μm
Surface Roughness (Ra)	0.4	μm
Tuning sensitivity		
Nose deformation	12 MHz/0.1 mm in gap	
Dimple tuner	1 MHz/tuner	

3.3 High Power Tests

The 3 GHz single-cell cavity underwent three high-power tests, conducted in winter 2010, fall 2011 and winter 2012. All the tests were performed in the CLIC Test Facility (CTF3) at CERN. The primary goal of this series of high-power tests was to measure the breakdown rate at field levels in the range of operation of CABOTO.

3.3.1 Preliminary High-Power Test at CTF3 in Winter 2010

Objectives

The main goals of this first high-power test were to check the RF behaviour of the test cavity, to debug the cavity setup and operation, and to identify the specifications of the diagnostic instrumentation, data logging and control system required for a precision test.

Experimental setup and diagnostic instrumentation

The cavity was installed in CTF3, the facility built at CERN which aims to demonstrate the feasibility of CLIC. A sketch of the facility is shown in Fig. 3.16. During the run of winter 2010, the cavity was installed in the linac hall (see Fig. 3.17). The RF power was supplied by a klystron operated at 50 Hz and delivering 5 μs-long RF pulses at maximum. A 20-meter long waveguide connected the klystron with the cavity. The resonant frequency of the installed cavity appeared to be around +2 MHz shifted with respect to the low power measurements performed after brazing. The operation of the cavity was still possible because the klystron operation frequency was centered at 2998.5 MHz with a frequency bandwidth of ±10 MHz. The coupling factor β_C was about 0.9, which leads to an acceptable power reflection percentage of 0.2%.

The incident and reflected power signals were monitored by a peak power meter. The resonant frequency and incoming power were controlled manually. Fig. 3.18 shows a screen shot of the peak power meter during operation at resonance (reflected power below 10% of incident power).

The field-emission current was collected in the Faraday cup connected to one of the bore holes of the cavity cell. No data logging or processing system was implemented for this run, so the breakdowns were identified by eye from the display of the field-emission current signal in a scope. Fig. 3.19 shows the screen shot of the scope which displays the field-emission current signal in the moment when a breakdown occured.

History and first measurements

The cavity was operated with 2 μs-long (flat-top) RF pulses at 50 Hz about 40 hours during which about 14000 breakdowns occured. The maximum surface electric field achieved in the cell was above 350 MV/m, corresponding to accelerating gradients of over 50 MV/m. The measured BDR at these field values was around 10^{-1} bpp/m.

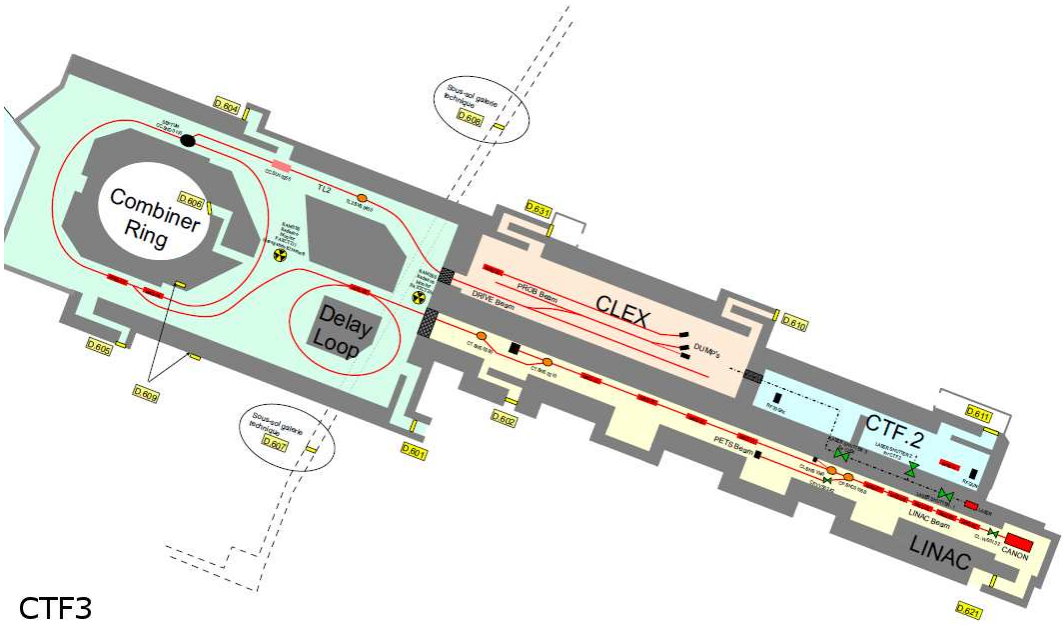

Figure 3.16: *CLIC Test Facility (CTF3) at CERN.*

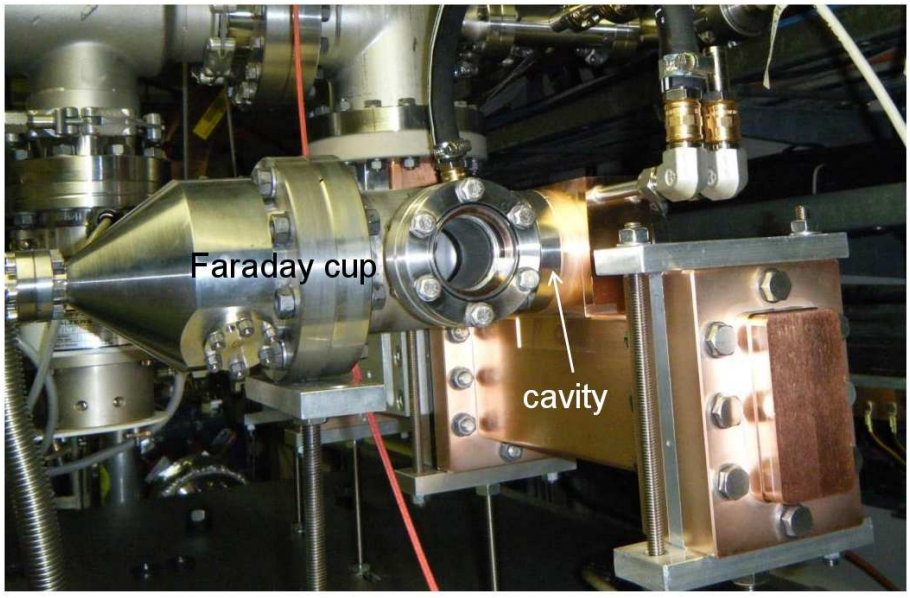

Figure 3.17: *3 GHz test cavity installed in CTF3 during the test of winter 2010.*

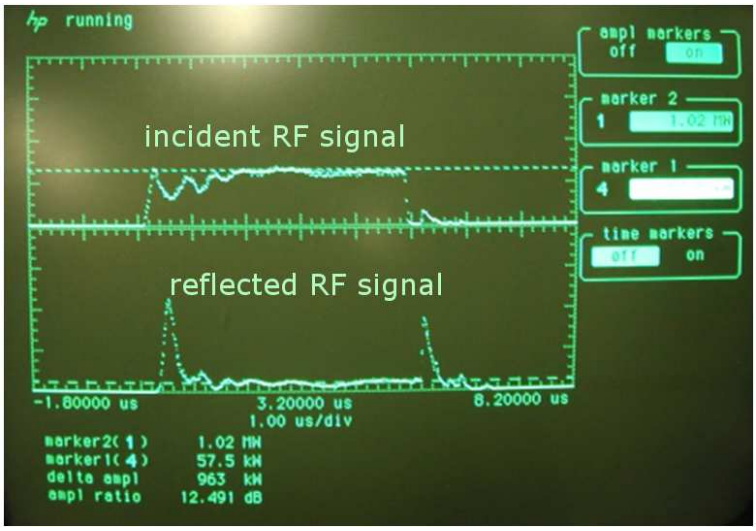

Figure 3.18: *Screen shot of the peak power meter during operation at resonance.*

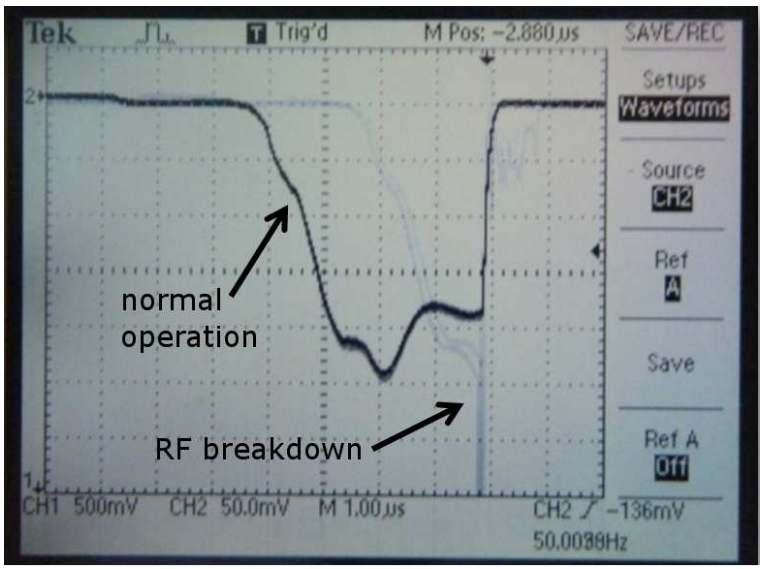

Figure 3.19: *Screen shot of the scope displaying the field-emission current signal during the test of winter 2010: [dark line] normal signal, [light line] breakdown signal.*

The nose region surface of the cavity, where maximum electric and magnetic field values and maximum Poynting vector are reached, was inspected with an optical microscope through the bore hole. A picture of one of the noses is shown in Fig. 3.20. The surface on this region of the cell was considerably damaged. There were many spots related with breakdown activity and some big, circular craters the origin of which is uncertain. The inspection of the cell surface also allowed the visualization of the copper grains and the surface roughness of the machining, as it is shown in Fig. 3.21.

After this first high-power test, the cavity was stored under a nitrogen atmosphere to reduce oxidation and molecular adsorption.

Conclusions

The operation of the cavity was successfully debugged. The cavity had an excellent RF behaviour, reaching a maximum surface electric field E_{max} over 350 MV/m.

The implementation of data logging and control systems for the next high-power tests raised a key point to help in the identification of RF breakdowns, characterize associated phenomena and get sufficient statistics to evaluate breakdown rates. Gained experience in this preliminar high-power test was taken into account for the specification of the data logging and control systems.

3.3.2 High-Power Tests at CTF2 in Fall 2011 and Winter 2012

The cavity was installed in CTF2 for the continuation of the high-power tests. The experimental setup was more sophisticated than the one used for the first high-power test of winter 2010. It incorporated control and data logging systems expressly implemented for the cavity testing which helped with the cavity operation and allowed a better characterization of the cavity behaviour under high power. The conditioning of the cavity could not be completed during fall 2011 and another run had to be scheduled for winter 2012 to complete the conditioning and performing the breakdown rate measurements. This section presents the objectives, experimental setup and history of these two runs.

Objectives

The first objective was to commission the new control and data logging systems. The cavity had to be conditioned, so that the breakdown rate measurements could be performed. The measurements should be done for different field levels and pulse lengths to evaluate the scaling laws that relate breakdown rate to the pulse length and to electromagnetic quantities such the electric field or the modified Poynting vector. Another measurement should be performed for an electric field in the range of operation of CABOTO. The events registered during the breakdown rate measurements would serve to characterize of the RF breakdowns and phenomena associated.

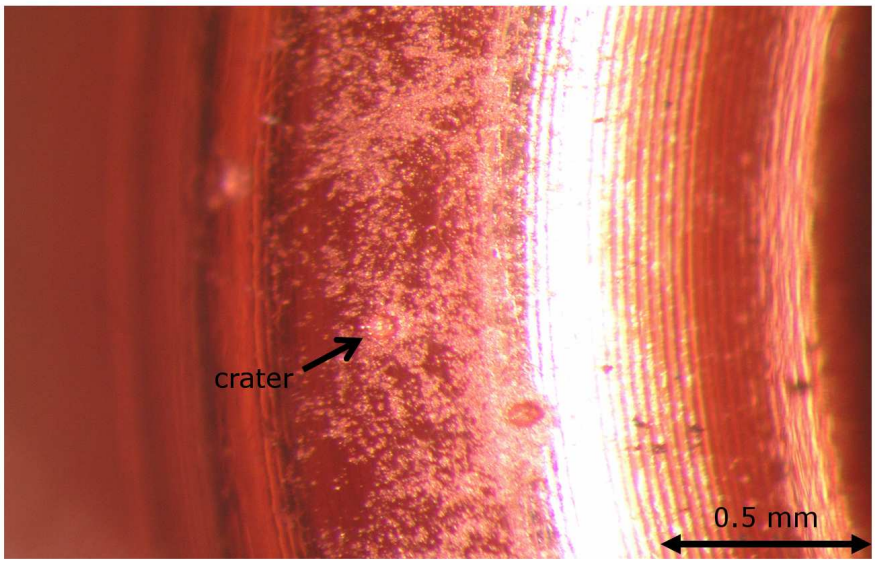

Figure 3.20: *Magnification of one of the noses of the cavity cell with many spots related to breakdown activity and some craters of uncertain origin.*

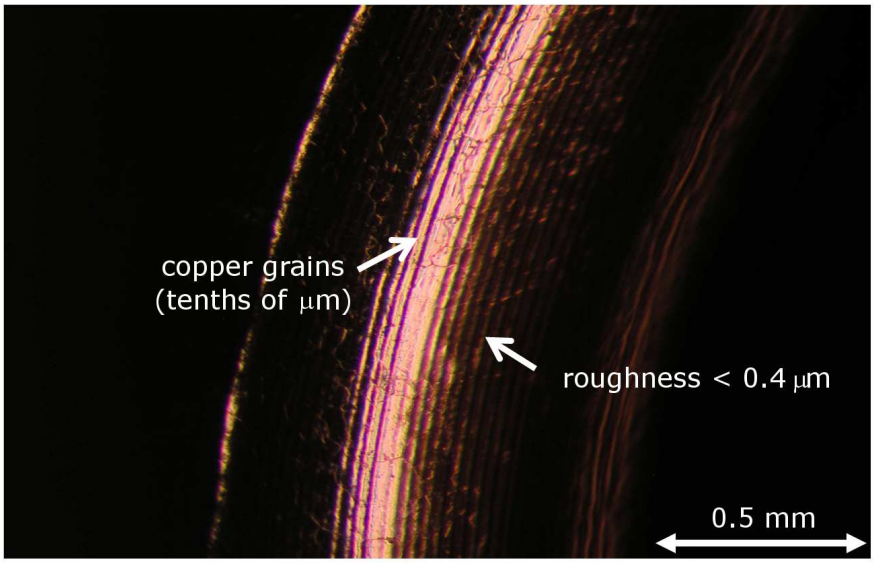

Figure 3.21: *Copper grains, with a size in the order of tenths of μm, and surface roughness of about 0.4 μm in the nose region of the cavity cell.*

Experimental setup, diagnostic instrumentation and data logging system

The cavity was installed in the CTF2 hall at CTF3 (see Fig. 3.16) for the tests of fall 2011 and winter 2012. It remained connected to the RF system between one run and the next one in order to prevent surface deterioration due to oxydation. The vacuum level was maintained below 10^{-8} mbar during all this time. Data logging software was used to record the main operation performances and diagnostic signals. Fig. 3.22 shows the experimental setup in CTF for these runs.

The main characteristics of the RF system, the cooling system, the vacuum system, the diagnostic instrumentation, the control system and the data logging software are presented in the following.

RF system

For the run of fall 2011, a 76 m-long waveguide system conducted the power from klystron number 30 in the CTF klystron gallery to the cavity placed in the CTF2 gallery. This klystron can deliver RF pulses with a maximum length of 5 μs at a maximum repetition rate of 5 Hz. No other klystron pulsing at higher repetition rate was available for this run. A higher repetition rate which would have served to reduce the time required to condition the structure. Klystron number 14 was used in the run of winter 2012, as it delivers RF pulses with a maximum length of 5 μs at a maximum repetition rate of 100 Hz. Fig. 3.22, 3.23, 3.24 show the downstream part of the RF circuit. Most of the circuit is under sulfur hexafluoride (SF_6) to reduce power losses. An RF window, shown in Fig. 3.22, separated the SF_6 atmosphere from the last meters of the RF circuit, under ultrahigh vacuum (UHV). More details on the vacuum system are given below.

The klystrons were operated far away from the saturation region because lower powers were needed to run the test cavity (about 1 MW peak power) compared to the nominal peak power power of the klystron, 50 MW. As a consequence, the power reflected from the cavity going back to the klystron affected the pulse shape, as explained below. The installation of a circulator in the RF circuit during the run of fall 2011 was necessary to obtain a nice square RF pulse. The circulator was kept in the RF circuit for the run of winter 2012.

The cooling system of the test cavity operated with thermalized water (T≈303 K) at the appropriate water flow (5 l/min) during these runs.

Vacuum system

Performances of high-gradient structures are greatly enhanced if the structures are operated under good quality vacuum. For this experiment, a vacuum station consisting of a conventional vacuum pump and an ion pump was installed in the proximities of the test cavity (last meters of the RF circuit before the test cavity, downstream the RF window). The vacuum pump was used to reach a low enough vacuum level at which

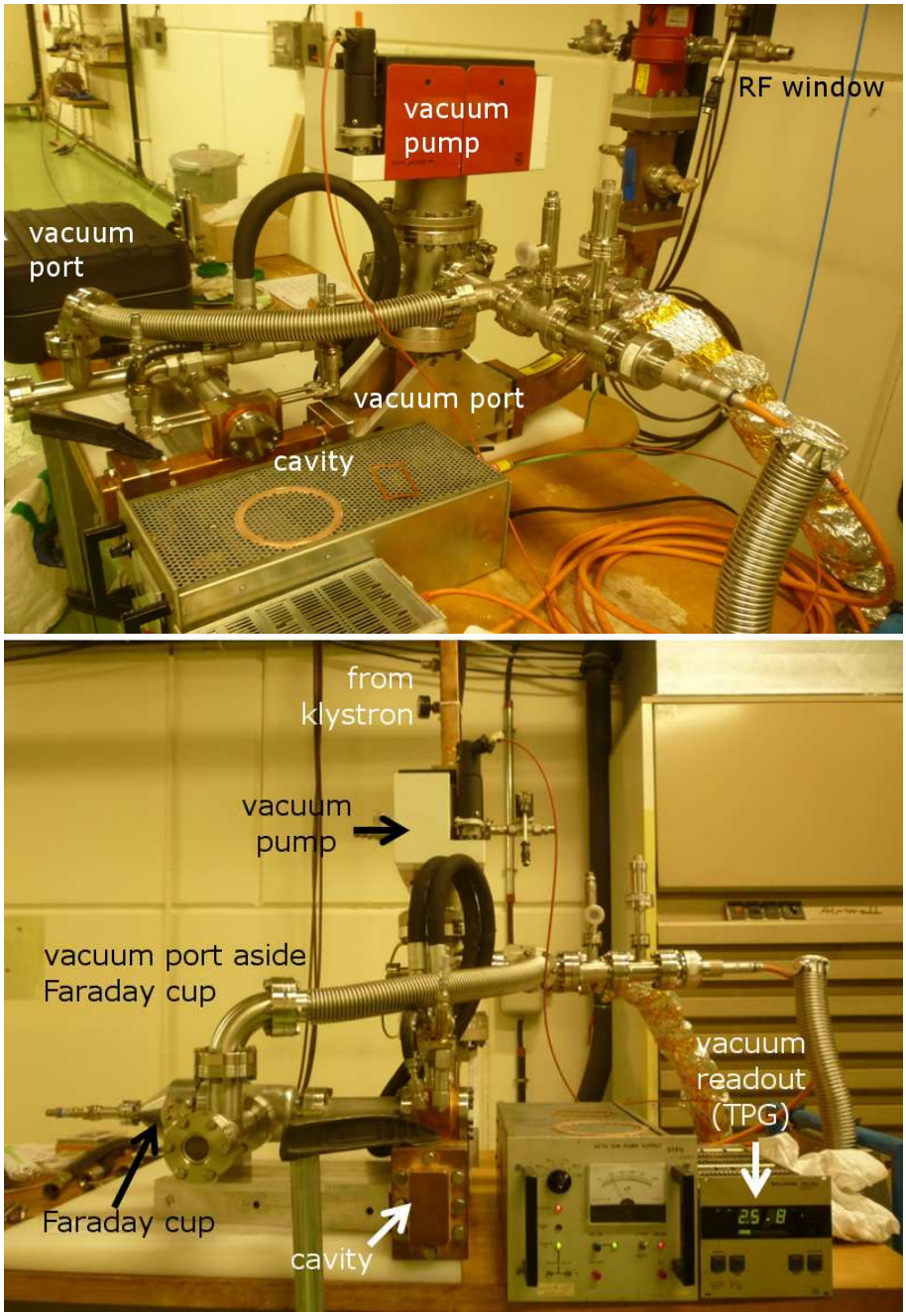

Figure 3.22: *Experimental setup in CTF2.*

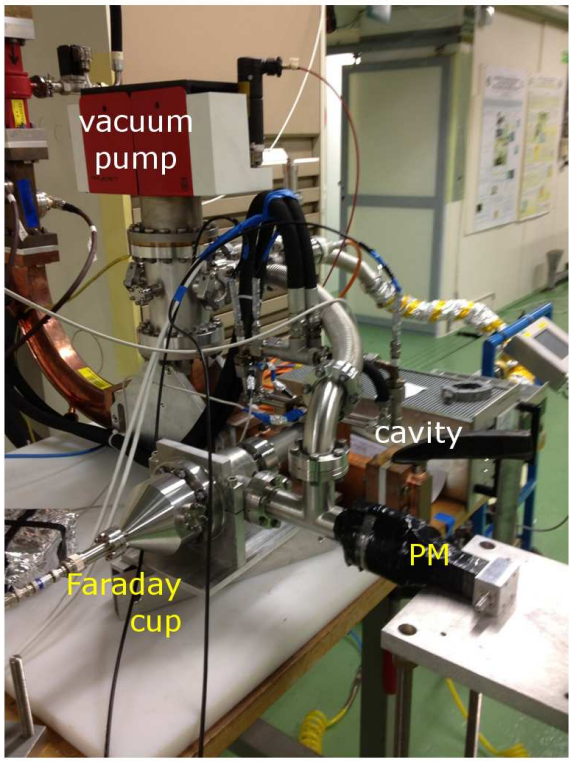

Figure 3.23: *Detail of the experimental setup in CTF2.*

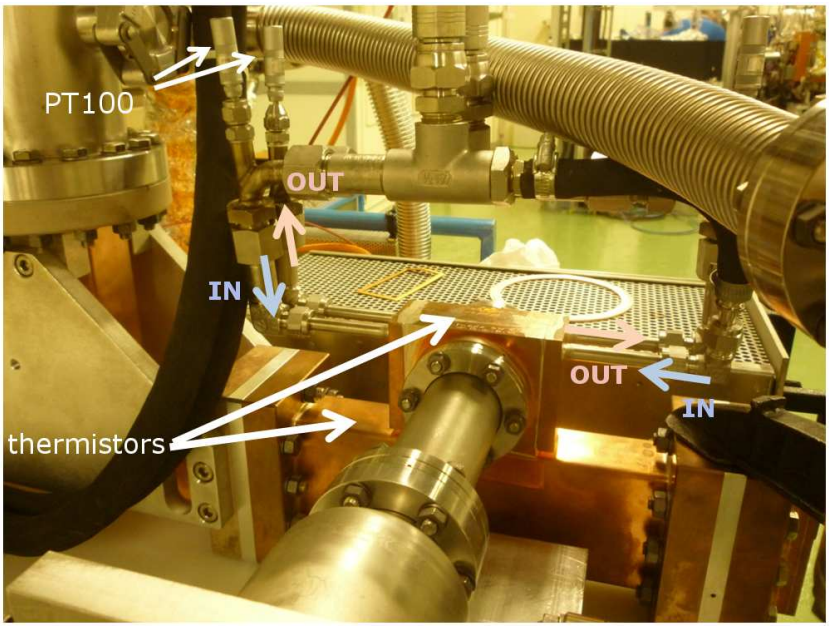

Figure 3.24: *Detail of the experimental setup in CTF2 showing the direction of the coolant (in and out channels) and the instrumentation to measure the temperature of the outer surface of the cavity (thermistors) and the coolant (Pt100).*

the ion pump could start working. The best vacuum level realized was 10^{-8} mbar. Two vacuum ports were placed in the proximities of the cavity for this purpose: i) upstream of the test cavity and ii) downstream of the test cavity, between the cavity and the Faraday cup (see Fig. 3.22).

Diagnostic instrumentation

The diagnostics for the high-power tests in CTF2 included:

- A Faraday cup for field-emission and breakdown current detection. The Faraday cup was connected to one of the bore holes of the cavity (approx. 50 cm distance), as shown in Fig. 3.22. The analog signal of the Faraday was then amplified 20 times before being sent to the interlock hardware and data acquisition card.

- Crystal detectors to measure incident and reflected RF power signals from the bidirectional coupler located upstream of the cavity. Each RF power signal was splitted into two branches: one was connected to a diode, for getting the amplitude information and the other one was connected to a mixer to get the phase information. The amplitude and phase signals were then sent into the data acquisition cards. The RF power signals were used to estimate the accelerating field inside the cavity, as explained below.

- A photomultiplier (PM) to detect the light emitted during RF breakdowns. The light emitted by the test cavity was reflected in a mirrored surface sitting at the interior of the Faraday cup and directed to the photomultiplier. The photomultiplier was included in the run of winter 2012 (see Fig. 3.23).

- Total pressure gauge TPG300 to monitor vacuum level inside the cavity, shown in Fig. 3.22.

- Two integrated-circuits temperature detectors (thermistors) to monitor the thermal behaviour of the cavity.

- Two platinum resistance thermometers (Pt100) placed on the inlet and outlet of the cooling circuit in order to check the water temperature (see Fig. 3.24). Voltage-to-frequency converters were employed to perform the data logging through a PC's sound card via a *Matlab* code.

Diagnostic signals during non-breakdown pulse are shown in Fig. 3.25. The field-emission current is also known as dark current because no light accompanies the emission of electrons. However, some light was detected during normal operation of the cavity. The signal was proportional to the field-emission current signal. The light registered by the photomultiplier during normal operation could be explained by secondary interaction of the field-emitted electrons with the mirror of the Faraday cup or

the viewport. The hypothesis that the light detected in the photomultiplier were X-rays was desestimated after checking that no signal was registered in the photomultiplier when it was covered with a black foil.

RF breakdowns are typically identified by the sudden, abrupt increase of field-emission current and/or by the increase of reflected power, resulting as the high amount of current emitted during RF breakdown short-circuits the cavity in operation. Fig. 3.26 shows the imprints of an RF breakdown in the field-emission current and the reflected RF power signals.

A sudden, abrupt increase of pressure is another feature of a breakdown event. The field-emission current signal and the vacuum signal were used to interlock the RF amplifier.

Data logging system

Two DC265 Acqiris cards with 4 channels each collected the signals - i) field-emission and breakdown current detected in Faraday cup (one channel), ii) incident and reflected RF power amplitudes and phases (four channels) and iii) light detected in the photomultiplier (one channel)- later sent to the data logging system (called CTF/TERA application in the following).

The vacuum signal was sent to a PC during the run of fall 2011 and then processed by a LabVIEW application which stored the vacuum level every second in a text file. The vacuum signal was sent to the data acquistion system during the run of winter 2012 to store all the signals under the same format and preserve synchronicity between the readings.

The CTF/TERA application, written in Java, allowed the user to define the characteristics for an event to be identified as a breakdown. For example, the amount of reflected RF energy, the amount of reflected RF power and/or the field-emission current intensity. The application was able to store:

a) amplitude and phase of incident and reflected RF pulses,

b) waveforms of incident and reflected power for some RF pulses during normal operation,

c) waveforms of incident and reflected power for all RF pulses which satisfied the conditions specified by the user to identify breakdowns,

It provided the visualization of signal waveforms and time evolution of the main operation quantities (incident RF power, reflected RF power, field-emission current and pulse length), computed the number of accumulated breakdowns and plotted the breakdown rate evolution in time (dynamic breakdown rate).

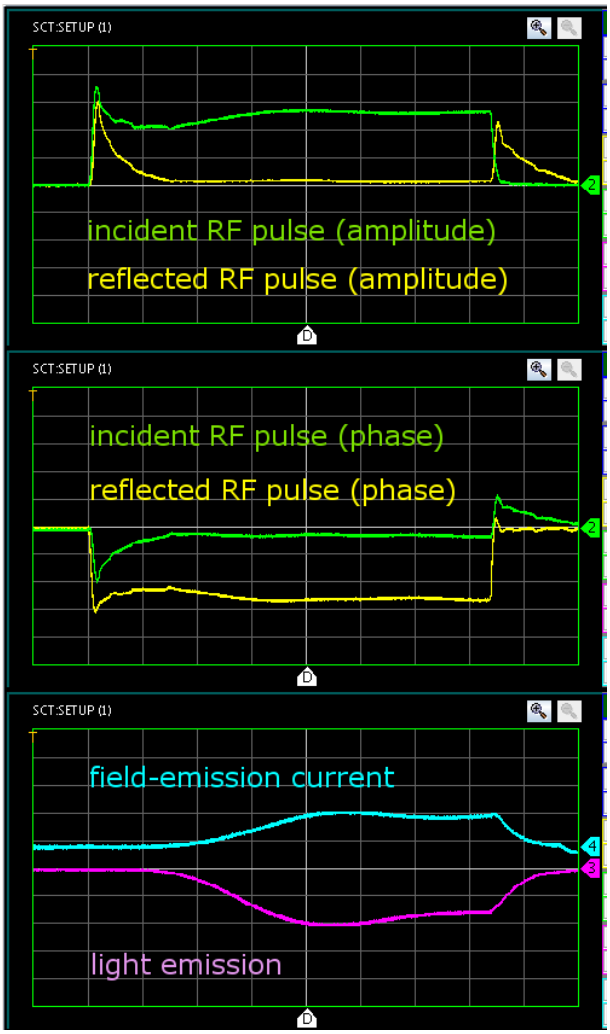

Figure 3.25: *Screen shot of display software Oasis [64] during normal operation of the cavity showing the amplitude and phase of the incident and reflected RF pulses as well as the field-emission current signal and the emitted light.*

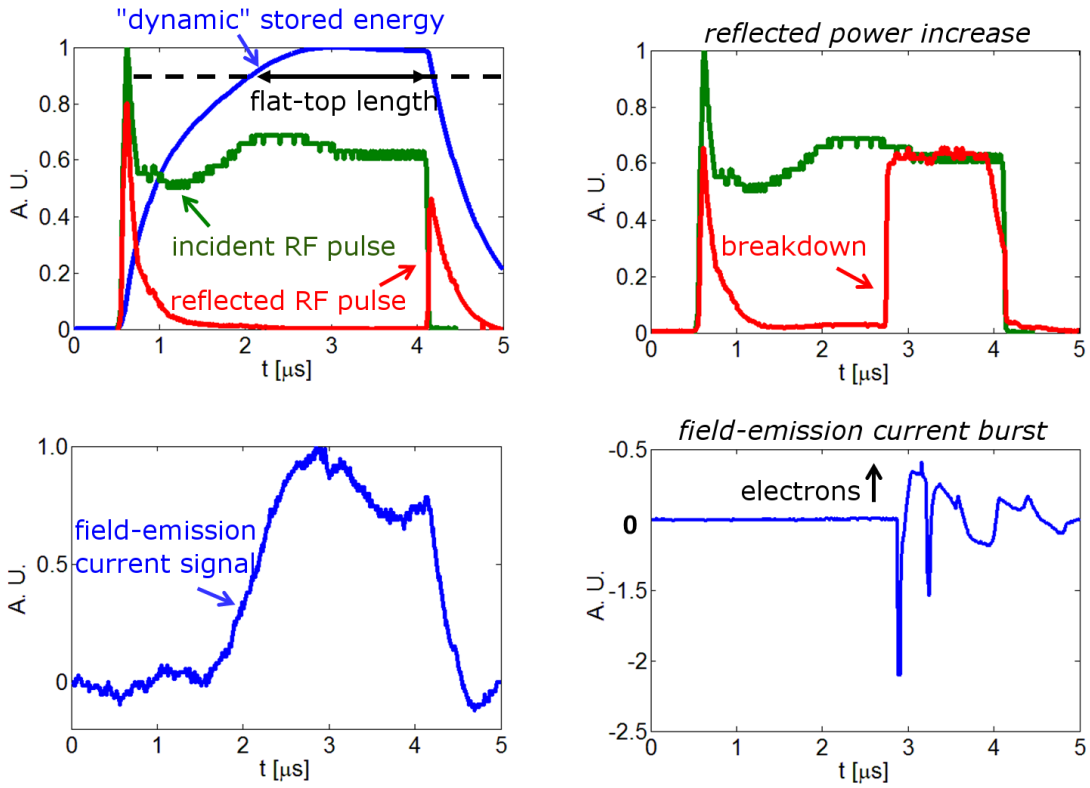

(a) For normal operation.

(b) During breakdown.

Figure 3.26: *Diagnostic signals: incident and reflected RF power amplitude and field-emission current measured with Faraday cup.*

Control system

The control system and conditioning software were designed to control the power going into the test cavity pulse to pulse. In the case of an abrupt increase of field-emission current or pressure, the pulsing of the power was interrupted. In the following the settings of these interlocks and the main characteristics of the power recovery software are described.

Two threshold levels were set for the vacuum interlock. SF_6 gas from the waveguide system and water used to cool down the RF window could come into the test cavity if the RF window would break as result of high pressures. Therefore, one threshold level was set at 10^{-5} mbar. If pressure exceeded this level, an electro-valve closed the water circuit. The other interlock, at 10^{-7} mbar, stopped the RF pulsing. A maximum threshold was set for the field emission current peak at 1 mA. Above this threshold, the interlock was activated and the RF pulsing stopped.

Some interfacing problems with the RF amplifier were found during the run of

fall 2011, and the power had to be restarted manually every time that the hardware interlocks were activated. Interfacing problems between the software and the RF amplifier prevented not only restarting the power after an interlock was activated but also controling the power settings remotely. In the last days of the run of fall 2011 the interlocks were disconnected to increase the operation time and perform some breakdown rate measurements. The RF amplifier could be controlled remotely for the run of winter 2012, and the control software was then used to condition the cavity. The software was able to reset the power sent into the cavity after an interlock was activated. After activation of an interlock, and at the end of the waiting period (5 seconds), pulsing resumed at a reduced power level. The power was then slowly increased until it reached the level it had before the interlock was activated. Fig. 3.27 illustrates the conditioning system implemented for the test. Fig. 3.28 shows a screen shot of the control system developed for the cavity test.

Safety considerations

The cavity was installed in the CTF2 gallery, a controlled radiation area. Noone could enter this area while the cavity was under operation. The cavity was operated 24/7, including nights and weekends. A camera controlled by the CERN Computer Center (CCC) was installed in the CTF3 control room in order to fulfill CERN safety regulations.

History

The run of fall 2011 started on September 28th and ended on October 21st. The first period was used to debug the control and data logging systems and to condition the cavity. The last three days were employed to perform BDR measurements for different power levels and pulse lengths.

The conditioning period lasted from September 28th until October 18th. The repetition rate was increased from 1.67 Hz up to 5 Hz in the first days of the run. The pulse length was gradually increased from 1 μs to 3.5 μs. A 3.5 μs-long constant-power RF pulse gives a 1.5 μs rise-time followed by a 2 μs flat-top time. A circulator was installed on October 7th to avoid perturbation of the klystrons output power caused by reflected power. The interlocks were disconnected on October 15th to facilitate the conditioning progress. The conditioning could not be supervised by anybody from October 15th until October 16th. Therefore, the cavity was run at low fields (200-240 MV/m peak surface electric field) during this period to avoid unstable operation. Dark current measurements were performed on October 18th and breakdown rate measurements started on October 19th, even though the conditioning was not completed yet. The cavity was exposed to more than 250 RF hours in which about 4.5 million RF pulses led to more than 4000 breakdowns during this run. Fig. 3.29 shows the history of the run of fall 2011 in function of the maximum peak RF power sent into the cavity.

The testing time available in winter 2012 was allocated to finish the cavity con-

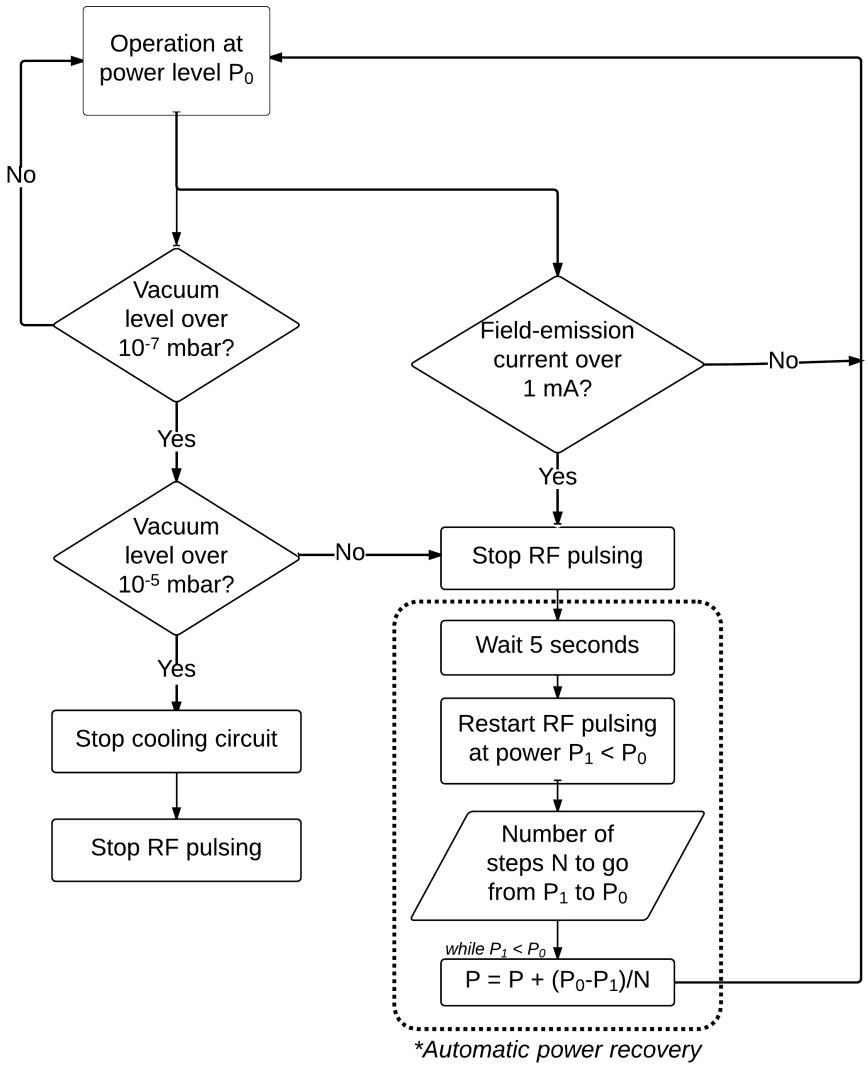

Figure 3.27: *Conditioning system implemented for the 3 GHz cavity test. The automatic powr recovery system was not available for the first high-power test due to interfacing problems between the control software and the RF amplifier.*

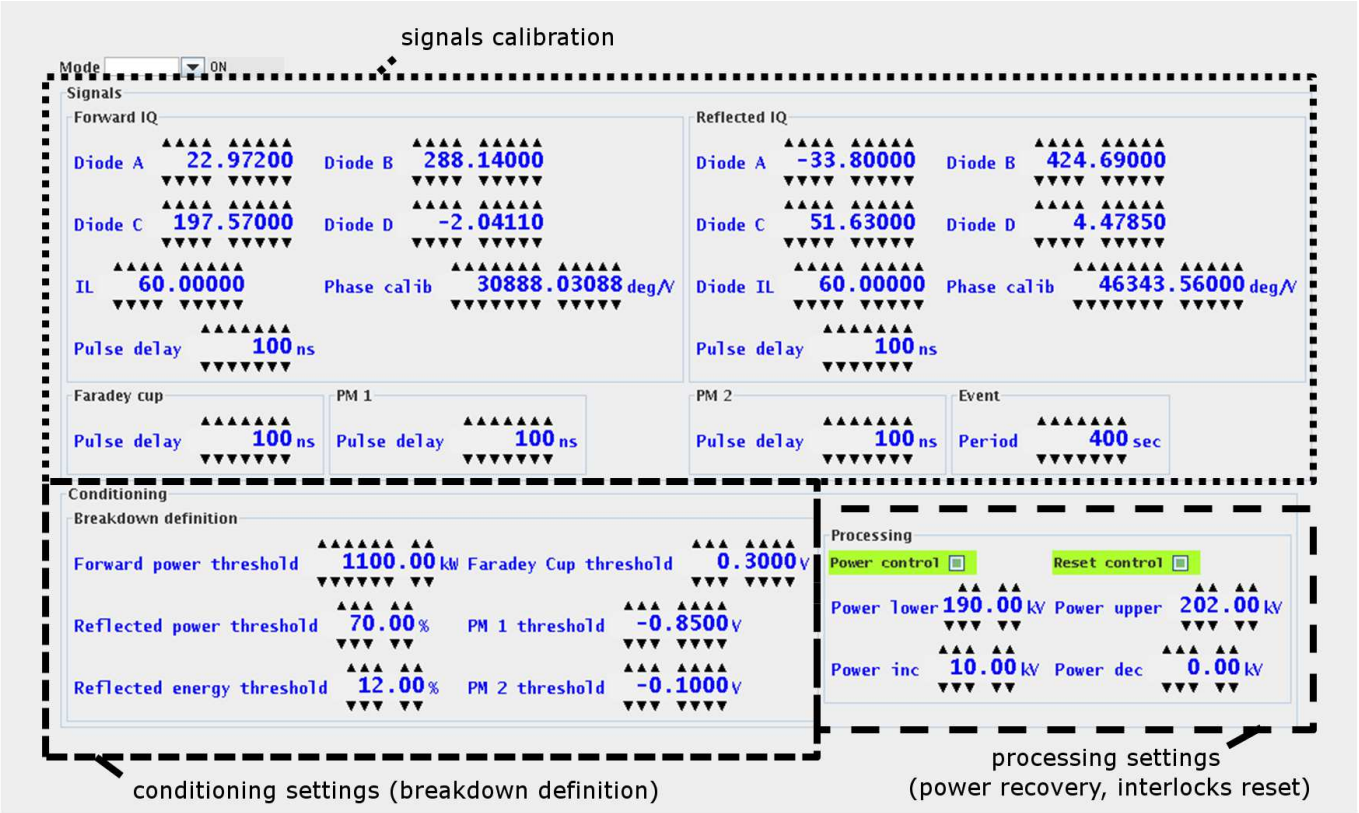

Figure 3.28: *Screen shot of the control system software used on the run of winter 2012. The software requires the user to provide the signals calibration, as well as the breakdown definition (in terms of reflected RF power, field-emission current and light) and the power recovery settings.*

ditioning and then perform the breakdown rate measurements of interest. The run of winter 2012 started on February 22nd. The repetition rate, limited to 5 Hz in the run of fall 2011, could be increased up to 100 Hz in winter 2012, allowing a faster conditioning of the cavity. However, the data logging system had some trouble synchronizing the storage of the different diagnostic signals at so high repetition rate. The repetition rate was consequently decreased to 50 Hz in order to preserve data synchronicity during breakdown rate measurements. RF pulses of 4 μs were typically used in winter 2012. The BDR measurements started in February 27th. Fig. 3.30 shows the history of the run of winter 2012.

During the tests, a maximum power of 1 MW was sent into the cavity, which corresponds to a maximum surface electric field E_{max} of about 420 MV/m. The pulsed surface heating ΔT was about 16 degrees for RF pulses of 4 μs. In total the cavity was exposed to 5×10^7 RF pulses and experienced about 10^4 breakdowns.

Conditioning status

The reduction of the breakdown rate measured for a certain field level indicates the conditioning status of the cavity. Fig. 3.31 shows how the breakdown rate measurements evolved from the run of winter 2010 until the run of winter 2012. The breakdown rate improves two orders of magnitude from the end of the run of winter 2010 until the end of the run of winter 2012 (i.e. within 5×10^7 RF pulses).

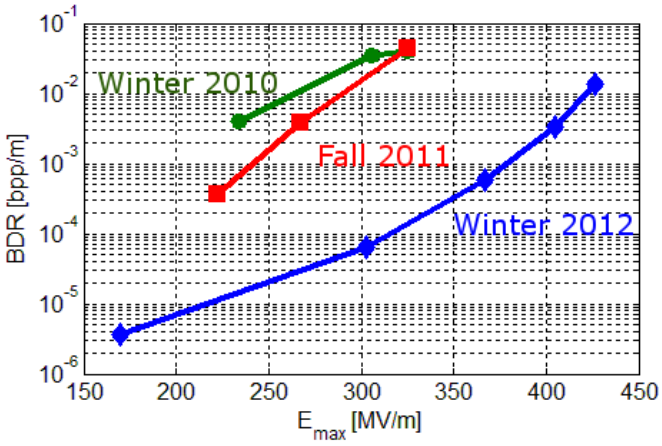

Figure 3.31: *Evolution of the breakdown rate measured for different stages of the cavity: (green) winter 2010, (red) fall 2011 and (blue) winter 2012.*

Fig. 3.32 shows the Fowler-Nordheim plot for the dark current measurements performed during the run of winter 2012. The field enhancement factor β_{FE} is 60–75. The cavity is fairly well-conditioned: the evaluated β_{FE} is comparable to the values found in literature [1, 3].

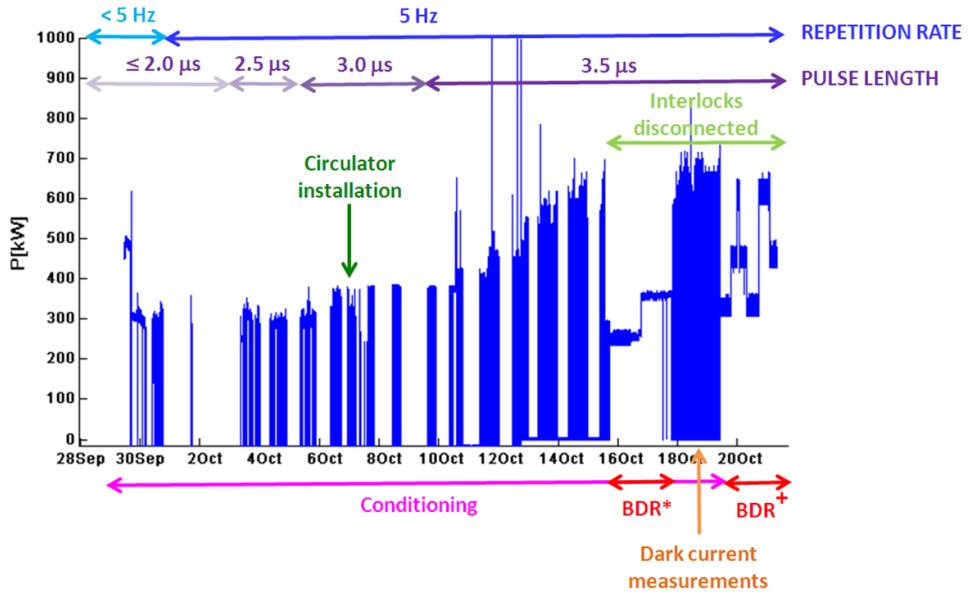

Figure 3.29: *History plot of run of fall 2011 in function of the maximum peak RF power sent into the cavity.*

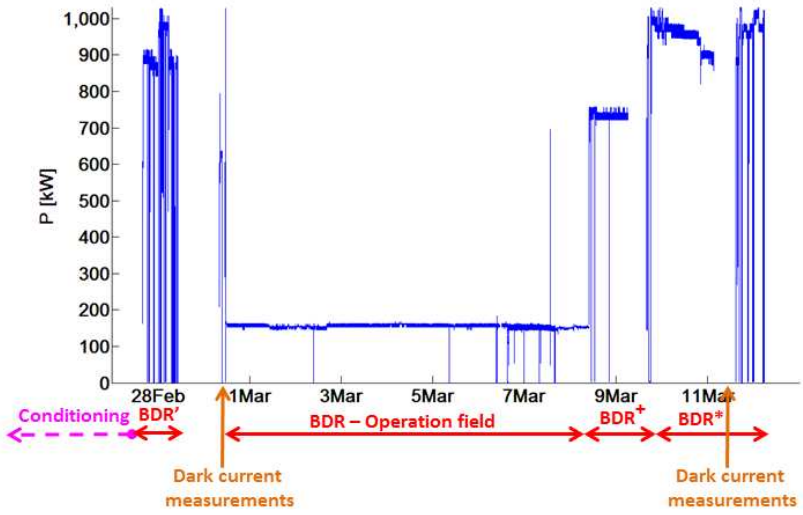

Figure 3.30: *History plot of run of winter 2012.*

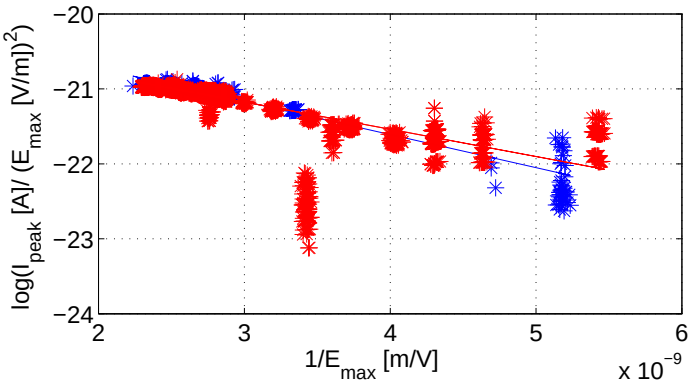

Figure 3.32: *Fowler-Nordheim plot with data taken on February 29th (blue) and March 11th (red).*

3.3.3 Measurements

Signals

Incident RF pulse

A circulator was installed during the run of fall 2011 in the RF circuit to avoid perturbation of the klystrons output power caused by reflected power. Fig. 3.33 shows the typical incident RF pulse before and after installing the circulator in the RF circuit. The interaction signal appeared 0.7 μs later than the start of the reflected RF pulse, which is consistent with the predictions: the total waveguide length was about 76 m and the group velocity was about 0.72c, which leads to a delay of 0.7 μs.

Reflected RF pulse

In standing-wave cavities, for every non-breakdown pulse, a large amount of the incident RF power is reflected back to the RF source during the filling of the cavity. Some RF power is also reflected back during the power draining. Fig.3.26 shows the typical reflected RF power of the 3 GHz test cavity, with two peaks: one corresponding to the filling of the cavity and the other corresponding to the discharge of the cavity.

The filling time τ, which gives the time needed to build up the fields in the cavity (this quantity also gives the time the field takes to decay by a factor 1/e), is:

$$\tau = \frac{Q}{\omega_0} = \frac{2}{\omega_0}\frac{Q_0}{\beta_C + 1} \tag{3.6}$$

The time constant $\tilde{\tau}$, which gives the rate at which the energy is stored in the cavity, is just half the filling time of the cavity: $\tau = 2\tilde{\tau}$. The expected $\tilde{\tau}$ for the test cavity, with $Q_0 = 9140$ and $\beta_C = 0.92$ (see Table 3.8), is 0.25μs, which corresponds to the value measured for the reflected RF power signal, as it can be seen in Fig. 3.26.

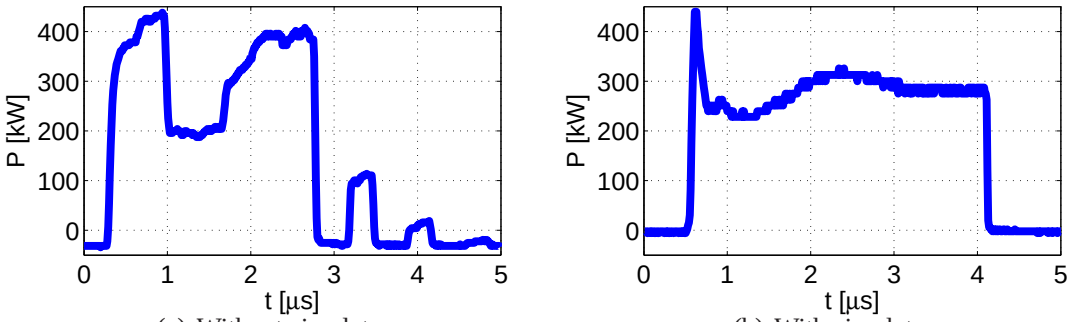

(a) Without circulator. (b) With circulator.

Figure 3.33: *a) Incident RF pulse when RF circuit did not have a circulator. The power reflected by the cavity goes back to the klystron and interferes with the incident RF pulse. b) Typical incident RF pulse after installation of circulator and used for the BDR measurements* .

The RF pulse reflected by the cavity was estimated from the incident RF pulse and the electromagnetic properties of the cavity and is compared with the measured reflected RF pulse in Fig. 3.26. Good agreement between both waveforms is found.

Field-emission current

Since field emission is a strong function of surface field, it provides a direct idea of the field excited in the cavity. Fig. 3.34 compares the field-emission current signal and the dynamic stored energy corresponding to the same incident RF pulse.

Breakdown characterization

Breakdowns are typically detected from the abrupt increase of reflected RF power and/or a sudden field-emission current burst. Breakdowns may also be accompanied by an increase in pressure. The following section describes the characteristic features that allow to distinguish a normal RF pulse from a breakdown event.

RF pulses

Breakdowns can typically be detected from either the reflected power or energy increase. The particular shape of the reflected RF power signal shown by standing-wave structures makes impossible to detect a breakdown by setting a power threshold, because the filling and discharge peaks may lead to false positives. An option would be to examine the shape of the reflected RF power waveform. However, the detection of a breakdown becomes simpler by setting a threshold to the reflected RF energy. A typical ratio between reflected energy and forward energy for no-breakdown pulses is about

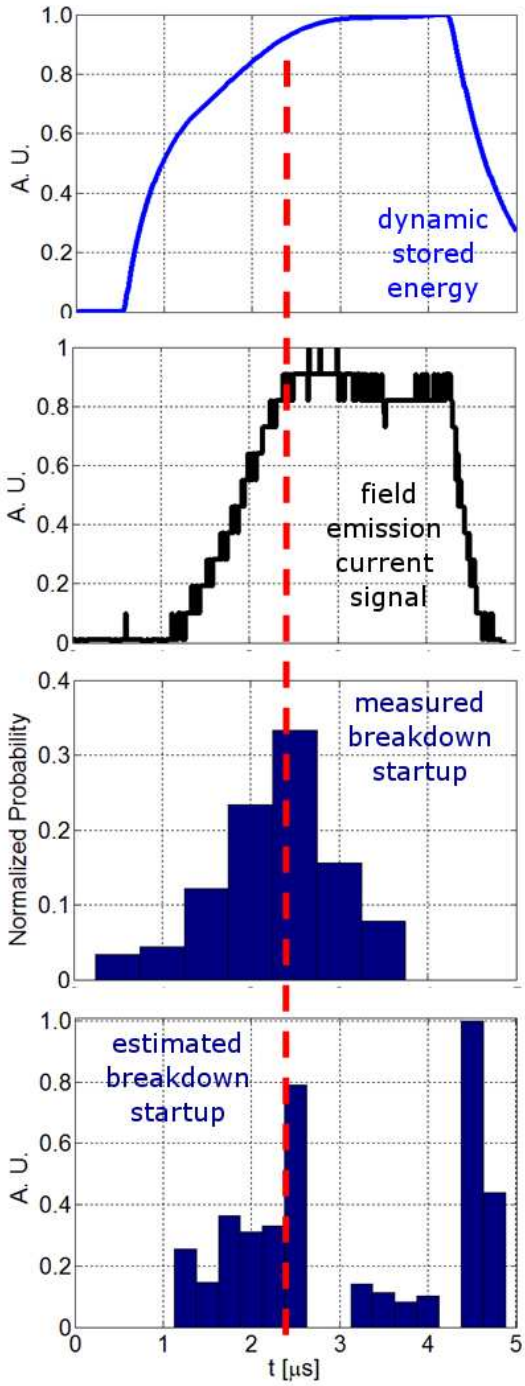

Figure 3.34: *Normalized field-emission current signal and normalized energy stored in the cavity due to typical incident RF pulse during normal operation as the one shown in Fig. 3.26. The probability of breakdown startup, estimated from the dynamic field-enhancement factor $\beta_{FE,dyn}$, agrees with the measured distribution of breakdown startups.*

12-20%. Typical reflected energy during breakdown events resulted in reflected energy increasing of 15-85% over the amount of energy reflected during no-breakdown pulses. Typical reflected energy for breakdows detected from field emission current burst is below 3% over the total amount of reflected energy during no-breakdown pulses (i.e. total reflected energy for this kind of breakdown events is below 20% of the incident energy, within the margins of reflected RF energy during normal operation).

If a breakdown reflects a large amount of energy, the acceleration might be compromised in the RF structure. The quantification of these breakdowns is essential to understand the performance limitations of high-gradient RF structures.

The probability of a breakdown occuring within an RF pulse is not equally distributed within the pulse. If a breakdown takes place, it preferably does when the cavity is almost fully charged. Studies of breakdown processes indicate that the surface fields induce stress in the surface material which in turn enhances the probability of initiating a breakdown at that time. An estimation of this stress would be given by the dynamic field enhancement factor $\beta_{FE,dyn}$, calculated from the electric field excited in the cavity at a certain time within the incident RF pulse and the corresponding field-emission current measured for that time. This quantity was evaluated for several incident RF pulses. Fig. 3.34 shows the estimated distribution of breakdown startups given by the value of $\beta_{FE,dyn}$ normalized value of $\beta_{FE,dyn}$. The dynamic field enhacement factor $\beta_{FE,dyn}$ increases within the building-up of the fields inside the cavity, reaching a maximum value when the cavity is almost completely charged. This is consistent with the experimental observations mentioned above and could be taken as an explanation to the tendency of breakdowns to occur during the building-up of the fields in the standing-wave cavity.

Field-emission current signals

During normal operation, for a maximum electric field around 400 MV/m, the instantaneous field-emission current is not higher than 200 μA. The total electron charge is around 0.8 nC per RF pulse, which corresponds to about 5×10^9 electrons. Fig. 3.35 shows the peak and averge intensities evaluated for different field values. For the same electric field, the typical breakdown current is of 3 mA in a hundred of ns (total electron charge: 30 nC, corresponding to about 200×10^9 electrons).

No pick-up probe was inserted in the cavity to avoid a possible breakdown enhancement, so the electric field reached inside the cavity was estimated from the incident RF power sent into the cavity. A strong field-emission current causes loading of the cavity, which may significantly affect the field value estimated from the incident RF power. Therefore, the RF loading suffered by the cavity in operation was estimated. For a maximum electric field of 400 MV/m in a 0.0189 m cell being operated with 4 μs-long RF pulses at 50 Hz, the field on-axis is about 62 MV/m and the field-emission current exiting from the bore hole is about 40 nA. The geometric correction factor for estimating the total current in the cavity from the measured current exiting from the 2.5 mm-radius bore hole is around 100, assuming that the current is emitted isotropi-

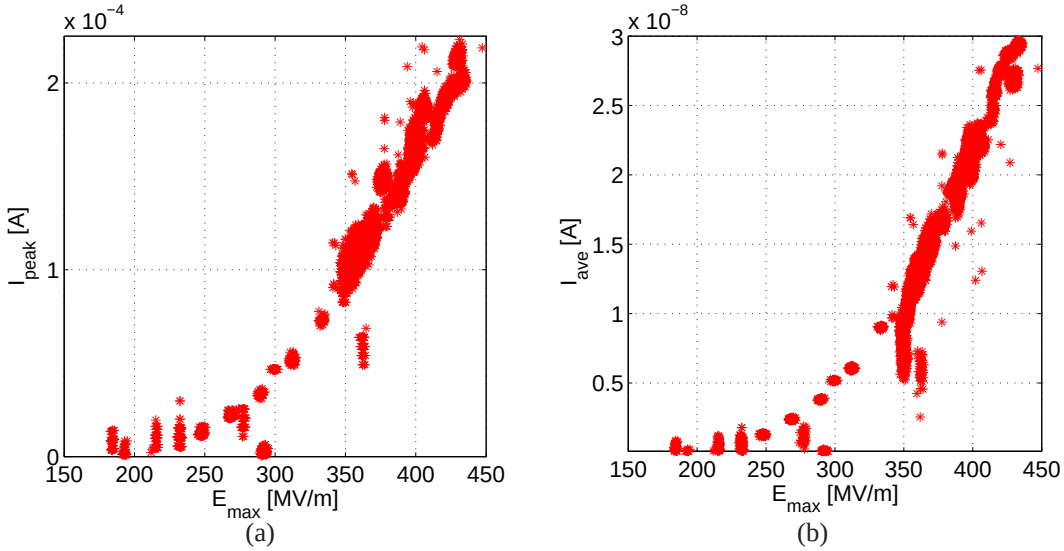

Figure 3.35: *a) Instantaneous field-emission current intensity measured for different field values. b) Average field-emission current intensity measured for different field values.*

cally. The power available to load the cavity will be P_{load} = 100 × 40 nA × 62 MV/m × 0.0189 m ≅ 5 kW, to be compared with the power needed to excite a maximum field of 400 MV/m in the cavity (about 900 kW). An RF loading power of 5 kW leads to a field drop below 1 MV/m, smaller than the field uncertainty.

Vacuum

During normal operation, the typical value of pressure at gauge was about 1.1–1.3×10^{-8} mbar. The pressure increased by one order of magnitude when a breakdown occured, going up to 10^{-6} mbar in rare cases. Vacuum recovered quite fast after a breakdown (typically 4–6 seconds). It was observed that only a small percentage (below 10%) of breakdown events detected by a field-emission current burst or reflected RF power increase are accompanied by a measurable pressure increase.

During conditioning the recovery times were longer. Big pressure increases (from 10^{-8} to 10^{-6} mbar, threshold value at which interlock was set) were mainly observed at the moment when the incoming RF power was increased. This pressure increase was very often accompanied by many breakdown events in the form of field-emission current bursts and/or increases of the reflected RF power.

Evaluation of quantities of interest

Electric field, E

No pick-ups were employed to directly measure the electric field excited in the cavity during operation in order to avoid possible breakdown enhancement from an element inserted in the cavity volume. The indirect method used to estimate the maximum electric field excited in the cavity is explained in the following.

Superfish and *HFSS* simulations provide the amount of power needed to excite a given field in steady state. But some time is needed to reach the steady state and, in addition, real RF pulses are not perfectly square pulses which provide a constant amount of energy to the cavity. The time evolution of the energy stored in the cavity by a given incident RF pulse can be calculated from the electromagnetic characteristics of the cavity, determined by the low-power RF measurements. Fig. 3.36 shows the calculated dynamic stored energy corresponding to a typical incident RF pulse (in solid green) and the dynamic stored energy calculated for a square incident RF pulse (in solid blue). The value of the stored energy in the steady state is equal for both incident RF pulses. This observation was used to simplify the computation of the field excited by each incident RF pulse in the cavity. As a rule of thumb an RF pulse of 128 kW excites a maximum electric field of 150 MV/m in the cavity. The dynamic stored energy profile is also used to determine the effective pulse length used in the scaling law evaluations.

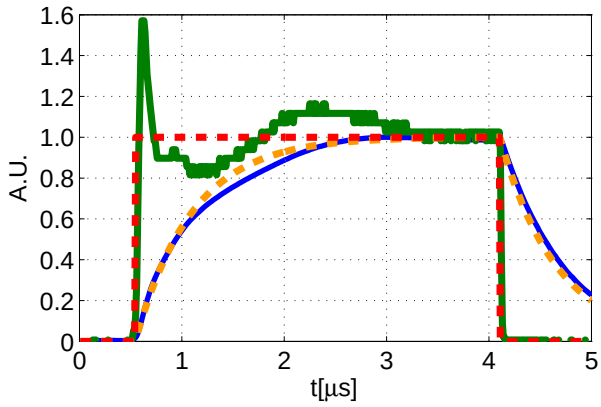

Figure 3.36: *Typical incident RF pulse (solid green) and the corresponding energy stored in the cavity for the given pulse (solid blue). The equivalent constant power RF pulse (dashed red) which leads to the same amount of stored energy at the end of the RF pulse (dashed orange).*

The errors assigned to the electric field correspond to the uncertainty in the calibration of the RF circuit, below 10% in power, which leads to an uncertainty in field determination of 5%. The power fluctuation due to klystron instabilities from pulse to

pulse is negligible compared with the uncertainty in the power calibration. For example, the variation in field due to power level changes from pulse to pulse is about 0.4% for data corresponding to the measurement for 3.5 μs RF pulses of 700 kW.

Flat-top length, $t_{Flat-top}$

The flat-top length was calculated as the width of the dynamic stored energy at an energy height of 90% the maximum stored energy. The pulse length used in the scaling laws corresponds to this flat-top length. An RF pulse of 3.5 μs has a flat-top length of 2 μs.

Breakdown rate, BDR

The breakdown rate, given in breakdowns per pulse per meter, was calculated as the number of breakdowns N_{bd} over the number of RF pulses N_{pulses} and the total length of the cell, L_{cell}=0.0189 m:

$$BDR\,[bpp/m] = \frac{N_{bd}\,[breakdowns]}{N_{pulses}\,[pulses]\,L_{cell}\,[m]} \tag{3.7}$$

Breakdowns were identified from the increase in reflected power within an RF pulse, as abovementioned. The errors assigned to the breakdown rate took into account: a) the statistical error associated of the event count, assuming a Poisson distribution (see Fig. 3.37 showing typical time distribution of breakdowns), and is calculated as the square root of the number of events, and b) the error associated to pile up in the logging system, not bigger than 4%. The increase in power due to some instabilities in the power supply can lead to a breakdown. Some detected events correspond to this situation. However, the error associated to the breakdown rate was assumed to be uncorrelated to the power for simplication.

The repetition rate and the time available to perform the tests limited the number of points measured for this study, as well as the statistics that could be collected for every data point. In the case of the measurement of the run of winter 2012 at the lowest field (E_{max}=170 MV/m), no event was detected for the time assigned to the measurement, and therefore, the corresponding breakdown rate measurement is just a maximum threshold for the respective field level.

3.3.4 Results and Discussion

Breakdown statistics

Time distribution of breakdowns

The distribution of breakdowns in time seems to follow a Poisson law. Fig. 3.37 shows the distribution of time between one breakdown event and the following one

(elapsed time, $t_{elapsed}$) for a certain period of the tests. Low elapsed times between breakdown events correspond to breakdown clusterization; high elapsed times correspond to the breakdown rate associated to the measurement. For high breakdown rates, elapsed times converge to the same value. Breakdowns usually come alone or followed by another breakdown in the next RF pulse. Breakdowns identified from a reflected energy increase are typically followed by another breakdown in the following second.

Long breakdown clusterization could compromise the performances of RF structures. However, according to observations, the machine would be down for less than few seconds due to breakdown for a maximum electric field of 325 MV/m.

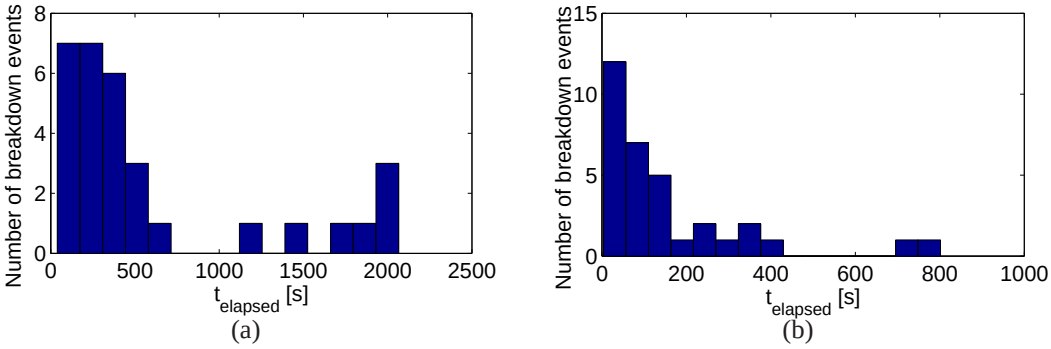

Figure 3.37: *Time distribution of breakdown events for a given power level: a) 405 kW and b) 600 kW.*

Scaling laws

Two different models try to explain the appearance of RF breakdowns during high-gradient structure operation. The breakdown rate measurements performed for the 3 GHz test cavity were fitted to the fit laws proposed by these models. All the fits presented in the following were performed with *Matlab*. Since the fit laws are not linear, the standard errors given for the fit parameter by the fit program might not represent correctly its uncertainty. The evaluation of the fit parameter and its corresponding uncertainty was thereby estimated as follows. Ten thousand sets of data were generated by sampling random values for each data point from its statistical distribution, defined by its mean value and standard deviation. A set of fit parameters was obtained after all sets of data were fitted. The standard deviation of this set of fit parameters was taken as the uncertainty associated to the mean fit parameter.

Power flow model The modified Poynting vector scales as the square of the electric field, so that: $BDR \propto S_C^X \propto E^{2X}$. Fig. 3.40 shows the breakdown rate measurements performed for the 3 GHz test cavity at a fixed pulse length fitted with the power flow model. Data in the low-field range $E_{max} \in [300, 370]$ MV/m fit to the model with a

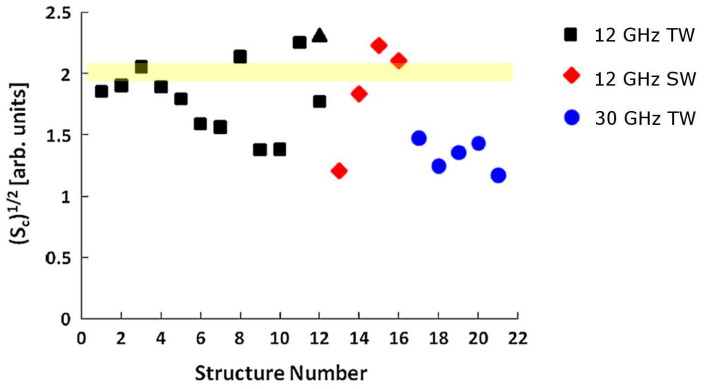

Figure 3.38: *Square root of the scaled modified Poynting vector calculated for the high-gradient performances of several accelerating structures [3]. Breakdown rate measurements for the 3 GHz TERA single-cell cavity are found in the yellow band.*

power of (10±5) on the electric field. Data in the high-field range $E_{max} \in [370, 420]$ MV/m fit to the model with a power of (16±5) on the electric field. Both fits have the same root mean square deviation, $\epsilon_{RMS} = 0.03$. Some experiments have shown a power dependence of breakdown rate on the electric field of about 30 [3]; other experiments have found a smaller value, around 13 [65]. The results of the 3 GHz cavity test seem consistent with results from other experiments and constitute the first experimental data for 3 GHz.

The dependence of the breakdown rate on the pulse length found in literature is: $BDR \propto t_{pulse}^{5}$ [3]. The measurements performed during the 3 GHz cavity tests at fixed electric field and different flat-top pulse length were fitted to the law: $BDR \propto t_{flat-top}^{Y}$ (see how the pulse length was defined in section 3.3.3). The breakdown rate scales with the power of (2.9 ± 0.5) on the flat top pulse length for the data collected in this experiment. The fit presents a square root mean square deviation ϵ_{RMS} of 0.03. Fig. 3.39 shows the breakdown rate measurements performed for the 3 GHz test cavity at a fixed electric field for different pulse lengths.

Stress model Fig. 3.40 shows the breakdown rate measurements performed for the 3 GHz test cavity fitted to the stress model [4] with a root mean square deviation of $\epsilon_{RMS} = 0.008$. The calculated value for ΔV is $(13 \pm 6) \times 10^{-25}$ m^3, which is consistent with the values obtained for data from other experiments.

Measurement for TERA applications

The measurement of the breakdown rate at field levels in the range of the operation field of CABOTO was the main goal of these series of tests. The E_{max}/E_0 for CABOTO is between 4 and 5 and $\sqrt{S_{C,max}}/E_0$ is around 0.024 $\frac{\sqrt{\text{MW/mm}^2}}{\text{MV/m}}$, so for an accelerating

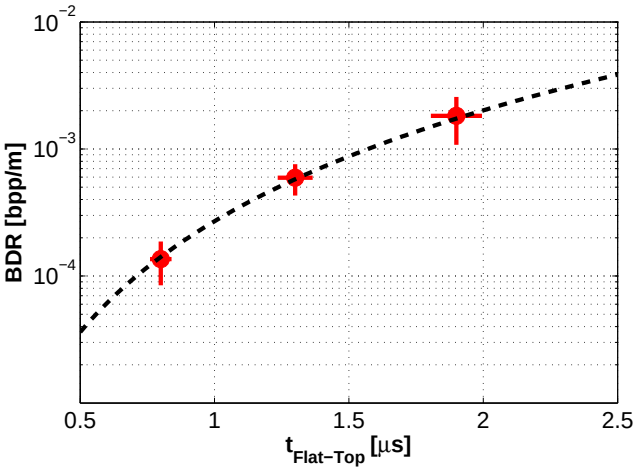

Figure 3.39: *Breakdown rate measurements performed for different flat top pulse lengths.*

gradient of 34 MV/m, the maximum electric field reached in the structure is about 170 MV/m and the maximum modified Poynting vector is about 0.70 MW/mm^2. In consequence, the test device was operated to reach a E_{max} of about 170 MV/m and a corresponding $S_{C,max}$ of 0.87 MW/mm^2 with flat-top RF pulses of 2.2 μs. No event was detected for the time assigned to the measurement, and therefore, the corresponding breakdown rate measurement, 3.6×10^{-6} bpp/m, is just a maximum threshold for the respective field level. This experimental data will be used in chapter 7 to evaluate the expected BDR for CABOTO.

Post-mortem inspection of the structure surface

An offset between the two half-cells was found during the inner surface inspection performed once the cavity had been tested. The rotation axis of both half-cells were still parallel but separated about one millimeter in the vertical direction. The offset introduced a discontinuity or step, as shown in Fig. 3.41, along the braze joint which joined the two half-cells. The expected frequency and quality factor of the cavity could have been changed so, for a better understanding of the measurements, the influence of this offset on the main electromagnetic quantities of the cavity was evaluated.

The quality factor Q was reduced less than 1% with respect to the evaluated for the designed cavity. The resonant frequency was 5 MHz smaller. Therefore, as the design frequency was about 3014 MHz, in reality the cavity with new geometry should have had a frequency of 3009 MHz, with an uncertainty of about ±10 MHz due to the mechanical tolerances. According to low-power measurements performed before tuning the cavity, the prototype resonated at 3013.6 MHz, which is within the limits

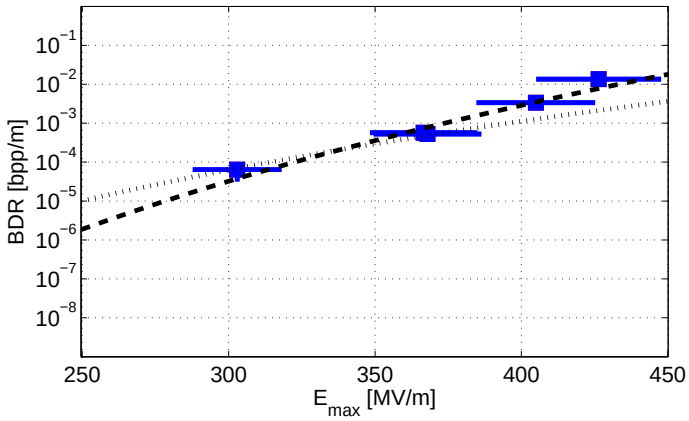

Figure 3.40: *Breakdown rate measurements with error bars performed for the 3 GHz test cavity (blue squares). The power flow model is fitted to low-field data,* $E_{max} \in [300, 370]$ *MV/m (dashed line), and high-field data,* $E_{max} \in [370, 420]$ *MV/m (dotted line).*

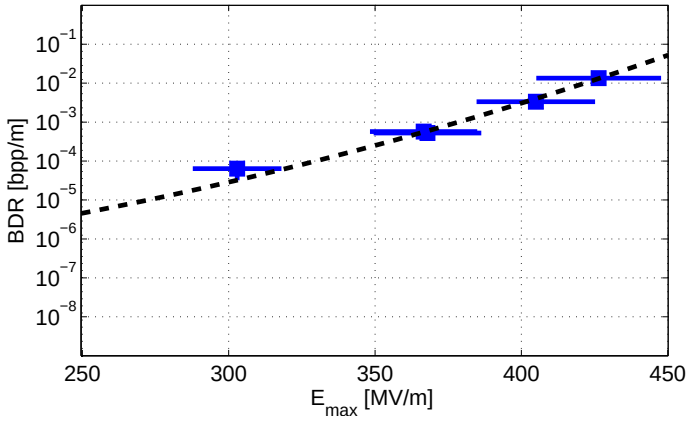

Figure 3.40: *Breakdown rate measurements with error bars performed for the 3 GHz test cavity fitted to the stress model. The blue arrow indicates that the point is a maximum threshold for the given electric field.*

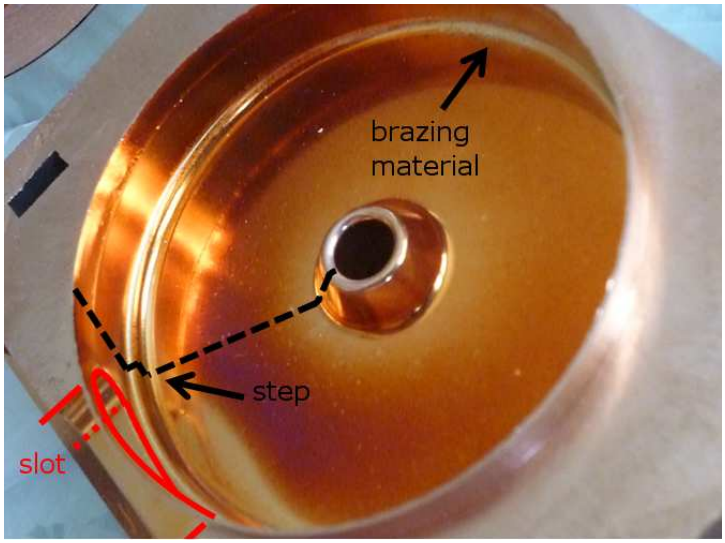

Figure 3.41: *Step during brazing. Some brazing material scapes from groove into the cell. A lot of breakdown activity is located around the brazing line.*

of the expected frequency value, which explains why there was no evidence of the misalignment during the mesurements of the cavity.

The evaluation of the ratio incoming power over maximum electric field P/E_{max} is of special importance for the correct estimation of the E_{max} excited in the cavity during the high-power measurements. Table 3.9 compares the values for the normal cell and the cell with offset. The results previously presented take into account the values obtained for the cell with offset. Fig. 3.8 shows the electric field distribution inside the accelerating cell for the designed and the real cavity. The field pattern is perturbed in the gap region by the offset of one halfcell with respect to the other, which modifies the ratio maximum surface field over accelerating gradient E_{max}/E_0.

A purple coloration can be seen with the naked eye in the region where the electric field is quite small. Fig. 3.43 show the purple coloration in the interior surface of both halfcells and the electric and magnetic fields and the modified Poynting vector distributions in the cavity. The coloration seems correlated to the modified Poynting vector distribution, which is a measurement of power flow. Possible effects on the performances of RF structures intented for long-duration operation should be studied.

A closer inspection of the surface was done with a Secondary Electron Microscope (SEM) [66]. Thousands of craters, caused by RF breakdowns, were found in the surface of the nose region, where the peak surface electric field E_S, the modified Poynting vector S_C and the peak surface magnetic field H_S reach the highest value in the whole structure. No breakdowns were found instead in other regions where the electromagnetic fields are not so high, as the flat part of the cell (between the nose and the outer corner radius), the coupling slot aperture or the cell offset, even if some silver alloy leakage was found in the surroundings of the halfcells brazing joint. Fig. 3.44 shows

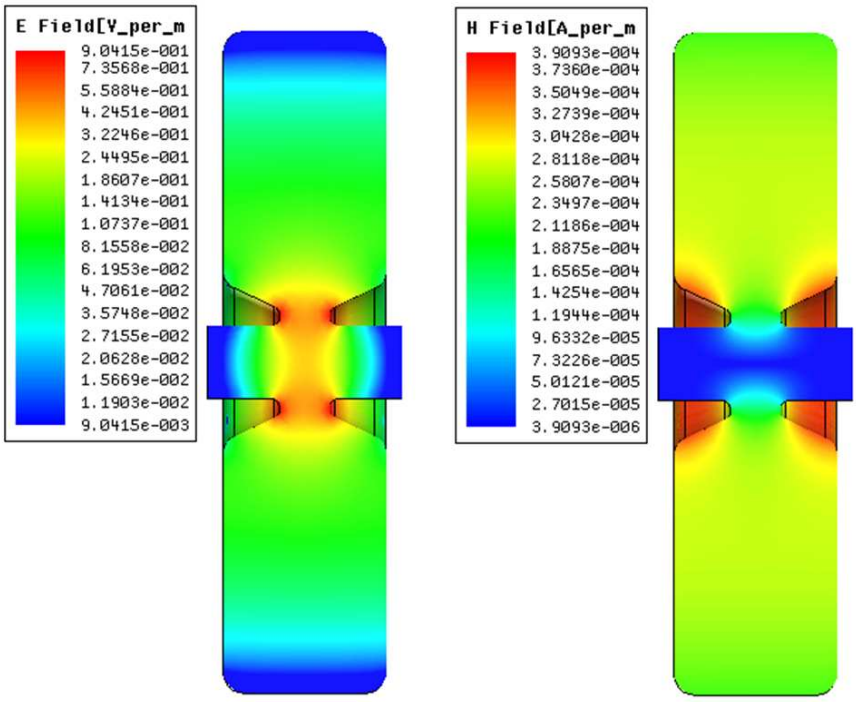

(a) Designed cell.

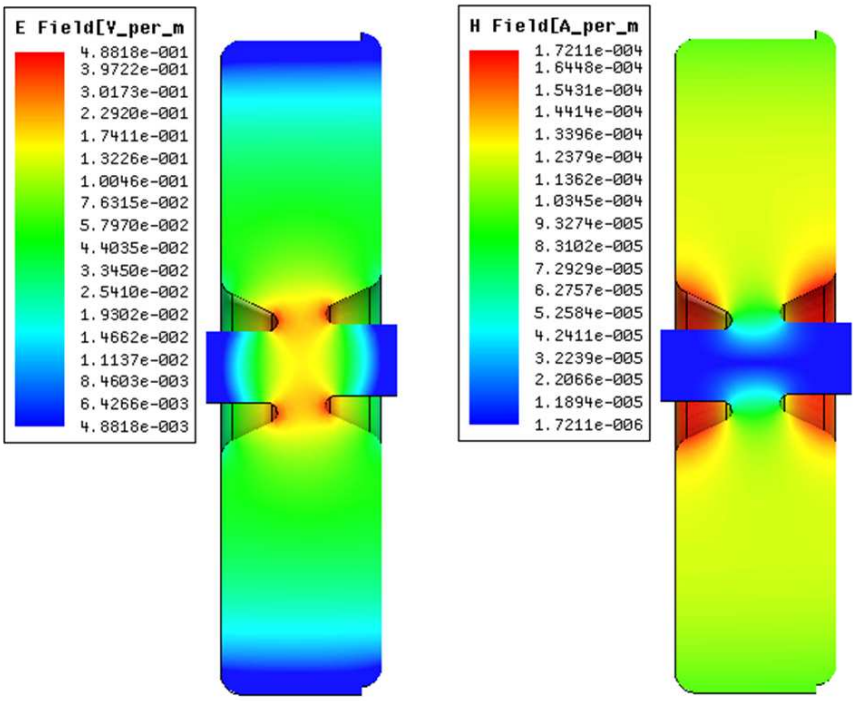

(b) Cell with offset.

Figure 3.42: *Electric and magnetic field distribution in designed cell and real cell (designed cell with step in the braze joint).*

Table 3.9: *Comparison of main electromagnetic quantities for the designed cell and the real cell (designed cell with step in the braze joint). The last column shows the relative difference between the two geometries,* $\Delta_{Cell,System}$.

Quantity		Normal Cell	Cell with Offset	$\Delta_{Cell,System}$[%]
Frequency, f_0	MHz	3018.3	3019.4	0.04
Quality factor, Q_0		8985	8917	0.8
E_0^2/P_{diss}	$\frac{(\mathrm{MV/m})^2}{\mathrm{kW}}$	4.43	4.38	1.1
Transit-time factor, T		0.892	0.893	0.11
Shunt impedance, Z	MΩ/m	83.9	83.3	0.7
Eff. shunt impedance, ZTT	MΩ/m	66.7	66.5	0.3
E_{max}/E_0		6.49	6.35	2
H_{max}/E_0	kA/MV	2.96	2.92	1.4
$\sqrt{S_{C,max}}/E_0$	$\frac{\sqrt{\mathrm{MW/mm^2}}}{\mathrm{MV/m}}$	0.032	0.029	9

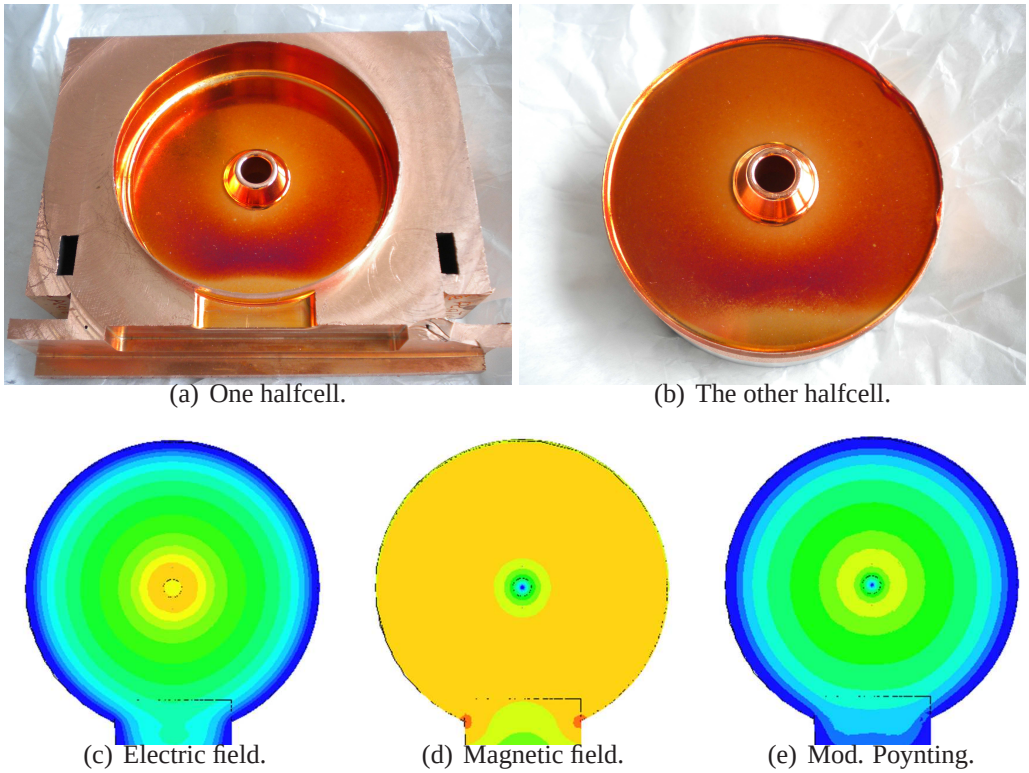

(a) One halfcell. (b) The other halfcell.

(c) Electric field. (d) Magnetic field. (e) Mod. Poynting.

Figure 3.43: *Above purple coloration in both halfcells. Below the electric and magnetic fields and the modified Poynting vector distributions in the cavity. The coloration seems to follow the distribution of the modified Poynting vector.*

a single crater and the accumulation of craters in the same site, forming the so-called crater clusters. Single craters had a typical diameter of about 5 μm.

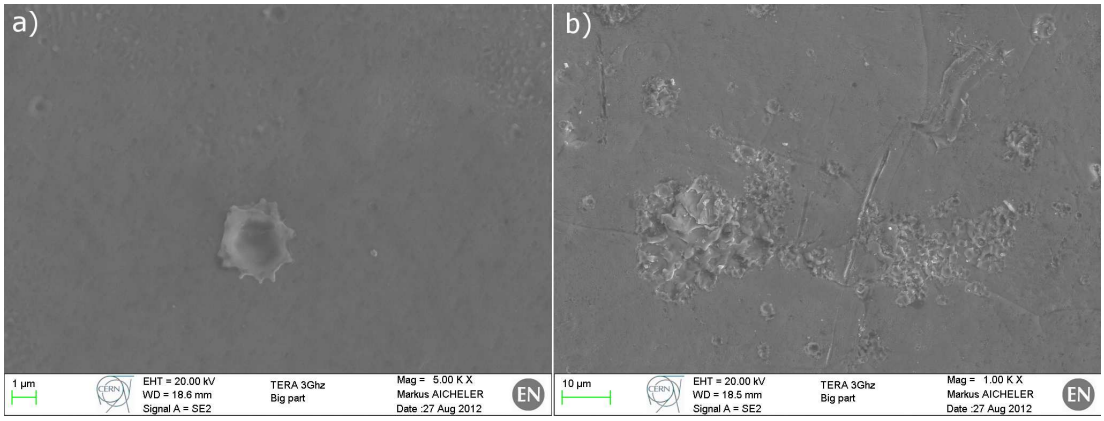

Figure 3.44: *Typical craters created by breakdown activity: a) single crater and b) crater clusterization. Notice the different scale.*

About 25 craters per cell side seemed to be bubbles which burst during cavity operation. The burst bubbles then behaved as RF breakdown sources. Fig. 3.45 shows some examples of these bubble-like craters, with a typical diameter between 20 and 50 μm. The smooth conformance of some bubble interior indicates that bubbles were not formed by RF breakdown. The bubble-like features were only found in the nose region, so most likely bubbles appeared during high-electric field application. A possible evolution of these bubble-like features could be the following: firstly a circular-shaped subsidence would appear in the surface flatness (Fig. 3.46(a)) in presence of very high electric fields (the maximum peak surface electric field reached during high-power operation was about 420 MV/m for 4 μs-long RF pulses), then it would lead to the formation of a projection of molten material or Taylor cone (Fig. 3.46(b)) which would potentially become a breakdown site, so that the tip would finnally blow up, resulting in a bubble-like crater (Fig. 3.46(c)). The formation of projections of molten material in presence of high electric fields was studied in [67].

The cell surface had some scratches. Many RF breakdowns can be found in the scratches surroundings, as seen in Fig. 3.47, indicating that these scratches acted as RF breakdown sources. Other scratches, however, do not present any breakdown in their surroundings, as seen for the scratches in Fig. 3.44. Some copper droplets were also found in the nose region, see Fig. 3.48, possibly coming from burst bubbles. Craters are found around some of these droplets.

3.4 Summary and Discussion

The design, prototyping, tuning, matching and high-power testing of a 3 GHz single-cell cavity were presented in this chapter.

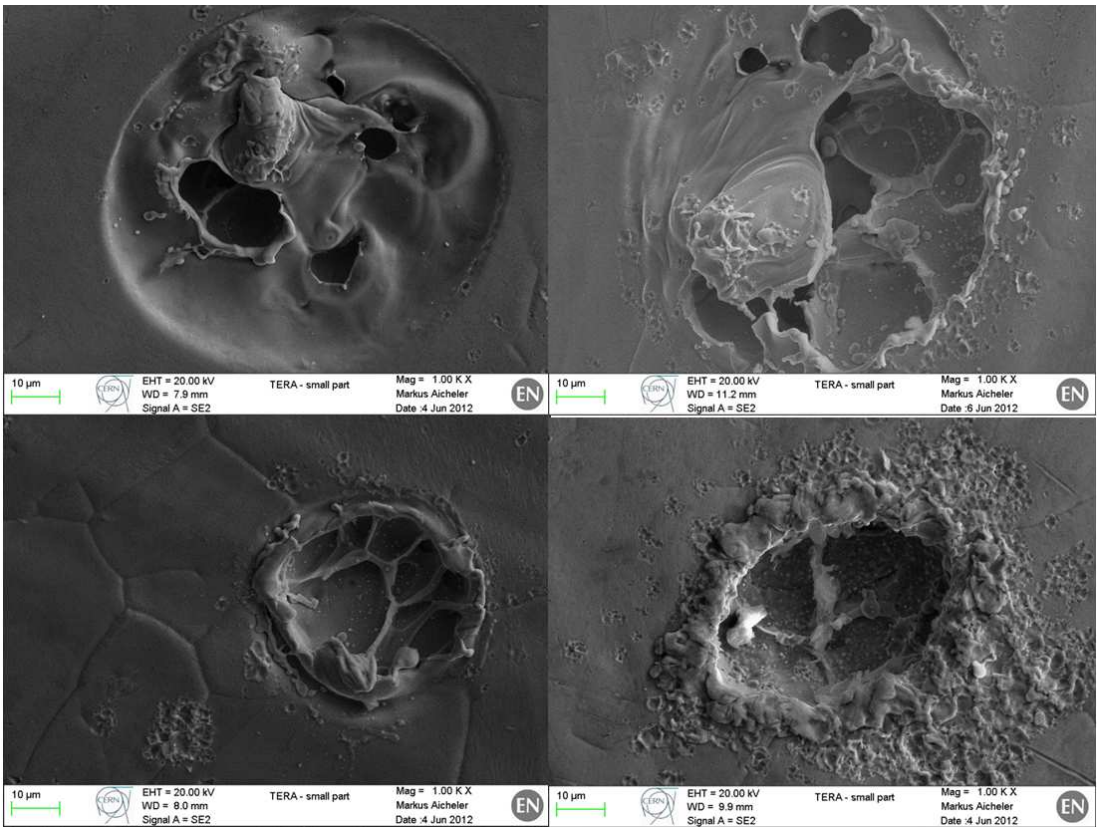

Figure 3.45: *Bubble-like craters.*

The low power measurements showed that the test cavity was well designed and prototyped. During the high-power tests, the cavity was conditioned and then the breakdown rate was measured for different electric field values and pulse lengths. The BDR scaled to the electric field with a power of between 10 and 16 (depending on the field range), in agreement with other experimental data. The BDR scaled to the pulse length with a power of about 3, when the typical value is around 5. The RF breakdowns seemed to follow a Poisson distribution; sometimes two succesive RF pulses presented both a breakdown. According to measurements for high field values, the machine would be less than few seconds down due to RF breakdown clusterization. In addition, a measurement of the BDR was realized at the normal operation field of CABOTO. The consequences of the measurement on CABOTO will be discusses in chapter 7.

The surface inspection of the cell interior showed the damage provoked by RF breakdown in the structure. The scratches and droplets found in the cavity surface during the post-mortem inspection were preferred sites for breakdown activity, as it was already known from other experiments. The structure surfaces which must operate at high gradients should be machined with much more care. The number of imperfections found in the surface of the 3 GHz test cavity suggests that the breakdown rates

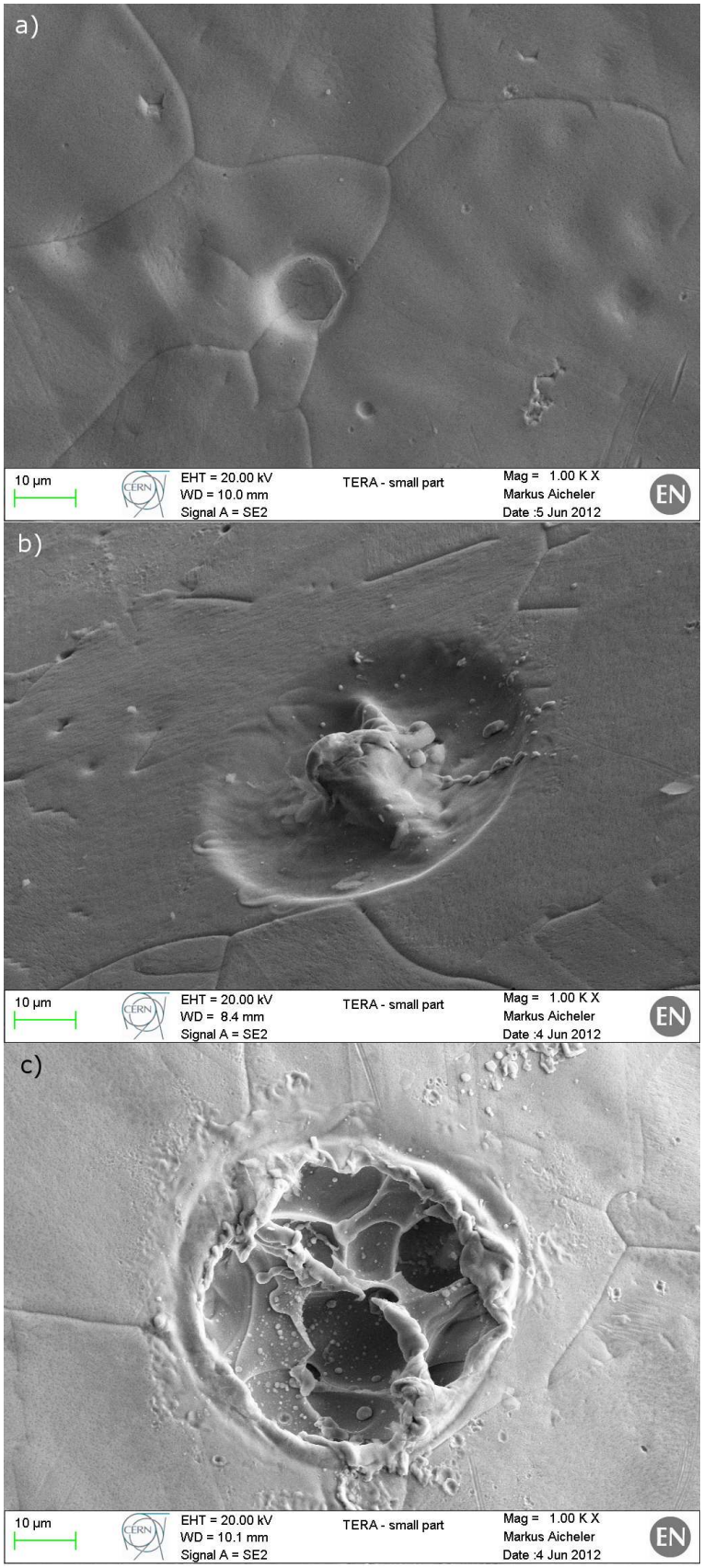

Figure 3.46: *Possible evolution of bubble-like features: a) surface depressions which can be the precursors of the bubble-like craters, b) projection of molten copper and c) burst bubble.*

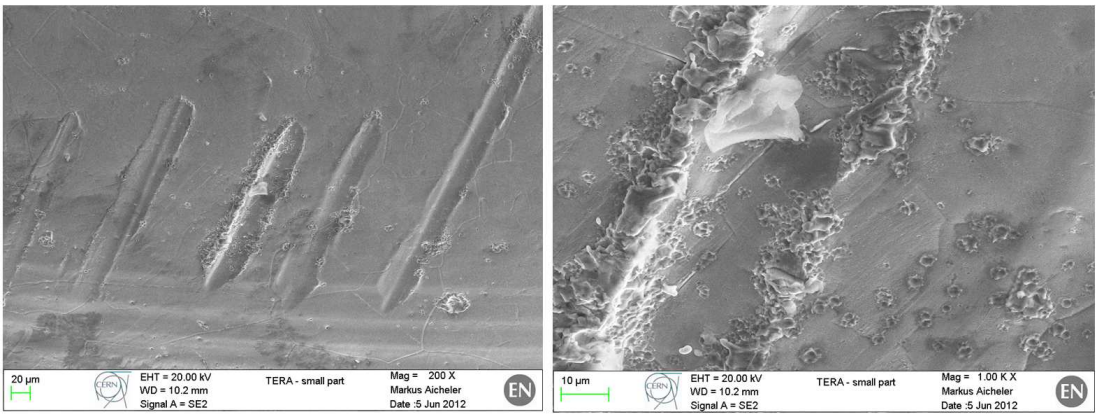

Figure 3.47: *The scratches found in the cell surface were a source of RF breakdowns.*

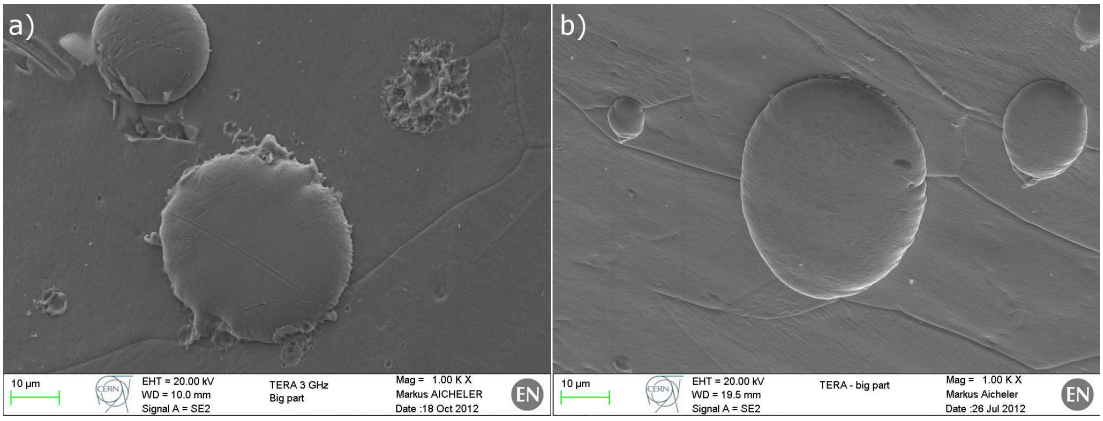

Figure 3.48: *Some copper droplets found in the surface of the nose region: a) with craters and b) without craters.*

measured during the high-power tests are conservative. An improved surface quality would lead to lower breakdown rates.

The cell surface was not inspected before high-power testing for timing reasons. The knowledge on the initial status of the surface would have been useful to determine the origin of some features on the cell surface after high-power testing, as well as its influence on the high-gradient performances of the structure.

The TERA high-gradient test program continues with the design, prototyping and high-power testing of the 5.7 GHz single-cell cavities, which performances should be compared to the ones of the 3 GHz single-cell cavity presented in this chapter.

Chapter 4

5.7 GHz Single-Cell Cavities Design and Test

The TERA High Gradient Test Program foresees the design, production and high-power testing of several 5.7 GHz single-cell cavities. The cavities have a geometry which is similar to that of the 3 GHz single-cell cavity presented in chapter 3 in order to facilitate the comparison of performances for cavities operating at different frequencies. A sketch of a 5.7 GHz single-cell cavity is shown in Fig. 4.

A total of 3 cavities will be produced and tested. Two cavities were machined with conventional tools and another one was machined with diamond tools to compare the influence of the surface roughness on the high-gradient performances of the cavities. Hereafter, the conventional-machined cavities will be called *Ring0s*; the diamond-tooled cavity will be called *Audrey*.

The cavities are still under preparation. This chapter explains the status of the design and production of the cavities at the moment this thesis was written.

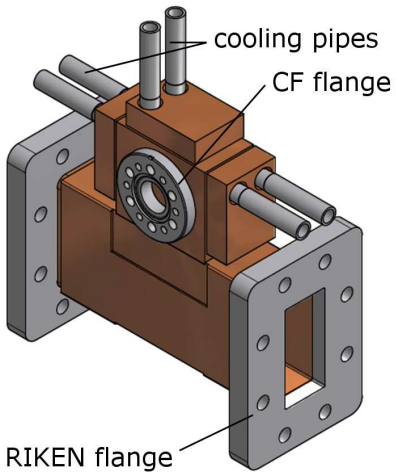

Figure 4.1: *Prototype sketch.*

4.1 Cavities Design

The main layout of the 5.7 GHz test cavities is based on the 3 GHz single-cell cavity (see chapter 3). The cavities are made of copper and consist in a cell operating in the TM_{010} mode magnetically coupled through a slot to a WR187 rectangular waveguide operating in the TE_{01} mode. The cells have noses and their geometry was optimized for a high effective shunt impedance.

4.1.1 Design of Cells

The main geometry parameters of the 5.7 GHz test cavities were fixed by a previous study realized with *Superfisherman* [6] and are summarized in Table 4.1. The bore hole radius was chosen to be 1.5 mm, as the shunt impedance, inversely proportional to the dissipated power in the cell, is higher for smaller bore holes. This bore hole size is too small for CABOTO or TULIP for beam dynamics reasons, but still will give valuable high-gradient results because data are rescaled according to the electromagnetic fields excited in the cavity. The cell diameter was left as a free parameter to adjust the resonant frequency of the cavity once the dimensions of the coupling slot were calculated.

Even though the use of high power sources at 5.7 GHz is expanding [44, 47], the availability of testing time at facilities working in this frequency is still limited. A candidate power source to perform the TERA high-power testing is the 2.5 MW magnetron owned by ADAM which operates at (5712±5) MHz. The 5.7 GHz test cavities can reach a peak surface electric field of about 400 MV/m with about 1 MW, so the power provided by the magnetron is enough to perform the high-power tests.

Table 4.1: *Geometry parameters of 5.7 GHz test cavities [6].*

Length, L	18.8	mm
Outer Corner Radius, R_{OC}	1.5	mm
Inner Corner Radius, R_{IC}	1	mm
Outer Nose Radius, R_{ON}	1	mm
Inner Nose Radius, R_{IN}	1	mm
Cone Angle, θ_{CONE}	25	deg
Flat Top Length, L_{FLAT}	0	mm
Wall Thickness, Web	3	mm
Bore Radius, R_{BORE}	1.5	mm
Gap Length, g	7.5	mm

4.1.2 Design of Waveguide Coupler

The coupling scheme of the 5.7 GHz cavities is the same as the one of the 3 GHz cavity: the single cell is magnetically coupled to a waveguide through a coupling slot

opened on one of the narrow waveguide walls. The waveguide chosen for the 5.7 GHz test cavities was the standard WG187, currently used at 5.7 GHz facilities of KEK (Tsukuba, Japan) and INFN-LNF (Frascati, Italy). The shape of the coupling slot is similar to that of the 3 GHz cavity (see Fig. 3.7). The waveguide coupler was designed following the same procedure used for the design of the coupler of the 3 GHz test cavity, which was explained in chapter 3. *HFSS* simulations were used for this purpose. The mesh specifications given to *HFSS* to simulate the different elements of the cavity are presented in Table 4.2. All the simulations were performed using curvilinear elements. Fig. 4.2 shows the mesh used for simulating the cavity volume.

Table 4.2: *Mesh used for the simulation of the cavity.*

	Cell corona	Coupler	Waveguide	
Max. El. Length, $l_{element,max}$	2.5	2.5	7	mm
Max. Surf. Dev., $\Delta_{surface,max}$	0.005	0.005	none	mm
Volume, V	7100	180	20700	mm^3
No. Tetraedra	36200	1000	4100	

The slot dimensions were chosen such that the coupling factor was about 1.4 for a $\lambda_Z/4$-long short-ended waveguide (the longitudinal waveguide λ_Z of the mode TE_{01} propagating in the standard waveguide WR187 is 62.9 mm). The length and width of the coupling slot were 17.7 mm and 3.7 mm, respectively for both *Audrey* and *Ring0s* designs.

The introduction of the coupling slot causes a frequency shift of the single cell with respect to the complete cavity. Table 4.3 presents the frequencies evaluated for both volumes. The cell diameter of *Audrey* was adjusted such that the brazed cavity under vacuum resonated at 5712 MHz during high-power operation. The corresponding *HFSS* model of the cavity, studied under vacuum assuming no thermal deformations, resonated at 5714 MHz. Thermo-mechanical studies performed with *Ansys* concluded that the maximum detuning would be of -3 MHz for an average power of 500 W (worst case scenario) in the cavity [59]. Thus the cavity resonates at a frequency of 5711 MHz for such high power, still in the frequency bandwidth and very close to the central frequency of the power magnetron. The specified machining tolerance band for *Audrey*'s cell profile was 5 μm. Such tight machining tolerance led to a frequency uncertainty of ±2 MHz, which is within the frequency band of the magnetron. No tuning method is therefore required for the diamond-machined cavity. Fig. 4.5 shows the electric and magnetic field and the modified Poynting vector distributions in *Audrey*'s cell. Instead, the machining tolerance band of the conventional-machined cavities, the *Ring0s*, was 10 μm, which led to a frequency uncertainty of ±12 MHz. The implementation of a tuning system was necessary. The cell diameter of the *Ring0s* was adjusted after determining the characteristics of its tuning device. The following section discusses the different tuning methods considered for the *Ring0s* and the main characteristics of the chosen method.

Table 4.3: *Frequency shift introduced by coupling slot.*

	Single cell	Cell, coupler and waveguide	
Frequency	5757	5715	MHz
Frequency shift		-42	MHz

4.1.3 Frequency Tuning of *Ring0s*

The frequency uncertainty associated with the machining tolerances of conventional-machined cells was about ±12 MHz, which exceeded the frequency band width of the magnetron. Therefore, different tuning methods were considered for adjusting the frequency of the *Ring0s*. As it was explained in chapter 3, tuning rods are not used since they present a risk for the high-gradient performance of the structures. Dimple tuners allow the cavity frequency to be increased in a maximum of 2 MHz per dimple, which is insufficient. And the deformation of the nose region of such small cells becomes tricky for mechanical reasons. Another possibility to tune the cavity frequency consists in adding a concentric ring around the bore hole of each half-cell. The radius, width and heigth of these rings determine the available frequency shift. So if the resonant frequency of the prototype is not equal the frequency goal, the height of the rings can be remachined to adjust the frequency. Fig. 4.3 shows the cell with tuning rings. The tuning rings have the non-neglibible drawback of requiring several manipulations of the cells. However the tuning band provided by the rings for the present test cavities is about 27 MHz, which makes them the best choice to tune the frequency of the conventional-machined test cavities.

The radius, width, heigth and other parameters of the tuning rings were fixed in a previous study performed with *Superfish* [6]. The rings had a total height of 1.20 mm. The maximum shift in frequency achieved by remachining the tuning rings was about 13 MHz.

In order to prepare for the tuning procedure, different tuning ring heights were simulated with *HFSS*. Fig. 4.4 shows the frequency dependence on the tuning ring height. The frequency response of the cavity to the height of the tuning rings changes from capacitive behaviour to inductive behaviour. The stored magnetic energy increases as the height of the tuning rings is reduced, and therefore the inductance increases, leading to a frequency increase. Below certain height of the tuning rings, around 1 mm for the cavities in study, the cavity response becomes capacitive. The shorter the tuning rings are, the higher the capacity becomes, because the electric field concentrates more and more between the cell noses. In consequence, the cavity frequence decreases.

The cell radius was chosen such that the resonant frequency of the cavity was 5715 MHz for a nominal value of the ring height of 0.35 mm. The frequency would shift a maximum of 3 MHz below the design frequency due to thermal deformations of the cavity during high-power operation. The final cavity design had 1.20-mm high rings, and thus a resonant frequency 13 MHz higher than the target frequency, 5728 MHz. The expected frequency of the prototype would then be between 5716 and

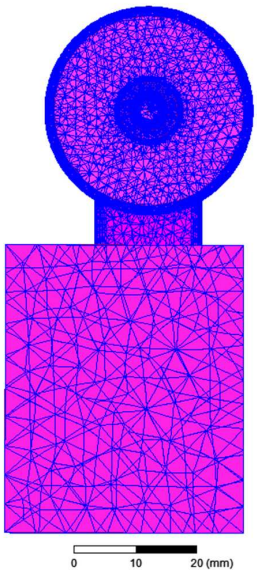

Figure 4.2: *Mesh used for the simulation of the cavity.*

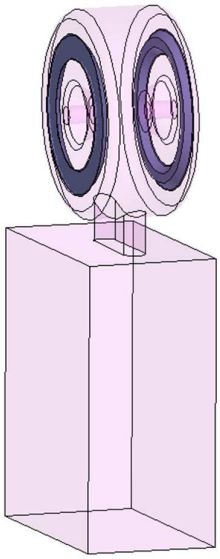

Figure 4.3: *Tuning rings implemented in Ring0s cavities.*

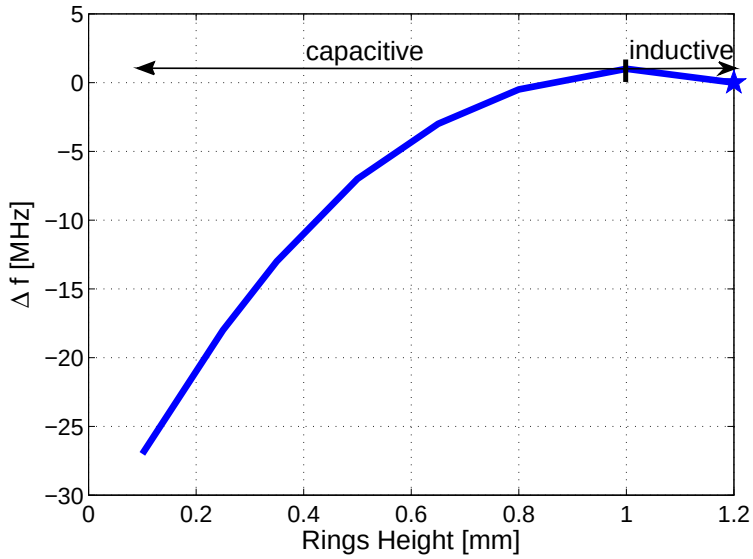

Figure 4.4: *Frequency shift expected from HFSS simulations with respect to the frequency measured for the nominal ring height value, 1.20 mm, by reducing the heigth of both rings of a Ring0 cavity to another value. The frequency response of the cavity to the rings height is inductive for rings higher than 1 mm and capacitive for rings smaller than 1 mm.*

5740 MHz, due to frequency uncertainty associated to mechanical tolerances, and the frequency of the cavity could be brought within the frequency band of the magnetron by remachining the tuning rings.

Table 4.4 summarizes the maximum field values in cell and coupler of *Audrey* and *Ring0s* cavities and Fig. 4.5 compares the field distribution in *Audrey* and *Ring0s* cells.

Table 4.4: *Maximum electromagnetic quantities of interest for high-power performance cavities design evaluated in the cell and in the coupler of the cavities. The location where these quantities are found is shown in Fig. 4.5.*

	Audrey		*Ring0s*		
Quantity	In cell	In coupler	In cell	In coupler	
E_{max}/E_0	4.6	0.8	4.6	1.2	
H_{max}/E_0	2.8	1.9	3.1	2.1	kA/MV
$\sqrt{S_{C,max}}/E_0$	0.025	0.008	0.025	0.008	$\frac{\sqrt{\text{MW/mm}^2}}{\text{MV/m}}$

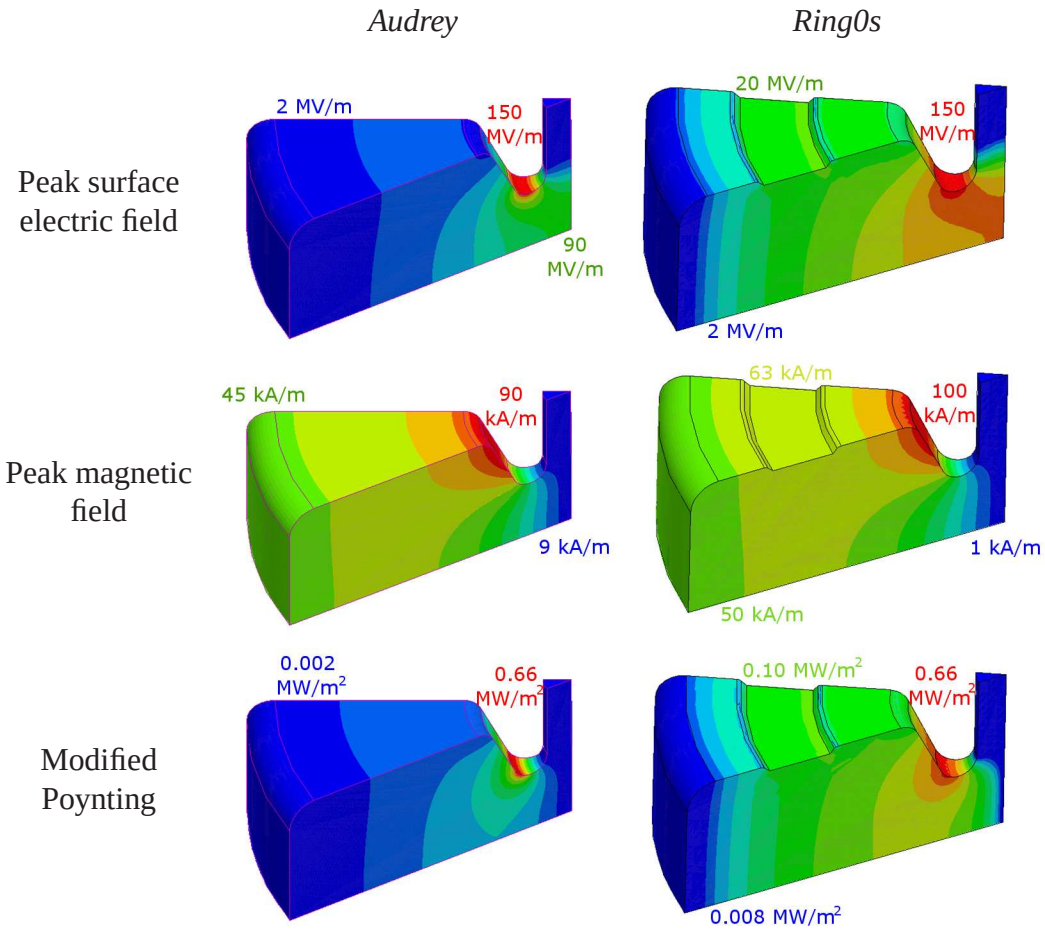

Figure 4.5: *Distribution of the electric and magnetic field and the modified Poynting vector in Audrey and Ring0s.*

4.1.4 Prototype Characteristics

Each prototype consisted in the following parts:

- The cell was divided into two halves. A cooper block contains part of the cell and the coupling slot and then there is a copper cell endcap which closes the block. Both parts are shown in Fig. 4.6.
- A copper waveguide with slot aperture terminated in a stainless steel RIKEN flange at one open for the connection to the RF source.
- A short circuit plate.
- Two stainless steel CF flanges to connect diagnostic instrumentation.
- Three cooling plates with stainless steel cooling pipes of 6-mm diameter. One cooling plate is placed on the top of the cavity, the other two are located at both sides of the cell, as shown in Fig. 4.6. The different cooling circuits are connected in parallel. The cooling pipes were sized to cool down an average power of 500 W with a turbulent water flow of about 3.5 l/min. The thermo-mechanical properties of the cavities were studied in detail in [59].

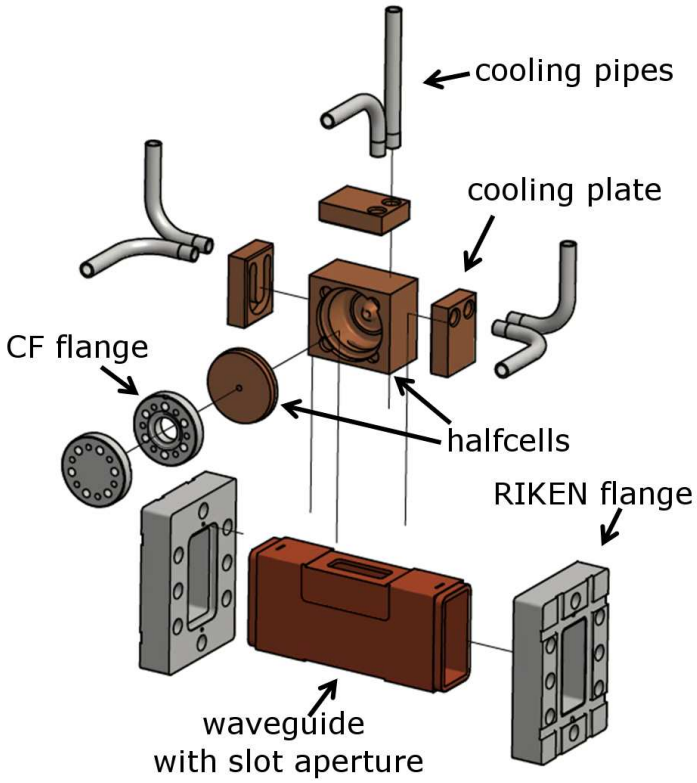

Figure 4.6: *Exploded view of the 5.7 GHz test cavity.*

The 5.7 GHz test cavities were made of the same material of the 3 GHz test cavity, and were cleaned and brazed following the same procedure as for the 3 GHz test cavity described in chapter 3. The cell profile of the *Ring0* cells was machined by turning at VECA (Modena, Italy) within a tolerance band of 10 μm and a arithmetic mean surface roughness specification of 0.4 μm. The tuning rings of the *Ring0s* were remachined several times to approach the target frequency carefully. The rings were remachined by turning in the CERN workshops (Switzerland) with a tolerance specification of ±10 μm, which leads to a frequency accuracy of ±0.5 MHz. The cell profile of the diamond-tooled cavity, *Audrey*, was machined in VDL (Netherlands) within a tolerance band of 5 μm and a surface roughness specification of 0.025 μm.

Surface Inspection of Interior Surface

The interior surface of every cavity cell was inspected before brazing the halfcells together. Initially, two *Ring0s* cells, dubbed Set 1 and Set 2, were produced. As the surface of Set 1 had some scratches, this set was rejected for high-power testing, so another set of halfcells, dubbed as Set 3, was produced to replace Set 1. Still the halfcells of Set 1 were used to validate the tuning procedure and evaluate the frequency shift caused by brazing before tuning Set 2 and Set 3. The tuning rings of the *Ring0s* were remachined several times in the process of tuning. Some pits appeared in the surface of Set 2 after the remachining of one tuning ring, being smoothed manually with a plastic tool. Fig. 4.7 shows a magnification of the smoothed pits.

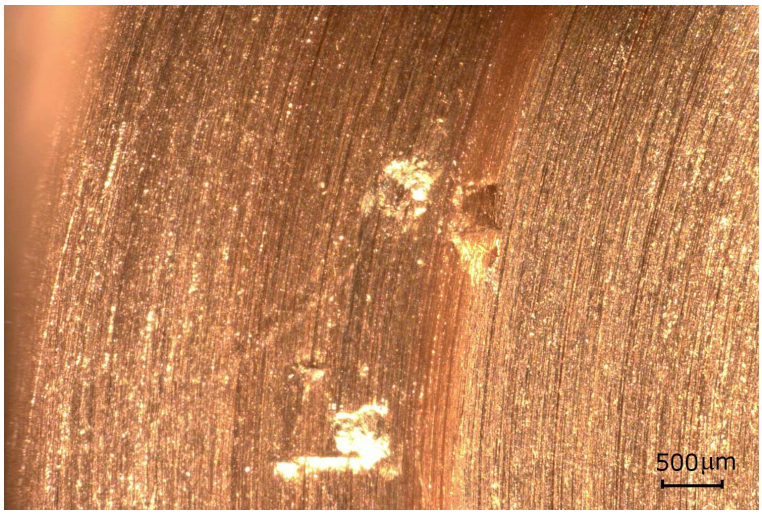

Figure 4.7: *Surface of Set 2 after smoothing the pits.*

The surface of the diamond-tooled halfcells barely presented any defect. Fig. 4.8 shows the surface of conventional machining and diamond-tool machined cavities. The diamond-tooling surface is much smoother, and thereby it is more likely to achieve great high-gradient performances with it.

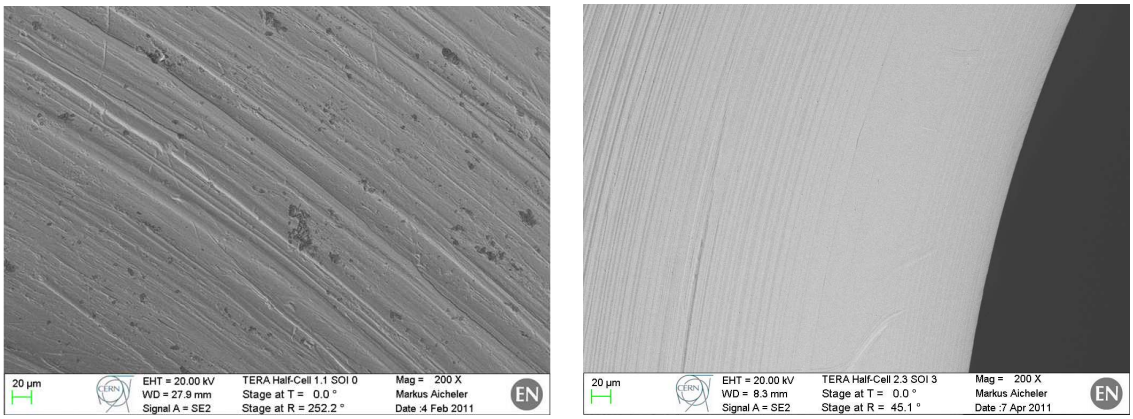

Figure 4.8: *Surface of a normal-machined halfcell (left) and a diamond-tooled one (right) with the same magnification. The diamond-tooling machining provides a better finish of the cell surface.*

4.2 Low Power Measurements, Tuning and Matching

This section presents the frequency and coupling tuning of the 5.7 GHz test cavities. The preparation of the cavities for high-power testing will be completed by October 2012 and the cavities will be high-power tested in 2013.

Experimental Setup

The low power measurements setup was similar to that for the 3 GHz single-cell cavity, described in chapter 3. During the tuning process the cavity pieces were not brazed together and several clamps had to be used to ensure a good RF contact between the pieces, as shown in Fig. 4.9.

Validation of *HFSS* calculations of frequency dependence on tuning ring height

The tuning curve which gives the frequency dependency on the tuning ring height according to *HFSS* simulations (see Fig. 4.4) was validated by measurements of the resonant frequency of Set 1 for different tuning ring heights. Table 4.5 presents the resonant frequency of Set 1 for different steps of the tuning process. The frequency difference between the value estimated from RF simulations, $f_0^{HFSS} = 5728$ MHz, and the one measured for the cavity prototype, $f_0 = 5719$ MHz, is within the expected frequency uncertainty due to mechanical tolerances of the cell profile, which is about ±12 MHz. The *HFSS* simulations predicted with an acceptable accuracy of some hundreds of kHz the resonant frequency of the cell for different tuning ring heights.

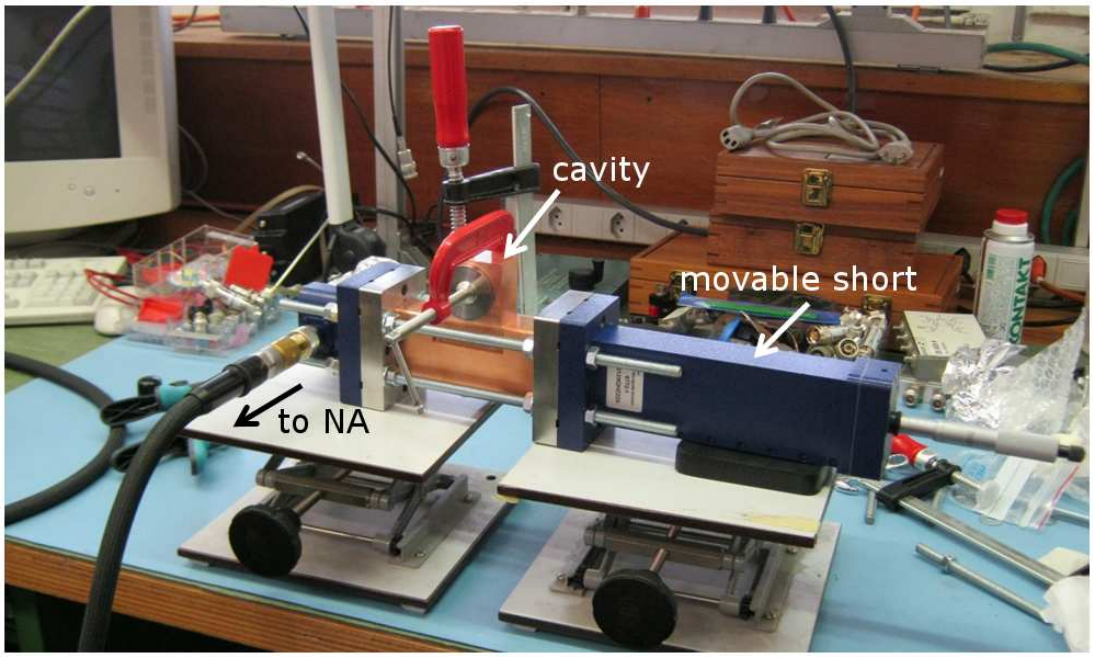

Figure 4.9: *Experimental setup for low power measurements of the 5.7 GHz test cavities performed with a Network Analyser (NA).*

Evaluation of frequency shift from brazing

A frequency shift often occurs after brazing because of cell deformations. A measurement of this frequency shift was performed in advance for Set 1 to define the tuning strategy of Sets 2 and 3. The half-cells of Set 1 were brazed together. The measured resonant frequency was 5714.2 MHz. Then the cell was brazed to the waveguide, being the measured resonant frequency for this new setup of 5714.8 MHz. In total, the resonant frequency increased by 2 MHz during the brazing process. This number was taken into consideration in the tuning strategy of the other cell sets.

Tuning strategy for *Ring0s* (Set 2 and Set 3)

The frequency of a 5.7 GHz structure under vacuum is about 2 MHz higher than the frequency of the same structure in air and the frequency of the designed test cavities decreases by 3 MHz during operation. In addition, brazed cavities will have a resonant frequency 2 MHz higher than non-brazed cavities. Therefore, the tuning rings should be remachined after the low power measurements to have the appropriate dimensions to bring the frequency of the non-brazed cavities measured in air during the low power measurements to 5712 MHz. In this way the frequency of the brazed cavities under vacuum during high-power operation would be equal to the center frequency of the power source. The choice of the tuning ring height is done according

Table 4.5: *Resonant frequency of Set 1 for different steps of the tuning process. The difference between expected and measured frequencies for the initial machining step stays within the frequency uncertainty given by the machining tolerances. The accuracy to predict the resonant frequency of a cavity with remachined rings, remachine the tuning rings as requested and succesfully bring the cavity frequency to the desired resonant frequency are proven in the following machining steps.*

Machining Step		Initial	First	Second	Third	
Ring side-A Height	(requested)	1.20	1.20	1.20	0.54	mm
	(measured)	1.20	1.20	1.20		mm
Ring side-B Height	(requested)	1.20	0.75	0.54	0.54	mm
	(measured)	1.20	0.74	0.54	0.54	mm
Frequency	(expected)	5728	5718	5716	5713	MHz
	(measured)	5719	5718	5716	5713	MHz

to the frequency-ring heigth dependence curve shown in Fig. 4.4, which was validated during the frequency tuning of Set 1.

The initial frequency in air of Set 2 was 5718.8 MHz. The height of one tuning ring was reduced from 1.20 to 0.48 mm. The new frequency was 5716.3 MHz, so the height of the other tuning ring was reduced from 1.20 to 0.45 mm in order to achieve a resonant frequency of about 5712 MHz. The resonant frequency measured during the low power measurements of the cavity in air after brazing half-cells and waveguide together was 5712.9 MHz.

The Set 3 initially resonated at 5721.1 MHz in air, thus the height of one tuning ring was reduced from 1.20 to 0.43 mm. The new frequency was 5716.9 MHz. The height of the other tuning ring was reduced from 1.20 to 0.45 mm to bring the resonant frequency to the goal frequency of 5712 GHz. The resonant frequency measured in air during low power measurements of Set 3 after brazing together half-cells and waveguide was 5713.5 MHz.

Therefore, both Set 2 and Set 3 are expected to resonate at 5711.9 and 5712.5 MHz respectively, under vacuum during high-powerr operation.

The use of tuning rings to tune the cells turned out to be not so simple as the tuning method used for the 3 GHz single-cell cavity tuning. Many steps are required to tune the cavities with this technique, and the probability of damaging the cell surface increases with the number of times that the cell undergoes a machining. This tuning method is not advisable for industrial production of accelerator cells for two main reasons: a) difficult setup (many dismountable pieces that must be conveniently mounted and adjusted and specially high sensitivity (about MHz) to pressure exerted on halfcells to have good RF contact between them); b) multiple steps until the cavity is finally tuned, which delays the tuning process.

Frequency check of *Audrey*

The resonant frequency of the brazed cavity in air was 5708.8 MHz. The frequency will increase by 2 MHz when the cavity was under vacuum, thus the resonant frequency would be about 5710.8 MHz. During operation the frequency is expected to decrease about 3 MHz due to heating, so the frequency of the cavity will still be within the frequency band of the power source.

The cavities were matched by adjusting the position of the short-circuit plate after brazing the halfcell assembly and waveguide together. The dependence of the coupling factor on the position of the short plate for one of the *Ring0s* is shown in Fig. 4.10. The β_C is proportional to $\cos^2(2\pi\frac{d_{short}}{\lambda_Z})$. The distance from the slot center to the short plate was set to 29.35, 29.38 and 29.81 mm, respectively, for *Ring0*-2, *Ring0*-3 and *Audrey*.

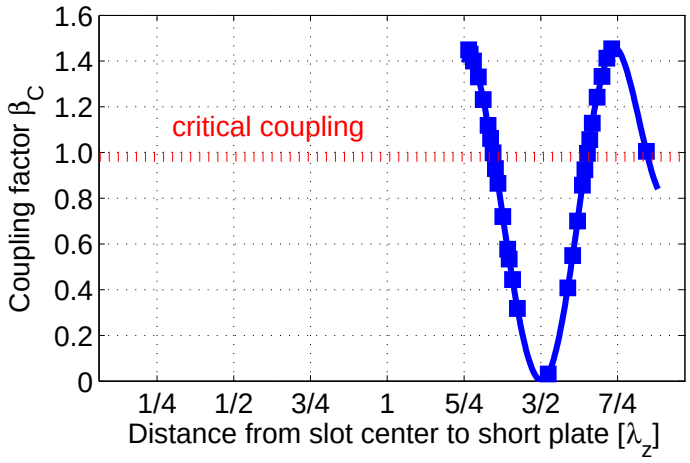

Figure 4.10: *Dependence of the coupling factor β_C on the short position for Set 3 (the other cavities also show the same behaviour). The horizontal axes gives the distance from the slot center to the short plate d in λ_Z units (λ_Z = 0.0629 mm) and the vertical axes gives the coupling factor β_C. In blue, experimental data measured during low power measurements. The coupling factor β_C is proportional to* $\cos^2(2\pi\frac{d}{\lambda_Z})$.

4.3 Summary and Outlook

This chapter dealt with the design and prototyping of the 5.7 GHz single-cell cavities. Table 4.6 summarizes the main characteristics of the 5.7 GHz single-cell cavities. The coupling factor of the cavities will be known after remachining the machining of the short-ended waveguide. In principle, the length of the short was chosen during the low power measurements so that β_C was around 1 (critical coupling).

Once the short-ended waveguide is machined for each cavity, the cavities will be ready for high-power testing. Most likely the cavities will be high-power tested in

2013 with a 2.5 MW magnetron lend by ADAM S.A., using similar diagnostic instrumentation and software to that of the 3 GHz cavity test.

Table 4.6: *Main characteristics of the 5.7 GHz test cavities.*

Cavity geometry	*Audrey*	*Ring0*-2	*Ring0*-3	
Cell Radius, R_{cell}	17.19	17.27	17.27	mm
Gap Length, g	18.8	18.8	18.8	mm
Slot Width, w_{slot}	3.7	3.7	3.7	mm
Slot Length, l_{slot}	17.7	17.7	17.7	mm
Electromagnetic quantities				
Frequency in air, f_0	5708.8	5712.9	5713.5	MHz
Quality factor, Q_0	8800	8500	8500	
Coupling factor, β_C	to be measured after short plate machining			
E_{max}/E_0	4.6	4.6	4.6	
H_{max}/E_0	2.8	3.1	3.1	kA/MV
$\sqrt{S_{C,max}}/E_0$	0.025	0.025	0.025	$\frac{\sqrt{\text{MW/mm}^2}}{\text{MV/m}}$
For operation at E_{max}=150 MV/m				
Required Power, P	192	200	200	kW
Pulsed Surface Heating, ΔT (t_{pulse} = 3 μs)	4	5	5	degrees
Mechanical				
Material	OFE10100 copper			
Tolerance band	5	10	10	μm
Surface Roughness (Ra)	0.025	0.4	0.4	μm

Chapter 5

High Gradient Test of the Frascati 5.7 GHz Structure

A prototype of a 5.7 GHz traveling-wave structure was designed, fabricated by a group from the SPARC project at Frascati and finally high-power tested at KEK in 2010. This chapter presents the main design and fabrication features of the prototype, describes the setup of the high-power test area and discusses the main results. An extensive explanation of the test is found in [9].

5.1 Motivation and Objectives

The SPARC project is an existing 150 MeV test-facility in INFN-LNF aimed at producing high brightness electron beams able to drive Self-Amplified Spontaneous Emission Free-Electron Laser (SASE-FEL) experiments. The experiments are in visible light and explore the most critical issues of the future X-ray source subsystems.

The high-gradient cavity is part of an upgrade project in which the output energy of the SPARC beam could be increased from 170 MeV to approximately 250 MeV by replacing one of the existing 3 m-long 2.856 GHz modules operating at about 15 MV/m accelerating gradient by two 1.4 m-long 5.712 GHz modules operating at about 35 MV/m, as shown in Fig. 5.1. The energy upgrade will shift the SASE radiation closer to the ultraviolet (UV) region and improve the seeding experiment. In addition, the installation of the new sections will allow the study of the combined operation of two systems of different frequency, 2.856 GHz and 5.712 GHz, in the same accelerator. The new structures will be fed by a Toshiba ET37202 50 MW 5.712 GHz klystron. The HV pulsed modulator and the 400 W solid-state driver for the klystron were manufactured by ScandiNova (Sweden) and Mitec Telecom (Canada), respectively, and have already been installed and power tested at LNF. The new system will also include a pulse compressor (a SLED called SKIP).

The SPARC upgrade relies on the assumption that an average acceleration field of more than 35 MV/m can be obtained in 5.7 GHz structures. A prototype consisting of

22 cells and having a total length of 54 cm was designed, fabricated and high-power tested to validate such assumption.

The high-power test of the prototype is of direct interest for the subject dealt in this thesis. The measured high-gradient performance of the structure is a reference of the highest achievable operation level of 5.7 GHz structures for medical applications. The test was also an opportunity to enlarge the data base of high-gradient structure performances, with the added value that no 5.7 GHz structure was yet included in the data base. Last but not least, the data collected could be used for a further understanding of the breakdown phenomena and the physics behind it, particularly by trying to fit the data to the proposed models which aim to explain the limit in high-gradient performances of these structures.

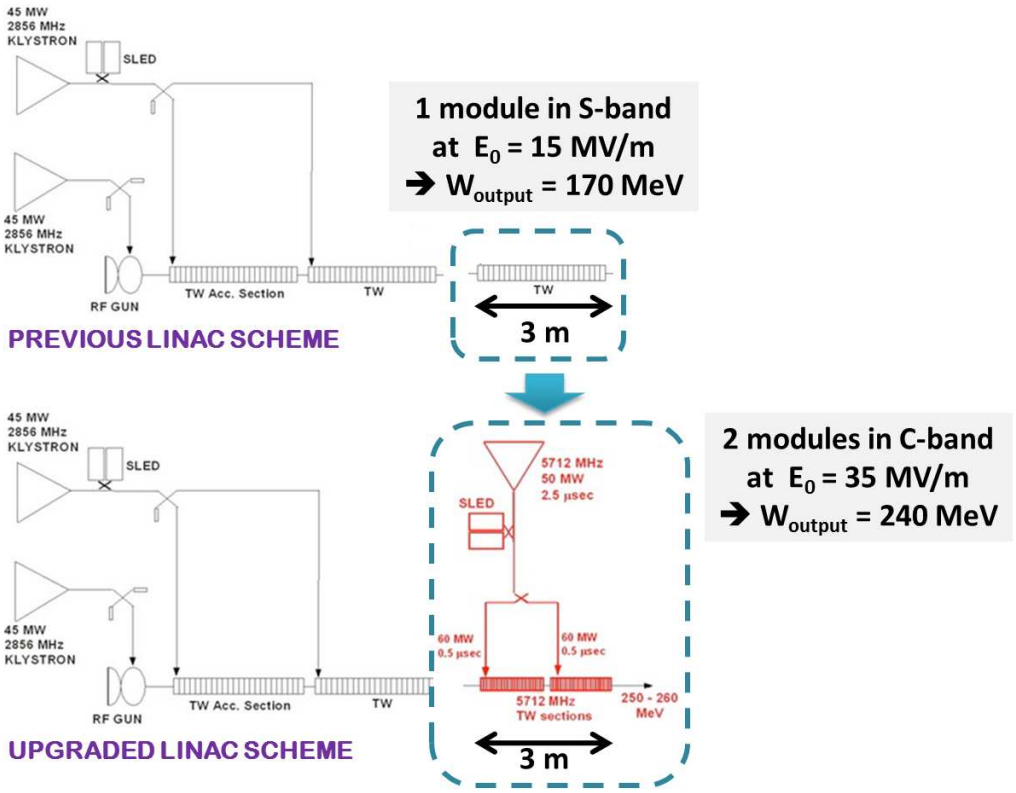

Figure 5.1: *Energy upgrade of SPARC by substituting one 3 GHz module operating at 15 MV/m accelerating gradient by two 5.7 GHz modules operating at 35 MV/m accelerating gradient, with the consequent output energy gain of 70 MeV.*

5.2 Structure Design and Fabrication

The prototype was a room-temperature constant-impedance travelling-wave accelerating structure. A sketch of the prototype is shown in Fig. 5.2. The power fed the accelerating structure through a waveguide coupler with splitter, shown in Fig. 5.3. The transmitted power came out from the accelerating structure through two symmetric waveguide ports connected to one RF load each. The structure length (including couplers) was 0.54 m. It incorporated a water cooling system. The design and production of the prototype were the responsibility of the RF group of the LNF [10].

The choices which drove the prototype design and fabrication procedure are explained in [9].

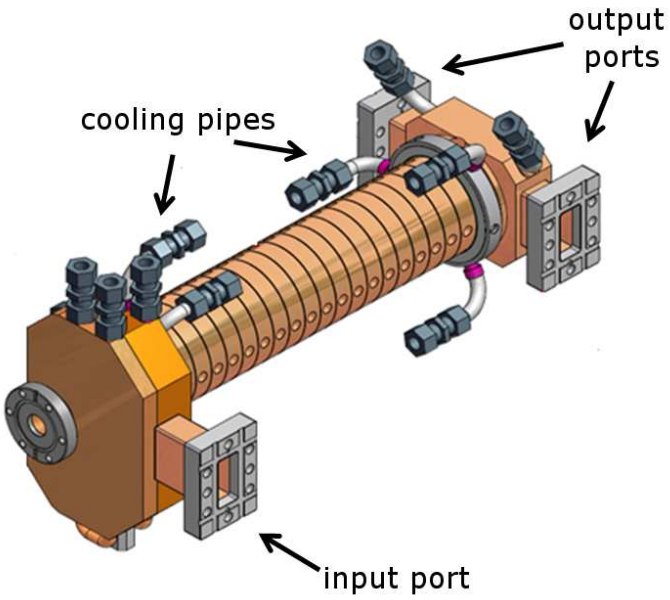

Figure 5.2: *Mechanical drawing of the prototype.*

5.2.1 Electromagnetic Characteristics

The prototype was a normal-conducting (copper) traveling-wave structure consisting of 22 accelerating cells with a phase advance per cell of $2\pi/3$, mode typically used for high energy electron acceleration. All the cells had the same radius (constant-impedance structure) to 1) simplify the fabrication process and 2) compensate the exponential shape of the SLED pulse with the field attenuation α along the structure, α=0.206 per meter, in order to obtain a rather constant accelerating gradient through the structure. Therefore, the group velocity v_{group} of the structure was constant through the whole structure, v_{group}=0.0283c, which led to a filling time t_{fill} of 50 ns. The cell geometry was optimized to reduce the peak surface electric field on the iris and

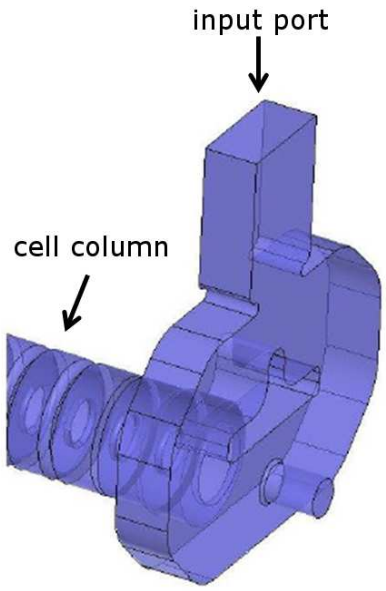

Figure 5.3: *Detail of the input coupler.*

reach an accelerating gradient of, at least, 35 MV/m with the power available with the klystron. The maximum surface electric field over the accelerating gradient E_{max}/E_0 was 2.4. The square root of the maximum modified Poynting vector over the accelerating gradient $\sqrt{S_{C,max}}/E_0$ was 0.024 $\frac{\sqrt{\mathrm{MW/mm^2}}}{\mathrm{MV/m}}$. Fig. 5.4 shows the electric and magnetic field and the modified Poynting vector distributions for the prototype.

5.2.2 Prototype Characteristics

This section describes the main fabrication and assembly characteristics of the prototype. Fig. 5.5 shows the different parts of the prototype.

The cells and coupler were made of OFHC (Oxygen-Free High Conductivity) copper. The accelerating cells were machined by turning with a precision of ±2μm and a surface roughness below 50 nm. The input coupler was machined by milling with a precision of ±10μm and a surface roughness below 200 nm. Output coupler tolerances did not need to be so tight as for the input coupler because power damps into the structure and consequently less power flows through the output coupler. Therefore surface roughness was asked to be below 600 nm and machining was performed with a precision of ±20μm. All the prototype pieces were machined by Comeb (Italy) [68].

The pieces were cleaned with an alcalin detergent (ALMECO-19) and a mixture of organic (citric) acid and distilled water, in an ultra-sound bath.

All pieces were vacuum brazed at LNF (Italy) in different steps. The couplers and flanges were brazed together in two steps, at 900°C with Palcusil 15 and at 860°C with

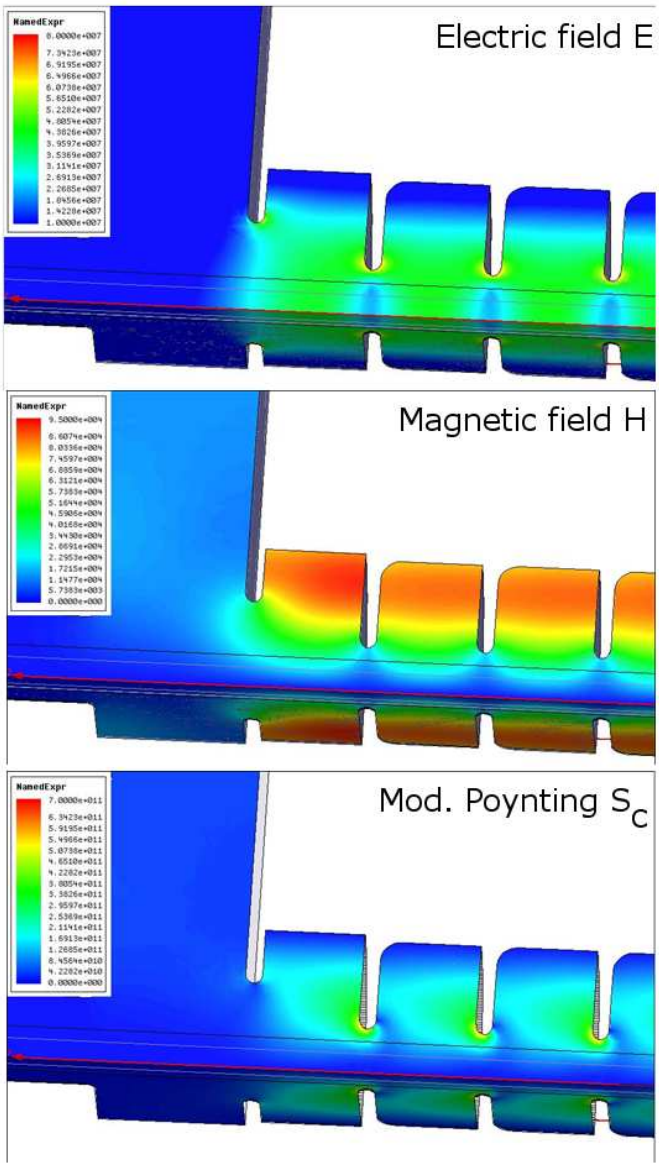

Figure 5.4: *Distribution of the electric and magnetic field and the modified Poynting vector in the prototype.*

Figure 5.5: *Single cell, input coupler and output coupler.*

Palcusil 10. Then the central cells were brazed at 860°C with Palcusil 10. For brazing the couplers and cell column together, the column of cells was positioned vertically in the vacuum furnace and brazed to the couplers at 810°C using Palcusil 5. The input coupler was located at the bottom, the ouput coupler was located on the top. A small angular tilt of the output coupler with respect ot the cell column was discovered during inspection after brazing, so the cavity was cut at the second cell from the outer coupler and rebrazed. The Palcusil is a high-purity alloy of palladium, copper and silver used for tight vacuum brazing. The number indicates the composition weight (in percentage) of palladium in the alloy.

5.2.3 Low-Power Measurements

The measurements were carried out by the RF group of LNF. The scattering parameters measured before the high-power test were $S_{11} = 0.078$, $S_{21} = 0.641$ and $S_{31} = 0.648$, where port 1 is the input port and port 2 and 3 are the output ports. The profile of the longitudinal electric field was measured by the bead-pulling technique and is shown in Fig. 5.6. A field unflatness of ±10% was measured. The three-cell periodic pattern indicates that some power was reflected by the outer coupler. Time did not permit to compensate the reflection by tuning and this work was finally done once the prototype was high-power tested [69]. Fig. 5.6 shows the profile of the longitudinal electric field after final tuning of the prototype.

The main characteristics of the 5.7 GHz traveling-wave prototype are collected in Table 5.1.

5.3 High-Power Test

The high-power test of the 5.7 GHz structure prototype for SPARC was performed during November and December of 2010 at the High Energy Accelerator Research Organization KEK in Japan. This section explains the main characteristics of the experimental setup. Futher information on this topic is found in [9].

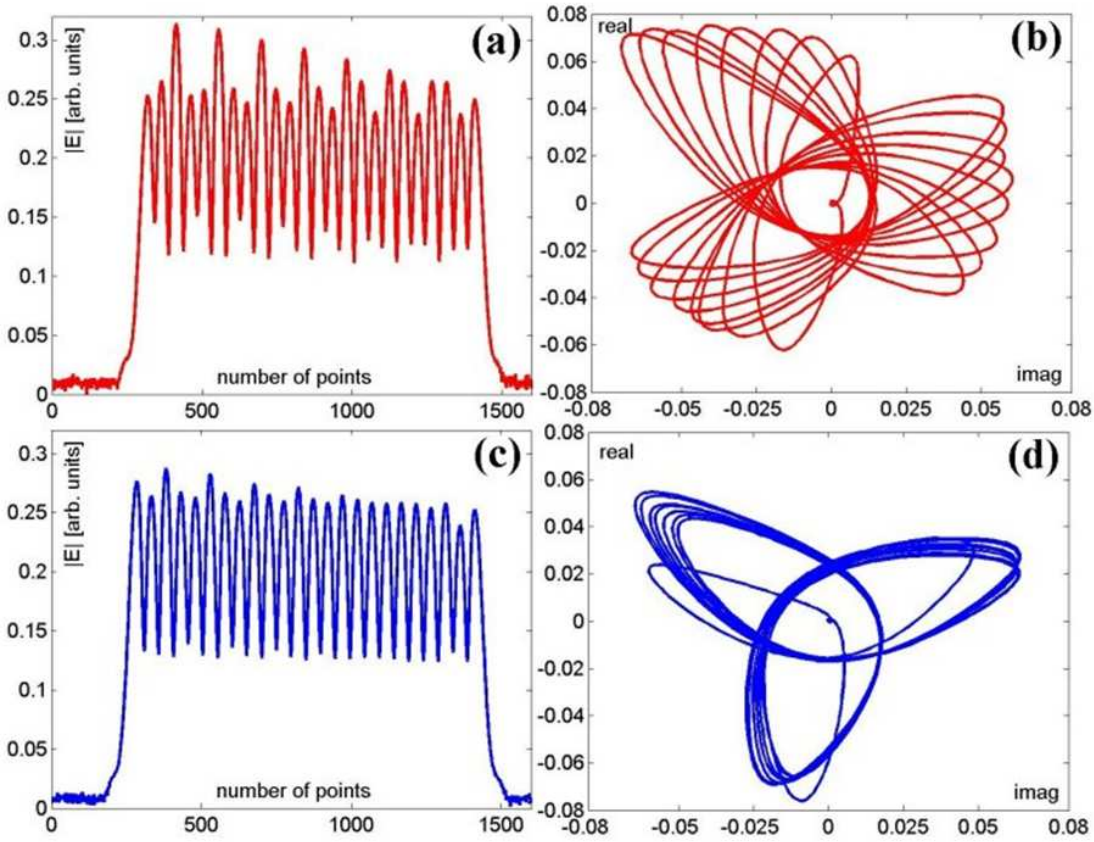

Figure 5.6: *Measured profile of the longitudinal electric field on axis for brazed structure: before (left) and after (right) tuning [69].*

5.3.1 RF Circuit Setup

RF power was provided by a 50 MW 5.7 GHz klystron driven by a Pulse Forming Network (PFN) modulator. The system produced 200 μs-long pulses at 50 Hz. A 22 m-long low-loss waveguide system transported the RF power to a SLED-type pulse compressor called SKIP [70]. SKIP could deliver 0.2 μs-long pulses to the prototype with a measured power gain of about 5. The output waveguides were terminated in matched SiC RF loads. Fig. 5.7 shows the layout of the testing hall at KEK. Fig. 5.8 and 5.9 show the interior of the testing bunker.

5.3.2 Vacuum System

Ion pumps were used to attain the ultra high vacuum (UHV) regime. They were connected through the evacuation ports located in front of the input coupler and in the output waveguides between the accelerating structure and the RF loads. The vacuum level at each evacuation port was readout with cold cathode gauges.

Table 5.1: *Main characteristics of the 5.7 GHz traveling-wave prototype.*

Electromagnetic quantities		
Frequency in air, f_0	5712	MHz
Quality factor, Q_0	9900	
Shunt impedance, Z	83	MΩ/m
Group velocity, v_{group}	0.0283	c
Attenuation factor, α	0.206	1/m
Filling time, t_{fill}	50	ns
E_{max}/E_0	2.4	
H_{max}/E_0	2.5	kA/MV
$\sqrt{S_{C,max}}/E_0$	0.024	$\frac{\sqrt{\text{MW/mm}^2}}{\text{MV/m}}$
Mechanical		
Material	OFHC copper	
Tolerance (cell profile)	2	μm
Surface Roughness (cells)	below 50	μm

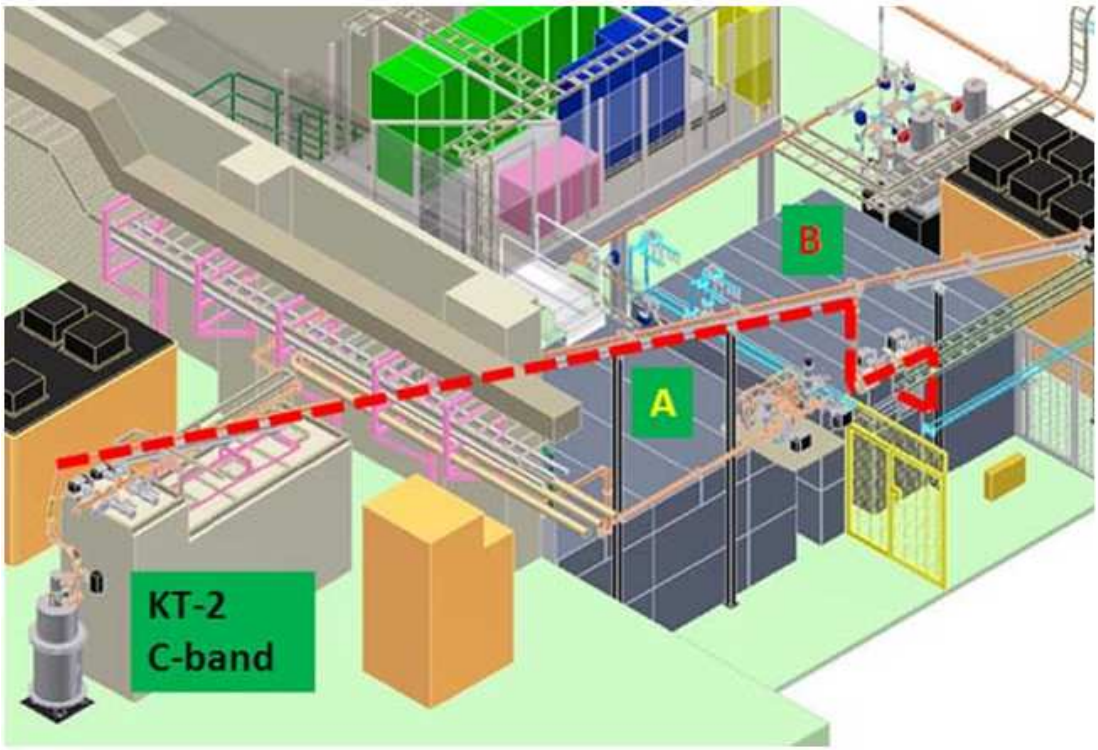

Figure 5.7: *Layout of testing hall at KEK. The RF power was delivered by a 5.7 GHz klystron and transported through a low-loss waveguide into a concrete hall.*

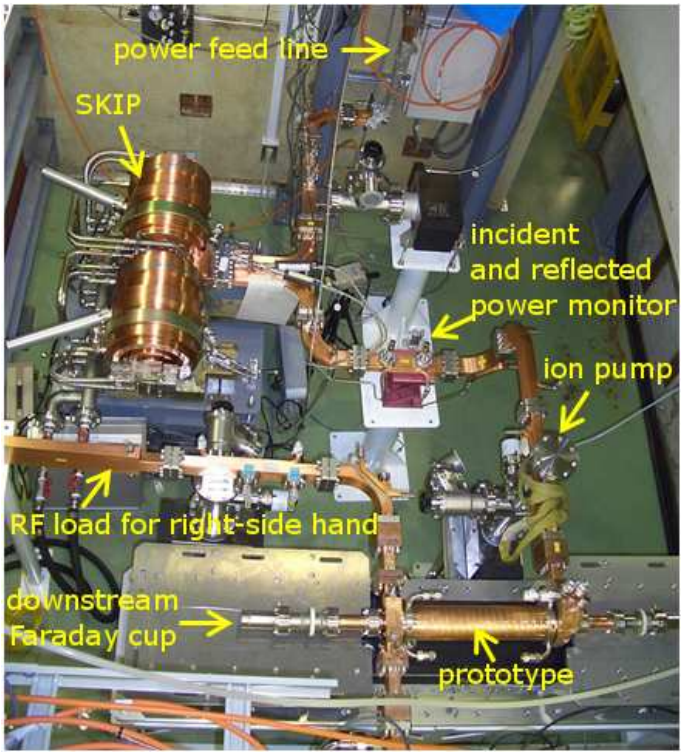

Figure 5.8: *Experimental setup inside shielded room.*

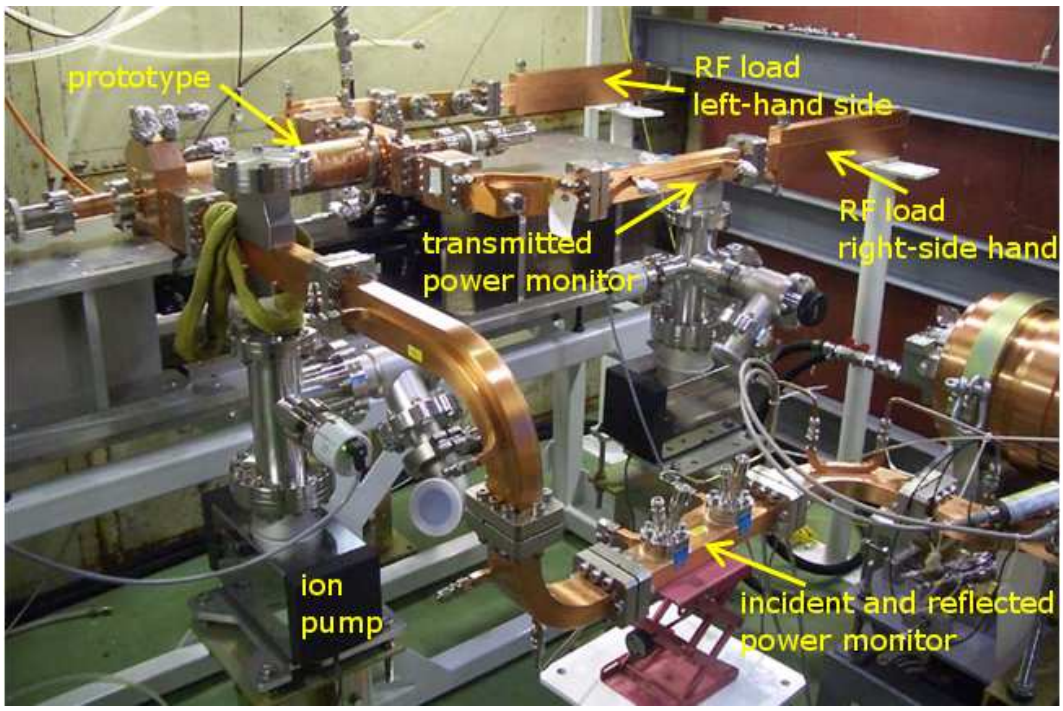

Figure 5.9: *Setup of accelerator test structure.*

5.3.3 Diagnostic Instrumentation, Data Logging and Control System

The test bench of the high-gradient test facility of KEK had data logging and control systems. The high-power test of the prototype included the following diagnostic instrumentation:

- Two Faraday cups connected at both beam ports of the accelerating structure to measure field-emission and breakdown current. The Faraday cup signals were sent into an Tecktronix oscilloscope and then retrieved into a PC using the Tecktronix interface software. The software managing this sequence was written in *Python* by KEK. The Faraday cup signals were used in this experiment to identify the breakdown events. When the field-emission current signal was above 2 mA, the hardware interlock stopped the RF pulsing of the RF amplifier for a few seconds and the waveforms of the RF and acoustic signals corresponding to the breakdown pulse were stored in the PC.

- Crystal detectors to measure incident, reflected and transmitted RF pulses from directional couplers located upstream and downstream of the accelerating structure. In traveling-wave structures, an additional RF pulse is available, the transmitted RF pulse. It serves in the breakdown location and evaluation of missing energy related to breakdown phenomena. The RF signals, incident, reflected and transmitted, were sent into an oscilloscope and then into a PC in the same manner as for the Faraday cup signals.

- An array of eight acoustic sensors placed along the cell column surface was implemented to monitor the sound burst which accompanies breakdown (see Fig. 5.15). The registered signals can be used to determine the breakdown location along the accelerating structure.

- Cold cathode gauges to measure the vacuum level. The typical vacuum level in the test prototype was about 3×10^{-8} mbar. The RF power level was reduced when the vacuum level was above $1 - 2 \times 10^{-7}$ mbar. The control system then recovered the power to the previous level in a similar way of the control system of the 3 GHz cavity test. The RF pulsing of the RF amplifier was completely stopped when the vacuum level exceeded a vacuum level of 10^{-6} mbar.

Fig. 5.11 is a schematic of the setup of prototype of the accelerating structure prototype and associated diagnostics. Fig. 5.12 and 5.13 show the typical RF pulse shapes for normal operation and during RF breakdown. Fig. 5.14 shows the typical field-emission current signal during normal operation.

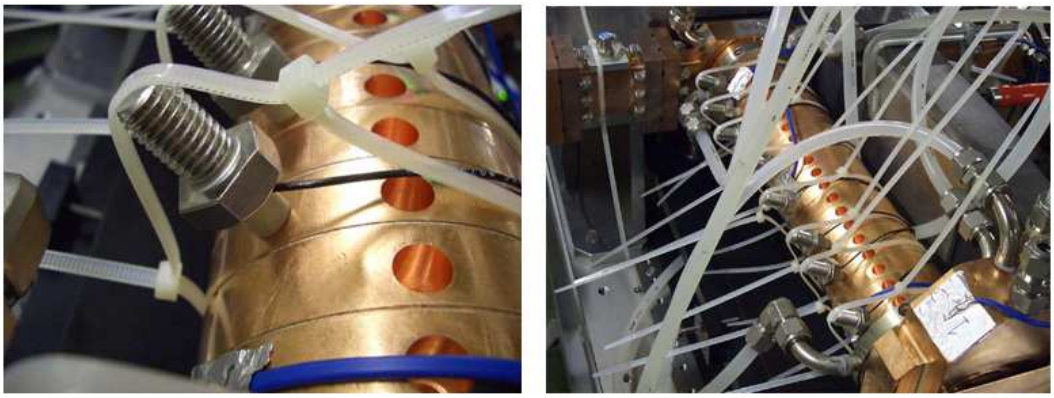

Figure 5.10: *Detail of acoustic sensors mounted on test structure and on waveguide.*

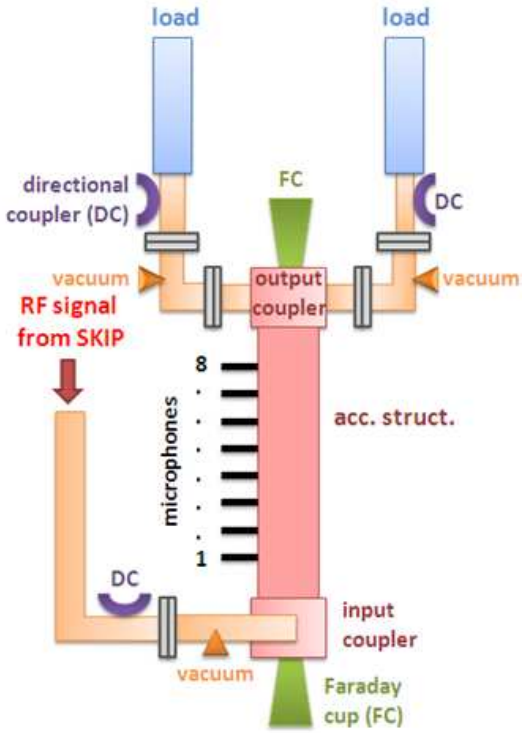

Figure 5.11: *Schematic of setup around accelerator structure.*

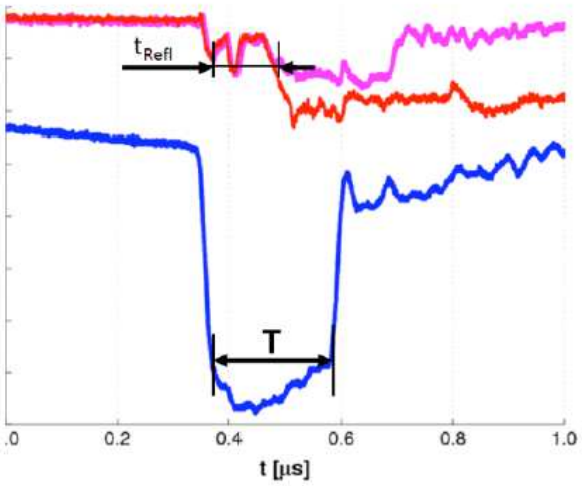

Figure 5.12: *Typical RF pulse shapes of breakdown: (a) RF pulse forward into accelerator structure (blue) and reflected from it (pink) during normal operation, and RF pulse reflected from accelerator structure during breakdown (red).*

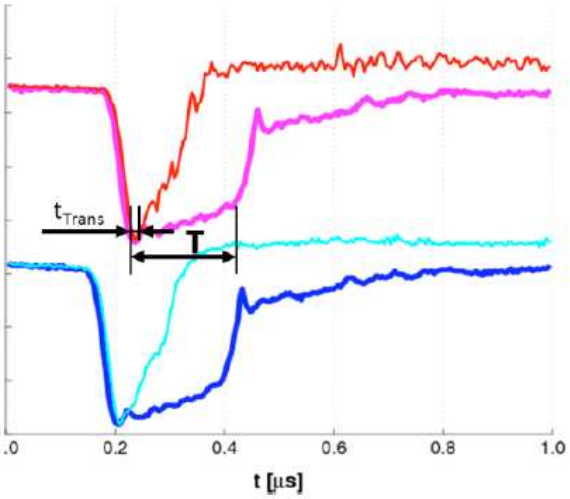

Figure 5.13: *RF pulse transmitted through structure toward left RF load (pink) and right (blue) during normal operation, and RF pulse transmitted toward left RF load (red) and right (cyan) during breakdown.*

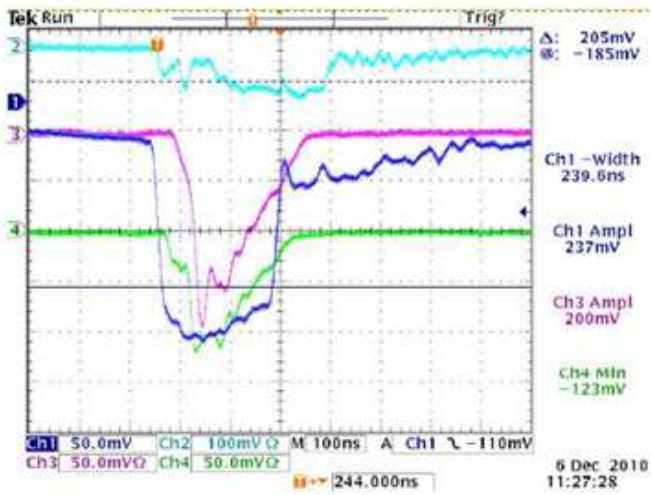

Figure 5.14: *Pulse shapes related to dark current during normal operation (no RF breakdown): transmitted pulse from SKIP (Ch1, blue), reflected power to SKIP (Ch2, cyan), dark current from downstream field-emission current signal (Ch3, pink) and dark current from usptream field-emission current signal (Ch4, green).*

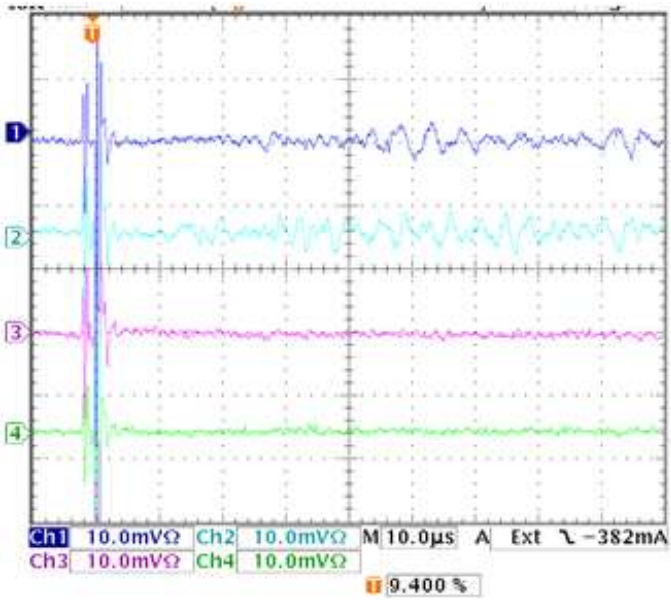

Figure 5.15: *Acoustic signal registered by the array of microphones. Each channel shows the signal registered by each microphone.*

5.3.4 High-Power Testing History

The high-power test started on November 5 and was completed on December 13, 2010. The structure processing, when the input power was increased little by little as the breakdown rate became stable for certain power level, extended from November 5 until December 2. In that period, more than 10^8 RF pulses of 200 ns width were sent into the structure with a repetition rate of 50 Hz. Just for a couple of days the RF pulse length was changed to 300 ns and only for one day (November 12) the repetition rate was decreased to 25 Hz.

On November 15, SKIP was switched on. After that, the power P_{IN} into the structure was about five times the power P_K delivered by the klystron. Fig. 5.16 shows the full test history in terms of the klystron output power P_K. The evolution of the test structure processing from November 22 until December 2 is shown in Fig. 5.17. Fig. 5.18 shows the attained accelerating gradient and the measured breakdown rate versus the accumulated number of breakdowns. The experiment run 24/7 to complete the conditioning within the available time slot and perform the breakdown rate measurements with enough statistics.

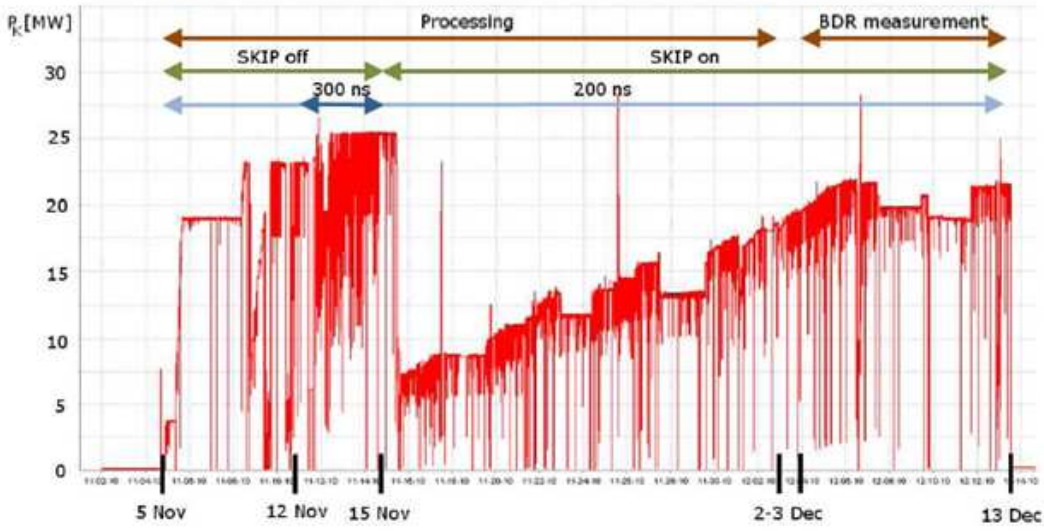

Figure 5.16: *History of high-power test of structure. The klystron power output is along the vertical axis and the time is along the horizontal axis.*

The conditioning process is necessary to achieve target performance, as a controlled rate of breakdowns serves to eliminate surface imperfections and oxygen trapped into copper surface. The prototype was considered to be conditioned, i.e. stable breakdown rate was achieved for the highest-gradient required performance, after more than 850 RF breakdowns.

The field-emission current was measured for different surface electric fields once the prototype was conditioned. The Fowler-Nordheim plot is presented in Fig. 5.19 for

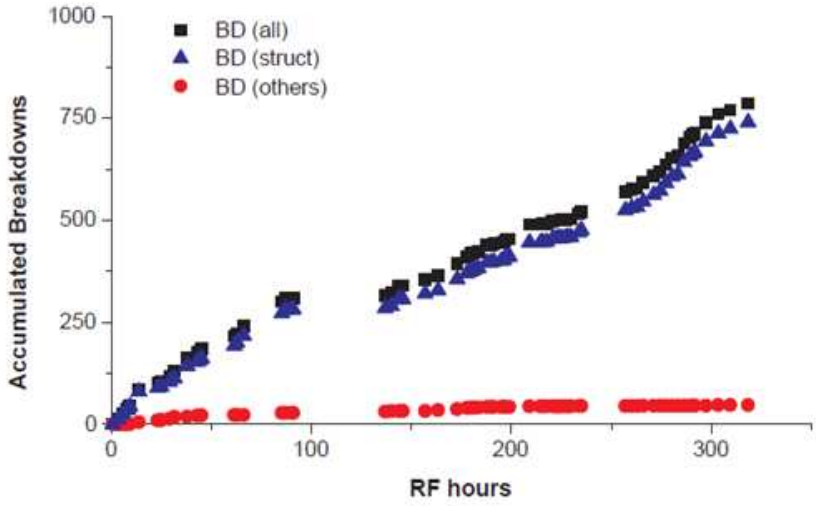

Figure 5.17: *Evolution of test structure processing from November 22 until December 2. Blue triangles represent breakdowns that occured within the structure. Red circles represent breakdowns that occured somewhere else in the RF circuit. Black squares represent the total number of breakdowns.*

the field-emission current measured in upstream and downstream Faraday cups. The field-enhancement factor β determined from the Fowler-Nordheim fit was about 90 for the structure prototype.

The conditioning status was observed in the great improvement of the measured breakdown rate for different electric field values. Fig. 5.20 shows the breakdown rate measured for different electric field values before and after finishing the prototype conditioning.

5.4 Measurements and Results

The breakdown rate (BDR) was computed for this experiment as follows:

$$BDR\,[bpp/m] = \frac{N_{bd}\,[breakdowns]}{N_{pulses}\,[pulses]\,L_{struct}\,[m]} \tag{5.1}$$

where N_{bd} is the number of breakdowns detected from the field-emission current signal, N_{pulses} is the number of RF pulses within the measurement and L_{struct} is the active lenght of the accelerating structure (total length of the cell column), 0.35 m.

Breakdown events were assumed to follow a poissonian distribution. The error associated to the breakdown rate measurements was then related to the error in breakdown counting, which corresponded to the square root of the counted value for phenomena governed by the poissonian law. The electric field in the structure was estimated from the incident power going into the prototype, assuming that the structure

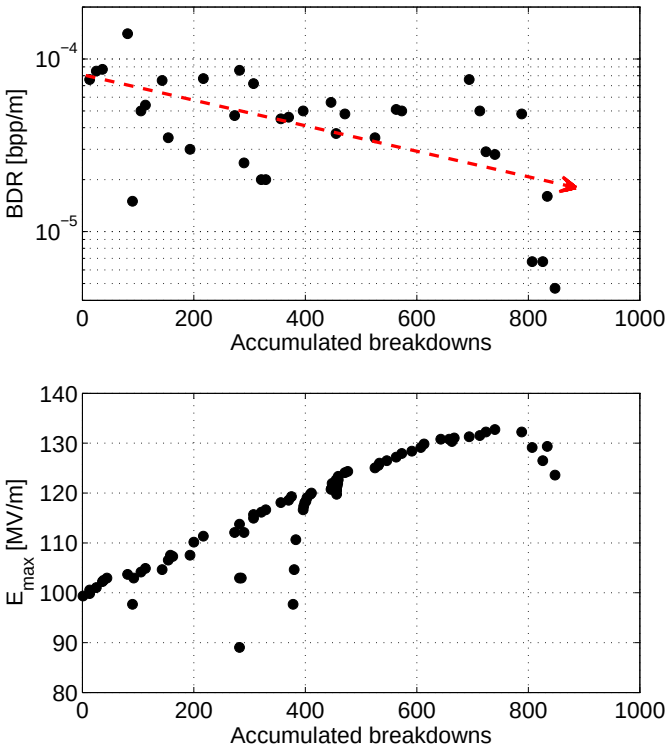

Figure 5.18: *Accelerating gradient and breakdown rate versus accumulated breakdowns from November 22 until December 2. The breakdown rate decreases and the "accessible" accelerating gradient increases as the number of accumulated breakdowns increases.*

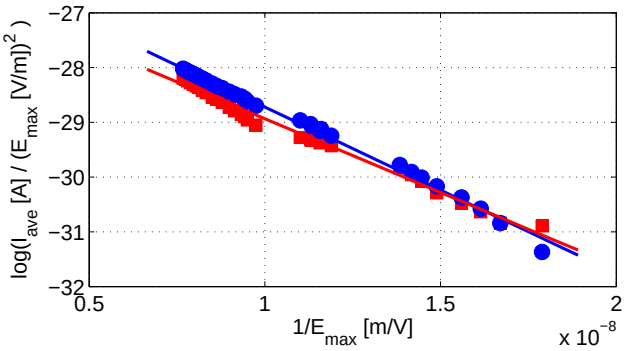

Figure 5.19: *Fowler-Nordheim plot of dark current measured at upstream (red squares) and downstream (blue circles) Faraday cups.*

was tuned. Therefore, there is a potential error of ±10% (maximum) on the electric field in the following high-gradient performance analysis.

Breakdown statistics: scaling laws

The breakdown rate was measured at different electric field values for two different stages of the test: before and after conditioning. A significant improvement in performance is observed between the two measurements. An exponential scaling law was fit to quantify the breakdown rate dependence on the accelerating field. The breakdown rate was proportional to the accelerating gradient to the power of around 30 for both cases, as it has been seen in other high-gradient tests [3]. For this analysis, data points for which a) more than 5 breakdowns were counted and/or b) the measurement lasted more than 4 hours were considered good measurements. The performance goal of the prototype was to achieve 35 MV/m with a breakdown rate below 5×10^{-5} bpp/m for a SLED pulse of 0.2 μs. The prototype performed much better than that: it could operate at even higher accelerating gradient with the same breakdown rate.

After conditioning, the breakdown rate was also measured for three different coolant temperatures (27.5, 28.5 and 29.5^0C) and a fixed accelerating gradient of 55 MV/m. The measured breakdown rate variation was not statistically significant. SKIP did not allow the RF pulse length to be varied, so the breakdown rate dependence on the pulse length could not be evaluated. Data were fitted using the power flow model and the stress model.

Power flow model Fig. 5.21 shows the equivalent modified Poynting vector of the prototype high-power test compared to other structures. The test results are consistent with other experimental data evaluated for accelerating structures operating between 12 and 30 GHz, which suggests that the modified Poynting vector may not be only a limiting quantity for the high-gradient performances of RF structures operating between 12 and 30 GHz, but also for those operating at 5.7 GHz.

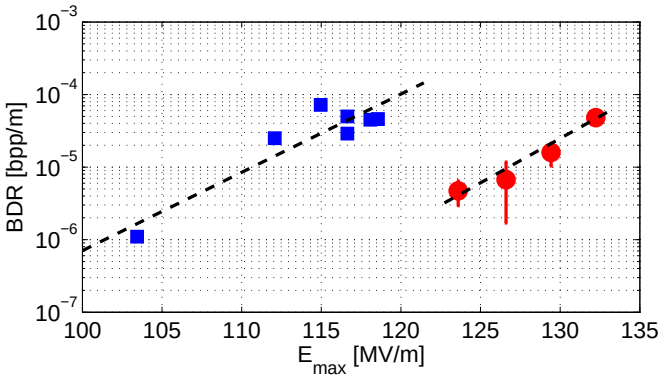

Figure 5.20: *Breakdown rate at different field values before (blue squares) and after (red circles) conditioning.*

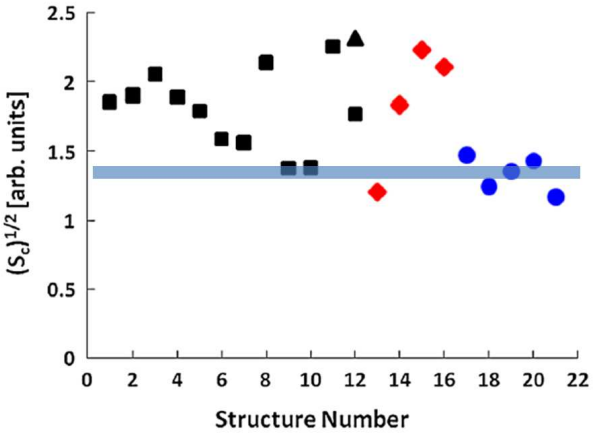

Figure 5.21: *Square root of the scaled modified Poynting vector calculated for the high-gradient performances of several accelerating structures as explained in section 1.3.2.*

Fig. 5.20 shows the present test data fitted to a power law which relates breakdown rate and electric field as follows: $BDR \propto E^X$. The breakdown rate scales to the electric field to the power of (35 ± 5) for the data measured after conditioning. The figure of merit of the fit is given by the root mean square ϵ_{RMS} and is equal to 0.014. The fitting procedure was the same as the one used for the data analysis of chapter 3.

Stress model The BDR vs gradient data was also fitted to the law proposed by the stress model described in section 1.3.2. Fig. 5.22 shows the fitted data. The root mean square deviation ϵ_{RMS} of the fit is 0.026. The defect volume predicted by the model is about $(2.9 \pm 0.4) \times 10^{-24}$ m^3.

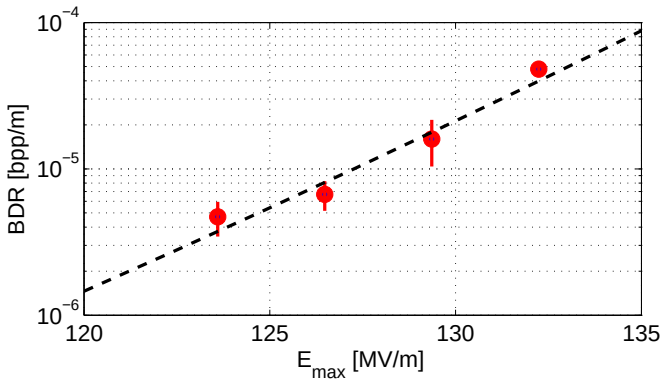

Figure 5.22: *Breakdown rate measurements performed for the prototype fitted to the stress model.*

Location of breakdowns along the structure

Surface inspection of structure inside after high-power test gives important information where breakdowns have occured in the test structure. However, transmitted and reflected RF pulse signals and the acoustic signals allows the breakdown location to be determined during testing and before cutting the test structure.

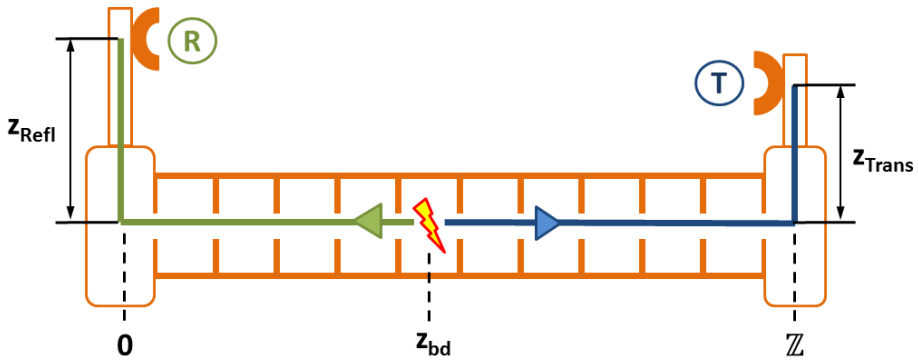

Figure 5.23: *Scheme of the experimental setup.*

From transmitted and reflected RF pulses The location of a breakdown event along a traveling-wave structure (Fig. 5.4) can be determined from the time when the power of the corresponding transmitted pulse starts dropping t_{Trans} (Fig. 5.12):

$$t_{Trans} = \frac{\mathbb{Z} - z_{bd}}{v_{struc}} + \frac{z_{Trans}}{v_{wg}} \tag{5.2}$$

and the time when the power of the corresponding reflected pulse starts increasing t_{Refl} (Fig. 5.13):

$$t_{Refl} = \frac{z_{bd}}{v_{struc}} + \frac{z_{Refl}}{v_{wg}} \tag{5.3}$$

where $\mathbb{Z}$ is the length of the accelerating structure, z_{bd} is the location of the breakdown event, z_{Refl} is the distance from the directional coupler where the reflected signal is measured and the beginning of the accelerating structure, z_{Trans} is the distance from the directional coupler where the transmitted signal is measured and the end of the accelerating structure , v_{struc} is the group velocity in the accelerating structure (constant along a constant impedance structure) and v_{wg} is the group velocity in the waveguide that connects directional couplers with accelerating structure.

The breakdown location z_{bd} is then given by the following expression:

$$z_{bd} = \frac{1}{2}\left(v_{struc}\left(t_{Refl} - t_{Trans}\right) + \mathbb{Z} + \frac{v_{struc}}{v_{wg}}\left(z_{Trans} - z_{Refl}\right)\right) \tag{5.4}$$

The distance between the structure input and the directional coupler for the present experimental setup is between 1.0 and 1.5 m, which introduces a round-trip time delay of about 10 ns in the detection of the reflected pulse. The group velocity is 0.0283c, consequently the filling time (for the 22-cell structure) is 50 ns. Therefore, the time delay corresponds, in distance, to 5 cells.

Fig.5.4 shows the distribution of breakdown events along the structure as determined from the study of the transmitted and reflected RF pulses. Most of the breakdowns occur at the downstream side of the prototype, which indicates the existence of a hot cell. A possible explanation for this is that the cell column was cut to correct angular tilting of the output coupler with respect to the cell column. This intervention could increase the likelihood of creating a hot cell. Blue (red) points have been calculated from the transmitted RF signal from the accelerating structure to left (right) load. The presented results have an uncertainty in breakdown location of about 2-3 cells. The phase measurement of the reflected RF pulse signal could have been useful to determine the breakdown location along the structure with more precision.

From acoustic emissions The breakdown locations were also estimated from the appearance of larger acoustic signals in one or several of the eight microphones placed along the structure. For example, Fig. 5.15 shows the acoustic signals registered by four microphones. The onset timing of the amplitude jump, which is related to the source location by the propagation of sound waves through the copper structure, was not utilized in this study. The result of the study is presented in Fig.5.4. Two hot regions were found along the structure: one was in the upstream portion of the structure, and the other was at the downstream end. This seems inconsistent with the RF signal analysis.

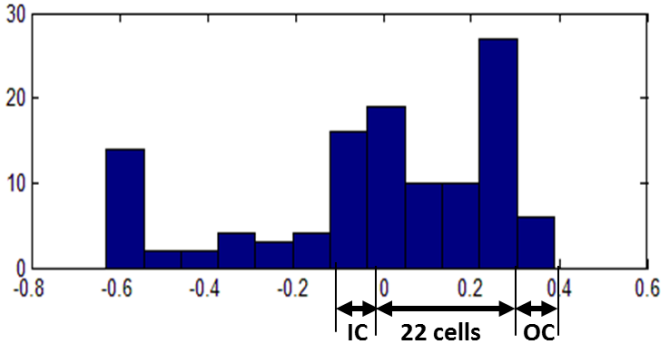

Figure 5.24: *Breakdown location from reflected and transmitted RF pulses.*

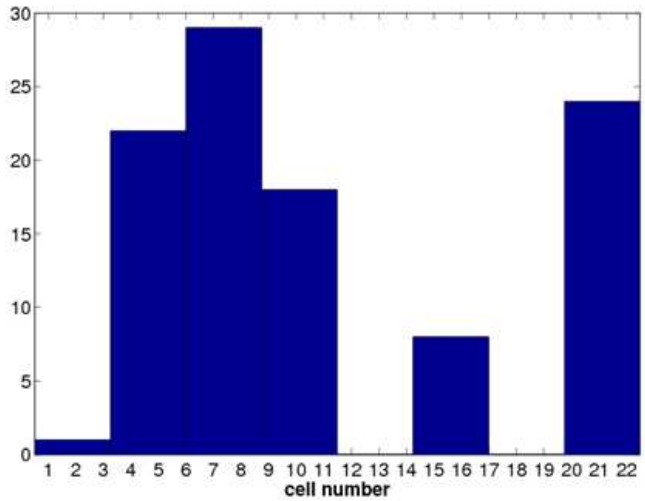

Figure 5.25: *Breakdown location from acoustic signals.*

Missing energy during breakdown event

The missing energy is the amount of RF energy "lost" during an RF breakdown, calculated as the energy balance of incident, transmitted and reflected signals during RF breakdown. Part of the missing energy is consumed by the vacuum arc itself [31]; the rest might be used in the acceleration of field-emission electrons [30]. For high-power tests of RF structures operating between 12 and 30 GHz, the missing energy can be over 50% of the incoming power, which corresponds to about a joule for the 12 GHz structures and about half joule for the 30 GHz ones [52]. The missing energy ϵ was evaluated for several breakdown events of the 5.7 GHz structure prototype by computing the difference between the energy of the incident signal E_{inc} and the sum of energy of the reflected signal, E_{refl}, and the two transmitted signals, E_{trans}, taking into account the ohmic losses in the structure, which are given in section 5.2.3. The missing energy was up to 20% of the incident power, which corresponds to a couple of joules. Fig. 5.26 shows the energy balance for an RF breakdown measured during the high-power tests of the 5.7 GHz prototype.

5.4.1 Surface Inspection

The prototype was cut and the interior surfaces of the first cell, a middle cell and the last cell of the accelerating structure were inspected. Fig. 5.4.1 show the surface of the first cell. Breakdown craters are observed by the naked eye in the low region field of the first cell, but none of them appeared in the other inspected cells. The craters were close examined with a SEM. Typical diamater of breakdown craters was about 50 μm (see Fig. 5.4.1). The surface analysis concluded that most of the breakdowns were located upstream of the cell column (as it is expected for traveling-wave constant-impedance structures), which differs from the estimation perfomed from the reflected and transmitted RF pulses but is consistent with the estimation from the acoustic signals.

A possible explanation for this is that the shape of the reflected RF pulse made it difficult to determine the starting time of the breakdown event within the reflected RF pulse. A good estimation of the breakdown location depends critically on the identification of the starting time of the breakdown within the reflected and transmitted RF pulses. The difficulties to find this starting time in the reflected RF pulse might have contributed significatively to get a bad estimation of the breakdown location from such RF pulses.

5.5 Conclusions and Outlook

The experimental results are relevant at a number of different levels. Firsly, the good high-gradient performances of the prototype allowed the longer accelerating sections necessary to increase the output energy of SPARC to start. The two 1.4-m

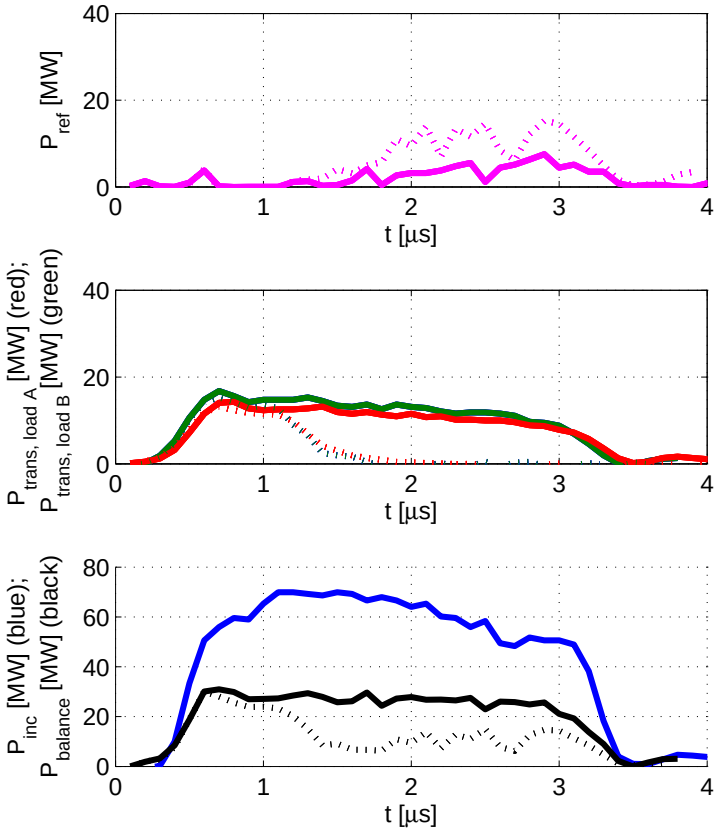

Figure 5.26: *Example of energy balance for an RF breakdown. The upper plot shows the reflected RF power signal for a normal RF pulse (solid line) and during breakdown (dotted line). The middle plot shows the transmitted RF power signal for both loads A and B (red and green curves, respectively) for a normal RF pulse (solid line) and during breakdown (dotted line). The lower plot shows the incident RF power signal (blue line), the energy balance during RF breakdown (black dotted line, sum of reflected and transmitted energies) and the expected energy balance for a normal RF pulse (black solid line).*

Figure 5.27: *Interior of first cell.*

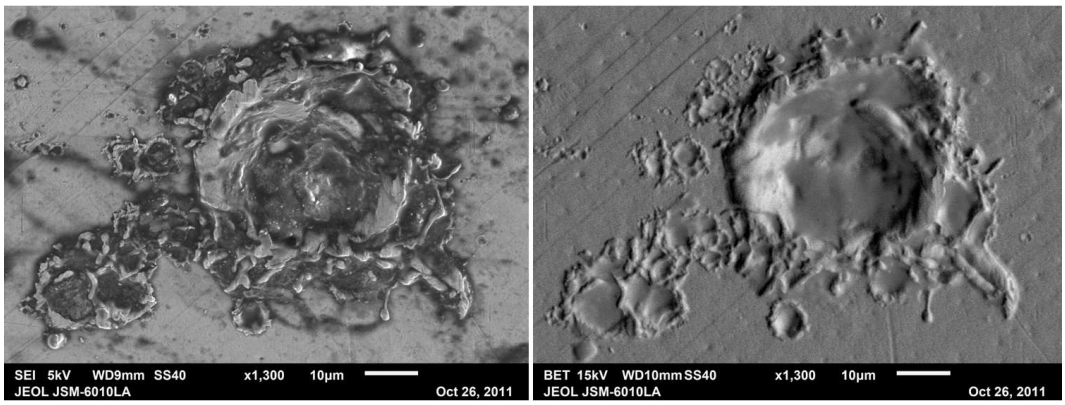

Figure 5.28: *Craters originated by RF breakdown activity found in the first cell.*

constant-impedance units are currently under production. The installation and conditioning of the RF structures is expected to take place from October 2012 onwards. The operation with beam of the complete 5.7 GHz system in SPARC is foreseen for Spring 2013. In addition, the breakdown rate measurements meant the possiblity to operate the structure at higher accelerating gradient than 35 MV/m, the design goal.

This experiment confirmed an accelerating gradient greater than 50 MV/m for 5.7 GHz structures. In Japan, where the high-gradient test was performed, the 5.7 GHz system of the KEKB injector linac has been operated for many years with an accelerating field of 40 MV/m and the 5.7 GHz linac of XFEL/Spring-8, consisting of 128 accelerator sections, has been commissioned to operate at 35 MV/m on average after 1000 hours of processing [71]. The good results of the present experiment open the possibility of applying higher accelerating gradients than the present operating levels to these 5.7 GHz accelerators if needed.

The experiment also allowed a rough estimation of the expected breakdown rate of CABOTO, which will be presented and discussed in chapter 7.

Chapter 6

Accelerators for Hadrontherapy

The International Agency for Research on Cancer (IARC) predicts that the number of deaths caused by cancer will increase from 7.6 millions in 2008 to 13.1 millions in 2030 [72]. The goal of cancer treatment is to save patients' lives with reduced negative consequences for their quality of life. Hadrontherapy is a modern radiotherapy technique which uses external beams of hadrons for tumour treatment. The field has greatly developed in the past two decades, thanks to a further understanding in biological response to radiation and enhanced treatment techniques. In consequence, the number of centers that offer this kind of treatment is increasing in the recent years. Even though all existing facilities are cyclotron and synchrotron based centers, new accelerator types are also being considered. Size and cost are the main challenges featured by hadrontherapy accelerators and gantries [73], and research and development of hadrontherapy accelerators and gantries is mainly focusing in delivering much smaller and cheaper machines.

The chapter introduces the basics of hadrontherapy, presents the requirements of an accelerator for hadrontherapy and reviews the different accelerator designs proposed for hadrontherapy.

6.1 Use of Ion Beams for Tumour Treatment

Hadrontherapy is a form of external radiotherapy using energetic beams of hadrons. The energy loss of a charged particle as consequence of the ionizations induced in the surroundings of its way through an absorber increases towards the end of its range, when the particle is almost stopped, reaching a maximum known as Bragg peak (see Fig. 6.1). The Bragg peak position, or alternatively the particle range, are function of the energy of the particle at the entrance of the absorber. The final dose delivered to the Bragg peak region depends on the absorber, the beam intensity and the particles charge. The particular depth-dose profile of hadrons allows to deliver high doses to the region where the Bragg peak seats while providing low doses to its surroundings, so that high doses can be deposited in a deep seated tumour while minimizing the

radiation effects in adjacent healthy tissues. While DNA damage caused by low dose radiation is quickly repaired, high dose radiation provokes cell death and arrest of the cell cycle due to gross chromosomic aberrations.

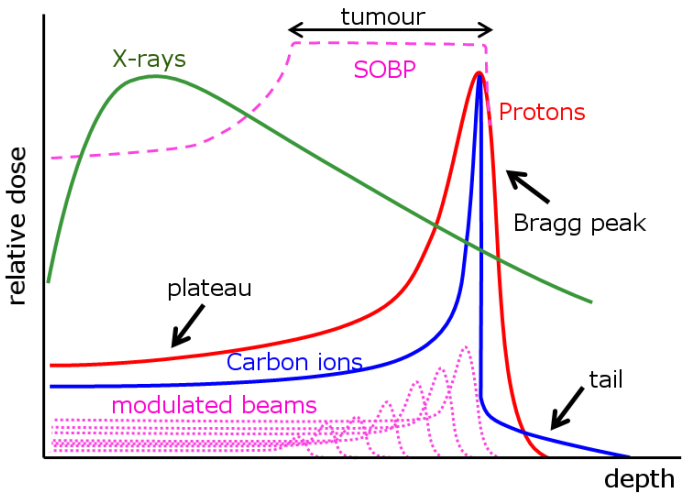

Figure 6.1: *Relative dose deposition of monoenergetic X-ray, proton and carbon ion beams with depth. The Spread Out Bragg Peak (SOBP) is formed as the addition of multiple modulated beams with different energies in order to cover all the tumour volume.*

Proton and carbon ion beams are typically used in hadrontherapy, but there is also much interest in exploring the possibilities of other ions like helium, lithium or oxygen [74, 75]. Heavy ions like carbon present a considerable high radiobiological effect while compared with photons and protons, which makes them suitable for the treatment of radioresistant tumours. As a drawback, nuclear fragmentation processes of particles heavier than protons result in the formation of a tail beyond the pristine Bragg peak, as shown in Fig. 6.1, associated to the lighter particles created during fragmentation.

The sharp Bragg peak, just a couple of millimeters for protons, is not large enough in most of the cases to cover all the tumour volume, which can extend beyond 10 cm. There are two ways to widen the Bragg peak and cover all the tumour volume: the passive spreading technique and the active energy modulation. The passive spreading technique consists in interposing variable thickness absorbers that change the particles range to reproduce the desired depth-dose profile. The sum of modulated curves gives place to the so-called Spread-Out Bragg Peak (SOBP), illustrated in Fig. 6.1. The collimator aperture defines the treatment field size in the transversal planes, as illustrated in Fig. 6.2. A more advanced approach, the active spreading technique, uses a pencil-like beam which is transversally oriented with magnetic fields. Fig. 6.3 shows how magnetic fields are used to scan the tumour volume in both transversal planes. Tumour irradiation with pencil-like beams can be done in two manners: i) by

a continuous scanning of the tumour volume (raster scanning system) or by virtually dividing the tumour volume in small volume units, or voxels, and providing a beam shot to each voxel (spot scanning technique). The beam intensity can be modulated to provide a better dose conformity to the tumour volume with the Intensity Modulated Particle Therapy (IMPT) technique. The active energy modulation consists in actively changing the beam output energy in the accelerator for irradiation, which results more convenient when using heavier particles to avoid nuclear fragmentation and neutron activation in the beam line. The spot scanning technique, when combined with tumour multipainting and assisted by a 3D feedback system, is the best technique for moving organ treatment. Tumour multipainting reduces the uncertainty in dose delivery originated from systematic errors in the delivered dose average and also if a spot is missing (the so-called "cold spot") [76].

Range straggling in monoenergetic beams appears due to the stochastic nature of energy loss processes. The beam also becomes broader as results of the multiple Coulomb scattering. Both effects are taken into account while designing the treatment delivery for a patient.

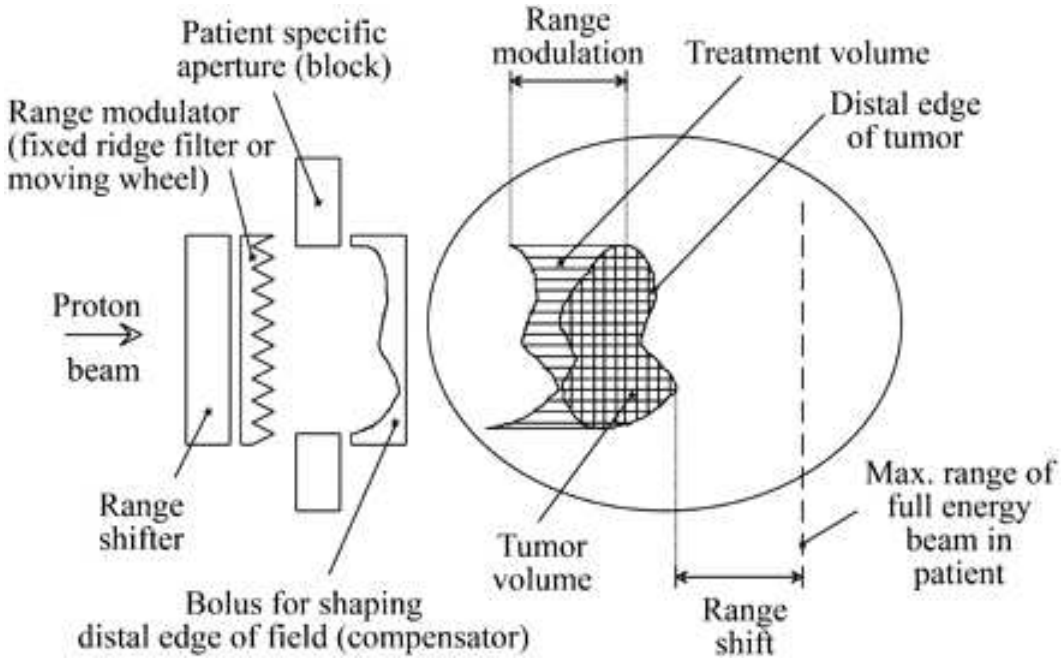

Figure 6.2: *Passive spreading technique.*

6.2 Requirements of a Hadrontherapy Accelerator

Beam parameters are determined by clinical specifications [77] (see Table 6.1) and may vary due to different tumour locations and delivery modalities [78, 79]. The most

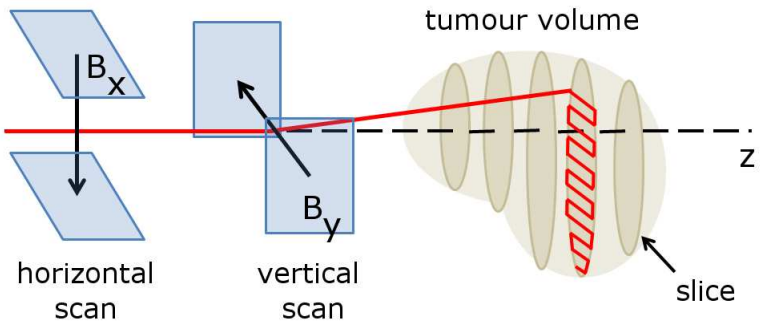

(a) Raster scanning technique.

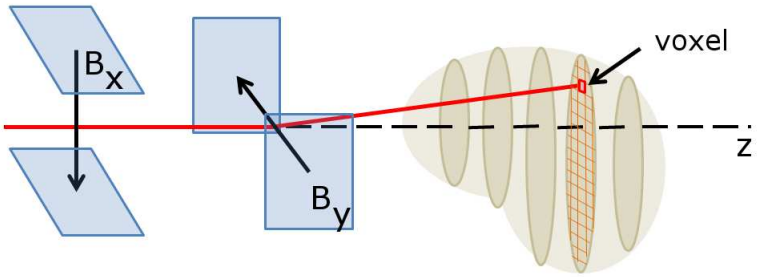

(b) Spot scanning technique.

Figure 6.3: *Transversal scanning of the tumour volume by using magnetic fields.*

significant beam performances for hadrontherapy and their acceptable values have been presented by different authors [80, 81]. A proton beam energy between 60 and 230 MeV and a carbon beam energy between 110 and 430 MeV/u correspond to a 3 to 32 cm range in water-equivalent tissue. A good energy selection system, preferably without absorbers, is required to avoid beam quality degradation and activation of accelerator and nozzel components. A rapid variation of the energy with ±0.5 mm range precision (related to the energy spread of the beam) is required to profit of the rapid fall-off of the Bragg peak and accurately cover the target. Beam position and orientation, shape and size play a decisive role to ensure a conformal delivery of the dose to the tumour, which may translate into lower cancer recurrences and lower complication rates (due to better therapeutic ratio) [79, 82]. Magnet precision is a sensitive issue as it directly influences beam position and orientation [78]. If the beam is delivered with a repetition rate in the range of hundreds of Hz, the beam pulse can be synchronised with moving organs and "cold spots" can be corrected by painting several times the tumour volume within the same treatment session (multipainting technique). Furthermore, a beam with enough current is desired to reduce the duration of the treatment. The minimum dose rate is equal to 2 Gy/min in a 1 liter target [83]. Finally, a low emittance beam would permit to use magnets with smaller apertures and therefore smaller sizes [78].

Table 6.1: *Beam parameters and and their clinical significance.*

Accelerator Beam Parameter	**Significance for treatment field**	
Energy	Range	Good energy selection system to provide adequate penetration depths
Size, emittance	Dose distribution	Better dose distribution to reach better dose conformity
Shape, repetition rate	Organ motion	Possibility to apply multipainting technique
Current	Dose rate	Simple and efficient extraction to minimize neutrons production and maximize intensity for therapy
Position, orientation, size, shape, precision	Conformal dose delivery	Better dose delivery to reach better dose conformity
Timing (availability)	Radiobiological response, better patient experience; higher patient throughput	Higher beam availability leads to better results

The therapeutical beam must be stable, accurate and clean of neutrons and other particles coming from scattering processes in absorbers [79, 84]. The accelerator complex should incorporate a precise measurement system of the beam parameters (energy, size, position, intensity and emittance) as well as a reliable beam control system [85]. A versatile machine which provides fixed and movable beams, in different positions and orientations, and allows to use different delivery modalities would bring greatest benefit to patients. For safety reasons the beam must be decoupled from the patient and the accelerator must be perfectly shielded. A high extraction efficiency is required for low equipment activation and low exposure to personnel [78]. Power supply stability, stable performance of the machine, vacuum and cooling systems operation must be guaranteed. Power supply stability is especially critical in that it affects the energy, intensity and position stability of the therapeutic beam [78]. On the other hand, the complex has to be easy to operate, maintain and repair [79, 84]. An accelerator complex divided in modules facilitates maintenance, reparation, upgrading and extension of the facility.

Socio-economical aspects are especially important. Accelerators for hadrontherapy should have a relatively low price, require little plug power and have reduced dimensions [79, 84, 85]. Facilities based on accelerators which deliver beam to multiple rooms (multiple-room accelerators) are typically more economical than those based on single-room accelerators. Nevertheless, if there is a breakdown in a multiple-room accelerator, the treatment delivery has to be stopped in several rooms of the facility [86]. On the other hand, the choice of an adequate patients' flow will lead to a rapid investment recovery. Finally, hospital-based facilities show some advantages from the point of view of patient experience, beam time for therapy and availability of sanitary resources [78] but laboratory-based facilities allow R&D necessaries for advancing in the field.

Other requirements are more related to routine operation of the facility. The time availability of the accelerator complex should be higher than 99% [79]. Therapy for patients in the third or fourth week of treatment cannot be aborted: cancer recurrence probability increases dramatically in these cases, therefore, reliable operation is very important [78].

6.3 Review on Accelerators for Hadrontherapy

At present 35 facilities all around the world offer protontherapy and just 6 provide carbon ion therapy [87]. Although all these centers are cyclotron or synchrotron-based facilities, neither cyclotrons nor synchrotrons show the optimal characteristics for hadrontherapy. Cyclotrons excel at compactness, simplicity and reliability. The beam is extracted at fixed energy, so movable absorbers are needed to vary the beam energy. The use of absorbers for carbon ion therapy requires a long and complicated energy selection system due to carbon fragmentation and neutron activation of the line. The most remarkable feature of synchrotrons is the possibility to vary the energy of the extracted beam from pulse to pulse. However, 1-2 seconds separate the successive flat-tops during which the beam is extracted, too long to follow up the movement of organs with the beam spot. In addition, synchrotrons are larger and not so easy to operate as cyclotrons and require an injection linac and a sophisticated extraction system.

Recent research and development of novel accelerators for hadrontherapy focuses on providing compact accelerators, possibly pulsing at high repetition rate to treat moving organs. RF linacs and Fixed-Field Alternating-Gradient (FFAG) accelerators are both high repetition rate accelerators that may show the appropriate features for hadrontherapy applications.

An FFAG consists of a series of fixed field magnets forming a closed ring. The magnets are distributed and shaped in such a way that the beam can be strongly focused. The basics of FFAGs are explained in [90]. Different FFAG designs were proposed for hadrontherapy. A review on the designs is found in [90]. In principle, FFAGs pulse the beam at high repetition rates (in the order of hundreds of Hz), which is appropriate to treat moving organs. The use of fixed field magnets implies certain benefits like simpler operation and simpler and cheaper power supplies. In circular machines the beam sees the same magnet lattice several times. Small deviations in particle trajectory due to magnet misalignement or field imperfections occur periodically every turn. If this effect is synchronized with the beam motion, there is a resonance and the small deviations in particle trajectory or beam kicks add up. Resonances can provoke beam losses which activate and damage the accelerator structure. In some cases, the beam can be lost completely. The lattice of the so-called Scaling FFAG (S-FFAG) is designed to avoid resonances during the acceleration process. Such machines are in consequence easy to operate. A medical accelerator based on S-FFAG technology typically consists of a chain of rings which magnets are not so small and cheap. The magnets of Non-Scaling FFAG (NS-FFAG) are simpler and smaller, but lattices are dense, which make difficult to allocate injection and extraction systems. In addition, operation is complex due to resonance crossing. PAMELA, a Particle Accelerator for MEdical Aplications, is a proton NS-FFAG under research and development within the CONFORM collaboration. The lattice of the NS-FFAG was reviewed to leave enough room to the injection and extraction systems. The ring diameter is about 12 meters [93]. In addition, the American company Compact Particle Acceleration

Corporation is working on an isochronous NS-FFAG that assures a constant tune and greatly simplifies machine operation and power supplies. The ring for protontherapy is about 7 meter-diameter. Another ring could be added to the design for carbon acceleration.

The FFAG cannot compete at present with the RF linacs in terms of compactness, as illustrated in Fig. 6.4. RF linacs may offer the most compact solution for carbon ion therapy while allowing the best beam delivery modality for moving organ treatment. On the other hand, the development of compact gantries is still a pending issue. A typical gantry for protontherapy has a 5 meter-diameter [88], while the Heidelberg carbon ion gantry, the only one in the world, is 13 meters in diameter [89]. Certain accelerators like RF linacs and Dielectric Wall Accelerators (DWA) may be compact and light enough to be mounted on a gantry. The DWA is a chain of inductive cells with a ferromagnetic core that applies a voltage to a high gradient insulator consisting of alternated conductor and insulator sheets with periods of about 1 mm. The claimed compactness of DWA makes them a promising candidate for the future. However, the gradients achieved up to now, in the order of 1 MV/m, are still far from the target value, 100 MV/m. In this regard, the technology of high-frequency RF linacs is at this moment much more advanced than the DWA.

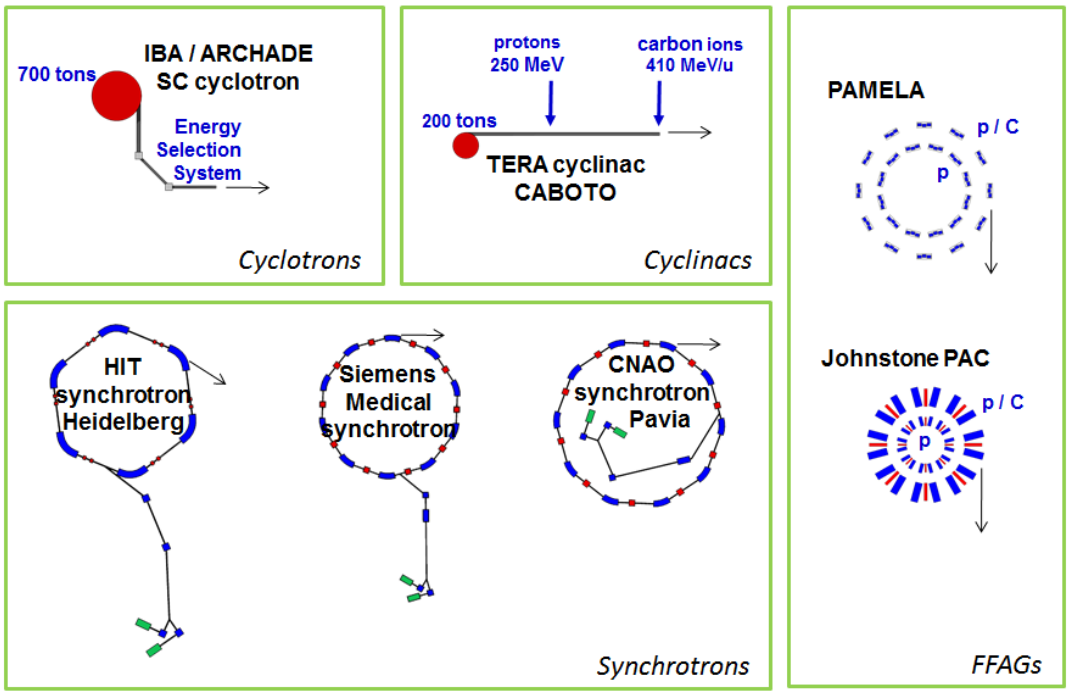

Figure 6.4: *Dimensional comparison of different types of accelerators proposed or already used for hadrontherapy (carbon ion therapy). FFAG-based complex sketches miss the preinjector and the extraction lines.*

6.3.1 RF linacs for Hadrontherapy

A compilation of the latest linac designs for hadrontherapy is presented. None of these linacs has been ever constructed. Just some parts or modules of some of them have been built and tested.

IDRA, a *cyclinac*-based facility for protontherapy

The concept of *cyclinac*, a cyclotron followed by a linac, was proposed by U. Amaldi in 1993 and developed by TERA. The first cyclinac design was based on LIBO (LInear BOoster), a 3 GHz (S-band) standing wave side-coupled linac (often called CCL for Cell Coupled Linac) which accelerates protons from 62 to 200 MeV at 400 Hz repetition rate. The linac is divided into 36 tanks grouped into 9 modules. Each module is fed by its own klystron. In total, the length of the linac is 13.5 m. The beam energy is modulated by reducing or switching off the power that arrives to the modules. The lattice of LIBO is very simple: a series of thin permanent magnetic quadrupoles are used along the linac to focus the beam.

A collaboration between TERA, CERN, the University and INFN of Milan and the University Federico II and INFN of Naples was established to build and test a scale prototype of the first module of LIBO (see Fig. 6.5). This module, 1.3 meters-long, is designed for achieving an accelerating gradient of 15.8 MV/m. It has to accelerate protons from 62 to 74 MeV with an RF peak power of 4.4 MW. During the tests, an accelerating gradient of 28.5 MV/m was achieved, which means that shorter modules could be still designed [2].

In 2001, TERA proposed a *cyclinac*-based facility for protontherapy called IDRA (Institute for Diagnostics and RAdiotherapy). A scheme of the facility is shown in Fig. 6.6. The facility uses a 30 MeV high-current commercial proton cyclotron as a preaccelerator. The cyclotron is followed by a side-coupled linac, based on the LIBO design, which accelerates protons up to 230 MeV. The linac is 18 meters-long and works at high repetition rate (100-200 Hz). The pulse length is 3.2 μs. The total peak RF power required by the linear machine is around 60 MW, which at 200 Hz corresponds to an average plug power of 150 kW. Commercial klystrons can be used to power the machine.

The ADAM (Application of Detectors and Accelerators to Medicine, S.A.) company, a CERN spin-off, will exploit the commercial possibilities of this kind of facility. Two prototype modules for accelerating protons from 30 to 41 MeV have already been built and high-power tested by ADAM at CERN (Switzerland).

ACLIP, a booster for a 30 MeV cyclotron

A collaboration which comprises the University Federico II of Naples, the INFN section of Naples, the University and the INFN section of Milan, the University and

Figure 6.5: *First module of LIBO [2].*

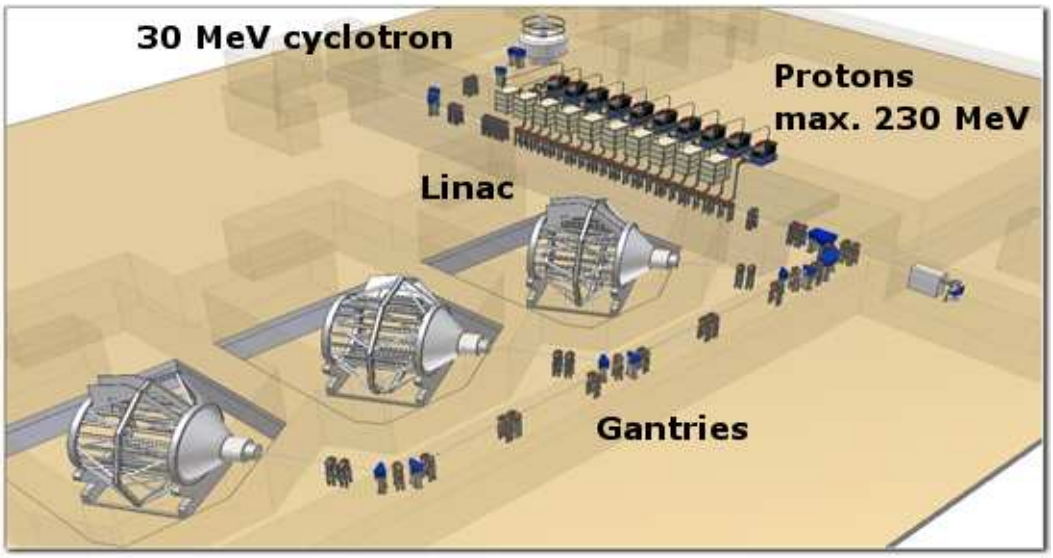

Figure 6.6: *The IDRA concept, a cyclinac-based facility for protontherapy [76].*

the INFN section of Bari, the University of Sannio, CERN and the e2v Technologies company has designed a 3 GHz (S-band) proton standing wave CCL which differs from LIBO because the half-cells forming an accelerating tank are cut in such a way that the number of pieces to be machined is reduced by a factor of 2 [95]. Based on this design, ACLIP receives the protons delivered by a 30 MeV cyclotron and accelerates them to 62 MeV. It will be followed by a LIBO to accelerate the protons from 62 to 200-230 MeV. ACLIP consists of 5 modules for a total length of 3.1 m. The first module, already built and tested, is divided into two tanks and should accelerate protons from 30 to 35 MeV (accelerating gradient of 16 MV/m). Acceleration tests performed at the Catania INFN cyclotron facility show that the structure can accelerate protons up to 33.5 MeV [96].

TOP project, all-linac solution for protontherapy

The TOP (Oncological Therapy with Protons) project proposes an all-linac solution for protontherapy. The project is followed by ENEA and ISS (Istituto Superiore di Sanità) at the oncological centre IFO in Rome. A Radio-Frequency Quadrupole (RFQ) followed by a Drift-Tube Linac (DTL) accelerates protons up to 7 MeV. Both accelerators operate at 425 MHz. Then, particles are injected into a 3 GHz (S-band) Side-Coupled Drift-Tube Linac (SCDTL), which accelerates them up to 40 MeV. The length of the SCDTL is around 10 m. RF power required to feed it is around 8 MW. Finally, protons achieve the appropiate energy for therapy in a 3 GHz side-coupled linac of LIBO type [97]. The facility based on this accelerator complex is called TOP-IMPLART and is shown in Fig. 6.7.

Figure 6.7: *Artist's view of the projected TOP-IMPLART facility [97].*

3 GHz CABOTO for hadrontherapy

CABOTO (CArbon BOoster for Therapy in Oncology) is a first solution proposed by the TERA Foundation for carbon therapy. An SC-EBIS (SuperConducting-Electron Beam Ion Source) produced by DREEBIT GmbH (Dresden) will deliver about 5×10^7 fully stripped carbon ions in 1.5 μs at 400 Hz. The ions will be preaccelerated up to 300 MeV/u in SCENT (Superconducting Cyclotron for Exotic Nuclei and Therapy), a superconducting cyclotron of 350 tons and 5 m diameter which has been designed in the INFN National Laboratory LNS in Catania [76]. Then the particles will be injected into a 3 GHz (S-band) high-gradient Side-Coupled Linac (SCL) which will accelerate C^{6+} from 300 to 430 MeV/u in 22 meters (the accelerating gradient is about 25 MV/m). The linac is divided into 16 accelerating modules. Each module is fed by its own klystron of 7.5 MW peak power. The beam energy selection is done by switching off certain number of the modules for high energies and regulating the power that is feeding the last active module. The linac operates at high repetition rate (≤ 400 Hz) and delivers short hadron pulses of 1.5 μs. An image of such a centre is shown in Fig. 6.8.

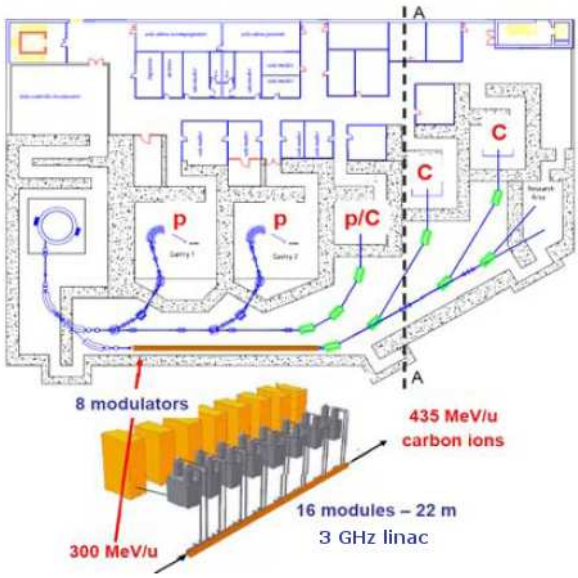

Figure 6.8: *Hadrontherapy facility based on the SCENT cyclotron and 3 GHz CABOTO [76].*

5.7 GHz CABOTO for hadrontherapy

Another design for CABOTO was proposed by TERA Foundation. The main difference between this design and the one presented in the previous section is the frequency and consequently, the maximum accelerating gradient which can be achieved in the linac while ensuring reliable operation.

The output intensity of C^{6+} ions that the $SC-EBIS$ can deliver at 400 Hz would not be enough for carbon ion therapy. Therefore, three SC-EBIS sources will provide a flux of 10^8 C^{6+} in 3 μs pulses at 300 Hz [98]. The ions are preaccelerated in a superconducting cyclotron up to 120 MeV/u before being injected into the side-coupled linac. The K480 superconducting cyclotron weights 190 tons and has a 4 m diameter. The linac boosts carbon ions from 120 up to 400 MeV/u. It is being designed for operating at 5.7 GHz (C-band) and achieving high accelerating gradients (around 40 MV/m), which will permit a reduction in the total length of the linac to about 24 m [99].

Klystrons of 12 MW peak power with 2 μs pulse length and working at 200-300 Hz will feed the 18 modules which compose the linac. The accelerator complex is shown in Fig. 6.9. By switching on and off the last modules of the linac and by adjusting the amplitude and phase of the power delivered by the klystron to the last module in operation, one can adjust continuously the output energy, as in all linacs described in this chapter. Commercial compact solid-state modulators power the klystron. ADAM is testing the reproducibility in adjusting the power amplitude and the RF phase of such a device.

The linac will also permit the acceleration of H_2 molecules for proton therapy. Total average plug power for running the complex is 800 kW [100].

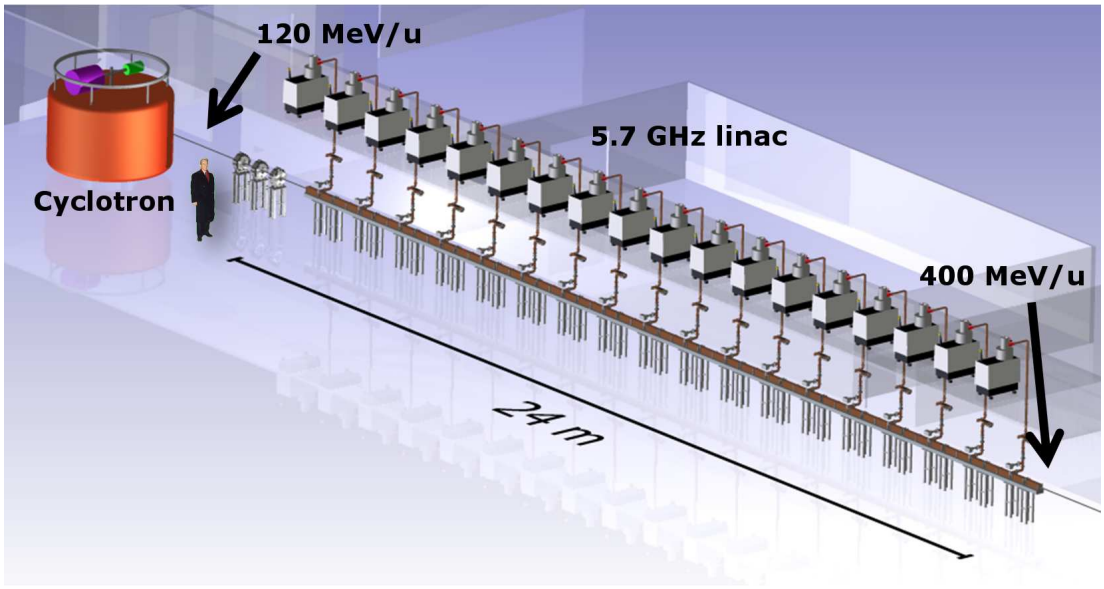

Figure 6.9: *Artist's view of 5.7 GHz CABOTO, TERA's proposal for hadrontherapy [99].*

A subsequent study found out that the best cyclotron output energy, in terms of machine costs and enhanced medical potentiallity, was 150 MV/m instead of 120 MV/m [102]. This Thesis presents in the following chapter the design of a CABOTO that receives the particles previously accelerated by a cyclotron at 150 MV/m. The

work is completed with a discussion on the beam and machine performances that make this new design a good solution for hadrontherapy.

TULIP, a TUrning linac for Protontherapy

TERA Foundation proposes to merge the cyclinac concept with a gantry in the so-called TULIP (TUrning Linac for Protontherapy). In consequence, the dimensions of the accelerator complex can be considerably reduced: the design foresees a total complex length of about 15 m. Two high-gradient 5.7 GHz (C-band) linear sections will rotate around the patient. The maximum accelerating gradient required in the linac is about 38 MV/m. A cyclotron will preaccelerate the protons that will be then accelerated by the two linear sections to the appropriate treatment energies. A sketch of TULIP is shown in Fig.6.10 [99].

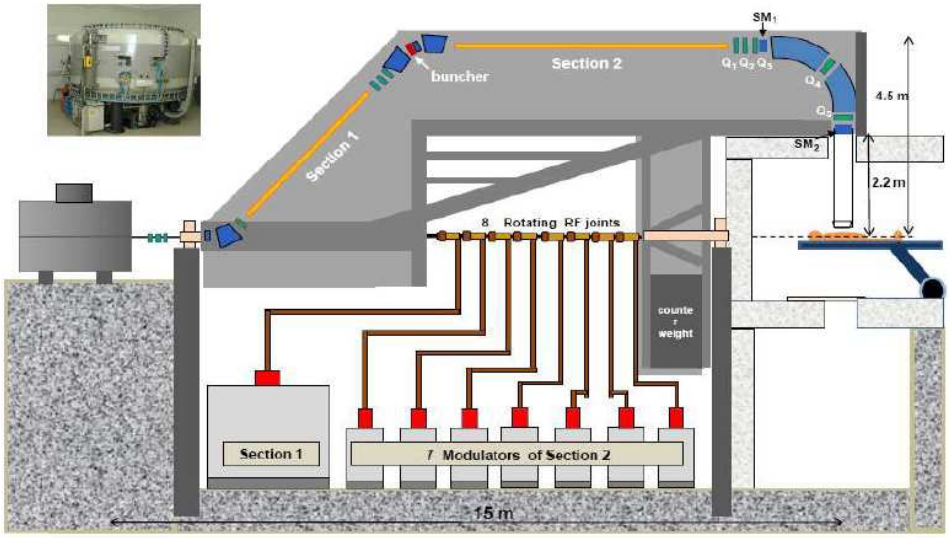

Figure 6.10: *Sketch of TULIP [99].*

SLAC X-band Proton Therapy Accelerator

The accelerator will be composed of two standing-wave linear structures, most likely side-coupled linacs. The first linac will receive 70 MeV protons from a cyclotron and will accelerate them to 200 MeV. A second linac, that would rotate around the patient, will decelerate by 50 MeV or accelerate by 50 MeV the particles delivered by the first linac in steps of less than 1 MeV (see Fig. 6.11). The operating frequency of the linacs has to be decided, but most likely it will belong to the X-band (9-12 GHz).

Preliminary studies show that the length of this second linac could be around 1 meter, short enough to place it in a moving gantry. More developments will be done to improve beam quality and structure performance [101].

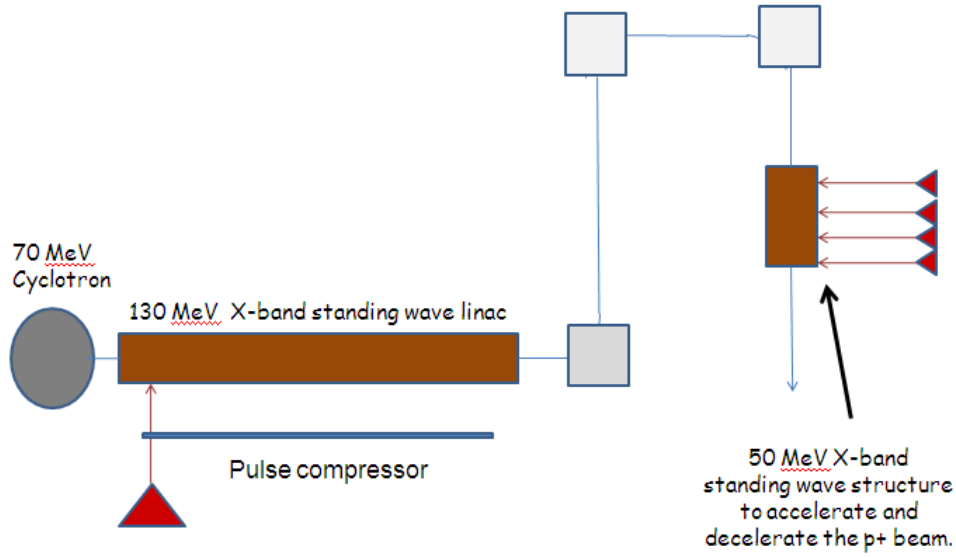

Figure 6.11: *Sketch of the SLAC X-band Proton Therapy Accelerator [101].*

6.4 Summary

The medical requirements for hadrontherapy accelerators were introduced in this chapter. Then, the current accelerator types used to deliver a clinical beam for hadrontherapy (cyclotron and synchrotrons) and the new accelerator solutions which may have enhanced performances for tumour treatment with hadrons (FFAGs, DWAs and RF linacs) were discussed. The RF linacs outstanded among the other accelerator options due to its high repetition rate and the possibility to actively change the energy of the beam - which would allow the treatment of moving organs - and thanks to its compactness. The chapter also presented different designs for a hadrontherapy complex based on RF linac technology.

Chapter 7

Feasibility Study of a High-Frequency Linac for Carbon Ion Therapy

The previous chapter discussed the main characteristics of an accelerator for hadrontherapy. While some characteristics were related to the beam performances, others corresponded to the performances of the machine itself, like size, energetic efficiency, reliability and maintenance.

The characteristics of CABOTO, a copper standing-wave high-frequency linac expressly designed for hadrontherapy appplications, make it a suitable candidate for the next generation of hadrontherapy accelerators. This chapter goes through the design of CABOTO, from the cell optimization and linac layout to the study of the beam performances and machine reliability. It also explains the choices that drive the final layout of the linac and how they affect its performances. A final discussion on the expected performances of CABOTO closes the chapter.

7.1 CABOTO, a High-Frequency Linac for Carbon Ion Therapy

The RF structure of CABOTO is a copper standing-wave Side Coupled Linac (SCL). The linac receives a beam of fully stripped carbon ions, $^{12}C^{6+}$, previously accelerated in a cyclotron. CABOTO will boost the particle energy from 150 up to 410 MeV/u. The carbon ions of 410 MeV/u reach a depth about 287 mm in water, necessary to treat deep-seated tumours. The input energy of the beam, 150 MeV/u, was demonstrated to be the optimal one for a hadrontherapy cyclinac in terms of machine costs and enhanced medical potentiality in a previous study [102].

The linac is divided in different sections called units. Each unit is fed by a single klystron. The division of the linac into independently fed units allows a rapid (1-2 ms) and continuous beam energy variation from pulse to pulse by varying the powering of the RF structures. This means that no absorbers are needed for scanning the tumour in depth. A general scheme of a linac structure for beam energy modulation without

absorbers is shown in Fig. 7.1. The beam energy can be changed from pulse to pulse by switching off the RF power of a given number of units and each unit increases the beam energy in steps of 15-18 MeV. For example if just the first unit is active, the beam energy will be about 163 MeV/u. And if all the units are on, the beam energy will be maximum, 410 MeV/u. Each unit is in turn subdivided in tanks. In Fig. 7.2 a cross section of a SCL tank is presented in 2 and 3 dimensions.

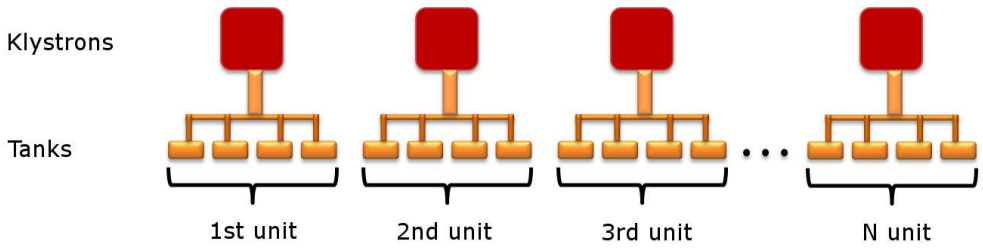

Figure 7.1: *Sketch of the general scheme of a linac structure for beam energy modulation without absorbers like CABOTO. The red boxes are the klystrons. Each klystron feeds one unit and each unit is divided into multiple tanks. The tanks are represented by orange boxes.*

The beam energy can be changed in smaller steps to provide a minimum equivalent step of 2 mm in water by varying the last active module power. This characteristic, together with the high repetition rate at which the machine can be operated (for this work, 300 Hz), makes the cyclinac suitable to apply the 3D spot scanning technique with multipainting, which can be applied to treat moving organs.

The transverse focusing of the beam is provided by a set of Permanent Magnetic Quadrupoles (PMQs), alternatively placed in the drift spaces between tanks, in a FODO structure which repeats every two tanks, as shown in Fig. 7.3. The particularities of this lattice includes:

- From quadrupole to quadrupole the particles traverse a tank, not a drift tube, so they receive a transverse kick from the RF defocusing forces.
- Every tank has a different length; therefore, the distance between quadrupoles is not constant.
- The quadrupole strengths can be different from tank to tank.

The linac could also accelerate H_2 molecules, which would reach 250 MeV/u at about half of the total length of CABOTO. With the RF power of the second half switched off, the output beam would produce 250 MeV protons by inserting a thin foil downstream of the linac. The energy of the proton beam could be modulated in the linac from 250 MeV to 150 MeV by acting on the RF system of the linac. Variable thickness absorbers could be used to reduce the beam energy below 150 MeV in order

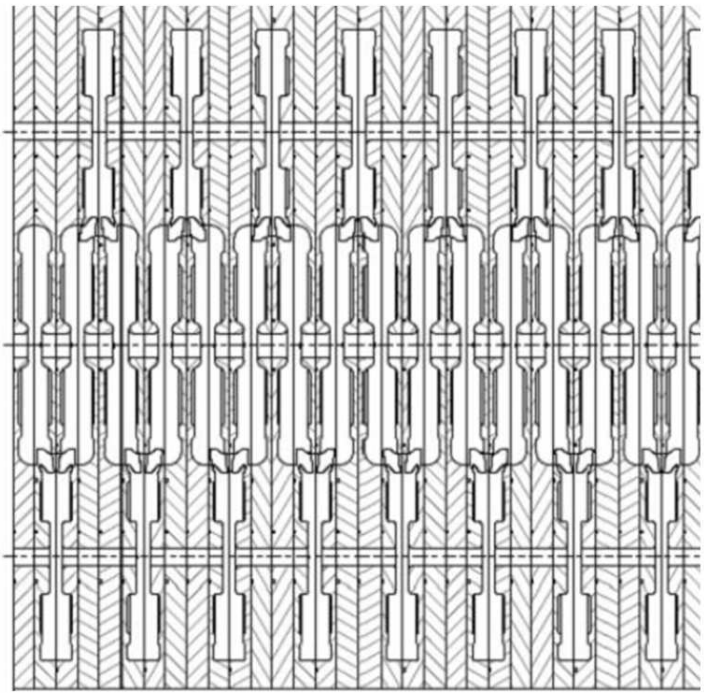

(a)

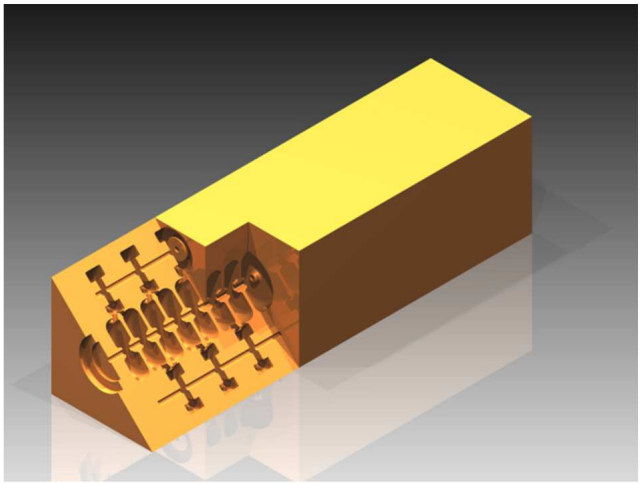

(b)

Figure 7.2: *Cross sections of a tank for a side-coupled cavity in 2 (a) and 3 (b) dimensions.*

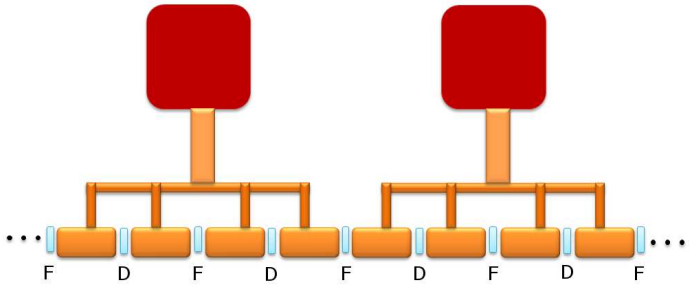

Figure 7.3: *FODO lattice in CABOTO. The quadrupoles are placed in the drift spaces between tanks. The F (D) quadrupole focuses (defocuses) in one transversal plane while defocuses (focuses) in the other.*

to treat more superficial tumours. Another option could be the use of the linac to decelerate the beam.

7.2 Cell Optimization

The cell design was optimized to reduce the energy consumption and minimize the probability of RF breakdown. CABOTO operates at a high RF frequency, 5.7 GHz, in order to: i) reach high accelerating gradients and therefore have a more compact layout and ii) reduce energy consumption. The shunt impedance per unit of length Z is the quantity that measures the energetic efficiency to excite a given accelerating gradient in a cavity, as already explained in chapter 1, which becomes the effective shunt impedance per unit of length ZTT after including the transit time factor T. The energy $W/\cos\,\phi_S$ gained by the particles accelerated in a linac of length L is:

$$\frac{W}{cos\,\phi_S} = \sqrt{ZTT \cdot P \cdot L} \tag{7.1}$$

The expression results from combining Eq.(1.13) and Eq.(1.16) and indicates that the required peak power P for a given energy gain can be reduced if ZTT is increased. ZTT strongly depends on the cell geometry.

Particles accelerated in CABOTO have a velocity range from $\beta = 0.5$ to $\beta = 0.7$, so the cells have noses to enhance the electric field along the cell axis and provide better acceleration, just as in the TERA test cavities. Fig. 1.4 shows the typical geometry of a CABOTO cell. The maximum surface electric field E_{max} and the maximum modified Poynting vector $S_{C,max}$ reached in the cell are located in the nose area, as it was already shown for the TERA test cavities in chapters 3 and 4. The optimization of the cell geometry is essential to minimize these values.

The cell optimization focused on the accelerating cells of CABOTO. Cell geometry was then optimized to maximize the effective shunt impedance (related to energy con-

sumption) while keeping the ratios peak surface electric field over accelerating gradient E_{max}/E_0 and maximum modified Poynting vector over accelerating gradient $S_{C,max}/E_0$ (related to breakdown rate) as small as possible. The cell optimization was performed for the cells corresponding to the energies 150, 200, 250, 325 and 400 MeV/u. The study was conducted with the macro *Superfisherman* and all RF simulations were performed with *Poisson Superfish*. The influence of the nose radii, the corner radii and the cone angle on ZTT, E_{max}/E_0 and $S_{C,max}/E_0$ were studied as well. The geometrical parameters which are restricted by mechanical, physical or beam dynamics reasons are listed in Table 7.1. A common cell radius was established for all the cells, independently of the energy for which they were designed, for simplifying machining. A bore hole radius of 2.5 mm was fixed for all the cells, small enough to provide high shunt impedance, but large enough not to lose too many particles in the transverse plane. Once optimized, the cells were tuned by changing their gap length. Fig. 7.5, 7.6 , 7.7, 7.8 and 7.9 show the relation between the effective shunt impedance ZTT and the ratio E_{max}/E_0 for different values of the geometrical parameters in study for each cell energy. From Fig. 7.5, 7.6 , 7.7, 7.8 and 7.9 it turns out that the nose radii have a great influence on the ZTT (about 10% per mm) while the corner radii nearly do not have an influence at all. The ZTT slightly changes for different cone angles (less than 1% per degree). The cell geometrical parameters and the main electromagnetic quantities for the optimal cell geometry are presented in Table 7.2. The effective shunt impedance ZTT is between 100 and 130 MΩ/m (values for lowest and highest energy cells, respectively). The ratio maximum peak surface electric field over accelerating gradient, E_{max}/E_0 is between 4.5 and 4.7. And the maximum square root of the modified Poynting vector over the accelerating gradient, $\sqrt{S_{C,max}}/E_0$, is practically constant for the whole linac, around 0.024 $\sqrt{\mathrm{MW/mm^2}}/\mathrm{MV/m}$. Fig. 7.4 shows the evolution of the main electromagnetic quantities along the linac.

Table 7.1: *Restricted cell geometrical parameters.*

Parameter	**Value**	**Unit**	**Reason**
Outer Nose Radius, R_{ON}	≥ 0.5	mm	Mechanical limitation
Inner Nose Radius, R_{IN}	≥ 0.5	mm	Mechanical limitation
Cone Angle, θ_{CONE}	$18-25$	deg	Cooling requirements
Wall Thickness, Web	≥ 2	mm	Mechanics and cooling
Bore Radius, R_{BORE}	$\geq 2,5$	mm	Beam dynamics
Flat Top Length, L_{FLAT}	0 or ≥ 0.5	mm	Mechanical limitations

Table 7.2: *Cell geometry parameters and electromagnetic quantities for different cell energies.*

Geometrical Parameters						
Energy, E	150	200	250	325	400	MeV/u
Length, L	1.3333	1.4897	1.6143	1.7526	1.8751	mm
Outer Corner Radius, R_{OC}	5.16	5.94	6.00	7.00	7.00	mm
Inner Corner Radius, R_{IC}	1.5	1.5	1.5	2.0	2.0	mm
Outer Nose Radius, R_{ON}	0.7	0.7	0.7	0.7	0.7	mm
Inner Nose Radius, R_{IN}	0.5	0.5	0.5	0.5	0.5	mm
Cone Angle, θ_{CONE}	18	18	18	18	18	deg
Flat Top Length, L_{FLAT}	0	0	0	0	0	mm
Wall Thickness, Web	2	2	2	2	2	mm
Bore Radius, R_{BORE}	2.5	2.5	2.5	2.5	2.5	mm
Cell Radius, R	19.15	19.15	19.15	19.15	19.15	mm
Gap Length, g	5.73	6.65	7.72	8.45	9.53	mm
Electromagnetic Quantities						
Quality Factor, Q	8540	9170	9590	9990	10280	
Effect. Shunt Impedance, ZTT	99.5	111.1	118.9	125.9	130.8	MΩ/m
Ratio E_{max}/E_0	4.5	4.5	4.5	4.6	4.7	
Ratio H_{max}/E_0	2.2	2.3	2.4	2.5	2.6	kA/MV
Ratio $\sqrt{S_{C,max}}/E_0$	0.023	0.023	0.023	0.024	0.024	$\frac{\sqrt{\text{MW/mm}^2}}{\text{MV/m}}$

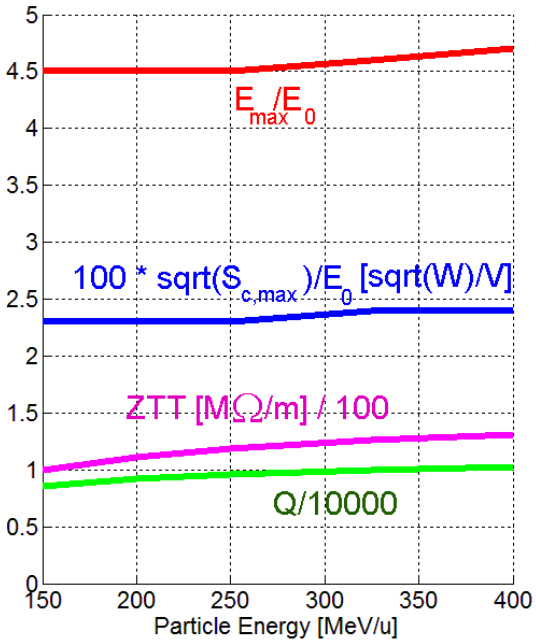

Figure 7.4: *Evolution of basic electromagnetic quantities along the linac after cell optimization.*

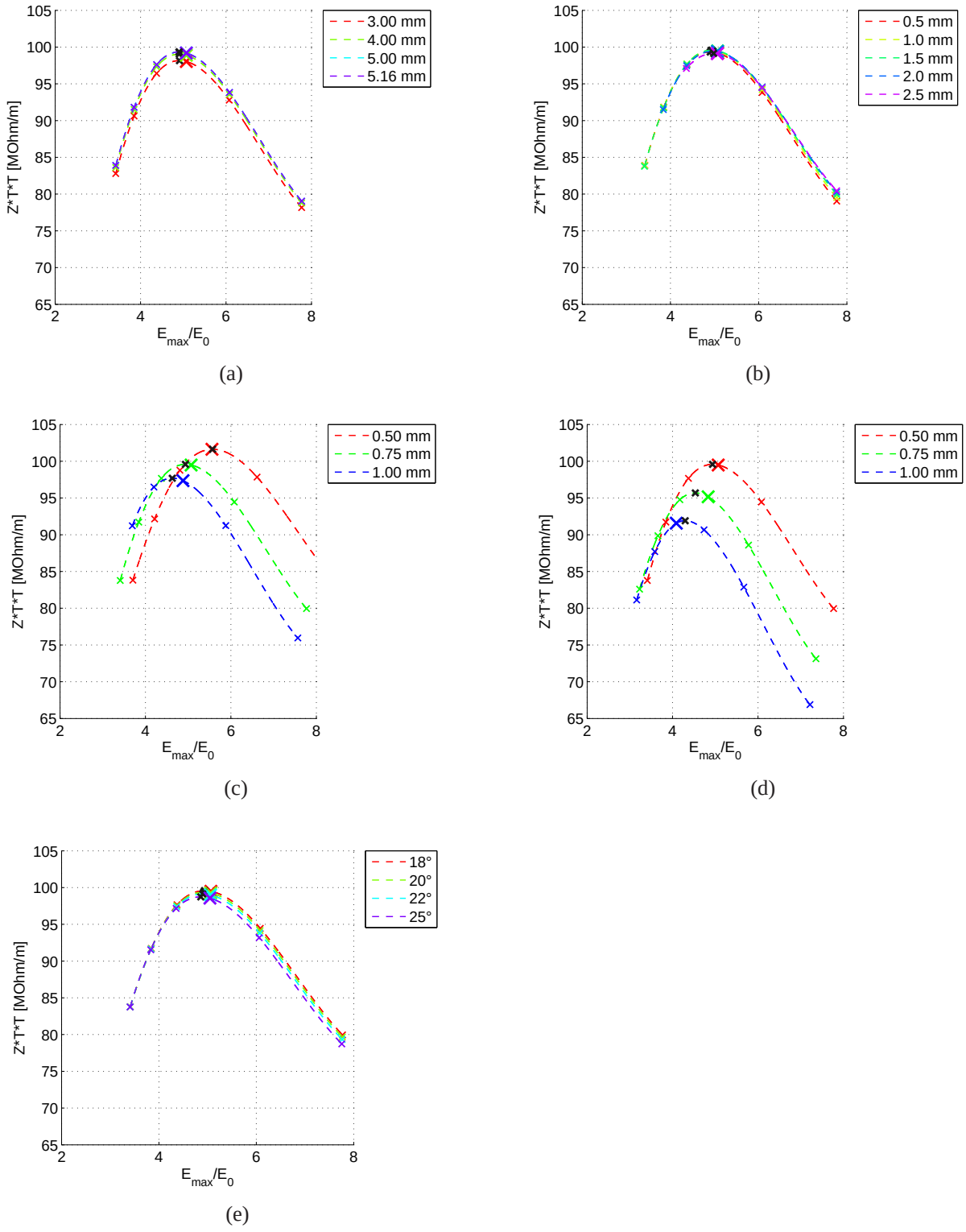

Figure 7.5: *Cells for 150 MeV/u particles. Relation between the effective shunt impedance ZTT and the ratio E_{max}/E_0 for different: a) Outer Corner Radii, b) Inner Corner Radii, c) Outer Nose Radii, d) Inner Nose Radii and e) Cone Angles.*

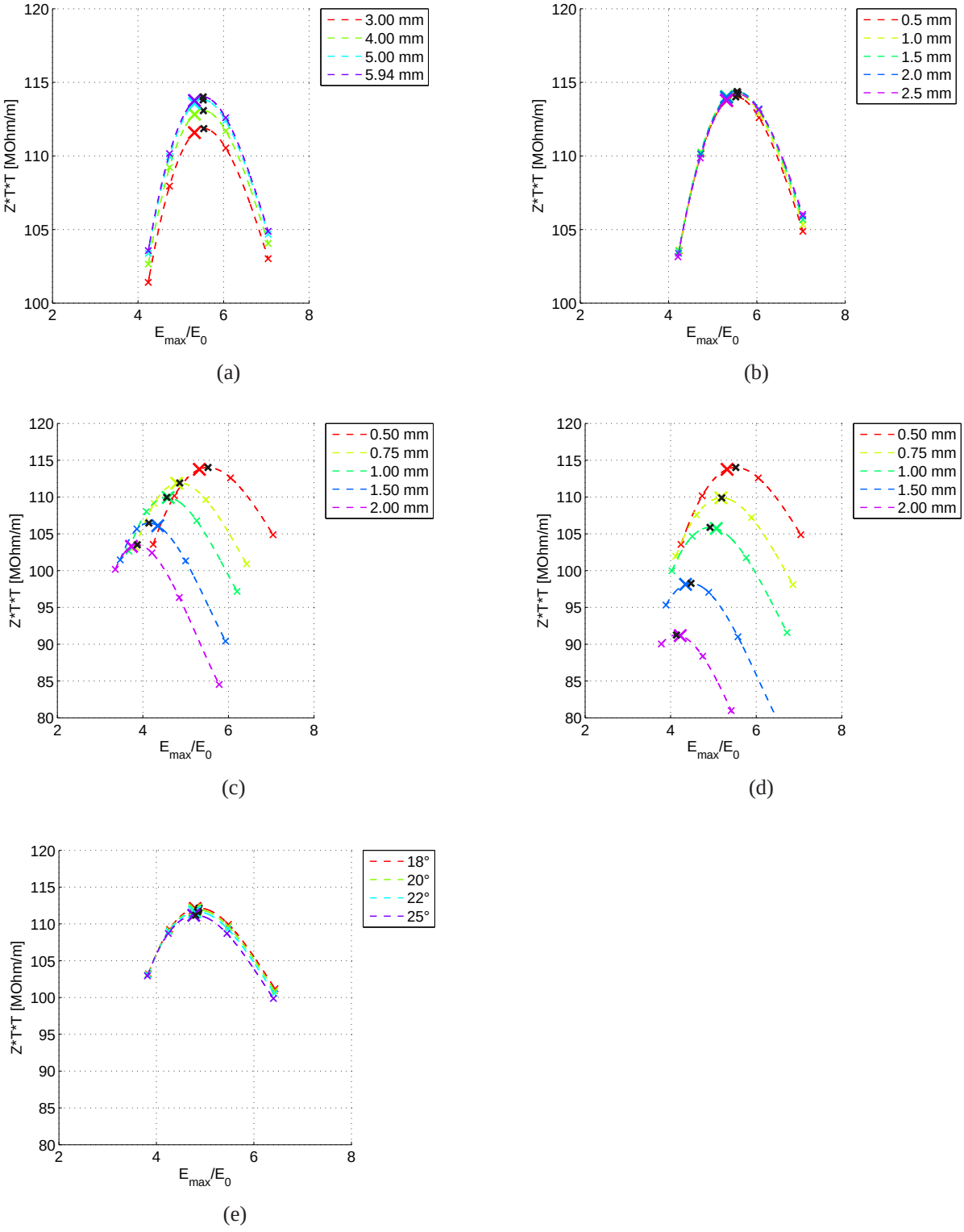

Figure 7.6: *Cells for 200 MeV/u particles. Relation between the effective shunt impedance ZTT and the ratio E_{max}/E_0 for different: a) Outer Corner Radii, b) Inner Corner Radii, c) Outer Nose Radii, d) Inner Nose Radii and e) Cone Angles.*

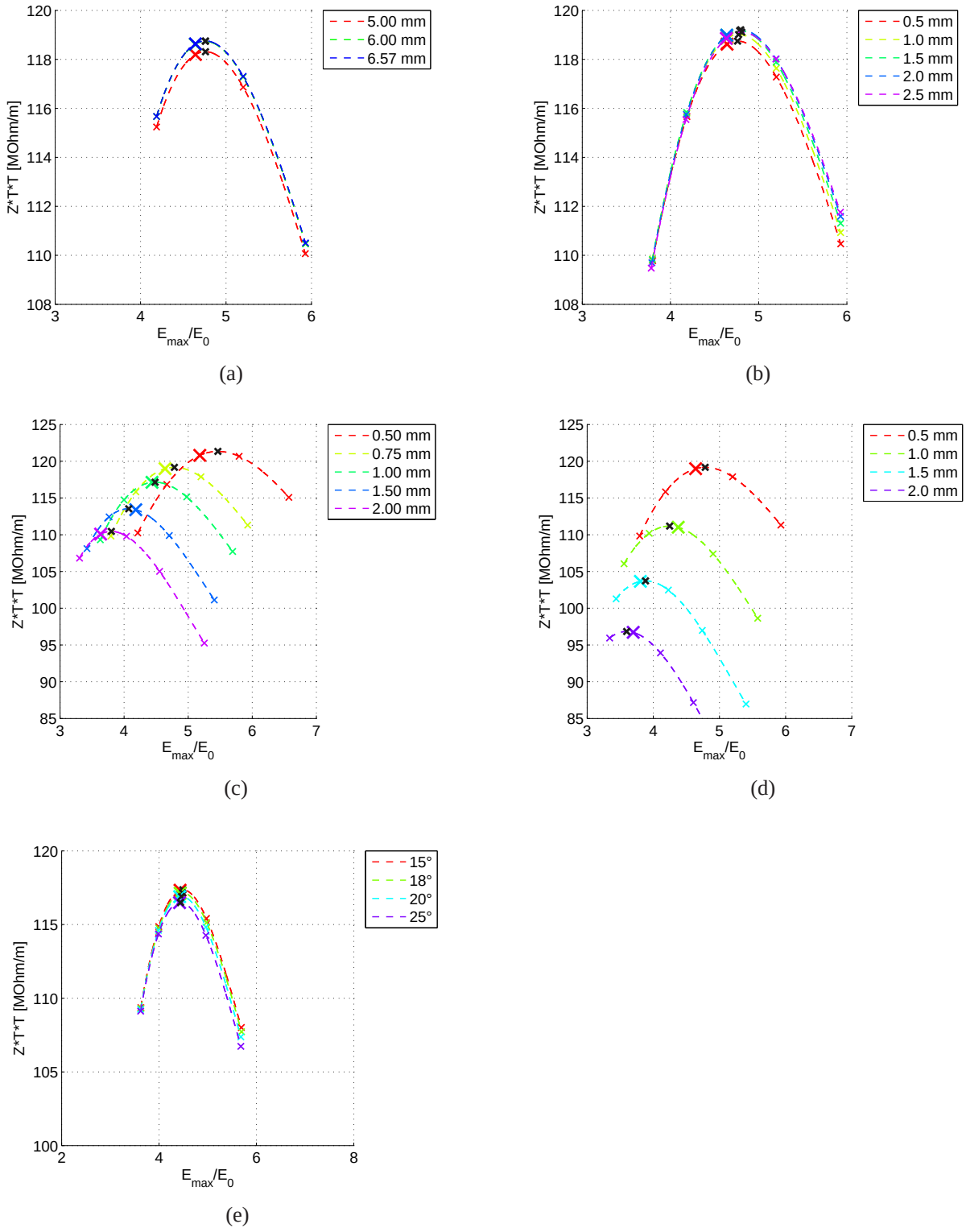

Figure 7.7: *Cells for 250 MeV/u particles. Relation between the effective shunt impedance ZTT and the ratio E_{max}/E_0 for different: a) Outer Corner Radii, b) Inner Corner Radii, c) Outer Nose Radii, d) Inner Nose Radii and e) Cone Angles.*

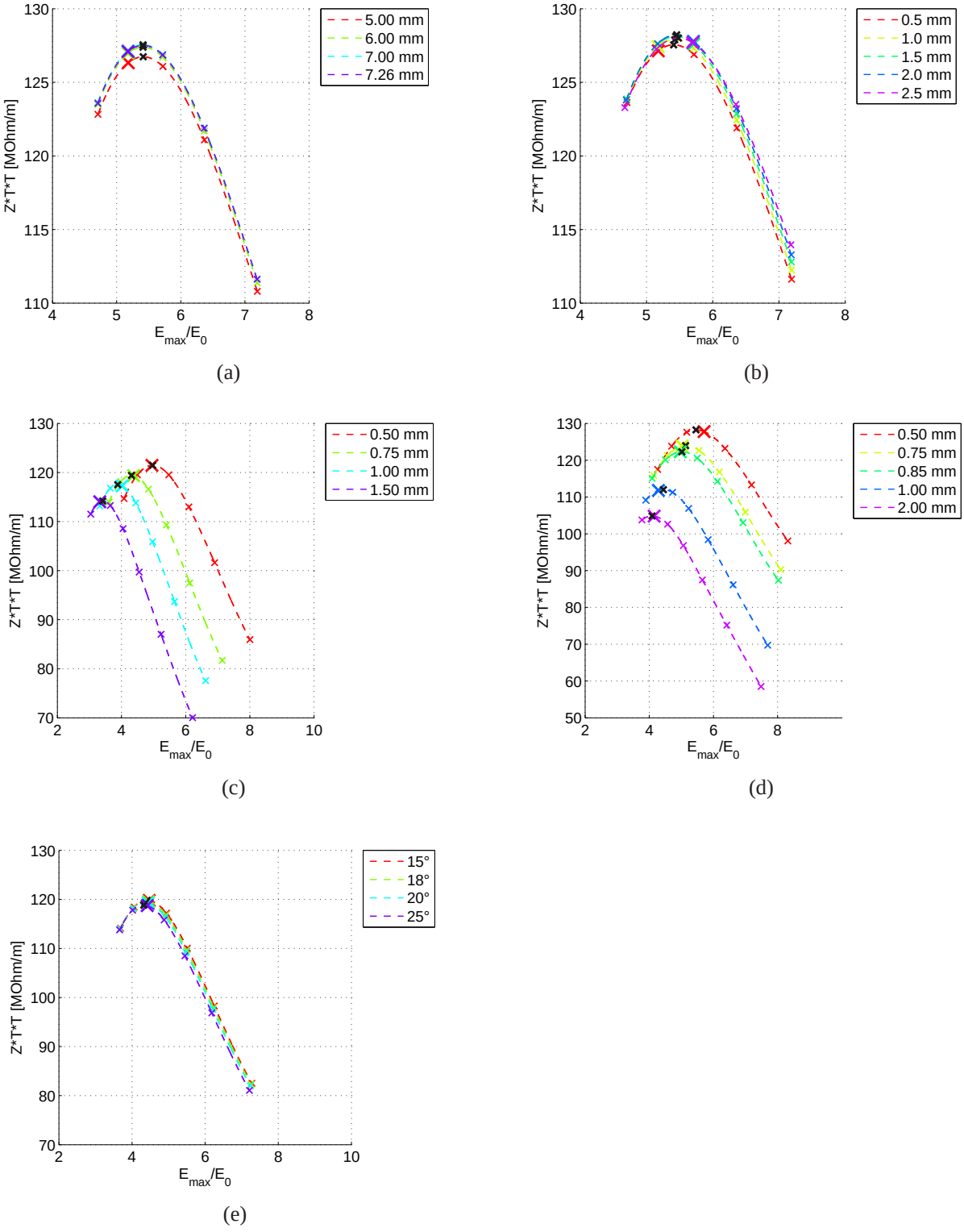

Figure 7.8: *Cells for 325 MeV/u particles. Relation between the effective shunt impedance ZTT and the ratio E_{max}/E_0 for different: a) Outer Corner Radii, b) Inner Corner Radii, c) Outer Nose Radii, d) Inner Nose Radii and e) Cone Angles.*

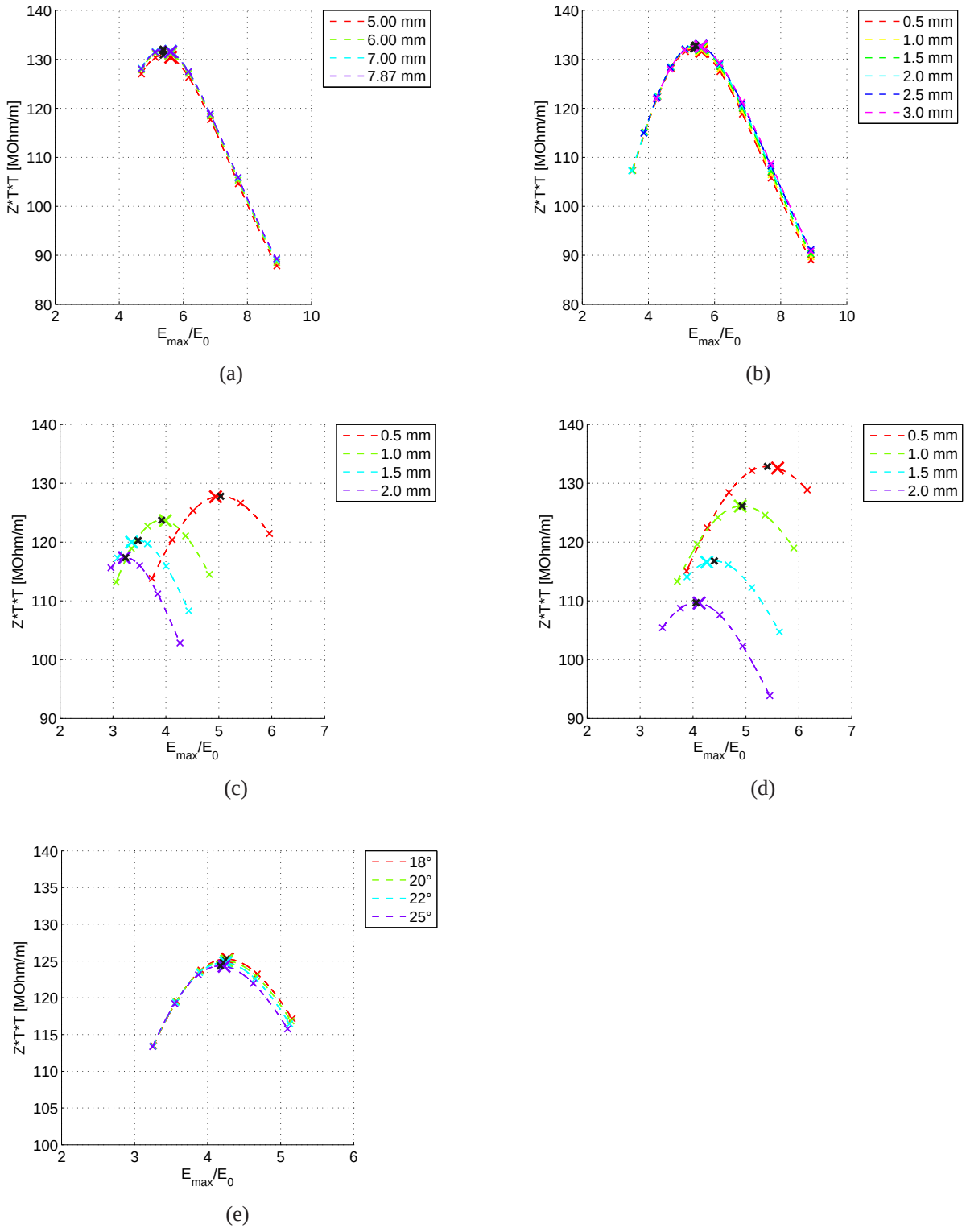

Figure 7.9: *Cells for 400 MeV/u particles. Relation between the effective shunt impedance ZTT and the ratio E_{max}/E_0 for different: a) Outer Corner Radii, b) Inner Corner Radii, c) Outer Nose Radii, d) Inner Nose Radii and e) Cone Angles.*

7.3 Linac Layout

The basic layout of CABOTO consists of an array of SCL cavities, or tanks, grouped in different independently-powered units. All the cells within a tank of CABOTO have the same length for machining simplicity, this length is determined by the mean velocity of the reference particle in its way through the tank. The cell length is consequently not exactly matched to the particle velocity and there is a deviation from synchronicity. This results in a phase slip between the beam (represented by the reference particle) and the RF waveform. The velocity of the reference particle is lower than the design velocity in the first cells of the tank, so that phase increases from cell to cell, while the velocity of the reference particle is higher than the design velocity in the last cells of the tank, and in consequence the phase decreases. The phase slip results in an increase of the energy spread of the beam. The phase slip in a tank is minimum if the reference phase at the entrance of the tank is equal to the reference phase at the exit of the tank [16]. The approximate maximum phase slip $\Delta\phi_{slip}$ through a tank of N_c cells is given by:

$$\Delta\phi_{slip} = \frac{\pi N_c}{8} \frac{\Delta W_{ref}}{\gamma_s^3 \beta_s^2 mc^2} \tag{7.2}$$

where ΔW_{ref} is the total energy gain of the reference particle in the tank, β_s is the design velocity relative to the speed of light and γ_s is its corresponding Lorentz factor. The subdivision of the units that constitute CABOTO in several tanks is addressed to minimize the phase slip along the structure.

The code *DESIGN* [12] was used to define the overall layout of CABOTO. For a given linac layout specified by the user, *DESIGN* calculates the phase for which this condition is satisfied. The phase slip inside the CABOTO tanks is illustrated in Fig. 7.10. The code also provides the phase advances, the zero-current Twiss parameters of the structure and the power required to excite a given electric field in each tank of the linac. This information is collected in two output files. *DESIGN* requires the user to specify the main linac layout (input energy of the beam, charge and mass of particles, number of linac units, number of tanks per unit, number of cells per tank, accelerating gradient in each tank, quadrupole strength and dimensions, desired synchronous phase and variation of Z and T along the linac).

During the design process, a compromise between the number of cells per tank and the accelerating gradient excited in the tank has to be found in order to get a reasonably short linac without consuming too much power. Section 1.1.3 explains why increasing the number of cells is more efficient from the energy consumption point of view than increasing the accelerating gradient for obtaining a given energy gain. However, the phase slip increases with the number of cells, as shown in Eq.(7.2). On the other hand, increasing the accelerating gradient is limited by the appearance of RF breakdowns associated to high electric fields.

The linac was divided in 16 units, each unit consisting of 4 tanks. All the tanks have the same number of cells, 18 cells per tank, to get a smooth transverse phase advance

progression. All the quadrupoles of the FODO structure are 60 mm long and have a strength of 200 T/m. The synchronous phase must be big enough to have big longitudinal acceptance but small enough to provide high effective acceleration $W \,/\, cos\ \phi_S$ with reasonable power and breakdown risk. The optimal synchronous phase is found to be -14 deg. The phase slip reaches a maximum value of 3 degrees for low-energy tanks and a minimum value of 1.5 degree for high-energy tanks. Fig. 7.10(b) shows the synchronous phase variation along the 1152 RF gaps of the linac.

The linac can accelerate carbon ions from the injection energy of 150 up to 410 MeV/u in 24.1 m. The total installed peak RF power is 192 MW, from 16 klystrons delivering 12 MW each. The total RF power used to feed the linac is about 142 MW, as expected power losses in RF circuit were 25% of total klystron power. The mean accelerating gradient decreases smoothly from 33.9 to 32.4 MV/m (from low-energy tanks to high-energy tanks) to keep power below the maximum RF power from klystrons.

Evaluation of the expected high-gradient performance

The expected high-gradient performances of CABOTO RF structures were estimated from the experimental data collected in the high-power tests of the 3 GHz TERA test cavity - similar to the cells of a high-gradient linac for a cyclinac - and the 5.7 GHz Frascati prototype - a traveling-wave structure. Table 7.3 shows the experimental data used to estimate the BDR of the present CABOTO design. The estimation was done assuming that the modified Poynting vector S_C is the electromagnetic quantity that limits high-gradient performance, which would mean that a given modified Poynting vector is related to a certain breakdown rate.

During the high-power test of the 3 GHz TERA cavity, a breakdown rate *smaller than* 3.6×10^{-6} bpp/m (no breakdown detected in about 81 hours of operation at 50 Hz in the 0.0189 m-long test cavity) was measured for operation at a maximum modified Poynting vector $S_{C,max}$ of 0.87 MW/mm^2 with 2.2 μs-long (flat-top) RF pulses. On the other hand, the ratio $\sqrt{S_{C,max}}/E_0$ for the present design of CABOTO is about 0.024 MW/mm^2, so the maximum accelerating gradient in a CABOTO cell is 39 MV/m for a maximum modified Poynting vector of 0.87 MW/mm^2 - same value as for the measurement of the 3 GHz TERA cavity. Therefore, if the modified Poynting vector is the quantity which limits high-gradient performance, then the expected breakdown rate for CABOTO receiving 2.2 μs-long (flat-top) RF pulses and being operated at 39 MV/m accelerating gradient is 3.6×10^{-6} bpp/m, i.e. the value measured in the experiment.

However, CABOTO is designed for operation at 34 MV/m accelerating gradient (at maximum) with 1.5 μs-long (flat-top) RF pulses, so the scaling laws evaluated during the high RF power tests of the 3 GHz TERA cavity were therefore used to estimate the expected breakdown rate for the nominal operation of CABOTO from the lowest field measurement performed during the tests. A power dependence of the breakdown rate *BDR* on the electric field E of about 10 (i.e. BDR $\propto$ E^{10}) was found for measurements performed in the range of $S_{C,max}\epsilon$ [1.88, 2.86] MW/mm^2, and the breakdown

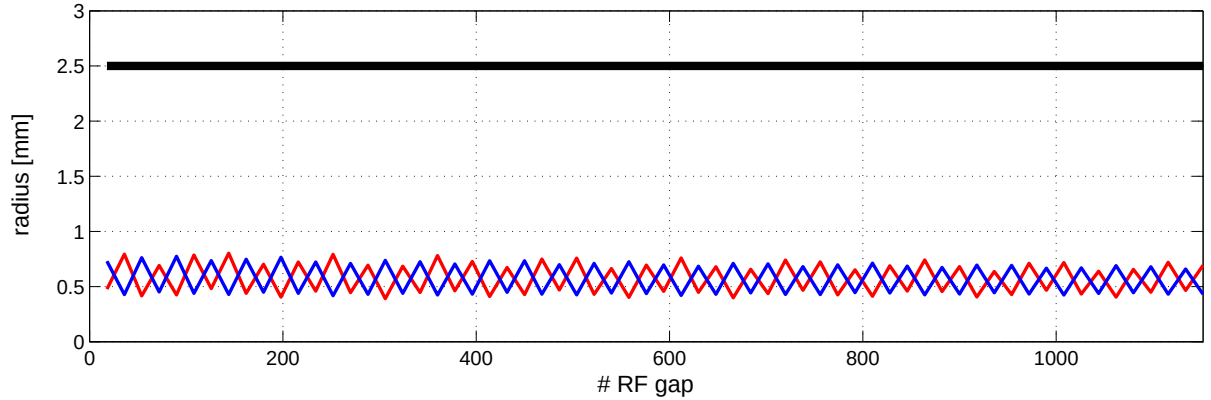

(a) Beam envelope reaching CABOTO acceptance. In black, bore hole radius; in red and blue, rms beam size for both transverse planes.

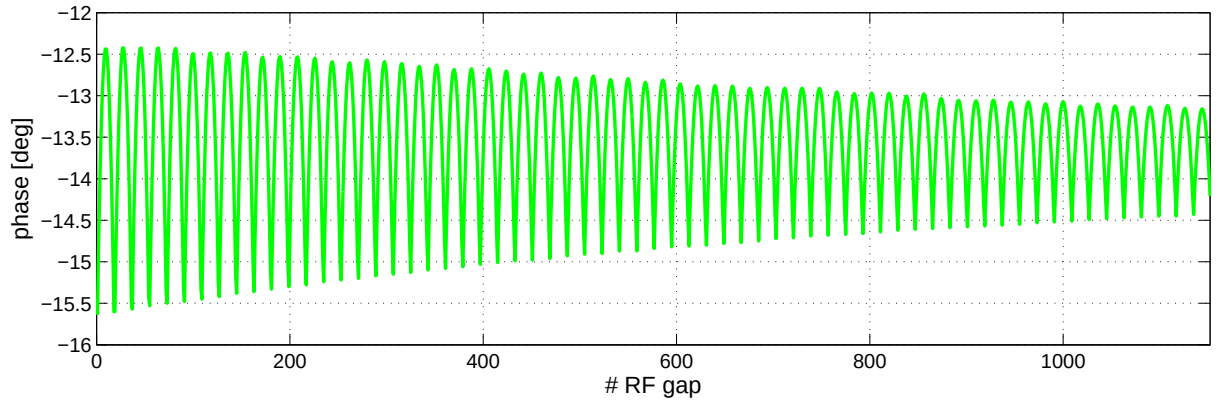

(b) Synchronous phase variation along CABOTO.

Figure 7.10: *Beam dynamics along the 1152 RF gaps (16 units × 4 tanks × 18 cells) of CABOTO.*

rate scaled to the pulse length τ to the 3*rd* power (i.e. BDR $\propto \tau^3$). According to the abovementioned experimental results and the scaling laws, CABOTO would present a BDR around 3×10^{-7} bpp/m for nominal operation, which is an acceptable breakdown rate value, as it corresponds to one breakdown every 8 minutes when operating the 24-meter CABOTO linac at 300 Hz. This BDR would be easily corrected with the multipainting technique.

The hypothesis that the same breakdown rate can be obtained for 3 GHz and 5.7 GHz structures was made in the previous calculations. However, this assumption is pessimistic since the expected limit to high-gradient performance increases with the frequency. The high-gradient performance of CABOTO at the frequency of 5.7 GHz can be estimated from the experimental data of the high-power test of the 5.7 GHz Frascati structure. A breakdown rate of 1.5×10^{-5} bpp/m was measured for operation at a maximum modified Poynting vector $S_{C,max}$ of about 1.67 MW/mm^2 with 0.2 μs pulses. The value of the modified Poynting vector and the pulse length are not in the order of the nominal operation of CABOTO, so that the estimated breakdown rate from this experiment will be just a rough estimation. The expected breakdown rate in CABOTO, operating at 34 MV/m accelerating gradient at maximum with 1.5 μs-long (flat-top) RF pulses from the 5.7 GHz Frascati structure high-power test, would be below 10^{-7} bpp/m, assuming that the scaling law that relates the breakdown rate with the modified Poynting vector and the pulse length is Eq.(1.36). This breakdown rate again satisfies the clinical requirements.

The measurement of the breakdown rate for the 5.7 GHz single-cell cavities presented in chapter 4 for operation in the range of the nominal field of CABOTO will be the next step in this study. The high-power tests will be conducted in 2013 with a modulator and magnetron system lent by ADAM S.A..

The pulsed surface heating is another quantity which must be considered when designing high-gradient performance structures. For CABOTO, the temperature increase due to pulsed surface heating is about 1 degree, which is well below values which can enhance BDR.

7.4 Acceleration of Cyclotron Beam in a High-Frequency Linac

The beam dynamics in CABOTO was studied with the multiparticle simulation code *LINAC* [13, 104]. Space charge effects were not included due to the small beam intensity required for therapy. The input beams were generated with the code *PATH Manager* [14]. The aim of these studies is to check if the beam performances of this CABOTO design - especially final output intensity, energy range and minimum energy step - are appropriate for hadrontherapy.

Beam structure of CABOTO

The present CABOTO design was powered with 2.2 μs-long RF pulses, being 0.7 μs the rise time and 1.5 μs the flat top length, at 300 Hz. Consequently, the duty cycle of CABOTO is about 0.7×10^{-3}. Fig. 7.11 illustrates the beam structure of CABOTO. As the current required for tumour treatment with carbon ions is about 0.1 nA (average intensity), CABOTO has to accelerate about 10^6 carbon ions per RF pulse.

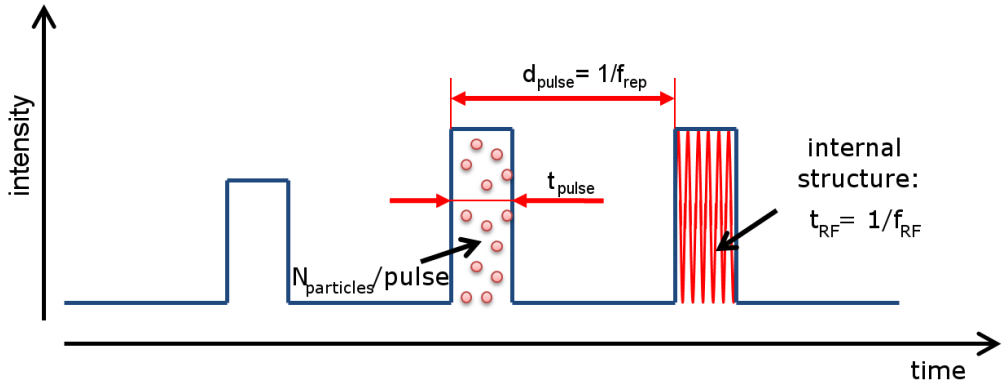

Figure 7.11: *Beam structure of CABOTO.*

Acceptance

Beams with Gaussian distributions were used for the study of the longitudinal and transverse acceptances of CABOTO. Fig. 7.10(a) shows the envelope of a beam that reaches CABOTO acceptance. In the acceptance studies, all the units are switched on and particles are then accepted if their energy is within ±10 MeV of the maximum output energy of CABOTO, 410 MeV/u. Transmission depends little on the beam energy spread dE/E for continuous beams ($\Delta\phi \sim \pm180$ deg), as seen in Fig. 7.12. About 40% of the particles are lost at CABOTO entrance due to transverse acceptance. The transverse acceptance is driven by the choice of using smaller bore holes to reduce energy consumption of the machine.

CABOTO will boost the energy of the carbon ions that have been previously accelerated in a cyclotron. So far there is no cyclotron which delivers carbon ions at 150 MeV/u. SCENT300 is a cyclotron that accelerates carbon ion beams up to 300 MeV/u. To study the beam performances of CABOTO, the carbon ion beam delivered by SCENT300 [106], with normalized emittances (95% of particles) of 2.15 and 4.3 mm mrad in the radial and vertical plane, respectively, was rescaled from 300 MeV/u down to 150 MeV/u. Simulations for the present acceptance study use this rescaled beam. Beam generators like *PATH* cannot generate continuous beams. The code *UniformMaker* [105], which allows to create a continuous beam from any kind of beam

Test	BDR [bpp/m]	$S_{C,max}$ [MW/mm^2]	t_{pulse} [μs]
3 GHz TERA test cavity	3.6×10^{-6}	0.87	2.2 (flat-top length)
5.7 GHz INFN prototype	1.5×10^{-5}	1.67	0.2 (SKIP pulse length)

Table 7.3: *Experimental data collected from high-power tests presented in chapters 3 and 5 and used to evaluate the RF breakdown risk in CABOTO.*

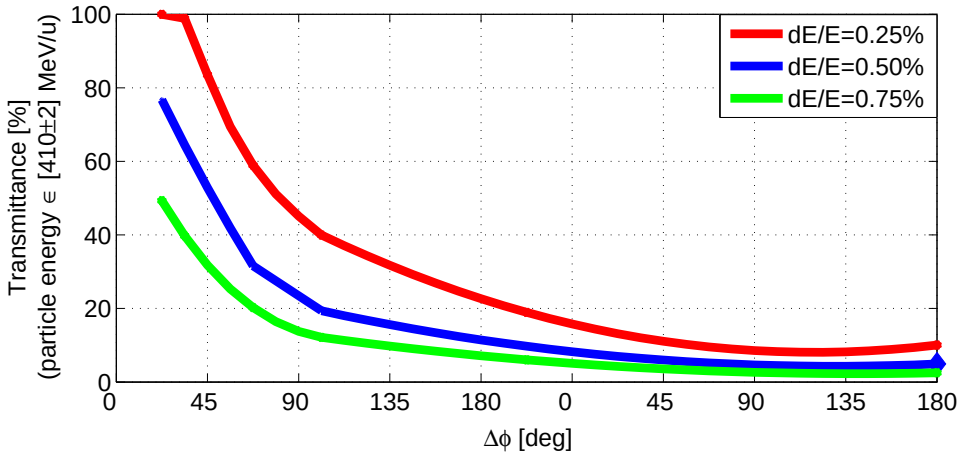

(a) Transmittance of point-like beam for different phase width and energy spread.

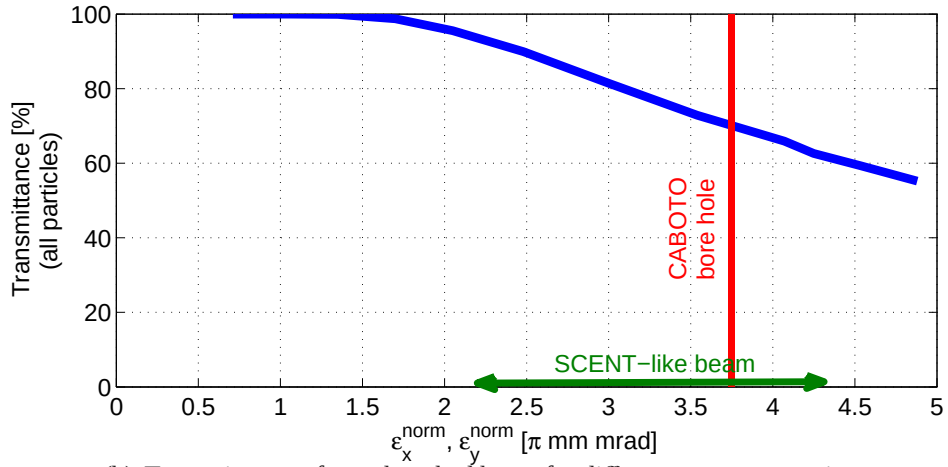

(b) Transmittance of very bunched beam for different transverse emittances.

Figure 7.12: *CABOTO acceptance. N_{good} is the percentage of particles that reach the end of the linac with the appropriate energy. N_{trans} is the percentage of particles that reach the end of the linac, independently of their final kinetic energy, over the initial number of particles. The acceptance defined by the CABOTO bore hole, 3.75 π mm mrad, is represented by the blue solid line. The emittance of the SCENT-like beam is 2.15 π mm mrad for the vertical plane and 4.3 π mm mrad for the horizontal plane.*

distribution, was used in the generation of a realistic input beam for CABOTO. The rescaled SCENT300 beam is shown in Fig. 7.13.

CABOTO has a small longitudinal acceptance for the typical beam delivered by a cyclotron, as it is shown in Fig. 7.13. CABOTO operates at 5.712 GHz while a typical 400 MeV carbon cyclotron pulses at some tenths of MHz. The cyclotron beam is practically continuous compared to the pulsing of the high-frequency linac. In turn, the beam is fragmented and spread over the whole RF bucket, it filamentates. Fig. 7.4 shows the evolution of a "rescaled SCENT-like beam" as it is accelerated in CABOTO. Some particles may get lost as they escape from the RF bucket.

The total transmittance of a cyclotron beam through CABOTO is about 2%. The final efficiency of CABOTO, given by the duty cycle times the total transmittance, in the order of 10^{-5}. Therefore, CABOTO could provide the sufficient current intensity for carbon ion therapy, around 0.1 nanoamperes, if the beam delivered by the cyclotron which serves as the injector to CABOTO had an average current intensity of about 8 microamperes.

Beam Energy Modulation

The layout of CABOTO is specially conceived for actively modulating the energy of the beam. The beam energy can be decreased in steps of about 15-18 MeV/u from the maximum energy of 410 MeV/u by switching-off the RF power of a given number of units. In order to reduce the energy step down to 2 MeV/u (corresponding to a range step of 2 mm in water-equivalent tissue), one can vary the amplitude of the power that feeds the last active unit. The range can be reduced from the maximum range (about 287 mm) in steps of 2 mm by decreasing in steps of 10% the amplitude field in the last active unit. Fig. 7.14 illustrates the beam energy modulation in CABOTO. Fig. 7.15 presents the energy distribution for different energy beams. The beam delivered by CABOTO has a tail which contains all the particles which remain outside the acceleration bucket. These particles will be removed from the beam with a bending magnet and a slit located downstream the linac.

The importance of the energy spread stems from its direct correlation with the precision in the range reached with a certain energy beam. The requested ±0.5 mm in range precision for carbon ion beams establishes that the energy spread should not exceed ±10 MeV for low energies and ±6 MeV for high energies. This criteria was taken into account to compute the transmittance of CABOTO for different beam energies, resulting about 2% of the input beam.

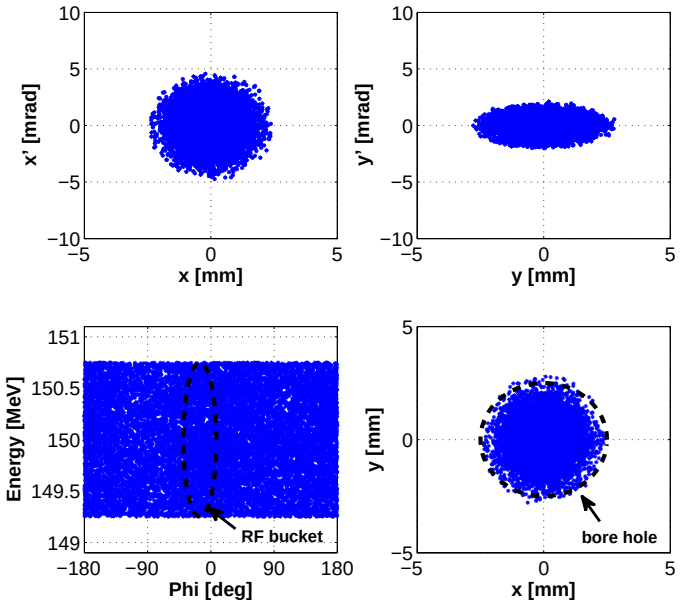

(a) SCENT300-like beam at the entrance of CABOTO; in black, RF bucket and bore hole of CABOTO.

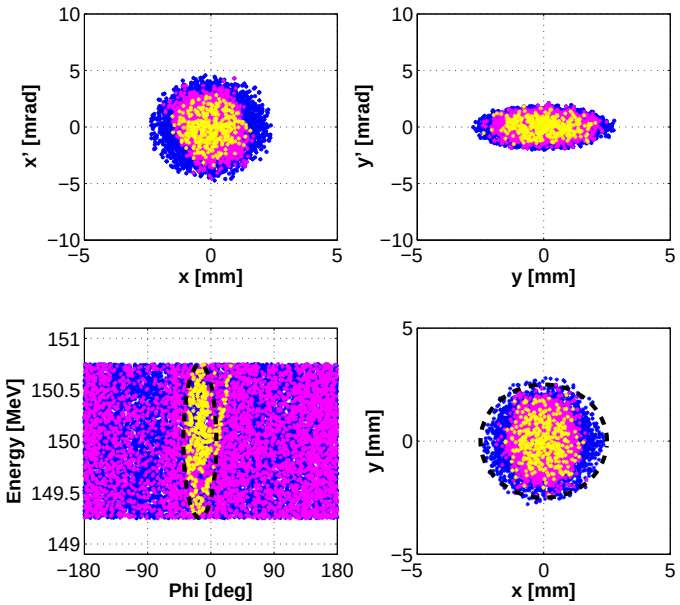

(b) In blue, all beam particles; in pink, particles transmitted through the linac; in yellow, those particles transmitted with the appropriate energy.

Figure 7.13: *Tracking simulation for CABOTO with a SCENT300-like beam.*

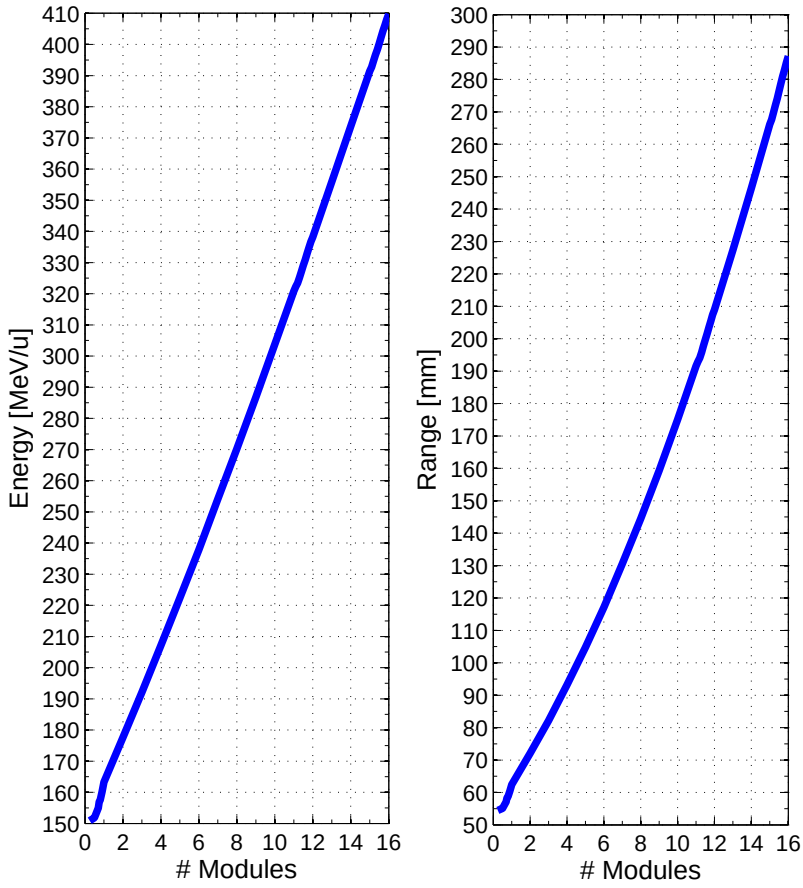

Figure 7.14: *The range in water-equivalent tissue can be varied in steps of about 2 mm (typical voxel size) as results of the small steps in beam output energy possible by switching off the last units of the linac and modulating the power that feeds the last active unit.*

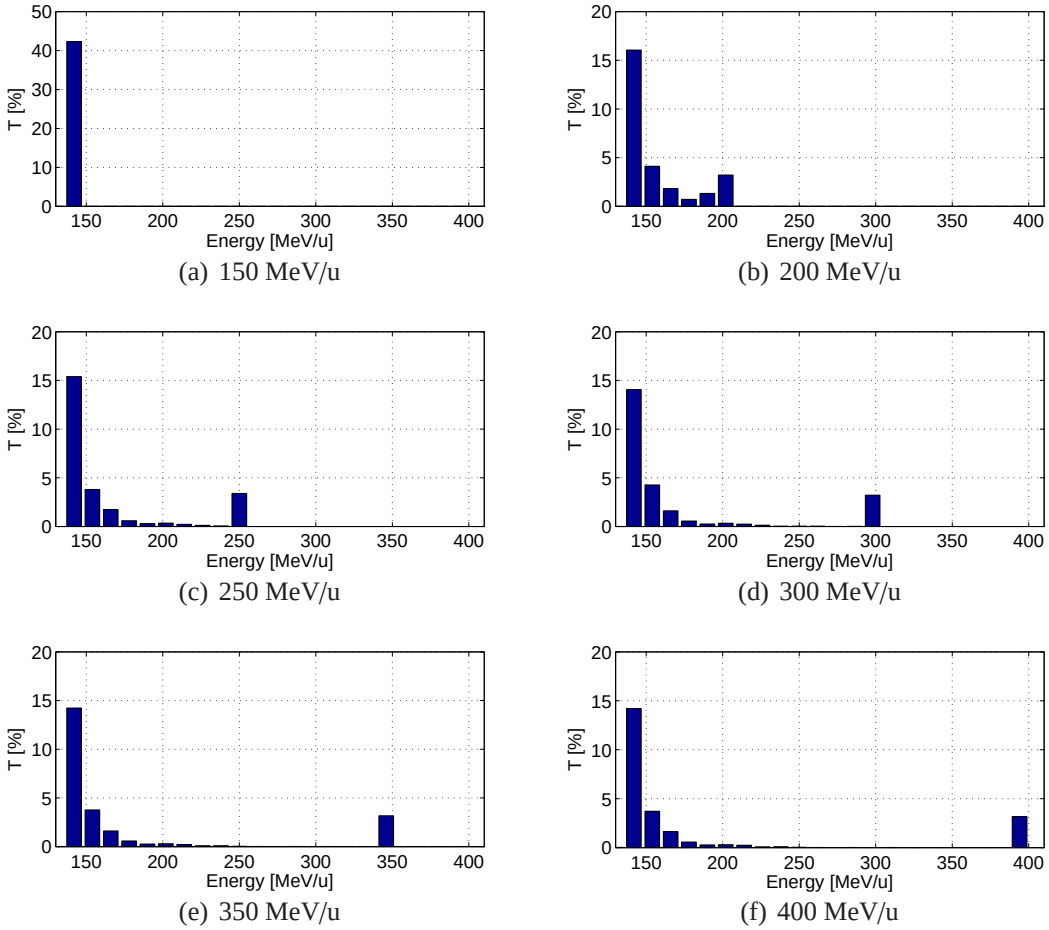

(a) 150 MeV/u (b) 200 MeV/u

(c) 250 MeV/u (d) 300 MeV/u

(e) 350 MeV/u (f) 400 MeV/u

Figure 7.15: *Energy distribution of a beam accelerated by CABOTO to different final energies. The horizontal axes represents the particle energy in MeV/u. The vertical axes is the percentage of particles that have a given energy at the linac exit. A bending magnet and a slit will be used to clean the low energy tail of the beam.*

7.5 Summary and Discussion

In CABOTO, compactness is possible thanks to the use of high gradients (32-34 MV/m) whereas reduced consumption is achieved by optimizing the cell geometry to maximize the effective shunt impedance (100-130 MΩ/m). The results of the high-power tests presented in this thesis show that the breakdown rate expected for the operation of CABOTO at these gradients will result in a linac which fulfills the clinical requirements. The structure operates at 5.712 GHz to reach high accelerating gradients for an acceptable breakdown rate and reduced energy consumption. Fully stripped carbon ions, $^{12}C_6^{+6}$, are accelerated from 150 to 410 MeV/u in 24 m. The particles are first accelerated up to 150 MeV/u in an isochronous cyclotron [102]. The linac requires a total peak power of 192 MW to provide the maximum output beam energy of this cyclinac design, 410 MeV/u, so the total plug power to run CABOTO is about 400 kW (the average power, given by 12 MW $\times$ 16 $\times$ 0.7 $\times 10^{-7}$ = 150 kW, but to produce the RF power one has to divide this by the efficiency of the klystron - about 0.45 - and take into account the low power consumptions, so the final value is corrected by an overall factor equal to 3). The beam energy modulation is possible thanks to the division of the linac in the sufficient number of independently powered units, 16 units in the present design. The output beam energy is then changed by acting on the power that feeds each unit so that the penetration range of the CABOTO beam can vary in steps of 2 mm. The modularity of the machine also allows the installation of the facility in different phases and eases its maintenance. The appropriate beam intensity relies on the choice of the bore hole size and the synchronous phase (both features also affecting energetic efficiency). The beam intensity can be reduced from its maximum value by acting on the ion source. The high repetition rate of CABOTO, 300 Hz, is required to keep the application of multipainting technique within reasonable timings. In addition, a high repatition rate, together with a 3D feedback system, allow treatment of moving organs. The machine reliability and the beam availability are related to the breakdown rate. According to the high-power tests presented in chapter 3 and chapter 5, RF breakdown should not compromise the operation of CABOTO. Table 7.4 contains the main features of the CABOTO design presented in this thesis.

The particular way in which CABOTO modulates the energy has the drawback that a large number of costly 5.7 GHz modulator/klystron systems are required, which increases the capital cost of the facility with respect to 3 GHz proton cyclinacs. However, the promising features of 5.7 GHz high-power technology are resulting in a major interest on this frequency, which could translate in a larger offer of RF power sources and control systems operating at this frequency in a near future.

The design presented in this chapter should be completed with studies on the effect of the energy jitter on the beam performances (the influence of the RF power instabilities on the beam would imply that the input power to the accelerating tanks of each unit was stable within 0.3–0.4%) and on the transport magnetic line and the slit(s) required to selection the particles with the desired energy from the output beam of CABOTO. Particle losses due to the particular beam dynamics of CABOTO may cause lead to

radiation-induced demagnetization of the permanent quadrupoles and premature wear of the first tanks of the linac, the regions where more particles are lost. The acceleration test of a CABOTO tank would provide not only useful information on the damage caused to the permanent magnets but also on the shielding required for the linac.

Table 7.4: *Main features of the CABOTO design.*

CABOTO		
Particles	C^{6+},H_2	
Input energy	150	MeV/u
Output energy	400	MeV/u
Energy step by switching off the linac units	15-18	MeV/u
Number of units and number of klystrons	16	
Total linac length	24.1	m
Accelerating gradient, E_0	32-34	MV/m
Maximum peak surface electric field, E_{max}	153	MV/m
Maximum modified Poynting vector, $S_{C,max}$	0.61	MW/mm^2
Synchronous phase	-14°	
Beam hole diameter	5	mm
Effective shunt impedance, ZTT	100-130	MΩ/m
Energy Consumption		
Duration of high voltage power pulses	2.2	μs
Duty cycle	0.066	%
Peak power per unit (with 25% losses)	12 (9)	MW
Total peak RF power (available with 25% losses)	192 (144)	MW
Wall plug power for the linac	400	kW
Transverse Focusing System		
Number of Permanent Magnetic Quadrupoles (PMQs)	65	
Gradient of the PMQs	200	T/m
Length of the PMQs	60	mm
Beam Performances		
Duration of RF pulse (flat-top)	2.2 (1.5)	μs
Repetition rate	300	Hz
Normalized transverse acceptance at linac entrance	2.79	π mm mrd
Transmittance	2	%

Chapter 8

Summary and Conclusions

The reduced length of linacs which use high-gradient RF structures potentially lowers their cost and makes them very attractive for their application in many different fields, from the free-electron lasers to the accelerators for hadrontherapy. However, the high-gradient performances of RF structures are limited by the RF breakdown phenomena. The studies carried out for the development of the linear colliders CLIC and NLC investigated the high-gradient performances of RF structures operating between 12 and 30 GHz.

The first part of this thesis focuses on the TERA high-gradient program. The first goal was to evaluate the high-gradient performance limitations of RF structures operating between 3 and 5.7 GHz. The preparation and high-power testing of different RF structures operating in such frequencies is presented in chapters 3, 4 and 5. This work allowed to extend the frequency range of the existing experimental data on high-gradient studies performed in the framework of the normal conducting linear colliders.

The second part of the thesis was dedicated to the accelerators for hadrontherapy - a field which could potentially benefit from the use of high-gradient structures thanks to their compactness and efficiency - and in particular, to the high-gradient linac solutions. Chapter 7 presented the design and performances of a compact, efficient, high-gradient linac for hadrontherapy, CABOTO. The expected breakdown rate for CABOTO was estimated from the results of the high-power tests presented in the first part of the thesis.

8.1 Main Contributions

The work conducted for the realization of this thesis has contributed to the field of high-gradient performance RF structures and to the field of accelerators for hadrontherapy.

The experimental data from the high-power tests of the 3 GHz single-cell standing-wave cavity and the 5.7 GHz multi-cell traveling-wave structure were used to 1) evaluate the scaling laws that relate breakdown rate with electric field and pulse length, 2)

study the applicability of the power flow model and the stress model to the description of the high-gradient limit of RF structures, and 3) evaluate the maximum operation level at which other RF structures could work reliably.

The breakdown rate dependency on the electric field was measured for a 3 GHz single-cell standing-wave cavity and a 5.7 GHz multi-cell traveling-wave structure. Breakdowns were identified by the field-emission current burst for the 5.7 GHz structure, and by the increase or reflected RF power in the test of the 3 GHz cavity. The breakdown rate dependency on the pulse length was also evaluated for the 3 GHz cavity.

The high-gradient performances of these test devices were compared - using the modified Poynting vector S_C - to other experimental data for RF structures operating between 12 and 30 GHz. The good agreement among data collected in high-power tests of RF structures operating between 3 and 30 GHz supports the idea that the maximum Poynting vector as a quantity that limits high-gradient performance of RF structures operating in that frequency range. Data also served to evaluate the applicability of the stress model to describe the high-gradient performances of RF structures. The stress model fitted well to the high-power test data of the 3 GHz cavity and the 5.7 GHz structure. However, the applicability of both models, the power flow model and the stress model, should still be evaluated for a larger number of experiments, for both traveling and standing-wave structures, and over a wider range of electric field values.

The main characteristics of RF breakdowns and associated phenomena in a standing-wave cavity similar to the regular CABOTO cells were also described in chapter 3. According to observations from the 3 GHz cavity test, most of RF breakdowns occur when the fields are building-up in the cavity, which also corresponds to the moment when the cavity surface experiences the highest stress (quantified by the dynamic field-enhancement factor $\beta_{FE,dyn}$). This stress triggers the RF breakdown within an RF pulse sent into a standing-wave structure. This observation could be confirmed with the high-power tests of the 5.7 GHz single-cell cavities.

Overall, a key contribution of this thesis to the field of high-gradient performance structure studies is the execution of high-gradient measurements for a new geometry (the 3 GHz cavity) and in a new frequency range (from 3 GHz to 5.7 GHz), for which the design and prototyping of the test devices, as well as the high-power tests, are well documented.

A major contribution was the determination of the maximum operation field at which the 5.7 GHz modules designed for the energy upgrade of the SPARC facility could work reliably (being reliable a breakdown rate below 3×10^{-6} bpp/m. The goal for the accelerating gradient was about 35 MV/m. The high-power test of the 5.7 GHz structure however operated reliably for an accelerating gradient of about 50 MV/m, which means that the linac modules could operate slightly above 35 MV/m reliably, with the subsequent increase of beam energy.

The thesis also provided the design of a compact, efficient, high-gradient linac for hadrontherapy, known as CABOTO. The linac, operating at 5.7 GHz, was designed to accelerate fully stripped carbon ions, $^{12}C^{+6}$, from 150 MeV/u to 410 MeV/m in

about 24 meters, using high accelerating gradients (E_0= 32 - 34 MV/m) which lead to maximum peak surface electric fields E_{max} in the structure between 140 and 170 MV/m. The linac was divided in different sections called units, each one fed by its own klystron, to allow the active modulation of the beam energy. The collection of programs (Superfish, Make_PLot) developed for geometry optimization of CCL cells was used in the cell optimization of the CABOTO design. A total of 192 MW were required to feed the 16 units in which the linac was divided. As the nominal repetition rate of the linac was chosen to be 300 Hz to allow the treatment of moving organs, the total plug power required to run the linac was about 400 kW.

High peak surface electric field values are reached in the CABOTO structure due to the high design accelerating gradients. The reliability of CABOTO was estimated based on data from the high-power tests of the 3 GHz single-cell cavity and the 5.7 GHz structure and assuming that the modified Poynting vector is the quantity that limits the high-gradient performances of RF structures. In addition, the breakdown rate for fields in the operation range of CABOTO was evaluated during the high-power test of the 3 GHz cavity to duplicate real conditions as closely as possible. It was concluded that CABOTO could operate reliably at the nominal accelerating gradient. However, even though the 3 GHz single-cell cavity was designed such that its layout was as close as possible to the regular CABOTO cells and that only electromagnetic quantities such electric field and modified Poynting vector should determine, at last term, the high-gradient performances of an RF structure, there is a substantial difference between the single-cell test cavity and the real cavities, that may lead to some differences in the resulting breakdown rate: the fact that real cavities have multiple cells which are coupled. The evaluation of the breakdown rate from the results of the 5.7 GHz structure presented in chapter 5, one must consider that this structure was a traveling-wave structure, while the current CABOTO design foresees the use of standing-wave structures. Even though just electromagnetic quantities may be the final issue that determines breakdown rate, difficulties in the production of multi-cell structures (during machining, brazing and specially cleaning) and location of coupling slots might increase the breakdown rate measured for them.

8.2 Future Work

The TERA high gradient test program is continuing. The 5.7 GHz single-cell cavities are expected to be high-power tested at the end of 2012, following the pathways drawn up during the high-power test of the 3 GHz single-cell cavity. The tests should show which frequency, 3 GHz or 5.7 GHz, is more suitable in terms of high-gradient performance, machining and manipulation requirements. Once these high-power tests have been concluded, a multi-cell structure will be designed, produced and high-power tested. The frequency of the structure will be chosen according to the performances of the single-cell test cavities. One interesting issue at that stage of the project would be to perform an acceleration test and check how RF breakdowns really affect the beam.

For CABOTO, the final beam intensity was calculated assuming that the cyclotron which serves as the injector delivers a beam of 8 microamperes. However a measurement of the typical beam performances of a cyclotron delivering carbon ions of about 150 MeV/u has not yet been made, so that the total transmission of CABOTO can not yet be accurately calculated. Another open question is how long the permanent magnets used in CABOTO - and more specially those in the first tanks of the linac, where the beam losses are larger - can resist the constant irradiation coming from particles lost in the linac.

The typical linac for a hadrontherapy cyclinac has always been a side-coupled linac (standing-wave structure). However, other options such as travelling-wave structures are being investigated by the TERA project in collaboration with the CLIC-RF structure development group at CERN.

Bibliography

[1] T. Higo, Y. Higashi, S. Matsumoto, K. Yokoyama, S. Doebert, A. Grudiev, G. Riddone, W. Wuensch, R. Zennaro, C. Adolphsen, V. Dolgashev, A. Jensen, L. Laurent, S.G. Tantawi, F. Wang, J.W. Wang, *Advances in X-Band TW Accelerator Structures Operating in the 100 MV/m Regime*. Proceedings of the International Particle Accelerator Conference - IPAC 2010, Kyoto (Japan, 2010).

[2] U.Amaldi, P. Berra, K. Crandall, D. Toet, M. Weiss, R. Zennaro, E. Rosso, B. Szeless, M. Vretenar, C. Cicardi, C. De Martinis, D. Giove, D. Davino, M.R. Masullo and V. Vaccaro, *LIBO - A Linac-Booster for Protontherapy: Construction and Tests of a Prototype*. Nucl. Instr. and Meth. A, vol. 521, pp. 512-529 (2004).

[3] A. Grudiev, S. Calatroni and W. Wuensch, *A New Local Field Quantity Describing the High Gradient Limit of Accelerating Structures*. Phys. Rev. ST Accel. Beams 12, 102001 (2009).

[4] K. Nordlund and F. Djurabekova, *Defect Model for the Dependence of Breakdown Rate on External Electric Fields*. Physical Review Special Topics - Accelerators and Beams 15, 071002 (2012).

[5] A. Degiovanni, private communication (2009).

[6] A. Degiovanni, private communication (2010).

[7] *Poisson Superfish* website: http://laacg1.lanl.gov/laacg/

[8] *HFSS* website: http://www.ansys.com/Products/Simulation+Technology/

[9] D. Alesini, R. Boni, G. Di Pirro, R. Di Raddo, M. Ferrario, A. Gallo, V. Lollo, F. Marcellini, L. Palumbo, V. Spizzo, A. Enomoto, T. Higo, K. Kakihara, T. Kamitani, S. Matsumoto, T. Sugimura, K. Yokoyama and S. Verdú-Andrés, *High gradient test of a C-band accelerating structure prototype for energy upgrade of Frascati photoinjector SPARC*. Technical Report SPARC-RF-11/05 and KEK Report 2011-6 (2011).

[10] D. Alesini, M. Ferrario, V. Lollo, R. Di Raddo, V. Spizzo and L. Palumbo, *Design, Realization and Low Power RF Tests of the C-Band Structure Prototype for SPARC*, TIARA-NOTE-WP8-2011-002 (2011).

[11] ADAM S.A. website: http://adam-geneva.com/

[12] K. Crandall, private communication (2006).

[13] K. Crandall, private communication (2006).

[14] A. Perrin, J-F. Amand, T. Mutze, *Travel v4.07 User Manual* (CERN, 2006).

[15] PARticle Training Network for European Radiotherapy: http://partner.web.cern.ch/

[16] T. P. Wangler, *Principles of* RF *Linear Accelerators*. John Wiley & Sons, Inc. (2008).

[17] H. Wiedemann, *Particle Accelerator Physics. Basic Principles and Linear Beam Dynamics*. Springer-Verlag (1993).

[18] E. Jensen, *Cavity Basics*. Proceedings of the CAS - CERN Accelerator School: RF for Accelerators, CERN-2011-007 (2011).

[19] P. Tenenbaum, *Fields in Waveguides - a Guide for Pedestrians*, Course Material of the US Particle Accelerator School - USPAS (2003): http://www.desy.de/~njwalker/uspas/coursemat/notes/unit_2_notes.pdf

[20] G. Dugan, *Introduction to Accelerator Physics*, Course Material of the US Particle Accelerator School - USPAS (2002): http://www.lns.cornell.edu/~dugan/USPAS/

[21] A. Streun, *Experimental Methods of Particle Physics: Particle Accelerators*, online course: http://people.web.psi.ch/streun/empp/

[22] R.H. Miller, *Comparison of Standing-Wave and. Traveling-Wave Linacs*, SLAC-PUB-3935 (1986).

[23] J. LeDuff, *Dynamics in Linear Accelerators*, Proceedings of the CAS - CERN Accelerator School: General Accelerator Physics, CERN-85-19 (1985).

[24] W. A. Barletta, *Standing Wave Linacs*, Course Material of the US Particle Accelerator School - USPAS (2012): http://uspas.fnal.gov/materials/12MSU/MSU_Fund.shtml

[25] W. A. Barletta, *Traveling Wave Linacs*, Course Material of the US Particle Accelerator School - USPAS (2012): http://uspas.fnal.gov/materials/12MSU/MSU_Fund.shtml

[26] F. Djurabekova, J. Samela, H. Timkó, K. Nordlund, S. Calatroni, M. Taborelli and W. Wuensch, *Crater Formation by Single Ions, Cluster Ions and Ion "Showers"*, Nucl. Instr. and Meth. B (2011), Vol. 272, pp. 374376.

[27] W.D.Kilpatrick, *Criterion for Vacuum Sparking Designed to Include Both RF and DC*, The Review of Scientific Instruments, VCRL-2321 (1957).

[28] E. E. Wisniewski, W. Gai, J. Power, Y. Du, J. Hua, L. Yan, Y. You, H. Chen, W. Huang, C. Tang, A. Grudiev and W. Wuensch, *Schottky-enabled Photoemission ans Dark Current Measurements - Toward an Alternate Approach to Fowler-Nordheim Plot Analysis*, Proceedings of the International Particle Accelerator Conference - IPAC 2012, New Orleans (EEUU, 2012).

[29] J.W. Wang and G.A. Loew, *Field Emission and RF Breakdown in High-Gradient Room-Temperature Linac Structures*. SLAC-PUB-7684 (1997).

[30] J. Kovermann, *Comparative Studies of High-Gradient RF and DC Breakdowns*. PhD Thesis, Aachen University (Germany, 2010): http://darwin.bth.rwth-aachen.de/opus3/volltexte/2011/3460/pdf/3460.pdf

[31] H. Timkó, *Modelling vacuum arcs : from plasma initiation to surface interactions* PhD Thesis, University of Helsinki (Finland, 2011): http://urn.fi/URN:ISBN:978-952-10-7075-4

[32] D.P. Pritzkau, *RF Pulsed Heating*, SLAC-Report-577, PhD Thesis, Stanford University (EEUU, 2001).

[33] V. Dolgashev, S. Tantawi, Y. Higashi, and B. Spataro, *Geometric dependence of radio-frequency breakdown in normal conducting accelerating structures*. Appl. Phys. Lett. 97, 171501 (2010).

[34] A. Grudiev, *Pulsed surface heating in TD18 tested at SLAC*. Talk at CERN in Indico.

[35] I. Wilson, *Surface Heating of the CLIC Main Linac Structure*, CLIC Note 52 (1987).

[36] CLIC Project website: http://clic-study.web.cern.ch/clic-study/

[37] Next Linear Collider (NLC) web site: http://www-project.slac.stanford.edu/lc/nlc

[38] *A Multi-TeV linear collider based on CLIC technology*. CLIC Conceptual Design Report edited by M. Aicheler, P. Burrows, M. Draper, T. Garvey, P. Lebrun, K. Peach, N. Phinney, H. Schmickler, D. Schulte and N. Toge (CERN, 2012): http://project-clic-cdr.web.cern.ch/project-CLIC-CDR/

[39] J. W. Wang, J. R. Lewandowski, J. W. Van Pelt, C. Yoneda, G. Riddone, D. Gudkov, T. Higo, T. Takatomi, *Fabrication Technologies of the High Gradient Accelerator Structures at 100 MV/m Range*. Proceedings of the International Particle Accelerator Conference - IPAC 2010, Kyoto (Japan, 2010).

[40] ATLAS Collaboration, *Observation of a new particle in the search for the Standard Model Higgs boson with the ATLAS detector at the LHC*, Phys. Lett. B 716 (2012) 1-29.

[41] CMS Collaboration, *Observation of a new boson at a mass of 125 GeV with the CMS experiment at the LHC*, Phys. Lett. B 716 (2012) 30-61.

[42] H. Winick, *Fourth Generation Light Sources*. Proceedings of the Particle Accelerator Conference - PAC 1997, Vancouver (2007).

[43] Linac Coherent Light Source (LCLS) web site: lcls.slac.stanford.edu/

[44] Spring8 Angstrom Compact free electron LAser (SACLA) web site: http://xfel.riken.jp/eng/index.html

[45] Free Electron Laser for Multidisciplinary Investigations (FERMI) web site: http://www.elettra.trieste.it/lightsources/fermi/fermi.html

[46] European XFEL web site: http://www.xfel.eu/

[47] SwissFEL web site: http://www.psi.ch/swissfel/

[48] Extreme Light Insfrastructure (ELI) web site: www.eli-np.ro/

[49] F. V. Hartemann, F. Albert, G. G. Anderson, S. G. Anderson, A. J. Bayramian, S. M. Betts, T. S. Chu, R. R. Cross, C. A. Ebbers, S. E. Fisher, D. J. Gibson, A. S. Ladran, R. A. Marsh, M. J. Messerly, K. L. ONeill, V. A. Semenov, M. Y. Shverdin, C. W. Siders, D. P. McNabb, C. P. J. Barty, A.E. Vlieks, E. N. Jongewaard, S. G. Tantawi and T. O. Raubenheimer, *Overview of Mono-energetic Gamma Ray Sources & Applications*. SLAC-PUB-15112 (2012).

[50] A. Grudiev, D. Schulte and W. Wuensch, *Optimum Frequency and Gradient for the CLIC Main Linac.* Proceedings of the European Particle Accelerator Conference - EPAC 2006, Edinburgh (Scotland, 2006).

[51] H. Braun et al., *CLIC 2008 Parameters*, CLIC Study Group Collaboration, CERN-OPEN-2008-021, CLIC-Note-764 (2008).

[52] W. Wuensch, *High-Gradient Breakdown in Normal-Conducting RF Cavities*, CERN-PS-2002-028-RF, Proceedings of the European Particle Accelerator Conference - EPAC 2002, Paris (France, 2002).

[53] *Matlab* website: http://www.mathworks.com/products/matlab/

[54] S. Verdú-Andrés, *Reducing the Power Consumption of a Carbon Ion Linac for Hadrontherapy*. Master Thesis, Universitat de València (Spain, 2009).

[55] A. Degiovanni, *High Frequency Linac for Carbon Ions Hadrontherapy*. Master Thesis, Università degli Studi di Milano (Italy, 2009).

[56] S. Verdú-Andrés, *First Feasibility Study of a High-Frequency Linac for Carbon Ion Therapy*. Second PARTNER deliverable of WP25 for the European Union under grant agreement number 215840-2 within the Seventh Framework Programme [FP7/2007-2013], Geneva, (Switzerland, 2010).

[57] U. Amaldi, R. Bonomi, S. Braccini, M. Crescenti, A. Degiovanni, M. Garlasché, A. Garonna, G. Magrin, C. Mellace, P. Pearce, G. Pittà, P. Puggioni, E. Rosso, S. Verdú-Andrés, R. Wegner, M. Weiss and R. Zennaro, *Accelerators for Hadrontherapy: From Lawrence Cyclotrons to Linacs*. Nucl. Instr. and Meth. A, vol. 620, pp. 563-577 (2010).

[58] P. Balleyguier, *External Q Studies for APT SC-Cavity Couplers*. Proceedings of the LINear Accelerator Conference - LINAC 1998, Chicago (EEUU, 1998).

[59] R. Bonomi, *Thermo-Structural Study and Experimental Analysis of Accelerating Structures for Hadrontherapy Linacs*. Doctoral Thesis, Università (Italy, 2011).

[60] R. Wegner, private communication (2009).

[61] VECA website: http://www.veca.it/

[62] Bodycote website: http://www.bodycote.com/

[63] M. Garlasché, *Report on the Production of the S-Band prototype in the frame of the High Gradient Test* . TERA Internal Note (2011).

[64] *OASIS* website: http://project-oasis.web.cern.ch/project-oasis/

[65] W. Farabolini, F. Peauger, J. Barranco, S. Bettoni, B. Constance, R. Corsini, M. Csatari, S. Doebert, A. Dubrovskiy, T. Persson, G. Riddone, P. K. Skowronski, F. Tecker, D. Gudkov, A. Solodko, M. Jacewicz, T. Muranaka, A. Palaia, R. Ruber and V. Ziemann, *Two Beam Test Stand Experiments in the CLEX CTF3 Facility*. Proceedings of the International Particle Accelerator Conference - IPAC 2011, San Sebastián (Spain, 2011).

[66] M. Aicheler, private communication (2012).

[67] P. B. Wilson, *A Theory for the RF Surface Field for Various Metals at the Destructive Breakdown Limit*. SLACPUB12354 (2007).

[68] Comeb website: http://www.comebsrl.it/

[69] G. Campogiani, Degree Thesis, University of Rome La Sapienza (Italy, 2011).

[70] T. Sugimura, T. Kamitani, K. Yokoyama, K. Kakihara, M. Ikeda and S. Ohsawa, *SKIP - A Pulse Compressorfor SuperKEKB*. Proceedings of the LINear Accelerator Conference 2004, Lbeck, (Germany, 2004).

[71] T. Inagaki, K. Shirasawa, T. Sakurai, C. Kondo, T. Ohshima, Y. Otake, and T. Shintake, *Operation Status of C-Band High-Gradient Accelerator for XFEL/SPring-8 (SACLA)*. Proceedings of the International Particle Accelerator Conference - IPAC 2011, San Sebastián (Spain, 2011).

[72] Globocan2008 (2010); globocan.iarc.fr/

[73] U. Amaldi, *Accelerators for Hadron Therapy*. EuCARD Newsletters, Issue 3, Article 4 (Physics for Health in Europe Workshop, 2-4 February 2010).

[74] O. Jakel, *Ion species beyond protons and carbon ions*. Talk in the European Society for Therapeutic Radiology and Oncology - ESTRO 31, Barcelona (Spain, 2012).

[75] A. Brahme, *Recent Advances in Light Ion Radiation Therapy*. Int. J. Radiat. Oncol. Biol. Phys. 58(2), 603-16 (2004).

[76] U. Amaldi, S. Braccini and P. Puggioni, *High Frequency Linacs for Hadrontherapy*. Review of Accelerator Science and Technology - RAST, Vol. II, World Scientific (2009).

[77] J. Flanz, *Beam Delivery Systems: Scattering, Scanning w/wo Gantries*. Talk in workshop on "Hadron Beam Therapy of Cancer", Erice (Italy, 2009): http://erice2009.na.infn.it/TalkContributions/Flanz1.pdf

[78] G. Coutrakon and J.M. Slater, *Design Considerations for Medical Proton Accelerators*. Proceedings of the Particle Accelerator Conference - PAC 1999, New York (EEUU, 1999).

[79] S. Peggs, T. Satogata and J. Flanz, *A Survey of Hadron Therapy Accelerator Technologies*. Proceedings of the Particle Accelerator Conference - PAC 2007, Albuquerque, New Mexico (EEUU, 2007).

[80] R. Orecchia, *Health Economic Aspects*. Lecture in PARTNER course on "Hadrontherapy: Today and Tomorrow", CERN, Geneva (Switzerland, 2010): http://indico.cern.ch/contributionDisplay.py?contribId=22&confId=84152

[81] K. Peach, J. Cobb, S. Sheehy, H. Witte, T. Yokoi, R. Fenning, A. Khan, R. Seviour, C. Johnstone, B. Jones, B. Vojnovic, M. Aslaninejad, M. Easton, J. Pasternak, J.K. Pozimski, N. Bliss, C.D. Beard, P. McInstosh, S.L. Smith, S.I. Tzenov, T.R. Edgecock, J. Rochford, D. Kelliher, S. Machida, C. Rogers, R.J. Barlow, H. Owen and S. Tygier Robert, *PAMELA Overview: Design Goals and Principles*. Proceedings of the Particle Accelerator Conference PAC 2009, Vancouver (Canada, 2009).

[82] W. Wieszczycka and W.H. Scharf, *Proton Radiotherapy Accelerators*, World Scientific Publishing Co. (2001).

[83] K. Peach, *Novel Technologies in Radiation Therapy*. Talk in workshop on "Physics for Health in Europe", CERN, Geneva (Switzerland, 2010): http://indico.cern.ch/

[84] M. Goitein, *Proton Medical Facilities: what next?*. Proceedings of Particle Therapy Co-Operative Group PTCOG39, San Francisco (EEUU, 2003).

[85] U. Linz, *Ion Beam Facilities from a Medical Perspective*. Talk in workshop on "Hadron Beam Therapy of Cancer", Erice (Italy, 2009): http://erice2009.na.infn.it/TalkContributions/Linz.pdf

[86] A.R. Smith, *Vision 20/20: Proton Therapy*. Med. Phys., vol.36, issue 2, pp. 556-568 (2009).

[87] Particle Therapy Co-Operative Group (PTCOG) web site: http://ptcog.web.psi.ch/

[88] U. Weinrich, *Gantry Design for Proton and Carbon Hadrontherapy Facilities*. Proceedings of the European Particle Accelerator Conference - EPAC 2006, Edinburgh (Scotland, 2006)

[89] Heidelberg Ion-beam Therapy center (HIT) website: http://www.klinikum.uni-heidelberg.de/First-heavy-ion-gantry

[90] S. Verdú-Andrés, *Comparison of RF Linacs and FFAGs for Hadrontherapy*. Third PARTNER deliverable of WP25 for the European Union under grant agreement number 215840-2 within the Seventh Framework Programme [FP7/2007-2013], Geneva, Switzerland (2011).

[91] Y. Mori, A. Takagi and K. Koba, *Multibeam Acceleration in FFAG Synchrotron*. Proceedings of the Particle Accelerator Conference - PAC 2001, Chicago (EEUU, 2001).

[92] S. Machida, R. Barlow, J. S. Berg, N. Bliss, R. K. Buckley, J. A. Clarke, M. K. Craddock, R. D'Arcy, R. Edgecock, J.M. Garland, Y. Giboudot, P. Goudket, S.

Griffiths, C. Hill, S. F. Hill, K. M. Hock, D. J. Holder, M. G. Ibison, F. Jackson, S.P. Jamison, C. Johnstone, J.K. Jones, L.B. Jones, A. Kalinin, E. Keil, D.J. Kelliher, I.W. Kirkman, S. Koscielniak, K. Marinov, N. Marks, B. Martlew, P.A. McIntosh, J.W. McKenzie, F. Méot, K.J. Middleman, A. Moss, B.D. Muratori, J. Orrett, H.L. Owen, J. Pasternak, K.J. Peach, M.W. Poole, Y. N. Rao, Y. Saveliev, D.J. Scott, S.L. Sheehy, B. J. A. Shepherd, R. Smith, S.L. Smith, D. Trbojevic, S. Tzenov, T. Weston, A. Wheelhouse, P. H. Williams, A. Wolski and T. Yokoi, *Acceleration in the linear non-scaling fixed-field alternating-gradient accelerator EMMA*. Nature Physics 8, 243247 (2012): doi:10.1038/nphys2179

[93] S. Sheehy, *Compact FFAGs & The PAMELA project*. Talk for the IoP Compact Accelerators Meeting (2012).

[94] D. Trobojevic, *NS-FFAG gantries*. Talk for 2nd Workshop on Hadron Beam Therapy of Cancer - Erice 2011.

[95] V.G. Vaccaro, C. De Martinis, D. Giove, M.R. Masullo, S.J. Mathot, A.C. Raino, R.J. Rush and V. Variale, *Design, Construction and Low Power RF Tests of the First Module of the ACLIP Linac*. Proceedings of the European Particle Accelerators Conference - EPAC 2008, Genoa (Italy, 2008).

[96] V. G. Vaccaro, M. R. Masullo, C. De Martinis, L. Gini, D. Giove, A. Rainó, V. Variale, L. Calabretta, A. Rovelli, S. Barone and S. Lanzone, *A Side Coupled Proton Linac Module 30-35 MeV: First Acceleration Tests*. Proceedings of the LINear Acelerator Conference LINAC 2010, Tsukuba (Japan, 2010).

[97] L. Picardi, S. Frulliani and C. Ronsivalle, *TOP-IMPLART Schema Progettuale* (Italy, 2009).

[98] A. Garonna, U. Amaldi, R. Bonomi, D. Campo, A. Degiovanni, M. Garlasché, I. Mondino, V. Rizzoglio and S. Verdú-Andrés, *Cyclinac medical accelerators using pulsed C^{6+}/H_2^+ ion sources*. Journal of Instrumentation, vol. 5 (2010).

[99] U. Amaldi, R. Bonomi, S. Braccini, M. Crescenti, A. Degiovanni, M. Garlasché, A. Garonna, G. Magrin, C. Mellace, P. Pearce, G. Pittà, P. Puggioni, E. Rosso, S. Verdú-Andrés, R. Wegner, M. Weiss and R. Zennaro, *Accelerators for Hadrontherapy: From Lawrence Cyclotrons to Linacs*. Nucl. Instr. and Meth. A, vol. 620, pp. 563-577 (2010).

[100] A. Degiovanni, U. Amaldi, R. Bonomi, M. Garlasché, A. Garonna, S. Verdú-Andrés and R. Wegner, *A Cyclotron + Linac Complex for Carbon Ion Therapy*. Talk in workshop on "Physics for Health in Europe", CERN, Geneva (Switzerland, 2010): http://indico.cern.ch/contributionDisplay.py?contribId=65&confId=70767

[101] S. Tantawi, *R&D at SLAC for Ultra High Gradient Accelerator Structures*. Talk in "X-band Structures, Beam Dynamics and Sources 2010" workshop, Cockcroft Institute, Daresbury (United Kingdom, 2010): http://agenda.hep.manchester.ac.uk/conferenceDisplay.py?confId=1963

[102] A. Garonna, *Cyclotron Designs for Ion Beam Therapy with Cyclinacs*. Thèse, École Polytechnique Fédérale de Lausanne (Switzerland, 2011).

[103] R. Zennaro, *Linacs for Hadrontherapy: CABOTO, a X-band CArbon BOoster for Therapy in Oncology*. Talk in the "44th ICFA Advanced Beam Dynamics Workshop", Cockcroft Institute, Daresbury (United Kingdom, 2008).

[104] S. Nath, R. D. Ryne, J. Stovall, H. Takeda, J. Xiang and L. Young. *Comparison of linac simulation codes*. Lawrence Berkeley National Laboratory (2001): http://escholarship.org/uc/item/1k41t4r1

[105] P. A. Posocco, private communication (2011).

[106] M. Maggiore, L.Calabretta, M. Camarda, G. Gallo, S. Passarello, L.A.C. Piazza, D. Campo, D. Garufi, R. La Rosa, *Design Study of Medical Cyclotron SCENT300*. Proceedings of the Heavy Ion Accelerator Technology - HIAT 2009, Venice (Italy, 2009).

Aknowledgements

I would like to express my gratefulness to TERA and IFIC for letting me participate in the research of accelerators for hadrontherapy. Many thanks to my supervisors, Prof. Ugo Amaldi, for his tireless and contagious passion for science and for the idea to start up this amazing project, and Dr. Ángeles Faus-Golfe, for the many useful advices and the constant support despite the distance. Special thanks to Prof. José Bernabéu, for convincing me to take this way in the hadrontherapy field.

Special thanks to Prof. Toshiyasu Higo and Prof. Sadayoshi Fukumoto, who made my stage in Japan to be a fruitful and enriching experience from the professional and personal points of view. Thanks to the Frascati group for letting me participate in the high-gradient test of the structure prototype for the SPARC upgrade, and in particular, to Dr. David Alesini.

Thanks to the CLIC-RF structure development group, for the precious scientific and technical support to this project. Special thanks to Dr. Walter Wuensch, for his conciliatory manner to discuss the way forward and his willingness to give always a hand. Thanks to CTF Group at CERN for technical and scientific support for the high-gradient cavity tests. In particular, thanks to Luca Timeo, Dr. Alexey Dubrovskiy, Dr. Jan Kovermann and Dr. Markus Aicheler, for all their immeasurable patience and time and their help.

Thanks to European Commision FP7, who financed my studentship. PARTNER has been a wonderful start up for my scientific career. Thanks to Prof. Manjit Dosanjh for coordinating such a wonderful training network, thanks for the involvement of all PARTNER collaborators and thanks to my PARTNERs for all the great moments lived together. I hope our lifes cross again pretty soon.

Thanks to all the TERA people, a marvellous bunch of extremely enthusiastic, hard-working and committed young researchers with a great heart, who became my family at CERN. In particular, my colleagues and friends Dr. Rossana Bonomi, Alberto Degiovanni and Marco Garlaschè, with whom I had passionate and enlightning discussions, about professional and personal subjects, but also human and divine ones. Special thanks to Dr. Rolf Wegner, for his constant support and sincere friendship. Thanks to Dr. Piero Posocco, for his readiness to discuss my work and his constructive criticism. Thanks to Maria Di Rosa for all the assesment in daily life and her administrative support.

Special thanks to my family and friends, because you wholehearted supported me

in this exciting adventure.